Charles University in Prague

Faculty of Mathematics and Physics

Azimuthal Correlations of High-p_T Pions in 158 AGeV/c Pb-Au Collisions Measured by the CERES Experiment

Doctoral Thesis

Mgr. Jana Slívová

Supervisor: Prof. Dr. Johann Peter Wurm

Max-Planck-Institut für Kernphysik, Heidelberg

May, 2003

Declaration of Originality

This doctoral thesis contains the results of my research carried out in the Max-Planck-Institut für Kernphysik in Heidelberg and in the Physikalisches Institut der Universität Heidelberg between November 1997, and May 2003.

Excluding introductory parts the research described in this thesis is original unless where an explicit reference is made to work of others. Some of this work was carried out within the CERES/NA45 Collaboration. I further state that no part of this thesis or anything substantially the same has been submitted for any qualification other than the degree of Doctor of Philosophy at the Charles University in Prague.

Abstract

The production of charged particles ($h^{\pm}$), and pions ($\pi^{\pm}$) with large transverse momenta is studied in 158 AGeV/c Pb-Au collisions. The analyzed data sample, measured by the CERES/NA45 experiment at the CERN SPS near mid-rapidity ($2.1 < y < 2.6$), consists of 42 millions of events taken at the most central 30% of the geometric cross section (σ_{geo}).

Transverse momentum spectra of h^- ($0.2 < p_T < 2.5$ GeV/c) and high-p_T pions ($1.2 < p_T < 3.5$ GeV/c) are nearly exponential over the covered p_T range. The average inverse slope parameter is $T = (195 \pm 5)$ MeV for h^- and $T = (235 \pm 5)$ MeV for high-p_T pions, respectively. The local inverse slope rises by about 50% in the p_T range of 0.5 to 3.0 GeV/c. In comparison to scaled p-p data, there is an enhancement in yield at $p_T > 1$ GeV/c observed and $\alpha(p_T)$ rises up to a value of 1.25 at $p_T = 3.5$ GeV/c, which is ascribed to the Cronin effect.

The main objective is the study of azimuthal anisotropies in order to unravel dijet-like correlations from elliptic flow. For this purpose, we study both the azimuthal distributions of particles with respect to the reaction plane, and two-particle azimuthal correlations, which might at large p_T reveal also relics of primary scattering in the semi-hard sector. The differential elliptic flow coefficient v_2 rises linearly with p_T and flattens above $p_T \approx 1.5$ GeV/c at about 11% in semi-central collisions. The measured v_2 remains below hydrodynamical expectations which indicates that only a partial equilibration is achieved. Two-pion azimuthal anisotropies for $p_T > 1.2$ GeV/c exceed the elliptic flow values by about 40% in semi-central collisions. This discrepancy increases with p_T and decreases with centrality. We argue that the observed non-flow anisotropies are due to near-side and back-to-back jet-like correlations. While the Gaussian width of the near-side component remains narrow at $\sigma = (0.23 \pm 0.03)$ rad at all centralities and is consistent with fragmentation, the back-to-back component exhibits centrality dependent broadening up to $\sigma = (1.26 \pm 0.28)$ rad in central collisions of $\sigma/\sigma_{geo} =$ (6-15)% and disappears in the most central collisions. The yield of the semi-hard components grows with number of binary collisions. Both components display a weak preference for emission in the reaction plane.

Contents

List of Figures

List of Tables

1

Introduction

Experimental studies of hot and dense nuclear matter created in collisions of heavy nuclei are of common interest to nuclear and particle physics, astrophysics and cosmology. The ultimate goal is the observation and exploration of a new state of matter, the *Quark Gluon Plasma (QGP)* and of a related phase transition in which *chiral symmetry* is restored. It is believed that the early Universe has consisted of QGP up to a few microseconds after the Big Bang [1, 2] and QGP may still exist in the interior of neutron stars [3–5].

Many dedicated experiments have been designed and built to study in a systematic way various signals associated with QGP production. However, its experimental observation and exploration is still a challenging task because of its elusive characteristics. Besides the small size of the reaction volume (several fm in diameter) and very short lifetime of QGP (5-10 fm/c), a major problem is posed by the competition between signals coming from QGP and emission from the hot hadronic gas phase complicated by final state interaction during the hadronization process. The general opinion is therefore, that only from a combination of various signatures one might eventually conclude, whether the quark-gluon plasma was created or not.

The main purpose of the CERES (**C**h**E**renkov **R**ing **E**lectron **S**pectrometer) experiment is to measure low-mass electron-positron pairs ($0.1 < m_{e^+e^-} < 1.5$ GeV/c^2) produced in p-A and A-A collisions at the CERN SPS accelerator. Dileptons, together with photons, are an especially attractive probe of hot and dense matter since they are produced at all stages of the collision, and in contrast to hadrons, interact only electromagnetically. Thus, they probe directly early stages of the collision and carry this information essentially unperturbed to the detectors.

The low-mass region is governed by the light quark flavors – u, d and s. In the limit of vanishing quark masses, the QCD phase transition is associated with chiral symmetry restoration which should show up in medium modifications of the light vector mesons (ρ, ω and ϕ). Here, the ρ meson is of a particular interest because of its short lifetime (τ = 1.3 fm/c) in comparison to the lifetime of the fireball (τ = 10–50 fm/c). Its decays sample the state of the hot and dense medium during its time evolution.

Low mass dilepton pairs are produced only with a 10^{-5} fraction relative to pions. Their detection in the environment of Dalitz decays, conversion pairs and pions is very difficult [6–12]. Whereas the p-Be and p-Au data at 450 AGeV [13] are well reproduced

by final state hadron decays, the S-Au measurement at 200 AGeV [14] as well as Pb-Au measurements at 40 AGeV [12, 15] and 158 AGeV [16, 17] show an enhancement of the yields of low-mass electron pairs above that of known hadron sources by factors of 2–5, albeit with large errors. Since the final state in A-A collisions is characterized by a large pion density, the observed increase of the dilepton yield can be mainly attributed to the $\pi^+\pi^- \rightarrow l^+l^-$ annihilation. The in-medium modifications of the ρ meson have been proposed as the solution for the remaining discrepancy [18] . Currently, two different scenarios are discussed, a dropping vector meson mass scenario [18–21], and broadening of the ρ mass peak [22–24]. However, the precision of the data does not allow yet to distinguish between these two approaches.

A very different, hadronic observable probing the early stages of a heavy-ion collision is *elliptic flow* [25, 26] which manifests itself in an azimuthal anisotropy of emitted particles with respect to the reaction plane. This collective effect is driven by anisotropic pressure gradients built up during early stages of the collision in the geometrically anisotropic overlap zone. By comparing the magnitude of elliptic flow to hydrodynamical calculations, the degree of equilibration achieved during evolution and important information about the equation of state of the nuclear matter may be obtained.

The measurement of two-particle azimuthal correlations, particularly at large transverse momentum (p_T), might also reveal, besides elliptic flow, relics of primary scattering in the semi-hard sector which escape complete equilibration. High-p_T particles, while traversing the hot and dense medium created in the collision, might loose their correlations due to scattering or absorption. Therefore, it is interesting to investigate the centrality behavior of the two-particle correlations as well as its relation to the orientation of the reaction plane.

In this work, a systematic study of both the azimuthal anisotropies of pions with respect to the reaction plane as well as the two-pion azimuthal correlations is performed in order to isolate semi-hard scattering from collective elliptic flow. This way, the Cronin effect which is masking the inclusive transverse momentum distributions at large p_T at SPS energy ($\sqrt{s}$ = 17 GeV) might be overcome. The full azimuthal acceptance of the CERES spectrometer together with its capability to detect high momentum pions ($p > 4.5$ GeV/c) provide an excellent experimental tool for such studies. The analysis of charged hadrons and high-p_T pions presented in this thesis is based on the Pb-Au data taken at 158 AGeV/c during six weeks of beam time in the fall of year 1996. Up to now, only dilepton [9–11] and direct [27] photon analyses on the full data set were performed. On a limited data sample, inclusive transverse mass spectra of charged hadrons were investigated [28].

The thesis is structured as follows. Chapter 2 introduces to the physics topics discussed in this work. Chapter 3 describes the overall CERES experimental setup, Chapter 4 the radial silicon drift detectors. Personally, I was involved in the installation of the equipment at CERN, its testing, and later in analyzing the data from these detectors. An overview of the tracking strategy, calibration procedures and momentum determination is given in Chapter 5. Chapter 6 describes the Monte-Carlo simulation of the spectrometer which is essential for various data corrections. In Chapter 7 we discuss the centrality determination and the event classification. In Chapter 8 we present the results of the inclusive transverse mass spectra of negative charged particles and high-p_T pions. The results are compared to other experiments and hydrodynamical models with an aim to extract in-

formation about the freeze-out parameters. Chapter 9 describes the determination of the event plane and the results on elliptic flow of charged hadrons and high-p_T pions obtained from the analysis of the azimuthal particle distributions with respect to the event plane. The centrality and transverse momentum dependence of elliptic flow is studied and compared to other experiments and hydrodynamical models. Measurements of two-particle azimuthal correlations of high-p_T pions are presented in Chapter 10 and compared to the results on collective elliptic flow. The observed non-flow component, presumably of the semi-hard origin, is studied for different centrality and p_T selections, and also its relation to the event plane is investigated. Finally, Chapter 11 contains conclusions and outlook.

2

Ultrarelativistic Heavy Ion Collisions

The physics program has started in 1986 when the first heavy ion beams became available both at the Alternating Gradient Synchrotron (AGS) in Brookhaven National Laboratory (BNL) and at the Super Proton Synchrotron (SPS) at CERN. Since that time many experiments were set up in order to investigate in a systematic way the features of heavy-ion collisions. This field of physics is still developing and three years ago a new facility, the Relativistic Heavy Ion Collider (RHIC) in BNL, has become operational and another one, the Large Hadron Collider (LHC), is currently under construction at CERN.

2.1 QCD Predictions

The strong interaction of quarks and gluons, which stabilizes nuclei, is described in the framework of quantum chromodynamics (QCD). This theory has two remarkable properties: (1) *asymptotic freedom*, at short distances the coupling constant goes to zero, and (2) *confinement*, at large distances the binding between quarks grows giving thus rise to a strong attractive force confining quarks into hadrons. As it was soon realized, the asymptotic freedom also implies that a transition from hadronic matter to a plasma of quarks and gluons (QGP) should occur at high temperature and/or when nuclear matter is compressed to a sufficiently high density.

Another important property which arises from the QCD Lagrangian is that of *chiral symmetry breaking* - the quarks confined in hadrons are not massless, but they possess a dynamically generated mass of a few hundred MeV. The expectation value of the *quark condensate* $\langle\bar{\psi}\psi\rangle \approx$ –(235 MeV)^3 describes the density of $q\bar{q}$ pairs in the QCD vacuum and the fact that it is not vanishing is directly related to the chiral symmetry breaking. In the limit of zero current quark masses, the quark condensate vanishes at high temperature and chiral symmetry is restored.

On the qualitative level the two extremes of the deconfinement curve can be estimated from the *M.I.T. bag model* [29–31]. The asymptotic freedom and the confinement, are in this simple model incorporated in a crude way. Quarks are treated as massless particles inside a bag of finite dimensions and are infinitely massive outside the bag. Confinement in this model is the result of the balance between the bag pressure directed inward and the

stress arising from the movement of the quarks. If the pressure of the quark matter inside the bag is so big that it cannot be balanced anymore an unconfined state is created. This can happen when a strong compression causes hadrons to overlap significantly, reaching density 3–5 times higher than that of an ordinary nuclear matter (0.17 fm^{-3}), or when temperature exceeds a critical value of $T_c \approx$140 MeV.

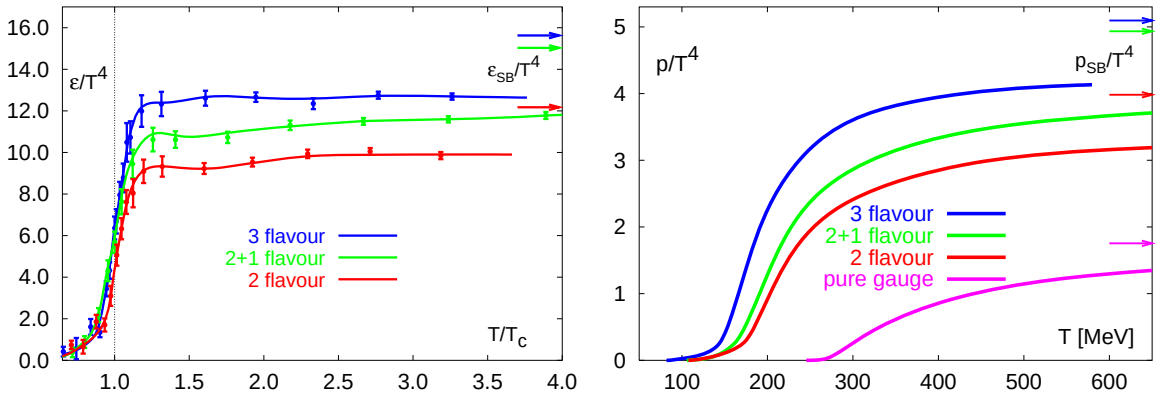

Figure 2.1: Energy density (left) and pressure (right) in the lattice QCD calculations with n_f = 0,2 and 3 light quarks as well as two light and a heavier (strange) quarks. Arrows indicate the ideal gas values of energy density and pressure. The figure is taken from [32].

More quantitative results are obtained from the QCD calculations. While in the perturbative QCD a lot of progress has been made, the analytical and numerical solutions in the non-perturbative QCD are still very tedious and difficult to obtain. Based on the numerical calculations on a lattice with 2 or 3 quark flavours at zero baryon density [32] the critical conditions for the phase transition are expected to be reached at a temperature of $T_c \approx 170$ MeV corresponding to the energy density $\epsilon_c \approx 1$ GeV/fm^3 (Fig. 2.1). Due to the finite size of lattice it is difficult to establish whether one deals only with a transitional behavior or with a phase transition and if so, of what order.

2.2 Space-Time Evolution of a Heavy-Ion Collision

Collisions of two heavy nuclei at high energies provide a unique opportunity to study hot and dense nuclear matter in laboratory under conditions similar to those that existed in the early Universe. For a collision at an energy of a few GeV per nucleon in the center of mass system (CMS), typical for the fixed target experiments at the AGS and at the SPS accelerators, the separation between the beam and the target rapidities is typically about 3 units. This fact together with the Lorentz contraction of the colliding nuclei, leads to a high baryon density of the matter created [33] possibly sufficient to create the quark-gluon plasma with a high baryon content. At much higher energies ($\sqrt{s} \geq 100$ GeV), as studied nowadays at RHIC and in the future at LHC, the separation between the beam and the target rapidities is much greater than a few units. After a central collision the rapidities of the beam and of the target baryons remain far away from the mid-rapidity region which

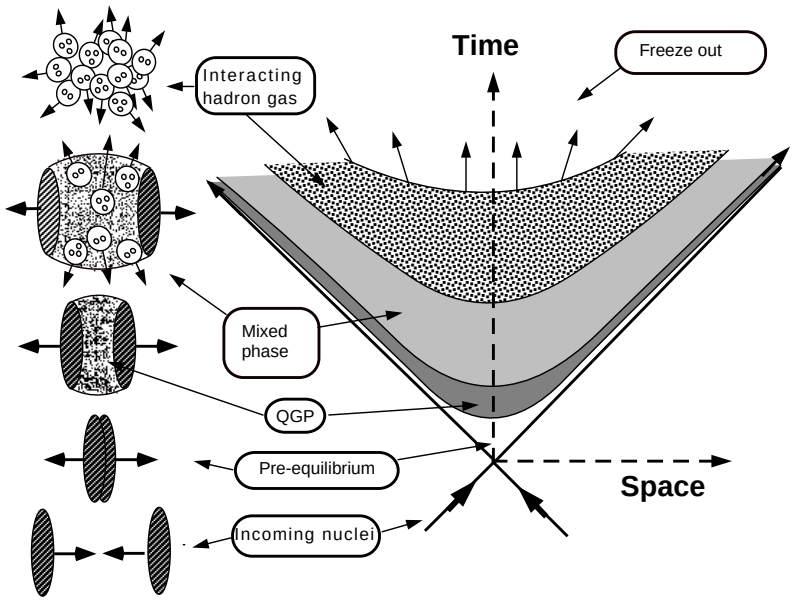

Figure 2.2: Schematic space-time evolution of a heavy-ion collision with QGP formation scenario. The hyperbola represents a constant proper time. The figure is taken from [34].

results in a very small net baryon content in the central rapidity region. Thus at those energies net baryon-free QGP can be explored.

Fig. 2.2 shows a schematic picture of the space-time evolution of a heavy-ion collision. Two incoming nuclei, which move almost with speed of light before their collision, are depicted as thin discs due to a strong Lorentz contraction (at the SPS 10:1). At the first instants after the collision a fraction of the original energy, which was deposited in a small region of space in a short duration of time, is redistributed in nucleon-nucleon collisions into other degrees of freedom, materializing into quarks and gluons after $\tau \approx 1$ fm/c (*formation time*). Parton-parton interactions might then lead, if the energy density is high enough, to formation of the QGP. The pressure inside the hot and dense medium leads to an expansion of the system while its temperature and density are decreasing. If created, the QGP would rapidly cool down during expansion and evaporation, going through a *mixed phase*, in which hadrons and blobs of plasma coexist, and finally condensate into ordinary hadrons. The interacting gas of hadrons further expands and cools to the point referred to as *chemical freeze-out*, where all inelastic interactions between the particles cease and the abundancies of hadrons are fixed. With further decrease of the temperature/density also the elastic interactions vanish (*thermal freeze-out*) and particles stream towards the detectors.

Fig.2.3 represents a phenomenological phase diagram of strongly interacting matter with temperature ploted versus chemical potential. Distinct phases of nuclear matter can be identified. Measuring the critical parameters governing the transitions among these phases is crucial for understanding the nuclear equation of state. The properties of the system at the freeze-out are quite well known from the systematic study of particle ra-

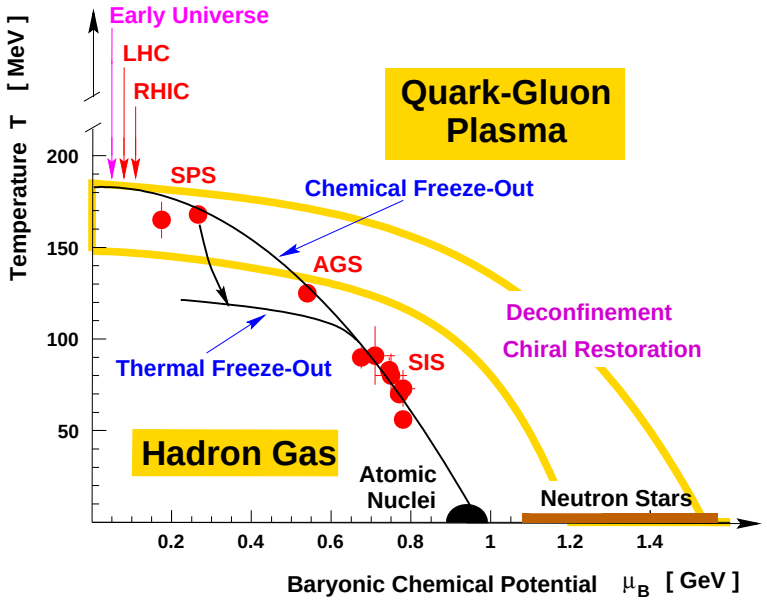

Figure 2.3: Phase diagram of hadronic matter. The points show chemical freeze-out of hadrons extracted from heavy ion collisons at the SIS, AGS, SPS, and RHIC. The figure is from [35].

tios. The extracted temperatures and baryon chemical potentials are at the beam energies beyond 10 AGeV very close to the expected phase boundary to QGP.

In order to prove the existence of the quark-gluon plasma we need to have observables (or *'signatures'*) sensitive to its presence. During the last years many different experimental observables were proposed as possible signatures of the QGP formation [1]. Among all of them, studies of collective phenomena allow a systematic comparison between the situation at lower beam energies dominated by hadron gas, and the higher beam energies where the new state of matter might be produced. Although many hadronic observables, like particle ratios [37–40], lose memory of the initial conditions, signatures based on collective flow, which is driven by the pressure gradients and is built up at all stages of the collision history, are expected to bring an important information about the properties of hot and dense matter created.

2.3 Collective Flow in Heavy Ion Collisions

The initial compression and heating build up a high pressure that in turn causes a significant collective flow of particles which is superimposed on top of the thermal motion. Provided the local thermal equilibrium is reached in the course of the collision, the expansion of the hot and dense system can be described by hydrodynamical models offering tremendous theoretical simplifications. From a hydrodynamical point of view the dynamics of the expanding system is described by the energy density ϵ, the pressure P, the temperature T, and the 4-velocity $u^\mu = dx/d\tau$ at different space-time points. These quantities are related by the *equation of state (EOS)*: $\epsilon = \epsilon(P, T)$. Investigation of the collective motion driven by the pressure gradients provides a diagnostic tool for studying the compressibility of nuclear matter and thus better understanding of the EOS.

[1] For a review of various QGP signatures is reader referred e.g. to [31, 36].

Assuming that the nuclear matter behaves like a compressible fluid Belenkij and Landau [41] applied a fluid dynamical model to describe the collisions of nucleons and nuclei. Later, an idea that a *nuclear shock wave* could be formed when a projectile moves through a nucleus at a velocity exceeding the nuclear speed of sound was proposed by Glassgold, Heckrotte, and Watson already in 1959. However it remained unnonticed until 1970's, when it was realized that the passage of a light projectile through the nucleus might not be sufficient to create the shock wave. This fact together with an increasing availability of heavy-ion projectiles led Scheid, Müller, and Greiner [42] and others [43–45] to apply the same concept into heavy-ion collisions and to predict collective flow in transverse direction. They showed that the matter should be pushed outwards perpendicular to the relative motion of the colliding nuclei. This effect was later called *squeeze-out* or *sideward flow*.

The first experimental evidence of the expected collective motion was obtained at the Bevalac accelerator in Berkeley [46, 47]. The data from 4π detectors confirmed the expected occurence of the sideward flow. Since that time the flow effects are investigated in a systematic way in a wide energy range, starting from low and intermediate energy experiments at $\sqrt{s} \approx 0.1$ AGeV, through the relativistic energy experiments at $\sqrt{s} \approx 1$ AGeV to the ultrarelativistic energies $\sqrt{s} \approx 10 - 200$ AGeV. A detailed review of the collective flow phenomena is given e.g. in [48, 49]. Two types of flow patterns develop as the hot and dense system created in the collision expands: (i) azimuthally isotropic *radial flow*, and (ii) azimuthally *anisotropic transverse flow*. Since both of them will be accessed in this thesis, they are discussed separately below.

2.3.1 Radial Flow

The radial flow is very important for a full thermodynamical description of a heavy-ion collision and the freeze-out parameters. Its existence is nowadays commonly accepted, since the measured features of the particle spectra can be only understood when the radial flow velocities are introduced.

Fireball model

The first attempt to describe the cross sections in heavy-ion collisions was based on the *fireball model* [50]. Assuming nuclear matter is an ideal gas globally thermalized at the end of reaction, the cross section can be determined from the thermal momentum distributions of the particles. The invariant momentum spectrum of particles radiated by a thermal source of temperature T is given by

$$E\frac{d^3N}{d^3p} = \frac{d^3N}{m_T dm_T dy d\phi} = \frac{gV}{(2\pi)^3} E e^{-(E-\mu)/T} \tag{2.1}$$

where E is the energy, g the spin-isospin degeneracy factor for the particle species, μ the grand-canonical potential and V is the volume of the source. The transverse mass spectrum is obtained by integrating Eq.(2.1) over rapidity:

$$\frac{dN}{m_T dm_T} = \frac{V}{2\pi^2} m_T K_1\left(\frac{m_T}{T}\right) \overset{m_T \gg T}{\longrightarrow} V' \sqrt{m_T}\, e^{-m_T/T}, \tag{2.2}$$

where K_1 is the modified Bessel function, which behaves asymptotically like a decreasing exponential for $m_T \gg T$. The basic characteristics of the measured m_T spectra is indeed

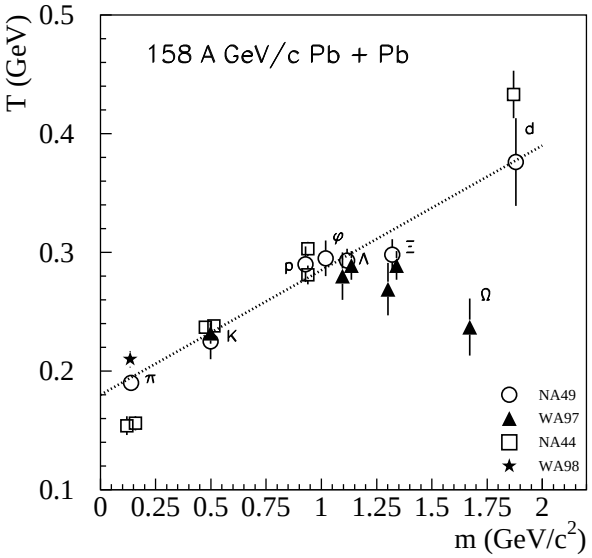

Figure 2.4: Dependence of the transverse mass inverse slope parameter on the particle mass at the SPS [35, 51–59].

the 'exponential decrease' over many orders of magnitude with an almost uniform slope $1/T$. However, a closer look at the spectra of charged pions shows a significant concave curvarture (*'low-m_T enhancement'*). In addition, the data exhibit a linear dependence of the temperature on the particle mass as depicted in Fig. 2.4. Moreover, the rapidity distributions of the emitted particles obtained by integrating Eq. (2.1) over the transverse components (for details see [60])

$$\frac{dN_{\text{thermal}}}{dy} \approx m^2 T(1 + 2\chi + 2\chi^2)e^{-1/\chi}, \tag{2.3}$$

where $\chi = T/(m\text{cosh}y)$, are too narrow in comparison with the data (cf. Fig. 2.5).

Blast-wave scenario

Later theoretical approaches lead to an idea, that the observed spectra may be understood as a consequence of a blast wave of exploding nuclear matter [50]. The blast wave explosion is a result of frequent collisions of the rapidly moving particles in the hot matter. In a hydrodynamical approach, valid in the limit of very frequent collisions, the matter acquires locally an outward-directed macroscopic flow velocity β_r by converting internal thermal energy into work through a pressure gradient $-\nabla P$. The velocities v of particles have thus two components

$$v = \beta_r + v_{\text{thermal}}, \tag{2.4}$$

where the collective flow velocity β_r is assumed to be the same for all particles, and the velocity v_{thermal} is deduced from the temperature of the thermal random motion. The average kinetic energy E of a particle with mass m is then

$$\langle E \rangle \approx \langle E_{\text{flow}} \rangle + \langle E_{\text{thermal}} \rangle = m \left(\frac{1}{\sqrt{1 - \beta_r^2}} - 1 \right) + \frac{3}{2} T. \tag{2.5}$$

While the thermal energy E_{thermal} is independent on particle mass, the collective contribution E_{flow} is proportional to mass, in line with the observations (Fig. 2.4). The energy

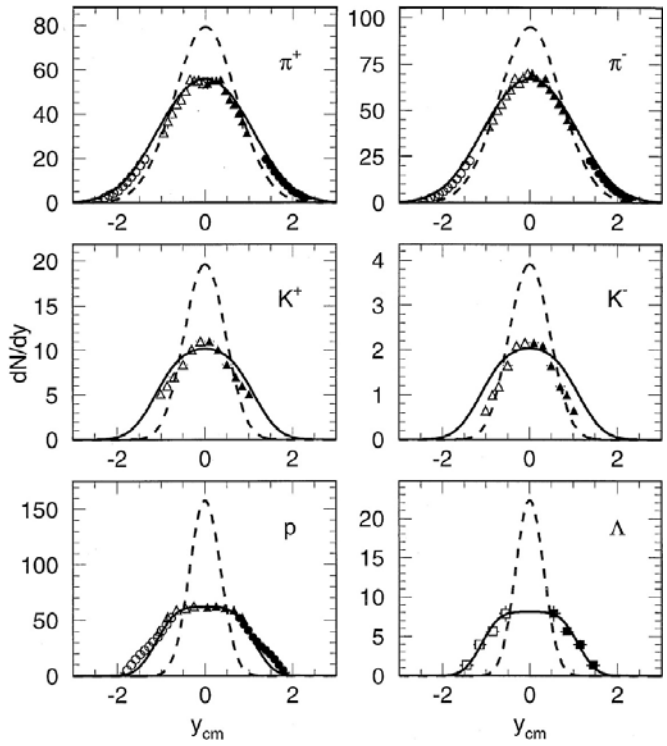

Figure 2.5: Rapidity density distribution for different particles in Au-Au collisions at 10.8 and 11.6 AGeV/c at the AGS. The dashed line indicates the distribution expected for isotropic emission from a thermal source at T = 120 MeV. The solid line includes a collective longitudinal expansion on top of the thermal motion. The data (solid symbols) are reflected about midrapidity (open symbols). The figure was taken from [49], where a compilation of the data taken by E802/866 (triangles, [61, 62]), E877 (circles, [63, 64]), and E891 (squares, [65]) experiments was performed.

distribution in the CMS system obtained from this model is given by

$$\frac{dN}{dEd\Omega} = \frac{8\pi e^{\mu/T}}{(2\pi\hbar)^3}\left[\left(\gamma + \frac{T}{E}\right)\frac{\sinh\alpha}{\alpha} - \frac{T}{E}\cosh\alpha\right]e^{-\gamma E/T}, \tag{2.6}$$

where E is the total energy, p particle momentum in the CMS system, $\gamma = (1-\beta_r^2)^{-1/2}$ and $\alpha = \gamma\beta_r p/T$. This expression describes well the 'shoulder arm' shape of the spectra.

While a common temperature for the radial flow was justified experimentally, the local flow velocity β_r was found to approximately follow a 'Hubble-like relation' $\beta_r = hr$ at all times. All observables (density, temperature, pressure, flow, etc.) are then found to be functions of the scaled radius r/R. In [66, 67] it was suggested to use a radial velocity profile of type

$$\beta_r(r) = \beta_s\left(\frac{r}{R}\right)^n, \tag{2.7}$$

where R is the freeze-out radius of the system, β_s is the maximum surface velocity and n is the parameter varying the form of the profile.

At low energy collisions, the radial expansion is not only azimuthally isotropic, but also spherically symmetric. However, at higher energies, which are of interest in this work, the radial expansion has to be considered separately in transverse and longitudinal directions due to the already mentioned Lorentz contraction of the colliding nuclei.

Longitudinal expansion

In order to achieve agreement with the rapidity distributions observed in the data, the *boost-invariant* longitudinal expansion model originally introduced by Bjorken [68] was applied. The particle spectrum results from the summation of the spectra of individual thermal sources distributed uniformly in flow angle η. However, since this model

was formulated in the limit of asymptotically high energies, it had to be modified to account for the limited available beam energy by restricting the boost angle η to the interval (η_{min}, η_{max}). The rapidity distribution is then given by

$$\frac{dn}{dy}(y) = \int_{\eta_{\min}}^{\eta_{\max}} d\eta \, \frac{dn_{\rm th}}{dy}(y-\eta). \tag{2.8}$$

Comparison to data shows very good agreement as demonstrated in Fig. 2.5 for several particle species.

Transverse expansion

In the same phenomenological approach [60], the transverse mass distributions (Fig. 2.6) of particles are the result of a superposition of individual thermal sources, each boosted with the angle $\rho = \tanh^{-1}\beta_r$:

$$\frac{1}{m_T}\frac{dN}{dm_T} \propto \int_0^R r dr m_T I_0\left(\frac{p_T \sinh(\rho)}{T}\right) K_1\left(\frac{m_T \cosh(\rho)}{T}\right), \tag{2.9}$$

where I_0 and K_1 are the modified Bessel functions. It can be shown [60, 69] that in the limiting case for large m_T the inverse slope ('temperature') of the m_T spectrum is larger than the original temperature by a *'blue shift factor'*

$$T_{\rm eff} = T\sqrt{\frac{1+\beta_r}{1-\beta_r}}. \tag{2.10}$$

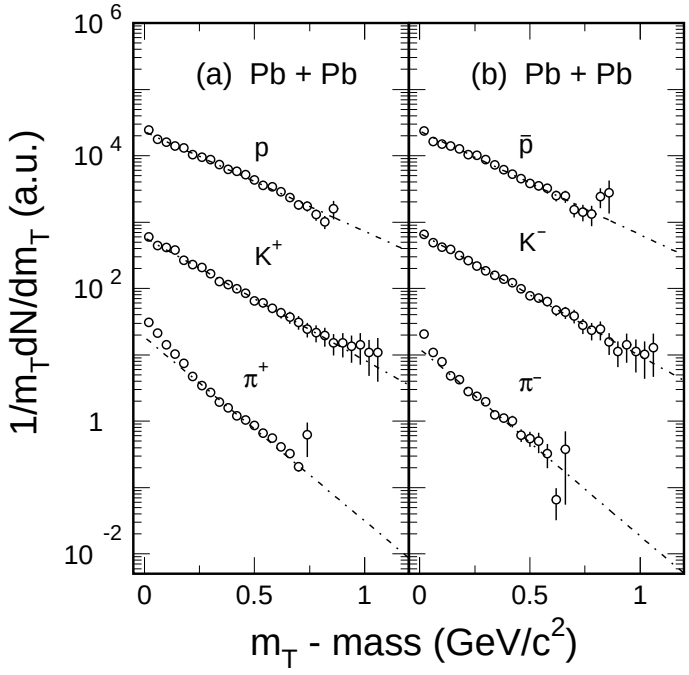

Figure 2.6: Transverse mass distributions from pions, kaons, protons and their antiparticles from 158 AGeV/c Pb+Pb central collisions measured by the NA44 experiment. Dashed lines represent exponential fits. The figure is taken from [51].

2.3.2 Anisotropic Transverse Flow

Another type of flow that develops in the course of an A-A collision is an azimuthally anisotropic transverse flow. The origin of this flow effect is different from the above discussed radial flow. It results from the geometrically anisotropic overlap zone of projectile and target nuclei in non-central collisions which is schematically depicted in Fig. 2.7. The reaction plane is the plane spanned by the beam axis and the impact parameter of the two colliding nuclei. The matter has a natural tendency to flow in the direction where

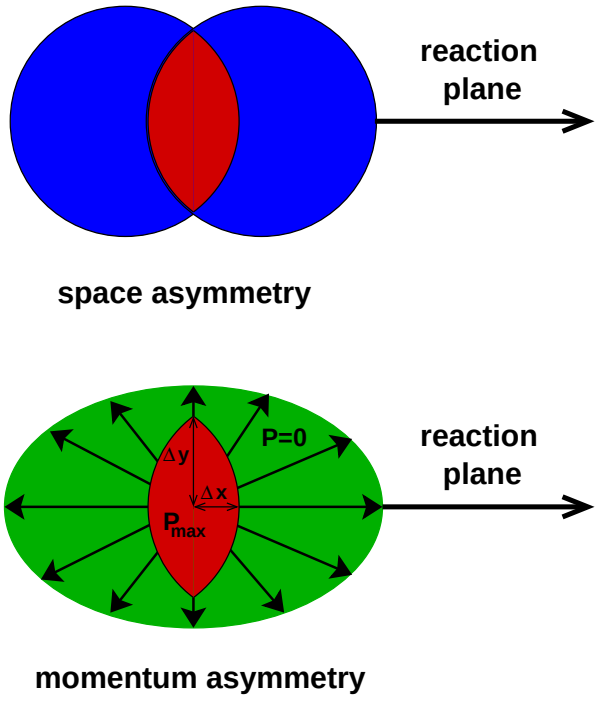

Figure 2.7: Schematic view of a nucleus-nucleus collision in the transverse plane. The space asymmetry in the collision (top) is reflected in the momentum asymmetry (bottom) of the produced particles. See text.

the pressure gradient is largest. As a consequence, the transverse expansion will generate collective motion pronounced along the direction of the reaction plane and it will be reflected in the transverse momenta preferentially oriented along the same direction.

Two types of azimuthally anisotropic flow are distinguished and studied extensively both, experimentally and theoretically: *directed flow* and *elliptic flow*. The first mentioned type of flow describes sideward motion of particles, the second one is connected with an elliptic deformation of azimuthal distributions of emitted particles.

The standard and commonly accepted method which enables to extract information on directed and elliptic flow is a Fourier decomposition of the azimuthal distributions of emitted particles with respect to the reaction plane [70]

$$\frac{dN}{d(\phi - \Psi_R)} = A\{1 + \sum_{n=1}^{\infty} 2v_n \cos[n(\phi - \Psi_R)]\}, \tag{2.11}$$

where A is the uncorrelated background, ϕ is the azimuthal angle of a particle, Ψ_R the reaction plane angle, and n denotes the order of the Fourier harmonics. The first Fourier coefficient v_1 quantifies the strength of the directed flow, and the second Fourier coefficient v_2 the magnitude of the elliptic flow. However, the orientation of the reaction plane is a priori unknown in any experiment and it has to be estimated from the measured data.

Another possibility to extract information on directed and elliptic flow is the method of two-particle azimuthal correlations [71, 72]. The idea behind is that correlations of particles with the reaction plane introduce correlations among particles themselves. The two-particle correlation can be again described using the Fourier method as

$$\frac{dN}{d(\phi_i - \phi_j)} = B\{1 + \sum_{n=1}^{\infty} 2v_n^2 \cos[n(\phi_i - \phi_j)]\}, \tag{2.12}$$

where B is the uncorrelated background, ϕ_i and ϕ_j are the azimuthal angles of the emitted particles. The expected flow signal in two-particle correlation method is very small in magnitude, since the coefficients v_n, which are of the order of several percent, enter quadratically. However, there is no need to reconstruct the reaction plane. Moreover, the two-particle correlations are sensitive to direct particle-particle correlations (see Section 2.4 below). [2]

We will concentrate in this work on elliptic flow. The excitation function of elliptic flow displayed in Fig. 2.8 shows a monotonic behavior. A 'kink' at some specific energy could point to a significant change in the properties of the hot and dense matter created in the collision and indicate thus a phase transition. As can be seen, elliptic flow vanishes in two different regions of beam energy and changes its sign in between. What are the physics mechanisms causing the observed behavior?

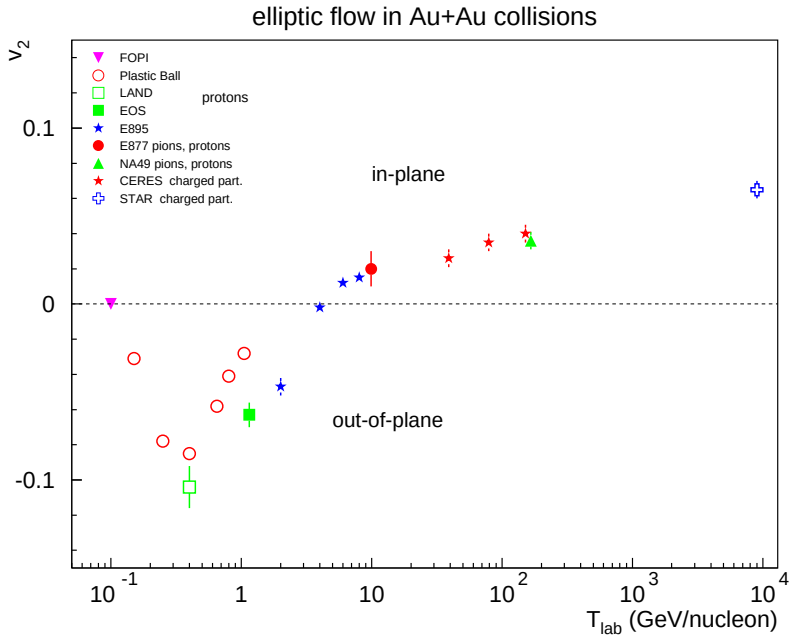

Figure 2.8: Dependence of the elliptic flow on beam energy. The figure is taken from [76].

[2] Recently, a *cumulant method* based on multiparticle correlations was suggested by Ollitrault *et al* [73–75]. This method cannot be applied on the data analyzed here, since at high-p_T the particle multiplicities are very small to be able to construct multiparticle correlations.

The origin of elliptic flow at various beam energies depends on different physics mechanisms. While in the regime below 100 AMeV (MSU, GANIL) the angular momentum transferred by the projectile enhances particle emission from the fast rotating compound nucleus in the reaction plane giving thus rise to a positive elliptic flow component [77], at energies of 100-1500 AMeV (SIS, Bevalac), the net nuclear potential is repulsive, and the passage time of the spectators ranges from 15-45 fm/c. Since considerable compression and heating of the nuclear matter is reached at these energies, the physics scenario of a rotating compound nucleus is inappropriate and a vanishing of the elliptic flow is expected. This disappearance of the elliptic flow was reported close to energy of 100 AMeV for Au-Au collisions [78]. Above this energy, the magnitude of elliptic flow was found to be negative or in other words *out-of-plane* [78–82]. It is a direct consequence of the shadowing effect of the passing spectators, which reduce the mean free path of particles emitted in the reaction plane with respect to the emission in the perpendicular direction. Around 4-6 AGeV (AGS, [83–85]) the elliptic flow vanishes again and above this energy it is oriented in the reaction plane and increases continuously its strength [86–88] towards SPS [76, 89–91] and RHIC energies [92–95]. This observation was explained by the counterplay of a reduced shadowing and a preferred in-plane emission of particles from the fireball [26]. It indicates also an increased pressure builds up along the direction of the impact parameter as Ollitrault predicted [25]. The transition point, where the elliptic flow changes its orientation from out-of-plane to in-plane, could therefore be sensitive to the EOS.

2.4 Jets as a Probe of Hot and Dense Nuclear Matter

Jet production is a direct consequence of parton scatterings predicted by perturbative QCD. The description of the measured inclusive particle spectra from high energy p-p collisions within the pQCD parton model was one of the early successes of this model [96–99]. For p-A collisions, the model had to be extended to include the nuclear modification of the parton distributions [100] and the nuclear enhancement at high-p_T [101].

Already in the late 1980's, jets produced in collisions of two heavy nuclei were suggested as one of possible quark-gluon plasma probes [102–104]. Like other hard processes, parton jets with large transverse momentum are produced at early stages of a heavy-ion collision. In contrast to p-p collissions, jets from heavy-ion collisions have to travel through the hot and dense nuclear matter produced in the collision before they hadronize. This may significantly affect the momentum distributions of the outgoing hadrons. Theoretical studies have shown that partons will suffer a significant energy loss via induced gluon radiation while propagating through a medium [105–109] . Since the radiated gluons will eventually become incoherent from the leading parton fragmenting into high-p_T hadrons, one expects a suppression of those particles at large $\sqrt{s}$. This effect, commonly referred to as *'jet quenching'*, is experimentally observed at RHIC [110–113] where the charged particle and pion spectra in central collissions are suppressed in yield as shown in Fig. 2.9. At the SPS, however, an enhanced production of high-p_T particles was observed and interpreted in terms of initial state p_T broadening effects (*'Cronin effect'*, [101]).

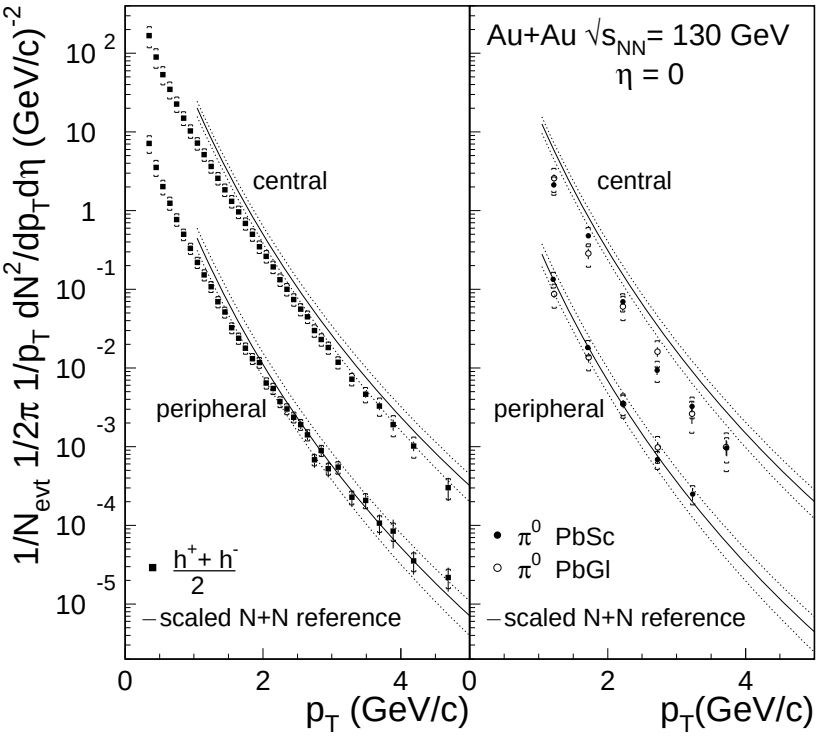

Figure 2.9: The inclusive p_T spectra of $h^{\pm}$ (left) and π^0 (right) measured by the PHENIX Collaboration in Au-Au collisions ($\sqrt{s} = 130$ GeV) for 60–80% (lower) and 0–10% (upper) fractions of the geometric cross section. The error bars indicate the statistical errors on the yield; the surrounding brackets indicate the systematic errors. Also shown are the scaled p-p references (the bands indicate the uncertainty in the p-p reference and in the scaling.). The figure is from [110].

Experimentally, jets are identified in p-p collisions as hadronic clusters whose transverse energy E_T is reconstructed from the energy deposited in calorimeters. However, in nucleus-nucleus collisions the cluster-finding method becomes difficult or even impossible due to a large background of soft particles. In [114, 115] a study of the transverse momentum dependence of the two-particle correlations was suggested as an alternative method to resolve (mini)jet contributions to particle production. Since particles from jet fragmentation cluster together in phase space, the two-particle correlation is expected to be enhanced. In particular, two-particle correlation at large p_T in the azimuthal angle difference $\Delta\phi$ should be strongly peaked at both forward ('near-side') $\Delta\phi = 0$, and backward ('back-to-back') $\Delta\phi = \pi$ directions. Moreover, a pair of minijets can be produced with a large rapidity gap in between. Therefore, the two-particle correlation in a limited rapidity window will have reduced minijet contribution to the backward correlation, while the forward correlation still remains and is even enhanced due a short-range character of two-particle correlation [114]. At the SPS, besides preliminary reports on $\gamma - \gamma$ correlations in Pb-Pb collisions [116, 117], no observation of dijet-like correlations of charged particles exists.

3

The CERES Experiment

Since the CERES/NA45 experiment is dedicated to the measurement of the low-mass e^+e^- pairs, its experimental setup had to be optimized for this experimentally challenging measurement. There are two main experimental difficulties which CERES has to deal with. The number of produced e^+e^- pairs compared to the number of produced charged hadrons is only of the order of 10^{-5}. This difficulty was attacked by using two RICH detectors with high Cherenkov threshold.The large amount of photons produced in the collision and e^+e^- pairs coming from their conversions causes the second difficulty, which was fight by minimizing material within the spectrometer acceptance.

Fig. 3.1 shows schematically the CERES experimental setup used during data taking in the years 1995/1996. The spectrometer covers pseudo-rapidity interval $2.1 < \eta < 2.65$ and has full azimuthal acceptance. Beam particles enter the spectrometer from the left

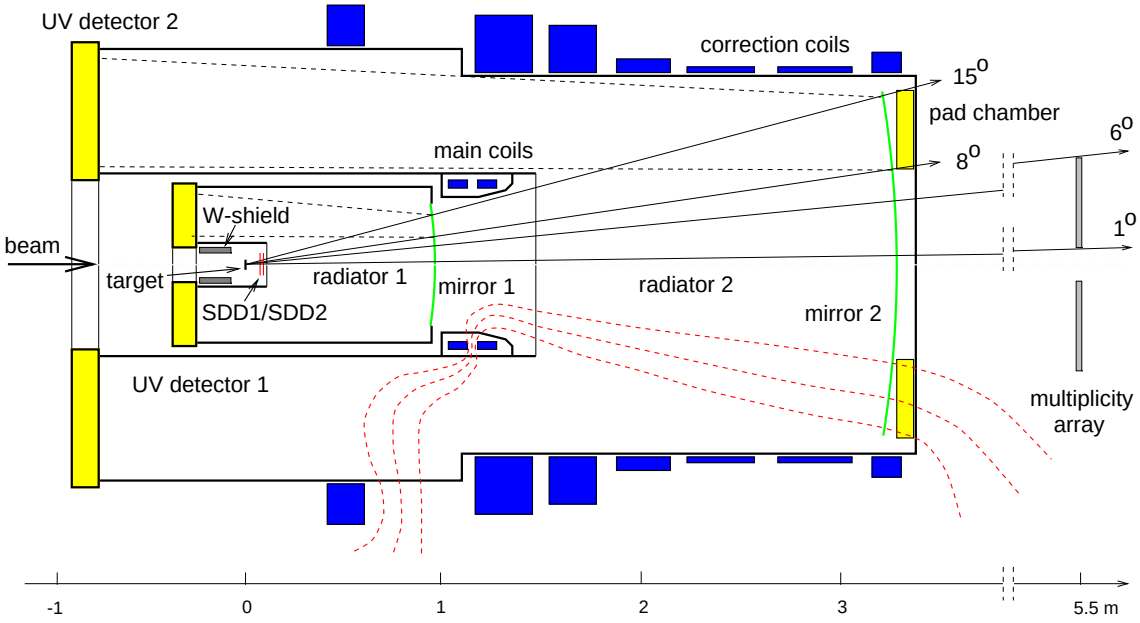

Figure 3.1: CERES experimental setup in 1995/96.

hand side and interact in the target. Charged particles produced in the collision generate first signal in the two silicon drift detectors (SDD1, SDD2), then cross the radiators of two ring imaging Cherenkov detectors (RICH1, RICH2) and in between them they are azimuthally deflected in the magnetic field produced by a superconducting magnet. The last point of the charged particle trajectory is measured by a multi-wire proportional chamber (PADC) at the downstream end of the spectrometer. The following sections of this chapter describe the main features of all detectors.

3.1 The Target Region with Two Radial Silicon Drift Detectors

Fig. 3.2 shows the target region of the CERES spectrometer with two radial silicon drift detectors (SDD1, SDD2) placed approximately 10 cm behind the target.

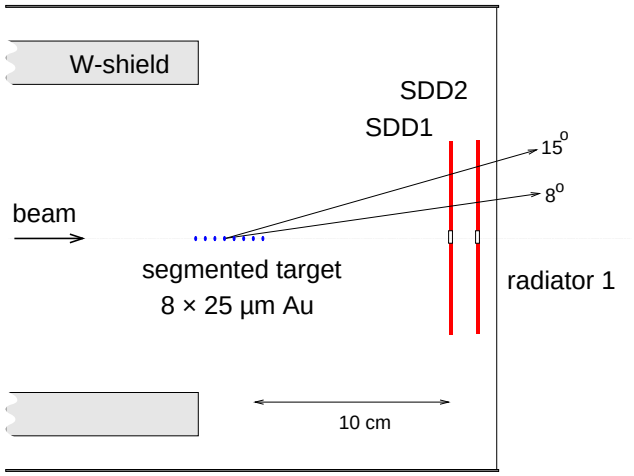

Figure 3.2: Target area of the CERES spectrometer with two radial silicon drift detectors (SDD1,SDD2).

The segmented target consists of eight Au-discs of 600 μm diameter and 25 μm thickness uniformly spaced by 2.8 mm along the beam axis. The distance between the discs was chosen such that the particles coming from a collision in a given target disc and falling into the spectrometer acceptance do not hit any other of the discs. This limits the effective material to 12.5 μm of gold corresponding to an effective radiation length of 0.55%. Each target disc is supported by 6 μm thick mylar foil and the entire target is precisely assembled in a thin carbon fiber tube. There is a tungsten shield installed around the target in order to absorb ionizing particles emitted backwards and decrease thus large background signals in the RICH1 detector.

The two silicon drift detectors form a *vertex telescope*, which is a central part of the event and track reconstruction (Fig. 3.2). These detectors provide:

- a measurement of energy loss and coordinates of hundreds of charged particles with high spatial resolution and high interaction rate
- a very precise reconstruction of an interaction vertex
- a track segment reconstruction before the magnetic field. For electrons, positrons and high momentum pions they give a prediction of the ring-center location in the first RICH detector.

- a powerful rejection of photon conversions

Since I was actively involved in the silicon drift detector group, there is a special chapter, Chapter 4, devoted to them.

The target together with both drift detectors and the beam counter BC3 (cf. Section 3.5) are mounted in a double-walled carbon fiber tube covered with aluminum and placed into the RICH1 detector.

3.2 The RICH Detectors

Cherenkov effect

A charged particle traversing a medium with a refraction index n produces Cherenkov light, if its velocity v is higher than the speed of light in the medium

$$v > \frac{c}{n}. \tag{3.1}$$

The emission angle θ_c of Cherenkov photons is given by

$$\theta_c = \arccos\left(\frac{1}{n\beta}\right), \tag{3.2}$$

where

$$\beta = \frac{v}{c} = \sqrt{1 - \frac{1}{\gamma^2}}. \tag{3.3}$$

From Eq. (3.2) it follows, that there exists a threshold value β_{th} (γ_{th}) for which the emission angle $\theta_c = 0$

$$\beta_{\text{th}} = \frac{1}{n}, \qquad \gamma_{th} = \frac{1}{\sqrt{1 - 1/n^2}}. \tag{3.4}$$

For $\beta \to 1$ ($\gamma \to \infty$) approaches the emission angle its maximal value given by

$$\theta_\infty = \arccos\left(\frac{1}{n}\right) \simeq \frac{1}{\gamma_{th}}. \tag{3.5}$$

The spectrum of Cherenkov photons is white with respect to their energy. The number of detected photons N for a radiator of length L is given by

$$N = N_0 L z^2 \sin^2\theta_c, \tag{3.6}$$

where z is the charge of the passing particle. The proportionality factor N_0 represents the specific response of the detector to Cherenkov spectrum. It includes the quantum efficiency for photon detection, the transmittance of the optical medium, the mirror reflectivity and thus constitutes a figure of merit for comparing different detectors. Using Eq. (3.2) and Eq. (3.3) we can express the number of Cherenkov photons as

$$N = N_0 L z^2 \left(1 - \frac{1 - 1/\gamma_{th}^2}{1 - 1/\gamma^2}\right). \tag{3.7}$$

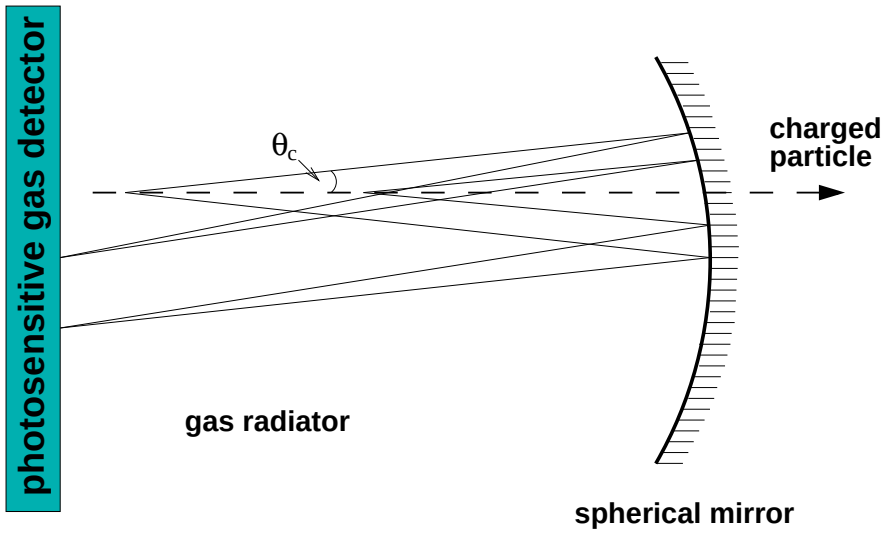

Figure 3.3: Schematic view of a RICH detector with a spherical mirror. The particle enters from the left, the emitted Cherenkov photons are reflected backward into a photon detector.

It follows, that the number of photons rises from zero at $\gamma = \gamma_{\text{th}}$ to the asymptotic value

$$N_\infty = N_0 \frac{L}{\gamma_{th}^2} \tag{3.8}$$

for $\gamma \to \infty$.

Principle of RICH detector

A ring imaging Cherenkov detector (RICH) is schematically shown in Fig. 3.2. Produced Cherenkov photons are reflected by a spherical mirror with a focal length f and focused onto the photon detector placed at the focal plane of the mirror. The resulting pattern is a circle of radius

$$R = f \cdot \tan\theta_c \tag{3.9}$$

which approaches for $\theta_c \to \theta_\infty$ its maximal value

$$R_\infty = f \cdot \tan\theta_\infty . \tag{3.10}$$

Both, the ring radius and the number of Cherenkov photons, depend on particle momentum and mass as

$$\frac{R}{R_\infty} = \sqrt{1 - \left(\frac{m\gamma_{\text{th}}}{p}\right)^2} \tag{3.11}$$

and

$$\frac{N}{N_\infty} = 1 - \left(\frac{m\gamma_{\text{th}}}{p}\right)^2 . \tag{3.12}$$

Knowing the particle momentum, such detector can be used for particle identification, or the other way around, knowing the particle mass, we can measure its momentum.

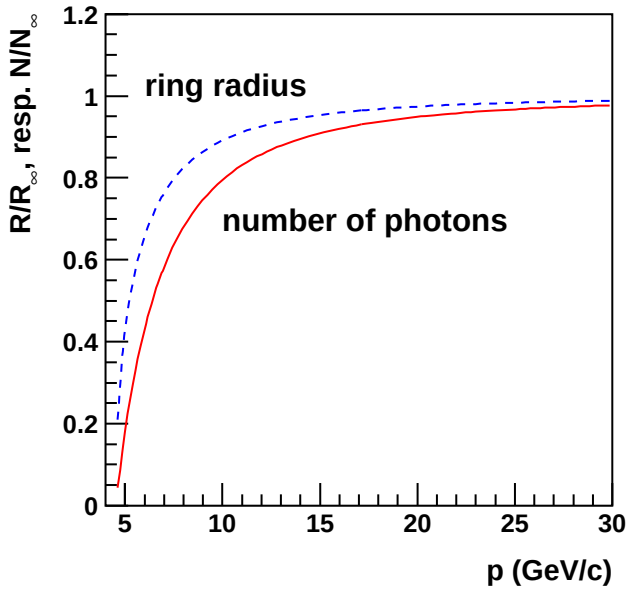

Figure 3.4: Ratios of ring radius and number of Cherenkov photons to their asymptotic values plotted as function of pion momentum.

CERES has two RICH detectors (RICH1 and RICH2) filled with CH_4 at atmospheric pressure. This radiator gas has a high Cherenkov threshold ($\gamma_{th} \simeq 32$) and from

$$p_{\text{min}} = m\sqrt{\gamma_{\text{th}}^2 - 1} \tag{3.13}$$

follows that practically only electrons produce Cherenkov light ($p_{\text{min}} \simeq 17$ MeV/c) while pions, the lightest hadrons, produce Cherenkov light only if their momentum reaches at least 4.5 GeV/c. Electrons reach the asymptotic ring radius already at $p = 120$ MeV/c, pions only at $p = 30$ GeV/c (cf. Fig. 3.4). The spectrometer is thus insensitive to more than 95 % of all produced charged hadrons ('*hadron blind*'), which is very important for the dilepton measurement. It also offers and excellent tool to study high-p_T pions.

The mirrors of the RICH detectors have a high UV-reflectivity and sufficient optical quality. The first mirror consists of a carbon fiber laminate of focal length $f = 126$ cm. Its thickness is only 1 mm corresponding to the radiation length of 0.4%, which significantly decreases the multiple scattering. The UV-reflectivity is higher than 85%. The quality of the mirror is excellent and the influence on the resolution is minimal ($\sigma < 0.10$ mrad). The RICH2 mirror is made of 10 glass segments with thickness of 6 mm. The UV-reflexivity is comparable to the RICH1 mirror, however the focal length is not uniform and varies between $f =$ (422-429) cm and consequently the optical quality is significantly worse ($\sigma \approx 0.35$ mrad).

The Cherenkov photons are registered in a UV detector. It is a gas counter filled with 94 % He + 6 % CH_4 at atmospheric pressure. The gas mixture containing TMAE (Tetrakis-di-Methyl-AminoEthylen) vapor is heated upto 42^{o}C to reach the partial TMAE pressure necessary for high photoionization. The detector is maintained at 50^{o}C to avoid TMAE condensation. The UV-detector is separated from the radiator by a UV-transparent window (CaF_2 for RICH1 and Quartz for RICH2).

The values of N_0 (Eq.3.6) were determined to 141 photons for RICH1 and 83 for RICH2. This corresponds to $N_\infty = 11.2$ for RICH1 and $N_\infty = 9.5$ for RICH2.

3.3 The Multi-Wire Proportional Chamber

The multi-wire proportional chamber with a pad readout (the pad chamber, PADC) is located closely behind the RICH2 mirror, 3.3 m downstream of the target. It was operated with Ar/CO_2 mixture in ratio 90/10. The pad size is, as for UV detector of RICH2, 7.62 x 7.62 mm^2. Its angular coverage (7.8^o-15.1^o) matches the spectrometer acceptance and corresponds to the pseudo-rapidity interval $2.0 < \eta < 2.7$.

The pad chamber provides an external tracking behind the magnetic field and gives information about the electron or pion ring center location in RICH2. This reduces the number of fake rings from high background. As a by-product, which is however of a vital importance for this work, PADC together with the doublet of silicon detectors allows to make a charged hadron tracking. The pad chamber plays in addition a very important role in the geometrical inter-calibration of the detectors, providing a common reference for the silicon drift and the RICH detectors.

3.4 The Magnetic Field

A pair of superconducting solenoidal coils located between the two RICH detectors produces a magnetic field for the momentum determination. The currents in the coils have an opposite sign and produce a sharply located azimuthal kick. The radiator of the RICH1 detector is essentially free of magnetic field and in the RICH2 detector the magnetic field lines are shaped by a set of warm correction coils such that the field lines are kept parallel to the particle trajectories (see Fig. 3.1).

Charged particles crossing the region between the RICH detectors are deflected in the azimuthal direction. The azimuthal deflection measured either between SDD and RICH2, or between SDD and PADC, gives the momentum measurement

$$p = \frac{144 \text{ mrad}}{\phi_{\text{SDD}} - \phi_{\text{RICH2}}} = \frac{96 \text{ mrad}}{\phi_{\text{SDD}} - \phi_{\text{PADC}}} \, [\text{GeV}/c]. \tag{3.14}$$

The polar angle remains to the first order unchanged. In the second order, the charged particle track is slightly bent by an angle

$$\Delta\theta = 66.2(\Delta\phi)^2 \frac{\text{mrad}}{\text{rad}^2} \tag{3.15}$$

towards the beam axis.

3.5 The Trigger

The trigger system consists of three Cherenkov beam counters (BC1, BC2, BC3) filled with air and two plastic scintillators - a veto counter (VC) and a multiplicity detector (MD). BC1 is located 60 m upstream of the experiment, BC3 is directly behind the target and BC2 is at the downstream end of the spectrometer. VC located 2 m upstream of the spectrometer is used to veto non target interactions. MD compounding of 24 plastic

scintillators is used as a fast decision about the charged multiplicity of the collision. It has a polar angle coverage between 1^o and 6^o and is placed 5 m behind the pad chamber.

The readout of the detectors is triggered, if a beam particle reaches the target, but does not enter the spectrometer. This can be schematically expressed in the following way:

$$BC1 + \overline{BC2} + \overline{BC3} + \overline{VC}$$

For the positive trigger decision is moreover required that the charged particle multiplicity registered by MD is higher than 100. This represents roughly 30 $\%$ of the geometric cross section in Pb-Au collisions.

3.6 The Data Acquisition System

With an average beam intensity of 10^6 Pb ions per burst[1] about 1000 triggered collisions were recorded. This is achieved by a data acquisition system (DAQ) with very high rate capability combined with a highly compressed data format. Zero suppression and Huffmann coding are directly built in hardware of the readout system of each detector.

Information coming from the detectors is stored in memory modules linked by a VME bus to the DAQ CPUs where an event builder program collects information from all of the memory modules, packs it for each event to the stream of given data and label structure and keeps in the memory until ten second long interval between two bursts comes. During this time the data, corresponding to about 50 kBytes per event, are transferred in parallel to nine digital audio tapes (DAT). In total, the data corresponding to 3.2 TBytes are stored on 1800 tapes. The readout and event-builder run asynchronously (two-event pipeline in between) reducing thus significantly the impact of their dead time.

3.7 The Upgrade by a Time Projection Chamber

In 1998, the spectrometer was upgraded by an additional tracking detector, a Time Projection Chamber (TPC) with radial drift field, which replaced the pad chamber. The aim of the upgrade was to achieve the mass resolution of $\delta m/m = 2$ % at $m \approx 1$ GeV/c^2 which would allow a precise spectroscopy of ρ/ω and ϕ vector mesons.

The CERES TPC is a cylindrical drift chamber filled with Ne/CO_2 gas mixture in ratio 80/20. The sensitive volume is about 9 m^3 and the length 2 m. It has 16 readout chambers with segmented pad-readout placed in a polygonal structure. Along the beam axis, the TPC is divided into 20 planes, each with 16 x 48 = 768 readout channels on the circumference. In total, 15360 individual channels with 256 time samples each, can be read out, allowing a three-dimensional reconstruction of particle tracks. The electric field is approximately radial and is defined by the inner electrode, which is an aluminum cylinder at a potential of -30 kV, and the cathode wires of the readout chambers at ground potential. Details can be found in [118, 119].

[1] *burst* = extraction of beam onto a target. SPS ion burst duration is 4.8 s out of 19.2 s total cycle.

4

The CERES Radial Silicon Drift Detectors

CERES was the first experiment using radial silicon drift detectors and looks now back at several years of successful pioneering work. These detectors have a very good position resolution even in the particle densities encountered in the ultrarelativistic heavy-ion collisions, and compared to both strip and pixel detectors need much smaller number of readout channels ($\approx \sqrt{N_{\text{pixel}}}$). The principle of operation of silicon drift detectors is described in the following sections, and supplemented by some details about the detectors used in CERES and their performance.

4.1 Principle of Operation

In 1984, E. Gatti and P. Rehak suggested a silicon drift detector based on the principle of a *sideward depletion* [120–122]. The principle of operation of such drift detector illustrates Fig. 4.1. Let's have a silicon wafer of n^- type with p^+ electrodes implanted on its flat sides. The wafer can be fully depleted by applying a reversed bias voltage on a small n^+ anode implanted on the wafer edge. The potential created inside the wafer has a parabolic shape with a minimum along the central dividing plane.

A charged particle traversing the depleted silicon wafer creates electron-hole pairs. For the creation of one electron-hole pair the ionization energy of 3.6 eV is needed [123]. A minimum ionizing particle traversing 250 μm of silicon creates thus around 25000 electron-hole pairs. By superimposing an additional linear electric field along the x-axis (Fig. 4.1), the electrons are transported along the field towards the outer part of the detector, where they are collected on the n^+ anodes. Holes are attracted to the p^+-electrodes on the detector surface.

Since the drift time of electrons depends on their drift distance, such detector is a position sensitive device. Small capacitance of the anodes allows to realize low noise detection systems with large detectors. However, a practical disadvantage of the drift detectors is a strong dependence of the electron mobility μ on temperature T

$$\mu \approx T^{-2.4} \tag{4.1}$$

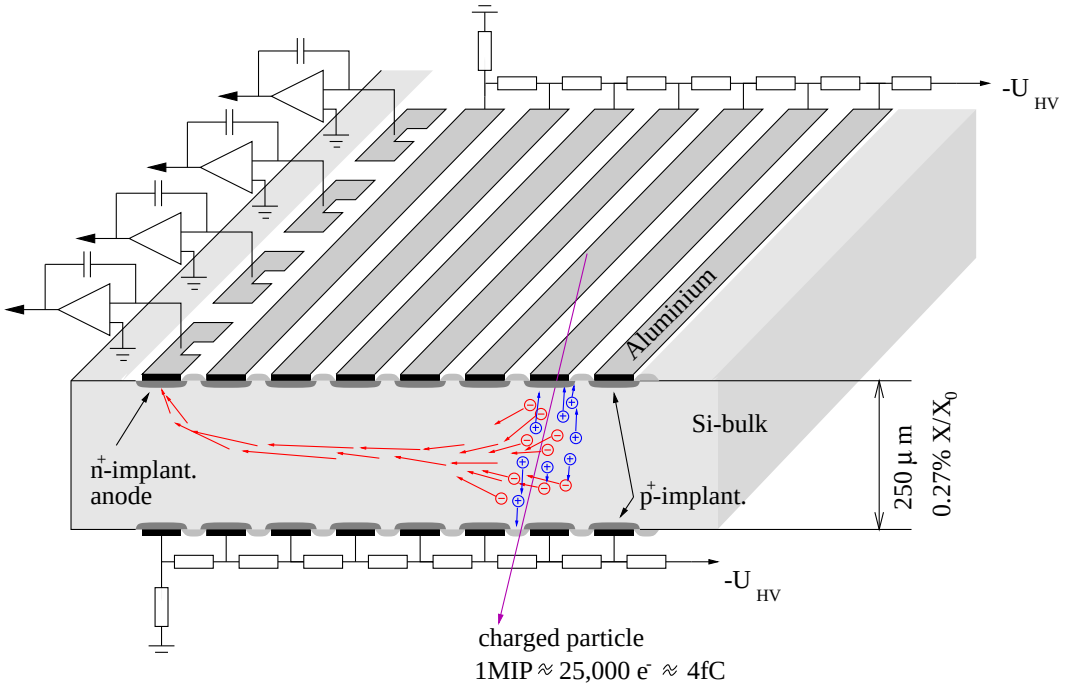

Figure 4.1: The principle of operation of a silicon drift detector. The linear drift field drives the electron cloud from right to left towards the anodes. The figure is from [124].

and consequently a temperature dependent drift velocity $\vec{v}_{\text{drift}}$

$$\vec{v}_{\text{drift}} = \mu \cdot \vec{E}. \tag{4.2}$$

Here $\vec{E}$ denotes the applied electric field.

Let us simplify the situation and suppose that holes are instantaneously collected by the p^+ electrodes. Then we need to solve the transport of an electron cloud inside the semiconductor. While drifting towards the anode region the electron cloud increases its size in the radial and azimuthal direction. This is caused by the electrostatic repulsion, diffusion and electric field geometry. In the case of small charge densities the broadening of the electron cloud caused by the electrostatic repulsion can be neglected [125, 126]. If we denote the charge distribution of the electrons $n(\vec{x},t)$ and the electric field $\vec{E}(\vec{x},t)$ then taking into account the diffusion we can write down the following equation of continuity:

$$\frac{\partial n(\vec{x},t)}{\partial t} = D \cdot \Delta n(\vec{x},t) + \nabla \vec{j}(\vec{x},t). \tag{4.3}$$

Here D is the diffusion constant (D = 35 cm^2/s at T = 300 K), μ is the electron mobility (μ = 1500 cm^2/Vs, [128]), and $\vec{j}(\vec{x},t)$ is given by

$$\vec{j}(\vec{x},t) = \mu \cdot n(\vec{x},t) \cdot \vec{E}(\vec{x},t). \tag{4.4}$$

By separating the charge distribution $n(\vec{x},t)$ into two parts - perpendicular (z) and parallel ($x_\perp$) to the detector surface,

$$n(\vec{x},t) = n(\vec{x}_\perp,t) \cdot n(z,t), \tag{4.5}$$

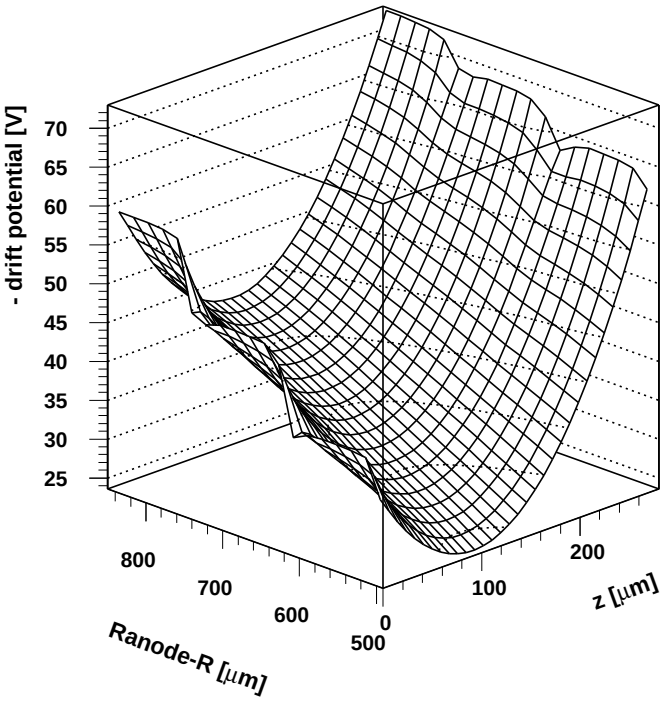

Figure 4.2: Shape of the electric potential in the radial silicon drift detector. The figure is from [127].

we can easily solve Eq. (4.3). The solution in the z-direction is a Gaussian curve of width

$$\sigma_z^2 = \frac{D}{k \cdot \mu}. \tag{4.6}$$

The constant factor k is given by

$$k = \frac{q \cdot N_n}{\epsilon_0 \cdot \epsilon_r}, \tag{4.7}$$

where N_n is the dopant density (N_n = 9·10^{11}cm^{-3}) and q denotes the elementary charge. Constant k has a value of $1.36 \cdot 10^{-3} V \mu m^{-2}$ and the initial Gaussian width in the z-direction is about $\sigma_z \approx 4\ \mu m$.

The broadening in the plane parallel to the detector surface is given by two dimensional time-dependent Gaussian distribution. The corresponding width in the radial direction is given by

$$\sigma^2_{\text{r,diffusion}}(r) = \sigma^2_{\text{r,0}} + 2 \cdot D \cdot \frac{r_{\text{max}} - r}{v_{\text{drift}}} \tag{4.8}$$

and in the azimuthal direction

$$\sigma^2_{\phi,\text{diffusion}}(r) = \sigma^2_{\phi,0} + 2 \cdot D \cdot \left(\frac{r_{\text{max}}}{v_{\text{drift}}} \left(\frac{r_{\text{max}}}{r} - 1 \right) \right). \tag{4.9}$$

4.2 4” AZTEC Detector

In order to match the symmetry of the CERES spectrometer, the drift detectors were designed with a radial symmetry. CERES is currently using the second generation of

the drift detectors with four-inch diameter and the AZTEC design [129], which replaced previously used three-inch detectors. The silicon wafers have thickness of 280$\pm$20 μm and 2–5 kΩcm specific resistivity. Charge is collected by 360 segmented anodes situated at the outer part of the detector.

The radial drift field is realized by applying high voltage on the field rings (p^+–implantations) isolated from each other by SiO_2 stripes. The pitch between successive rings is 120 μm. To every 12-th ring is by wire-bonds attached an external voltage divider and in-between them is voltage distributed using an internal voltage divider. The internal voltage divider is built up from implanted resistors, which are realized by p^+–implantations between two field rings. Near the center of the detector the resistivity is higher than outside, minimizing thus the temperature gradient in the wafer. The internal resistors have the advantage to avoid many wire-bonds. The electric field is about $E \approx 800$ V/cm, which corresponds to the drift velocity $v_{\mathrm{drift}} = 9$ μm/ns. The shape of the electric field between two field rings close to the detector surface is not parabolic, as it is shown in Fig. 4.3. In the radial direction, the field rings are on several places disconnected by narrow SiO_2 stripes (called *rivers*), which drain the surface current to the guard anode.

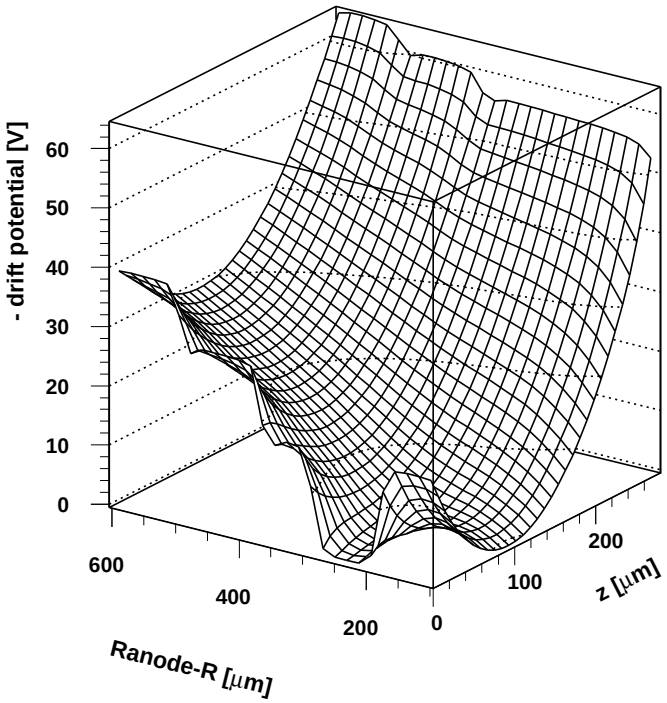

Figure 4.3: Shape of the electric field in the vicinity of anodes in SDD. The figure is from [127].

The second generation of the drift detectors benefits from the progress achieved in the technology of silicon wafer production and mask design software. Let us summarize briefly the improvements which increased the detector performance [129]:

1. The progress in the technology of the silicon wafer production enabled an increase of the detector active area from 32 cm^2 to 55 cm^2. This corresponds to the change

in the diameter from 3 to 4 inches and allows to install the detectors further away from the target and decrease thus the hit occupancy.

2. In the old design were the field rings approximated by 120-sided polygons which caused a deviation from the expected ideal radial field (*central anode effect*, [130]). The improvement of a litographic mask design allowed to approximate the field rings by 360 concentric polygons on both detector sides, which are rotated with respect to each other by 0.5°. In the middle plane of the detector, where the electrons are transported, the effective geometry is very close to an ideal cylindrical symmetry.
3. Development of an *interlaced anode structure* was crucial for the improvement of the charge sharing between anodes followed by the improvement of the azimuthal resolution. The azimuthal width of 1° anode is 732μm. Depending on the drift time, around 68% of the electron clouds reach, however, only the size of 100-300μm. The problem was solved with the new interlaced anode structure (Fig. 4.4), keeping the number of anodes still at 360 to avoid additional readout investments. Each anode is subdivided into five segments. The large central part (366 μm wide) is bonded to the front-end chip (Chapter 4.3 below) and connected with the two narrower segments (122 μm wide) and the narrowest segment (61 μm wide) of the neighboring anode on each side. The azimuthal resolution is thus equivalent to 720 simple anodes without increasing the amount of readout electronics.

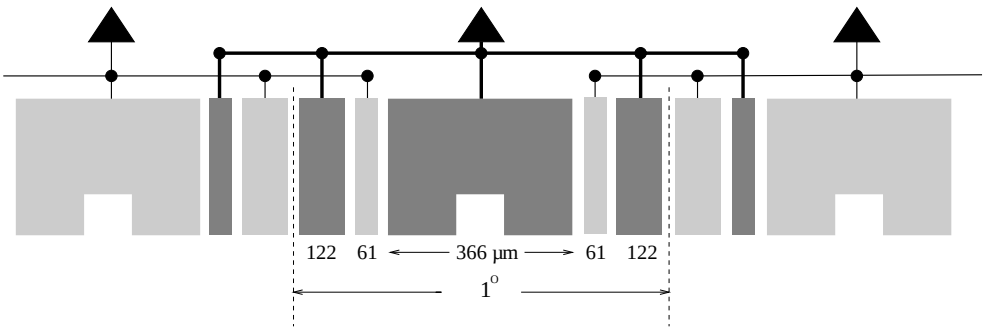

Figure 4.4: The anode structure of the AZTEC silicon drift detector. Figure from [124].

4.3 The Readout Electronics

The readout chain of the silicon drift detectors is schematically shown in Fig. 4.5. The signals registered on the anodes are first amplified and shaped in a *front-end chip*. The chip consists of a charge sensitive preamplifier, a quasi-Gaussian shaper and a symmetrical line driver. To take full advantage of the SDD low capacitance of about 0.1 pF, the chips are situated on the detector motherboard and directly wire-bonded to the anodes. During the '96 data taking the detectors were equipped with 32-channel front-end OLA chips (Operational Linear preAmplifier, [131]). During the vertex telescope upgrade

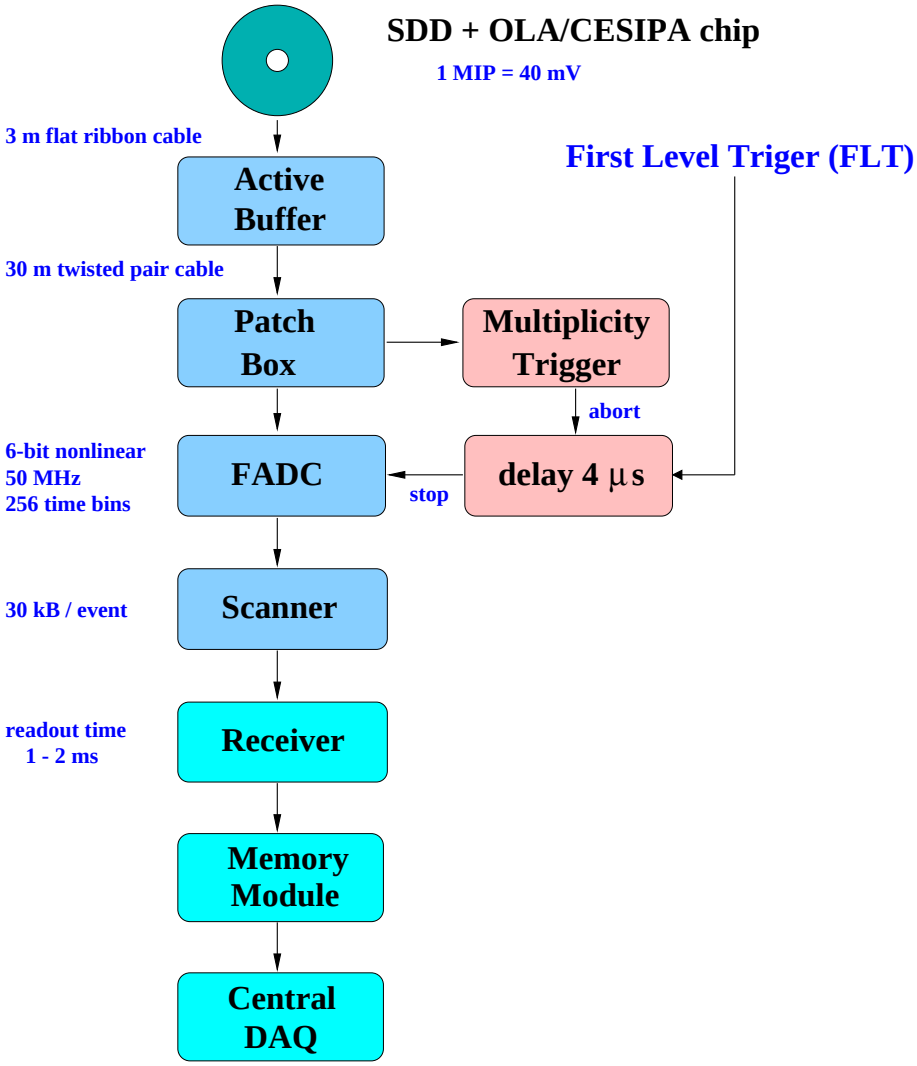

Figure 4.5: The scheme of the readout system of the radial silicon drift detectors.

(1998-2000) new detectors were built and assembled with new 16-channel CESIPA front-end chips (CEres SIlicon PreAmplifier, [132]). The CESIPA chips have in many aspects better performance and especially they do not show any strong oscillation behavior which necessitated an introduction of damping resistors into the output lines in order to achieve stable operation of the OLA chips (details can be found in [133]).

During the shaping process, which duration is given by σ_{elec}, a part of the amplitude is lost. Broad input pulses ($\sigma_{\mathrm{in}} > \sigma_{\mathrm{elec}}$) have smaller output amplitude than narrower pulses ($\sigma_{\mathrm{in}} < \sigma_{\mathrm{elec}}$) of the same input amplitude. This frequency dependent signal amplification causes a *ballistic deficit*. Since the pulse width depends on the radial position, also the ballistic deficit is radius dependent as demonstrated in Fig. 4.6.

The bipolar output signals from the front-end chips are sent to the *active buffers* placed already outside of the target area and from there transmitted over 40 m long flat cables

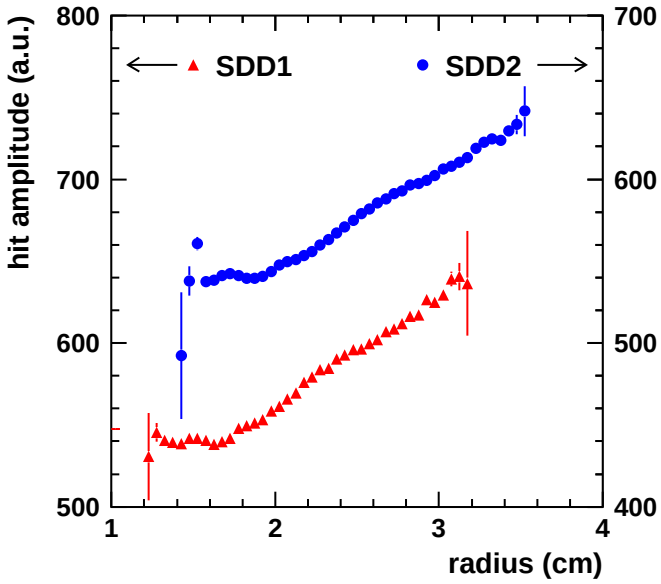

Figure 4.6: Radius dependence of the hit amplitude in the silicon drift detectors due to ballistic deficit. The latter is largest for long drift (small impact radius) because of the larger pulse width. Observe different ordinates.

to the flash analog to digital converters (FADC, DL300). At the input of the FADC's is a differential amplifier, which puts the bipolar signals together and amplifies them once more. The incoming signal U_{inp} is sampled with 50 MHz frequency[1] given by an external clock and non-linearly digitized with 6-bit resolution:

$$C = \left(\frac{U_{\text{inp}} \cdot 10}{U_0 + \alpha \cdot U_{\text{inp}} \cdot 10} \cdot 64 \right), C = 0, 1, ..., 63 \tag{4.10}$$

where $U_0 = 0.5$ V and $\alpha = 0.75$ are fixed in the system. The digitized signal is stored in 256 discrete time intervals (*'time bins'*, 1 time bin = 20 ns). The FADC modules are operated in the so called *'common stop mode'*: the sampling continues until it is stopped by an external stop signal. The stop signal occurs with the first-level trigger (FLT) signal described below. The SDD system acts as its own memory device which stores all hits during the electron drift time. In the case of a full memory, the FADC channel is from the beginning continuously overwritten. When the stop signal arrives, there are stored data from the last 5.12 μs in the FADC. This covers fully the detector drift time of 4 μs. Since the FADC is sensitive to the stop signal only at the falling edge (every 20 ns) and it is not synchronized with the FLT signal, the time difference between the stop signal and the next negative FADC falling edge has to be measured. This is done in the CAMAC TDC (Time to Digital Converter) and together with the stop signal stored for every event and corrected for in the offline analysis (*stop pulse correction*).

After the arrival of the stop signal, the FADC memory is scanned by a sampling and scanning module (*scanner*). The DL357 modules with the scanning frequency of 16 MHz used before the SDD telescope upgrade were replaced by new modules enabling scanning upto 100 MHz. Only the channels where at least two following time bins have an amplitude above a certain threshold are read out. In the case of the old scanners were two neighboring channels scanned simultaneously and it was enough if at least one of them

[1] 4 ns sampling time in 20 ns time bin.

fulfilled this condition. The readout continues until a time bin with an amplitude below the readout threshold is found. Additionally to the time bins with amplitudes above the threshold, also 5 time bins before and after (*pre- and post-samples*) are read out for an off-line reconstruction of the baseline.

From the scanner are the data transferred to the *receivers* for storage in the FIFO (First-In-First-Out) memories. In the receivers, the pre-samples are added together and the sum is written to the address of the 5-th pre-sample. Then are the data sent further to the *memory module* and from there continue to the central data acquisition system.

4.4 On-line Monitoring

For best data quality, each detector has to be continuously monitored. For the online monitoring of the silicon drift detectors during the 1998-2000 data taking period a monitoring program *MONITOR* has been developed. It is written in Tcl/Tk [134]. Tcl is a scripting language and Tk is a programming environment for creating graphical user interfaces under X-Windows. *MONITOR* can work in both, the local (slow) and global (fast) readout mode of the silicon drift detectors. It enables to monitor:

- *leakage current*, which is one of the limiting factors of the energy and the position resolution. More leakage current is produced in the Si-SiO_2 interface than in the bulk of the silicon drift detector. The measurement of the leakage current (via DC offset of 0.35 mV/nA) for the silicon drift detectors used during the 2000 data taking period is presented in Fig. 4.7.
- *temperature*, which is, as already discussed, an important factor influencing the drift velocity. The temperature of the silicon wafers is monitored by Pt100 resistors

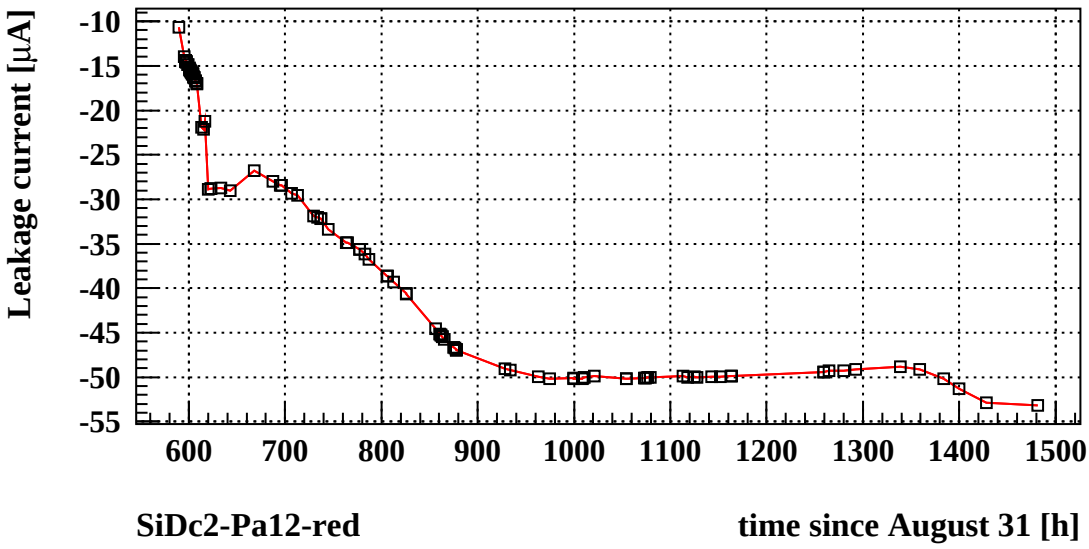

Figure 4.7: Monitoring of the leakage current in the second radial silicon drift detector (SDD2).

glued on both detectors. The output from the thermometer is directly connected to the computer (PC) placed in the experimental area, where the data are stored. The corrections for the temperature variations based on the monitoring results are later incorporated in the offline analysis (cf. Chapter 5.2.1).

- *drift time and azimuthal hit distribution* (not shown here).

MONITOR offers also two kinds of the SDD event display. The round display presented in Fig. 4.8 enables a realistic view of the detector. The rectangular one with anode position along the x-axis and time bin along the y-axis (not shown here), is interactive and allows zooming of different detector regions for a more detailed inspection. By selecting a certain anode it is possible to obtain the pulses on this anode and their neighboring anodes as displayed in Fig. 4.9.

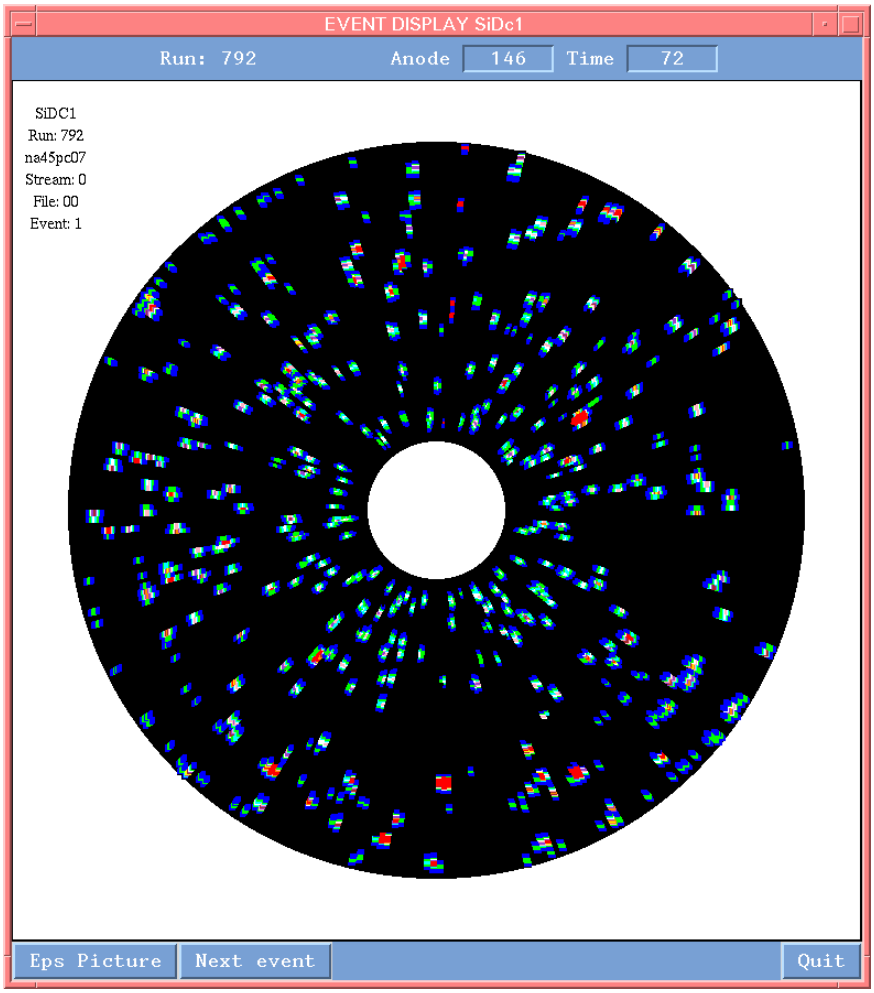

Figure 4.8: The event display of SDD1 from program *MONITOR*. The colors on the display correspond to an amplitude at the given (anode,time bin) position going from the lowest amplitudes in blue to the highest amplitudes in red.

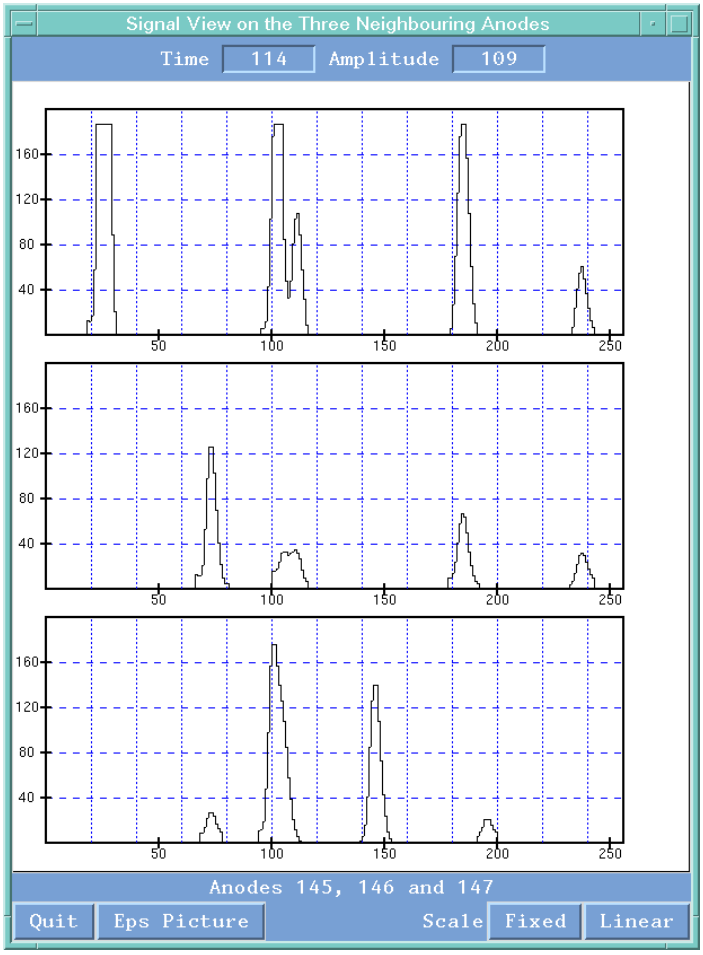

Figure 4.9: View of the measured charge signal on 3 neighboring anodes of SDD1 in 2000 beamtime from program *MONITOR*.

4.5 Drift Velocity Calibration

In order to achieve the best performance of the silicon detectors, a very careful calibration of the drift velocity is required. From the time information a drift distance can be calculated. To first approximation, the relation between the drift distance and time is linear. To the accuracy with which we know the radial extension of the detector active area Δd and the total drift time Δt we can calculate the drift velocity as

$$\langle v_{\text{drift}} \rangle = \frac{\Delta d}{\Delta t}. \tag{4.11}$$

The length of the drift is

$$\Delta d = r_{\text{max}} - r_{\text{min}}, \tag{4.12}$$

where r_{min} is the inner edge of the detector (10 mm, the inner most voltage ring) and r_{max} is the anode position about 42 mm. The total drift time can be calculated as

$$\Delta t = t_{\text{max}} - t_{\text{min}}, \tag{4.13}$$

where t_{min} is the time corresponding to the particles which don't drift and fall directly on the anodes, and t_{max} is the drift time of particles coming from r_{min}. The radial position is then given by

$$r = r_{\text{max}} - v_{\text{drift}}(t - t_{\text{min}}). \tag{4.14}$$

Fig. 4.10 shows a typical hit distribution in the drift time for SDD1. By fitting the edges of the spectrum, the values of t_{min} and t_{max} are determined.

Having done the preliminary calibration of the drift velocity, the geometrical alignment of both detectors and the determination of the interaction vertex can be done. All other corrections, such as the stop-pulse correction, temperature variations influencing the drift velocity, etc. are done regarding the vertex position and its stability. The calibration proceeds in an iterative way.

4.6 Analysis Software

The offline analysis software of the silicon detectors is a part of the objected oriented C++ package '**COOL**' (**C**ERES **O**bject **O**riented **L**ibrary, [27]). In this section we give an overview of the hit, track and vertex reconstruction.

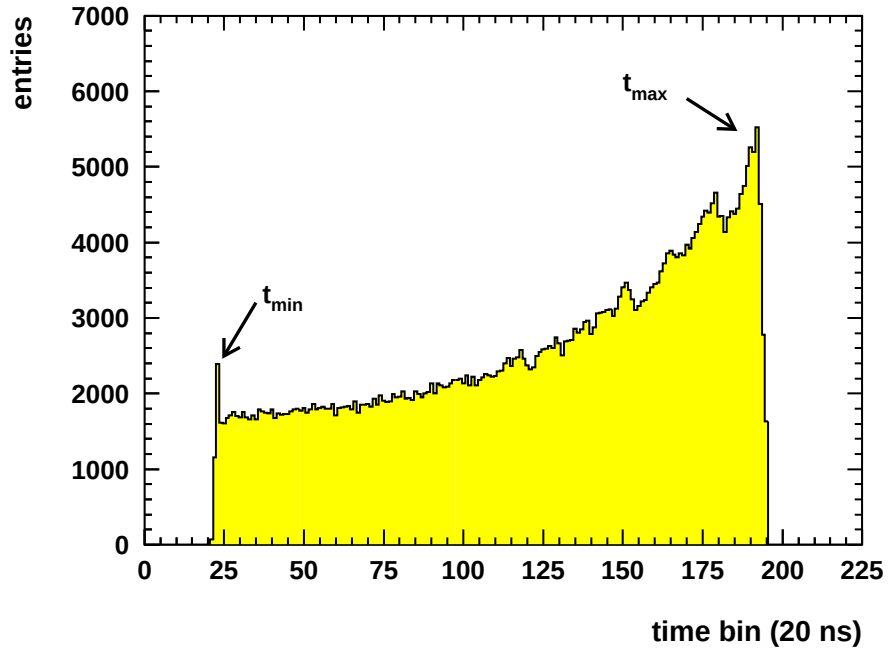

Figure 4.10: Drift time spectrum of SDD1. The global shape of this spectrum is given by the rapidity distribution of particles emitted in Pb-Au collisions. The small structures in the spectrum are due to local variations of the electric field and impurities of the silicon wafer.

4.6.1 Cluster and Hit Reconstruction

The raw data stored in the label structure are first 'unpacked'. The information about amplitude in a given anode and time bin is filled to a collection of *cells* (360 anodes x 256 time bins). A signature left by a charged particle which passed the silicon drift detector and deposited there a certain amount of its energy is called a *hit*. A signal produced by a minimum ionizing particle is spread typically over 8–12 time bins in the radial direction and 2–3 anodes in the azimuthal direction, implying there are around 20-40 cells belonging to one hit (cf. Fig. 4.11).

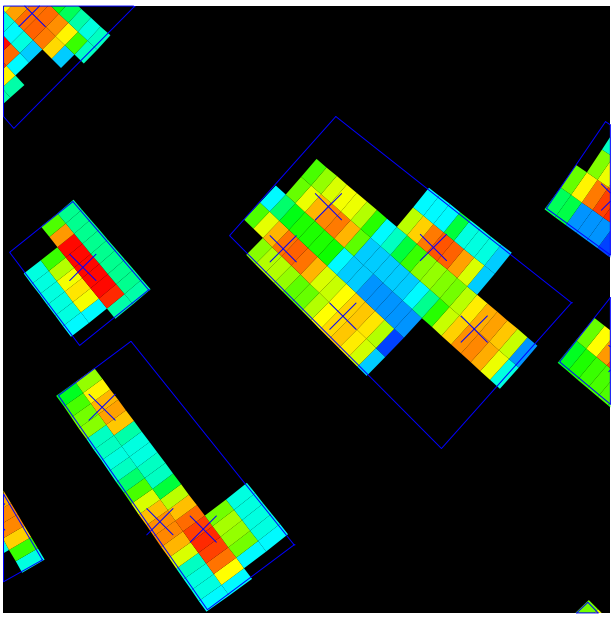

Figure 4.11: A magnified part of the SDD1 event display. The crosses correspond to reconstructed hit positions extracted from the amplitude information stored in cells. The color code goes from black, corresponding to low cell amplitude, to red for high cell amplitude respectively. The clusters are illustrated by blue rectangles. See text.

The cells which possibly belong at least to one hit are joined into a *cluster*. The creation of the cluster proceeds in the following way. Starting from one cell with given (anode, time bin) coordinates all adjacent cells, which have either the same anode or the same time bin coordinate and do not belong yet to another cluster, are joined to a currently being created cluster. For all cells which are newly added to the cluster the algorithm calls recursively itself until no more neighboring cells can be found. A cluster is defined by its size in the anode and time directions (Fig. 4.11).

Each of the clusters created can be decomposed into *subclusters*, which are slices of the cluster in the anode direction containing a group of cells of the same anode coordinate and without any empty time bin coordinate in between. In a given subcluster, there can exist one or more local *maxima* in the amplitude profile of the belonging cells. These maxima correspond in the most cases to one *pulse*, but in the case of two (or more) overlapping pulses also only one maximum is created.

Our motivation for writing of a new cluster and hit finding algorithm was to achieve an improvement of the two-hit resolution. The existing software had two main disadvantages. There was no possibility to resolve double (or multiple) hits along the anode direction even if a local minimum between two maxima in the amplitude profile was present. Moreover, we wanted to access the more ambitious problem and to resolve at

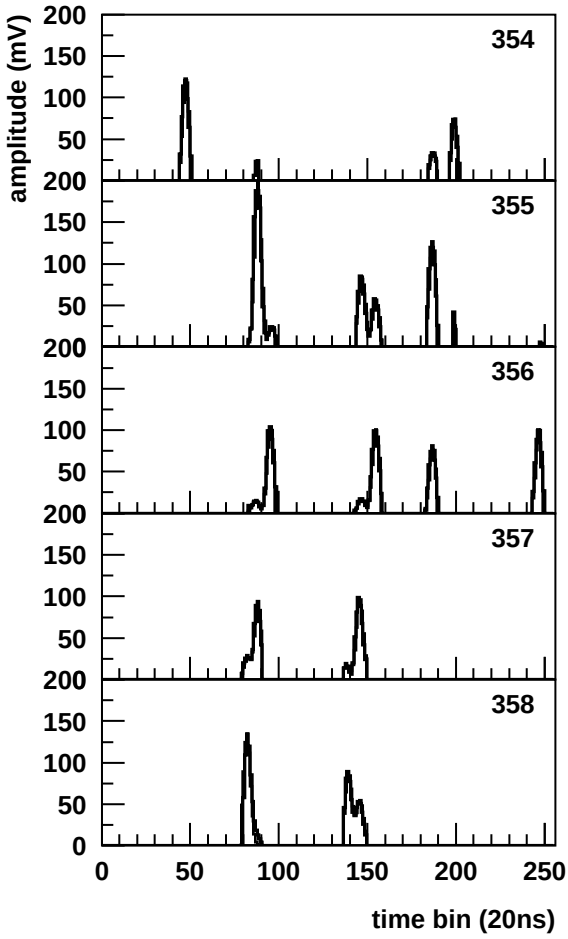

Figure 4.12: Digitized pulses from FADC-readout on five consecutive anodes (numbers in the upper right corner) in SDD1 shown as histograms together with Gaussian fits (line).

least partially two pulses in the time direction, which overlap without local minimum in between.

Signatures of overlapping pulses

Since the occupancy in the silicon detectors is not very high, we can assume that it is very unprobable to have more than two overlapping pulses at the same time (anode) position. If two pulses are close to each other, but we can still distinguish two local maxima with a minimum in-between, the situation is easy. The problem arises if only one broad peak is produced. In order to decide whether we are dealing with such case or not, we need to have good distinction criteria. In general, we can distinguish two cases:

a) The amplitudes of the overlapping pulses are very different and the smaller one is hidden under the bigger one. In such case we will observe a pulse asymmetry. It can be easily tested by looking at the difference between the position of the maximum and the center of gravity or using equivalently the 3rd central moment, which are both a measure of the *pulse skewness*.

b) The amplitudes of both pulses are comparable and the shape of the produced pulse is symmetric but much wider. It can be quantified by the variance (2nd central moment).

In addition, useful information can be in both cases provided from the neighboring anodes as shown on one example in Fig. 4.12. The broad pulse located on the anode 358

and time bin 80 is composed from two overlapping pulses as confirmed by information from its neighboring anode 357, where two close pulses within the range of the broad pulse are present.

Pulse shape observed in the data

Before trying to adjust the distinction criteria mentioned above, we have to understand a typical pulse shape in the data. As already mentioned in Section 4.1, the shape of the signal is a two-dimensional Gaussian and its width is influenced by diffusion and the drift geometry. However, because of the presence of the Gaussian shaper of a certain width, $\sigma_{\text{r,shaper}}$, the total width of the signal in the radial direction is given by

$$\sigma(r) = \sqrt{\sigma^2_{\text{diffusion}}(r) + \sigma^2_{\text{shaper}}}. \tag{4.15}$$

We have selected in the data a sample of single pulses and applied strong quality criteria in order to keep the admixture of double or multiple pulses as low as possible. Such selected pulses were fitted with a single Gaussian function. The obtained dependence of σ on the drift time is shown in Fig. 4.13(a). It is increasing linearly with the drift time. The reason is that the width of the pulse is dominated by σ_{shaper} which is about 40 ns (2 time bins). The data suggest that the pulse width also depends on the pulse height, especially pulses with amplitude below 45 mV show up strongly this behavior.

Another important quantity to be looked at is the distribution of the skewness parameter (3rd central moment). The measured skewness distribution is presented in Fig. 4.13(b). Clearly, the pulse shape is not an ideal Gaussian, but is slightly disturbed. Those values of the 'natural pulse skewness' thus restrict the criteria for finding a candidate for splitting based on the pulse shape asymmetry.

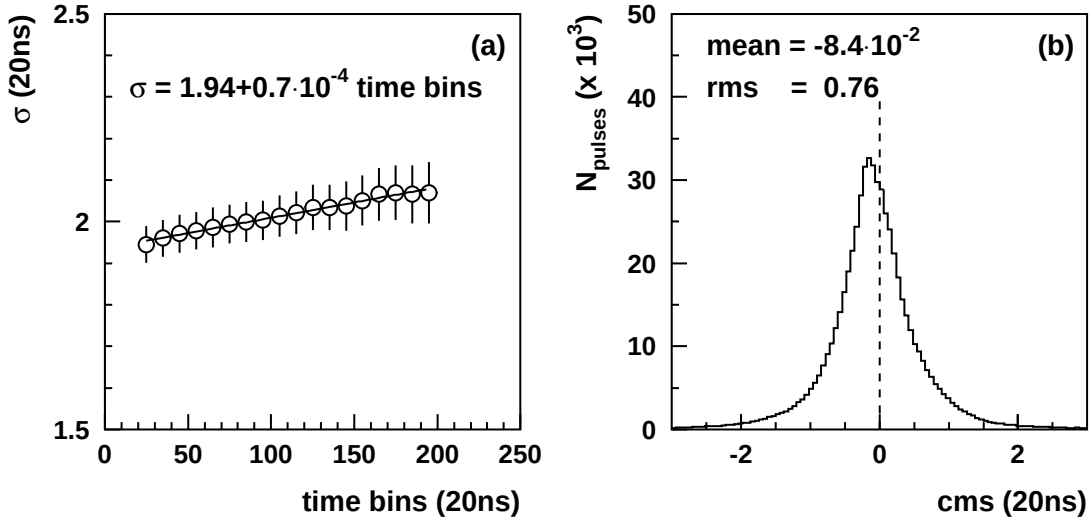

Figure 4.13: Gaussian pulse width as a function of the drift time for SDD2 (a). Distribution of the pulse skewness in SDD2 for the OLA preamplifier chip (b).

Scheme of the new cluster and hit finding algorithm

Let us here briefly describe the most important features of the new cluster and hit finding algorithm and its main differences to the old one.

1. In analogy with the old algorithm are first created clusters. Now also dead anodes, if present, are considered and included into the clusters. This should prevent additional creation of clusters and consequently artificial hits.
2. Each cluster is further analyzed separately. Subclusters of a given cluster are scanned to find local maxima in the amplitude profile in the time direction as well as local minima, if more than one maximum was found. If the amplitude of the minimum is less than 10% of that of maximum, the two pulses are separated and treated as if they were two single ones, otherwise the are further considered as two close pulses (see below).
3. All pulse candidates found have to pass several selection criteria discussed above in order to distinguish whether they correspond to one pulse or we deal with two overlapping pulses. Single pulses are fitted with a Gaussian. For the overlapping pulses a double-Gaussian fit method developed by [135] is used. If two local maxima in the amplitude profile can be still distinguished, the starting parameters of the fit are positions of these maxima. If only one maximum is present, the positions of pulses on the neighboring anodes are used if they exist. Otherwise are the starting parameters obtained from the shape of the broad pulse.
4. The obtained time positions of the pulses are eventually combined in the anode direction within a certain time window into hits. If there are more than two aligned pulses belonging to a hit candidate, we search for a minimum in the amplitude profile along the anode direction. If such minimum exists we split the hit candidate into two hits using the center of gravity to calculate its position along the anode direction.

Double-hit resolution

To study the double-hit resolution of the new algorithm and to make comparison with the previously used software, Monte-Carlo studies were performed using two different samples with two particles per event. The first sample, where the two particles are forced to be on the same anode and close to each other in time, allows to study the double-hit resolution in the radial (= time) direction. In the second sample are the roles exchanged and the algorithm's abilities in the anode direction can be tested.

We define the *double-hit reconstruction efficiency* to be equal to one, if both hits are found. Fig. 4.14 shows the comparison of the double-hit reconstruction efficiency for the old and new software. A big improvement in the double-hit resolution in both radial and azimuthal directions is achieved in the new software. The reconstruction efficiency reaches 1 in the azimuthal direction already at 2.5 anode separation, and in the radial direction at about 3 time bins separation, respectively. Moreover, in the radial direction, a substantial reduction of the artificial hit splitting (manifested by the reconstruction efficiency larger than 1, cf. Fig. 4.14), is achieved. However, in real data are the artificially split hits present, albeit reduced in comparison to the old software. This points to a not enough realistic simulation of the silicon detectors. A detailed studies on the artificial hit splitting in the data can be found in [11].

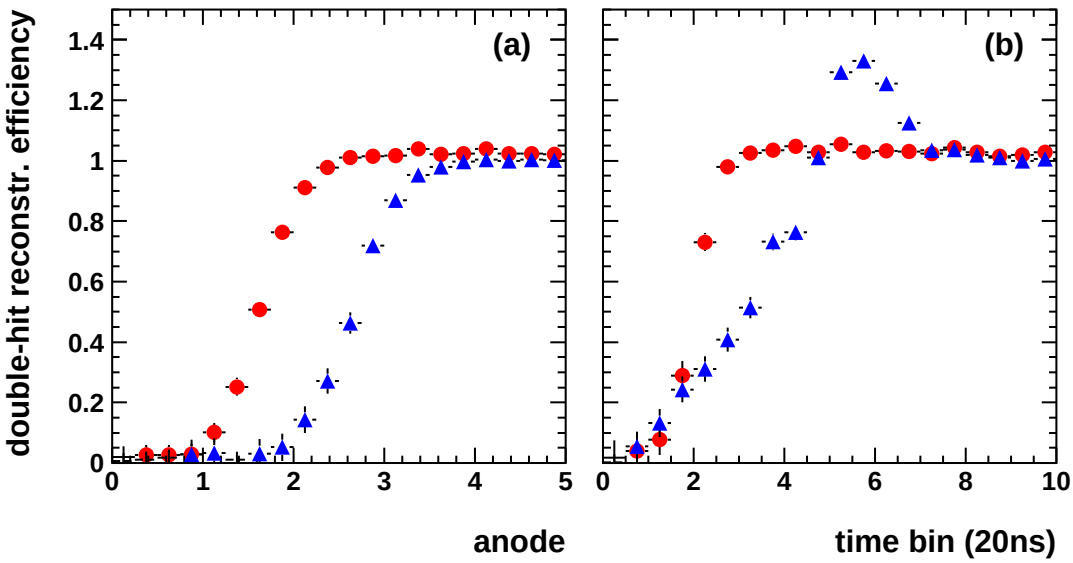

Figure 4.14: Comparison of the double-hit reconstruction efficiency in Monte-Carlo simulations for the old (triangles) and new software (circles) in the anode (a) and time (b) directions.

4.6.2 Track and Vertex Reconstruction

Once hits in the silicon detectors are reconstructed, the information about their position in the laboratory coordinate system can be used to combine them into *tracks* and find the location of the collision vertex (*vertex position*) to which all but very few of the tracks point to. Since the simple procedure minimizing the quadratic sum of hit mismatches between the two detectors and its iteration is extremely time consuming, another method is used in CERES, the robust vertex fitting approach [136]. In this method all hits in SDD1 and SDD2 are combined to straight track segments and a weighted sum of all their projected distances to an assumed vertex position is calculated. In the next iteration, this center of gravity becomes a new starting value for the vertex position and each track segment gets a new weight according to its deviation from the mean value in the step before. The procedure converges on average after five iterations and it is approximately 20 times faster than the old fitting method. After the determination of the z-position of the vertex, its position is refined to the exact position of the closest target disc. An optimized x-y vertex position is obtained by minimizing the sum of residual distances of the tracks pointing to the target. After refinement of the vertex position, an optimized set of the vertex track segments is obtained. Applying this procedure improves the vertex pointing resolution by 20%.

With respect to the previous analysis of the '96 data, there are some changes done in the tracking strategy for the data analysis on which these thesis is based. Let us here mention only the main modifications (details can be found in [11]):

1. For each hit in SDD2, a simple predictor into SDD1 is calculated. However, the observed tilt of 4° [27] of both drift detectors with respect to the beam axis was

not treated properly in the old predictor determination and it has been replaced by a method based on analytic geometry.

2. The size of the searching window for the best matching hit was adjusted to 7 mrad. It is now based on solid angles rather than polar and azimuthal angles used before.
3. In addition to the track segments sharing a common hit in SDD1 (called *V-tracks*) which could originate from a photon conversion in SDD1, also reversed V-tracks sharing a common SDD2 hit are included in order to keep all partially unresolved tracks within the detector resolution.
4. For a SDD track composed of a single anode hit in one of the detectors, the ϕ-coordinate of the multiple anode hit in the other silicon drift detector is preferred, rather than an average of both ϕ-coordinates.

Fig. 4.15 shows the vertex distribution along the beam (z) axis. All eight target discs are clearly resolved with the average Gaussian width of about 250 μm. Projecting the x-y distribution of the vertices on the x-axis and using high momentum pion tracks in order to avoid any multiple scattering, we obtain resolution of 28μm.

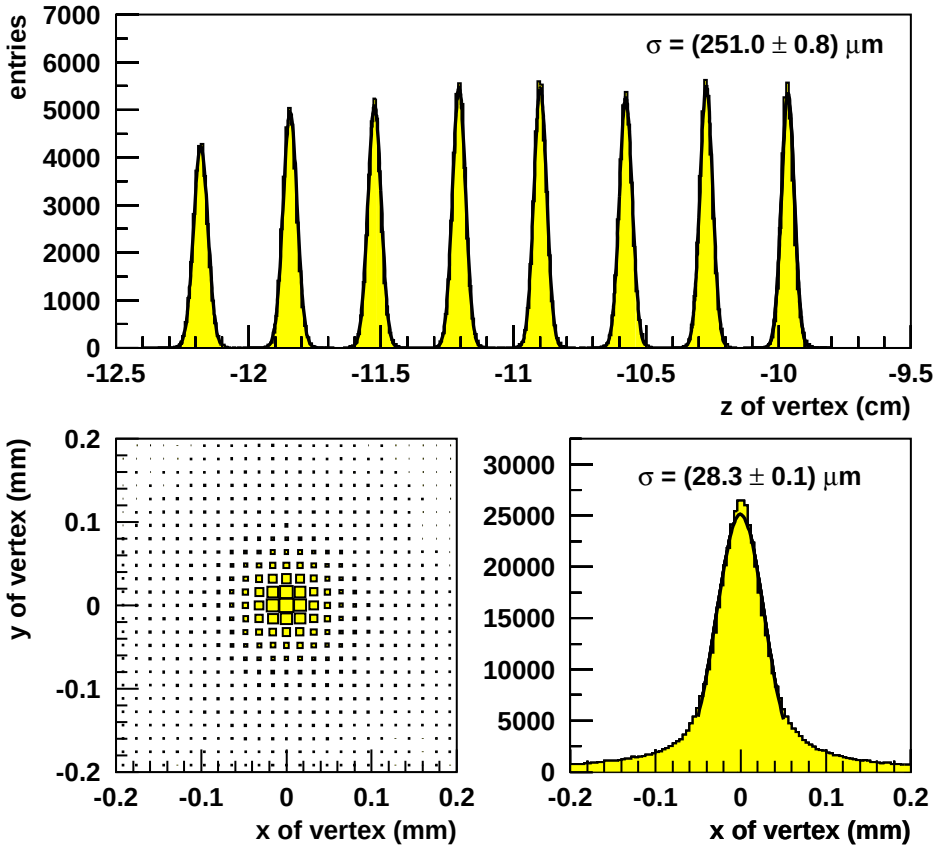

Figure 4.15: Top: Reconstructed z-position of interaction vertices. Each peak corresponds to one target disc. Bottom: Vertex resolution in the x-y plane determined from the high-p_T pions ($p > 5$ GeV/c).

4.7 The Energy Loss Distribution and Rejection Power

An example of the measured energy loss distribution in SDD2 for electron and positron candidate tracks is displayed in Fig.4.16. We can distinguish clearly two peaks. While the left peak corresponds to the energy loss of one minimum ionizing particle, the right one is due to the energy loss of two unresolved particles.

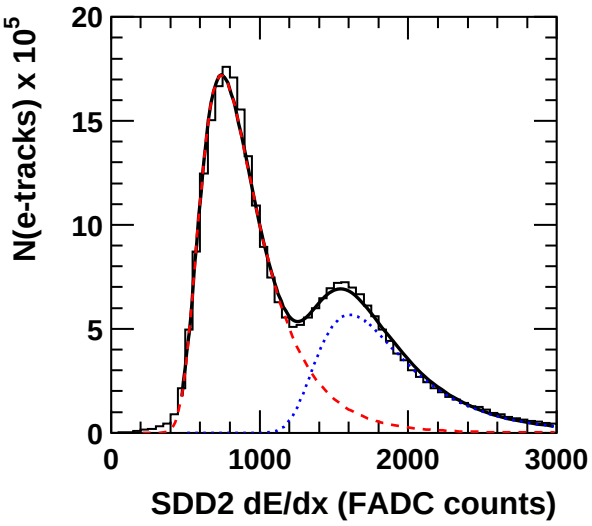

Figure 4.16: The energy loss distribution in SDD2. The full line represents the double Landau fit. The dE/dx distribution of one minimum ionizing particle is indicated by the dashed line, while that of two unresolved particles is represented by the dotted line.

With a thickness of 280μm, the silicon detectors can be still considered as thin absorbers. The energy loss of charged particles in such absorber is approximated by the Landau distribution [137]. The form of this distribution is affected by large fluctuations of the number of collisions involving large energy transfer, which result in a skewed distribution with a long high energy tail. The double Landau fit (Fig.4.16) apparently describes the experimental distribution very well. Only at small energy losses (below 600 FADC counts) is the measured distribution distorted by artificially split hits causing its shift towards the lower dE/dx values.

The measurement of the energy loss in SDDs is of a great importance for the analysis of low-mass e^+e^- pairs. In fact, the contributions of π^0 Dalitz decays, photon conversions (in the target and in SDD1), and the single tracks of partially reconstructed pairs overwhelm by three orders of magnitude the signal from dilepton pairs of interest. The conversions and Dalitz decays can be distinguished from other sources of dilepton pairs by their very low mass of $m_{e+e-} < 200$ MeV/c^2. Since the low momentum tracks with $p_T < 60$ MeV/c cannot be reconstructed in the magnetic field, such pairs are usually only partially reconstructed and information about their mass is lost. In such cases, an information about the opening angle can help to reject them, because most of them have an opening angle smaller than 35 mrad. Thus, if an additional hit is found in SDDs in the vicinity of the electron (positron) candidate, such candidate can be rejected. Although pairs with opening angle smaller than 2.5 mrad cannot be resolved even in the silicon detectors, they deposit twice the energy of a single particle. Correlating the dE/dx information from both detectors as demonstrated in Fig. 4.17 provides a powerful rejection tool. More details can be found e.g. in [9, 11] specialized on the dilepton analysis. Especially

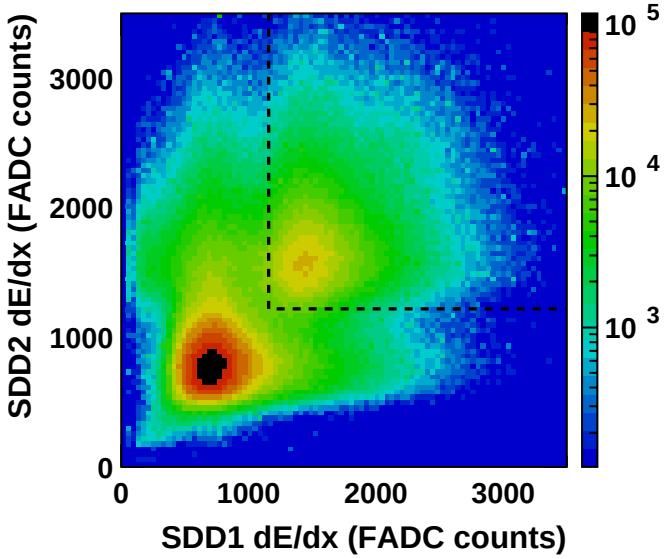

Figure 4.17: The energy loss distribution in SDD1 *vs* SDD2. The area corresponding to the deposition of double dE/dx mainly from close π^0 Dalitz decays and γ-conversions is surrounded by the dashed line and rejected in the off-line analysis.

in [11] a very detailed study including corrections of the ballistic deficit effect, anode dependencies and time variations was performed. This study resulted in the decrease of the width of the Landau distribution by about 30%, improving thereby the single and double dE/dx separation.

5

Calibration, Tracking and Particle Identification

The analysis presented in this work starts at the raw data level in order to reconstruct the event plane for both charged hadron and pion analyses. Compared to the previous analysis [28] the statistics of the charged hadron sample is significantly increased. In parallel to the pion analysis, a new dilepton analysis using a mixed-event technique for detailed background studies was performed [11]. In this chapter we describe the analysis steps up to the identified particle tracks and the momentum measurement.

5.1 From Raw Data to Particle Tracks

The full 1996 data sample contains $44 \cdot 10^6$ Pb-Au events. For the electron and pion analyses the full available set was used, for the charged hadron analysis a small fraction was sufficient. The data statistics is summarized in Table 5.1. The combined electron-pion data production was carried out at the CERN EFF PC cluster for two weeks simultaneously at 40 CPUs. The data for charged hadron analysis were processed at the CERES PC cluster for 4 days simultaneously at 14 CPUs. Both analyses were performed in the framework

Analysis step	**Number of events**
Available events	44 086 792
All detectors unpackable [1]	41 699 711
Pion analysis	
Good quality events	39 509 567
Events with a pion candidate	32 337 569
Charged hadron analysis	
Analyzed events	3 518 972

Table 5.1: Event statistics for high-p_T pion and charged hadron analyses.

[1] Reduction caused by DAQ problems.

of the C++ software package 'COOL' (**C**ERES **O**bject **O**riented **L**ibrary, [27]). The output has a form of particle tracks written into the column-wise HBOOK ntuples [138]. For each particle track necessary information from each detector is stored like hit amplitudes in the SDDs, number of hits on rings in RICHes, together with global event characteristics like centrality of collision, interaction vertex position, or event plane information.

The first step in the off-line analysis is similar for all detectors. The compressed raw data are unpacked in order to obtain primary detector information. In the case of SDDs, the raw data consist of amplitudes for all non-empty cells in the anode number, time bin coordinates. For the RICH detectors and the pad chamber it is a collection of pad coordinates (x, y) and corresponding amplitudes. The next step is individual for each detector type. For the silicon detectors the reconstruction of hits, track segments and interaction vertex was already described in Section 4.6.2. Since the pad-readout of the RICH detectors and the pad chamber is very similar, they are analyzed in the same way. First, adjacent pads having one of the two coordinates identical are connected to a cluster. All clusters then undergo a cleanup necessary to minimize the influence of background signals arising from various sources like electronic noise, pedestal fluctuations in readout modules, or ionizing particles [27], and causing later problems for ring recognition algorithms. The cleanup procedure was carefully studied in order to avoid efficiency losses. Each local maximum in a given cluster and surrounding pads is identified as a hit of a UV-photon in the RICH detectors, or as an ionizing particle in the pad chamber.

From now on, complete particle trajectories are reconstructed. The next paragraphs describe briefly the tracking methods used for charged hadrons, electrons and pions.

5.1.1 Charged Particle Tracks

Once the interaction vertex and the SDD track segments are reconstructed, the trajectory of charged particles is extrapolated downstream to the pad chamber. If a pad chamber

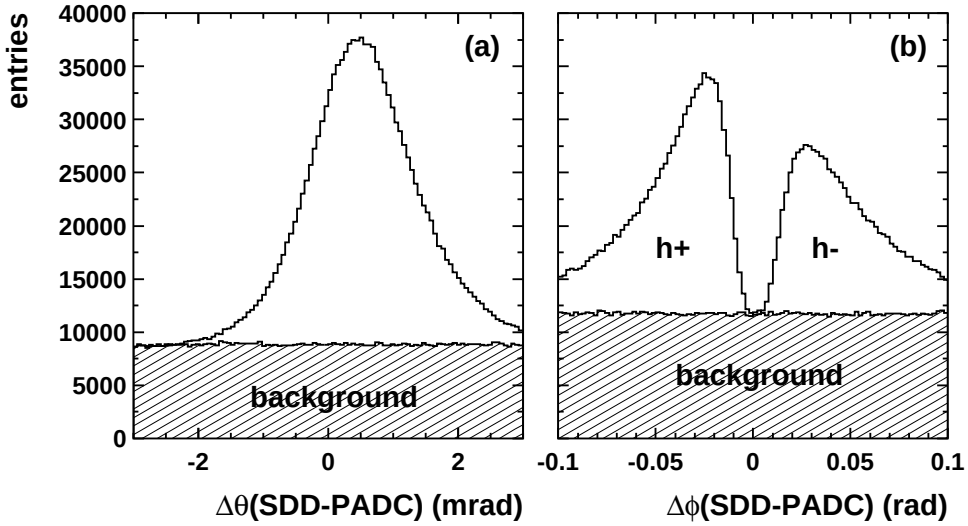

Figure 5.1: Matching distributions between SDDs and PADC for charged track candidates in polar angle θ (a), and in azimuth ϕ (b). The hatched area represents the random background determined using the method of detector rotations.

hit is found within a certain matching window, a charged particle track candidate is created. The size of this window, taking into account multiple scattering, is 3 mrad in θ, and 100 mrad in ϕ direction corresponding to the lower momentum cut-off of 1 GeV/c (Fig. 5.1). Since the correct match is not known, all possibilities within this window are considered as charged track candidates.

The contribution of random background, which is shown by the dashed area in Fig. 5.1, can be estimated using a method of detector rotations. Since the signal between the two silicon detectors is highly correlated, the main background contribution comes from the combination of SDD track segments with hits in PADC. By rotating the PADC hits in a given event by a random angle with respect to the silicon detectors, the true physics signal is destroyed and the found 'charged particle tracks' can be thus ascribed to the background tracks.

5.1.2 Electron Tracks

The electron identification is based on capabilities of the RICH detectors. Ring pattern recognition is performed by a point to ring Hough transformation [139]: around each photon hit a ring with asymptotic radius is created in the transformed plane. The intersection of such rings indicates the center of an electron (positron) ring candidate in the original pad-plane. For precise determination of the ring center, a robust fit procedure with two free parameters, x and y position of the ring center, is used [140]. Background ring candidates are rejected by requiring matching with the tracking detectors [9, 27].

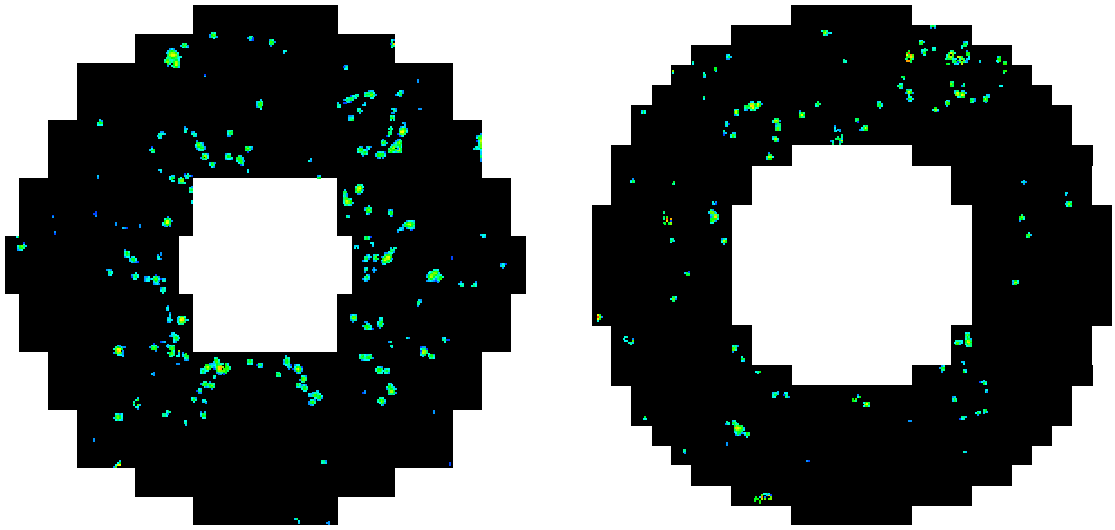

Figure 5.2: Event displays of RICH1 and RICH2. A close e^+e^- – pair is seen at 1 o'clock position. A ring belonging to a high-p_T pion is at 5 o'clock position.

5.1.3 Charged Pion Tracks

Charged pions above the Cherenkov threshold can be distinguished in the RICH detectors from electrons by their smaller ring radii. Their identification makes full use of the

external tracking detectors. The size of the (θ, ϕ)-matching window between SDD and PADC used for the charged hadron tracking can be now decreased in both directions. For identified pions having momentum at least 4.5 GeV/c is the size of the matching window in ϕ decreased to ± 25 mrad. The size of the θ-matching window is only driven by the matching quality between SDD and PADC since the multiple scattering contribution is negligible. Knowing the coordinates of the pion candidate before and after magnetic field, the position of the ring centers in the RICH detectors can be predicted. All photon hits around the predictors are collected and used as an input for a robust free radius fit procedure [140] which minimizes the function

$$f(x, y, r) = -\frac{1}{N-3} \sum_{i=1}^{N} \exp\left(\frac{\sqrt{(x_i - x)^2 + (y_i - y)^2} - r^2}{2\sigma_f^2} \right). \tag{5.1}$$

Here, x, y are the coordinates of the ring center with radius r, and σ_f is the width of the distribution of photon hits on the ring with coordinates x_i and y_i.

Fig. 5.3 shows a correlation between the RICH ring radius and the deflection by the magnetic field as determined from SDD and PADC. Clearly, there are two isolated islands present which correspond to positive and negative charged pion tracks, respectively. For comparison, the dashed curve indicating the expected correlation between the deflection angle and the pion momentum, expressed in terms of the ring radius (cf. Eq. (3.11) and Eq. (3.14)), is also plotted.

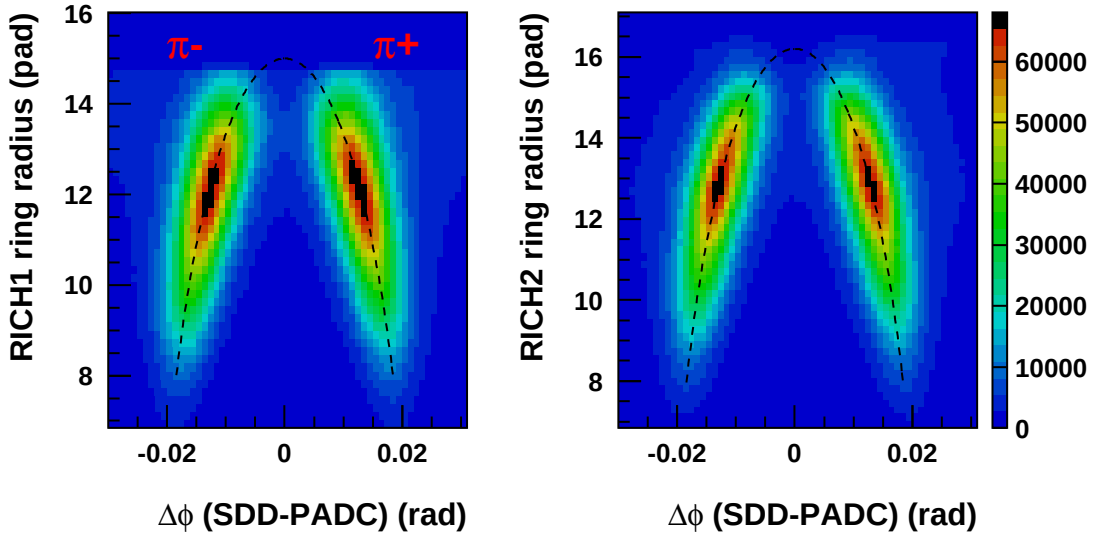

Figure 5.3: Correlation between the Cherenkov ring radius and the deflection by the magnetic field measured by SDD and PADC, for RICH1 (left) and RICH2 (right). The dashed curves indicate the expected correlation between ring radius and deflection angle.

5.2 Spectrometer Calibration

Before starting any particle tracking, all detectors have to be properly intercalibrated. A precise geometrical alignment of the detectors was carried out in the previous analy-

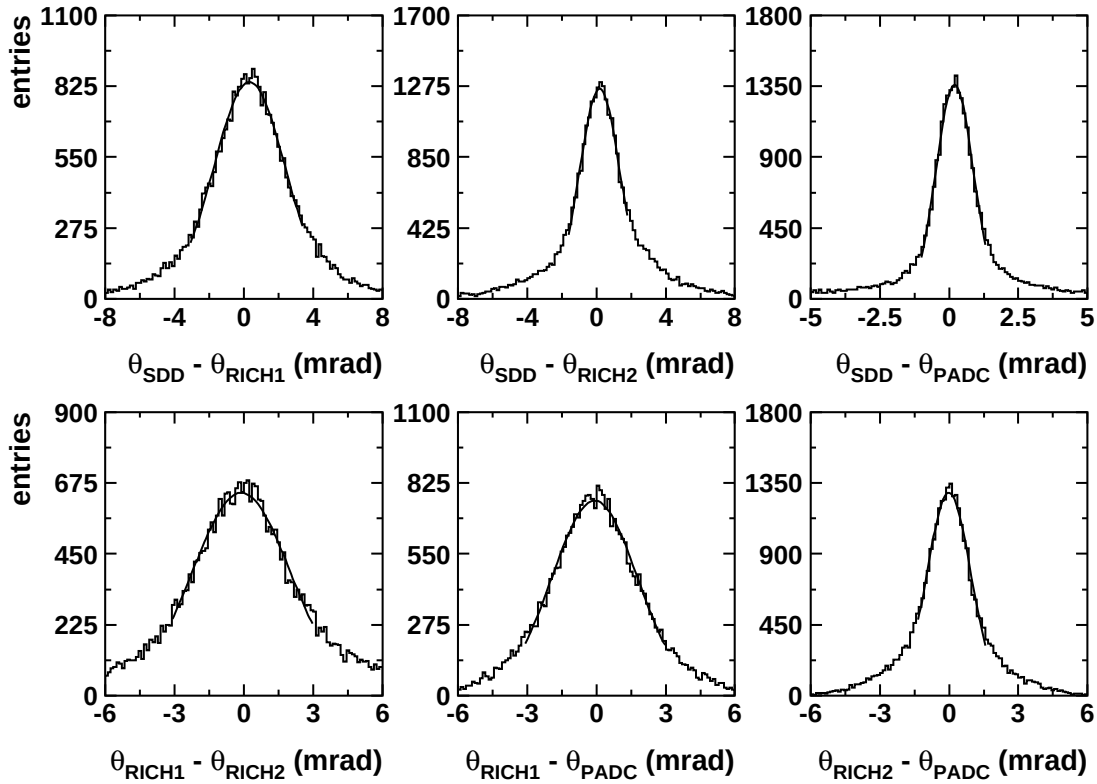

Figure 5.4: The θ-matching distributions for various detector combinations determined using charged pions with $p > 8$ GeV/c.

sis [27] using a sample of high momentum pions ($p > 5$ GeV/c), which are almost free of multiple scattering and therefore serve as an excellent calibration tool. Starting with an internal calibration of the SDD vertex telescope described in Section 4.5, the remaining detectors (RICH1, RICH2 and PADC) are aligned with respect to the center of SDD1 used as a reference point.

Fig. 5.4 shows the θ-matching distributions for different detector combinations. From their width we can determine individual detector resolutions according to

$$\sigma_{\text{matching(a-b)}} = \sqrt{\sigma^2_{\text{resolution(a)}} + \sigma^2_{\text{resolution(b)}}}. \tag{5.2}$$

Values of the Gaussian width σ of the θ-matching distributions for all possible detector combinations and from there calculated detector resolutions are summarized in Table 5.2.

5.2.1 Time Stability

During a long data taking period different factors can influence the spectrometer performance. Thus the calibration performed on a limited data sample is not necessarily valid for all data and has to be carefully checked. In the following paragraphs we discuss the stability of the calibration for all detectors.

Detector combination	$\sigma_{\triangle\theta}$ (mrad)
SDD1-SDD2	0.40
SDD-RICH1	2.07
SDD-RICH2	1.17
SDD-PADC	0.67
RICH1-RICH2	2.14
RICH1-PADC	1.85
RICH2-PADC	0.95

Detector	σ_{θ} (mrad)
SDD1	0.28
SDD2	0.28
RICH1	1.90
RICH2	0.94
PADC	0.54

Table 5.2: Values of the Gaussian width of the θ-matching distributions for various detector combinations (left) and the extracted θ-resolution of the individual CERES detectors (right). Pion tracks with $p > 8$ GeV/c were used.

Silicon drift detectors

As mentioned in Chapter 4.1, the drift velocity in silicon detectors is very sensitive to temperature. Fig. 5.5 shows the temperature measured on the wafers of silicon detectors. The temperature changes are in both detectors correlated. Despite the water and the air cooling, the temperature variations are of the order of one degree. This is reflected in 1% relative change of the drift velocity and corresponds to 300 μm shift on the full drift distance. The temperature variations change the position of the right edge of the drift time spectrum t_{max} (cf. Chapter 4.5). In [141] an automatic procedure was developed which by fitting the right edge of the drift spectrum determines run-to-run dependent values of t_{max}. The new approach for hit reconstruction using the Gaussian fit resulted in a systematic shift of the reconstructed hit position in comparison to the old center of gravity method. This caused subsequently a systematic offset of the reconstructed vertex position. To

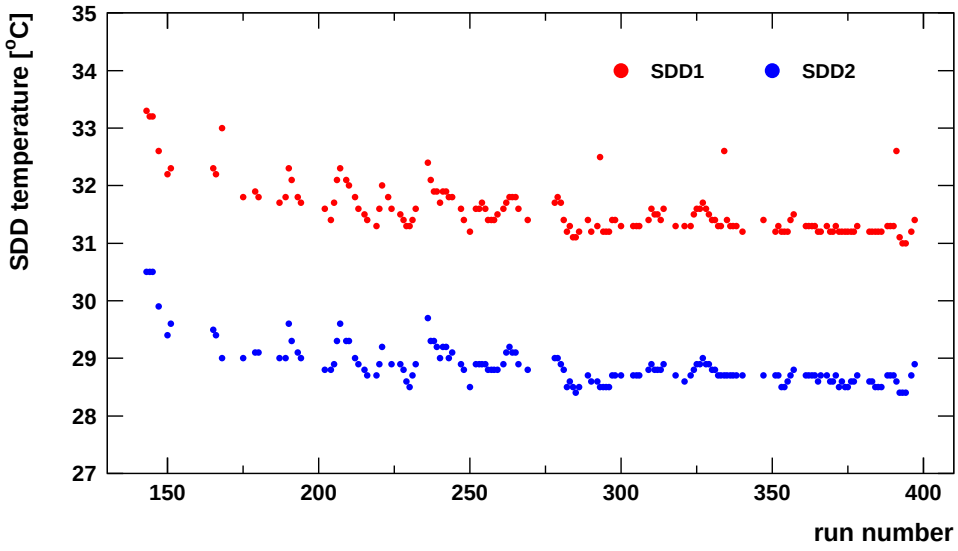

Figure 5.5: Temperature variations on the wafers of the silicon drift detectors.

avoid a tedious recalibration of the silicon drift detectors, we decided to use a simplified approach. We have shortened artificially the radial scale by decreasing the outer radius of SDD1 by 24μm. The remaining run-to-run dependent offsets between the expected and the reconstructed vertex position we have corrected by applying a multiplicative factor

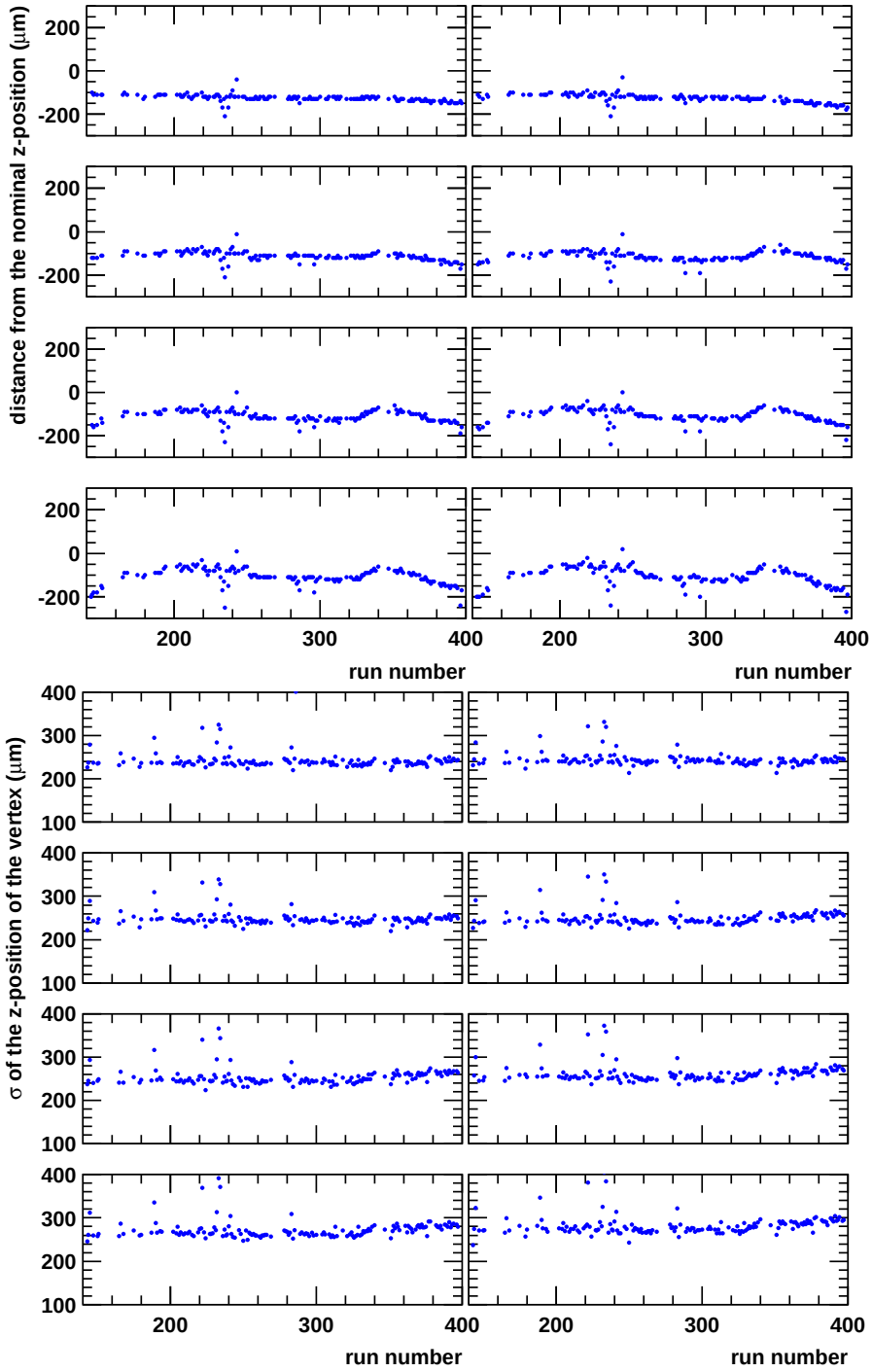

Figure 5.6: Run-to-run stability of the reconstructed z-position (a) and of the Gaussian width (b) of the interaction vertex for the individual target discs.

(slightly different from 1.0) on the drift velocities in both detectors.

The top part of Fig. 5.6 shows the obtained z-position of the eight target discs in different runs. The shift of the SDD1-SDD2 θ-matching distribution due to the residual offset of about 100 μm of the reconstructed position from the nominal target disc position is negligible in comparison to the width of the matching distribution. The bottom part of Fig. 5.6 displays the corresponding Gaussian width of the vertex distribution in the z-direction. The better double-hit resolution of the new hit reconstruction software (cf. Chapter 4.6) improved the vertex resolution in the z-direction on average from 280 μm quoted in [27] to 260 μm.

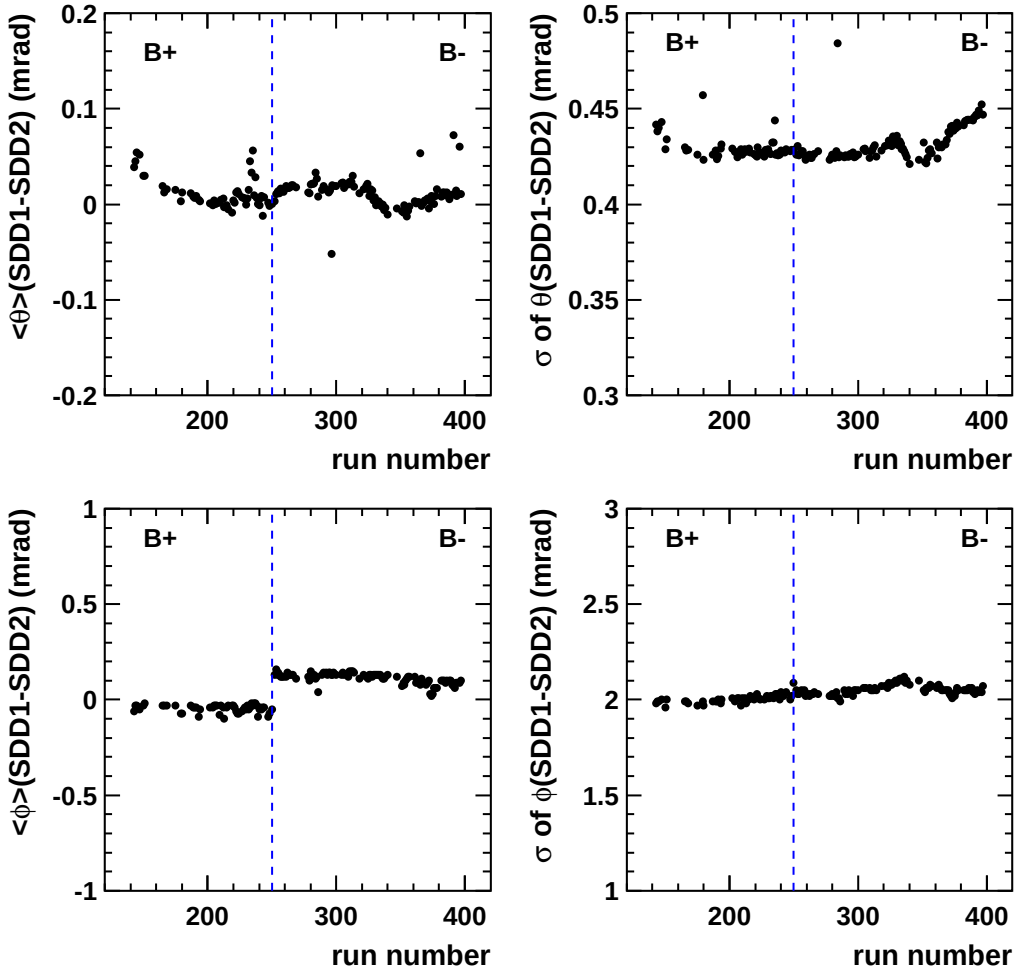

Figure 5.7: Run-to-run stability of position and Gaussian width of the θ and ϕ-matching between SDD1 and SDD2. The vertical line indicates the change of the magnetic field polarity (B+, B-).

The time variations of position and Gaussian width of the θ and of the ϕ-matching distributions are shown in Fig. 5.7. Since the selection criteria for charged hadrons and high-p_T pions demand certain level of matching quality, the observed time variations have to be taken into account in order to avoid efficiency losses.

RICH detectors

The changes of the atmospheric pressure during the data taking influence the value of the asymptotic ring radius. The time variations of the pressure shown in Fig. 5.8 are clearly coincident with changes of the asymptotic ring radius determined from the sample of electron rings in each run. Since the momentum of high-p_T pions is determined from the measured ring radius (cf. Eq. (5.7)), the observed variations of R_∞ were incorporated in the off-line analysis.

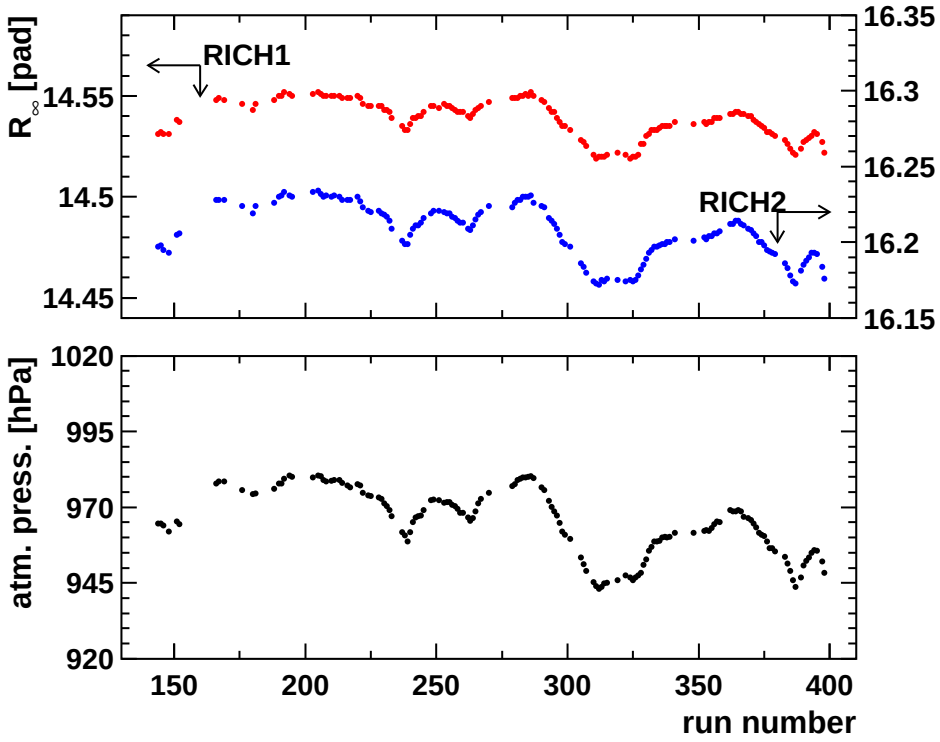

Figure 5.8: The run-to-run variations of the asymptotic ring radius of RICH1 (top) and RICH2 (middle) and its correlation with the atmospheric pressure (bottom).

SDD-PADC system

The remaining miscalibration of the vertex telescope is reflected in time variations of the θ-matching between the silicon detectors and PADC shown in Fig. 5.9. Since a cut on the width of this matching is used in both charged hadron and pion selection criteria, the observed changes are considered there.

Another important quantity, which needs to be checked, is the correlation between the deflection in the magnetic field and the ring radius measured in the RICH detectors (cf. Fig. 5.3). Using a sample of high-p_T pions we have discovered an azimuthal dependence of the deflection angle. This is demonstrated separately for positive and negative pions and both magnetic field polarities in Fig. 5.10. We have selected pions with momentum (7.0-7.5) GeV/c determined from the RICH2 ring radius. The expected value of the deflection angle calculated from Eq. (3.14) was taken as a reference point for the correction procedure (Fig. 5.10).

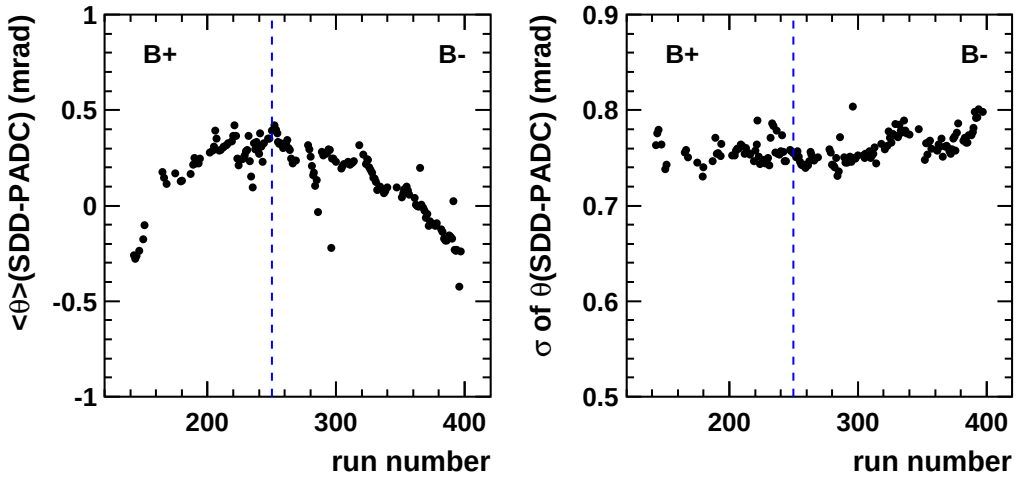

Figure 5.9: Run-to-run stability of the position (left) and width (right) of the θ-matching peak between SDD and PADC. The vertical line indicates the change of the magnetic field polarity.

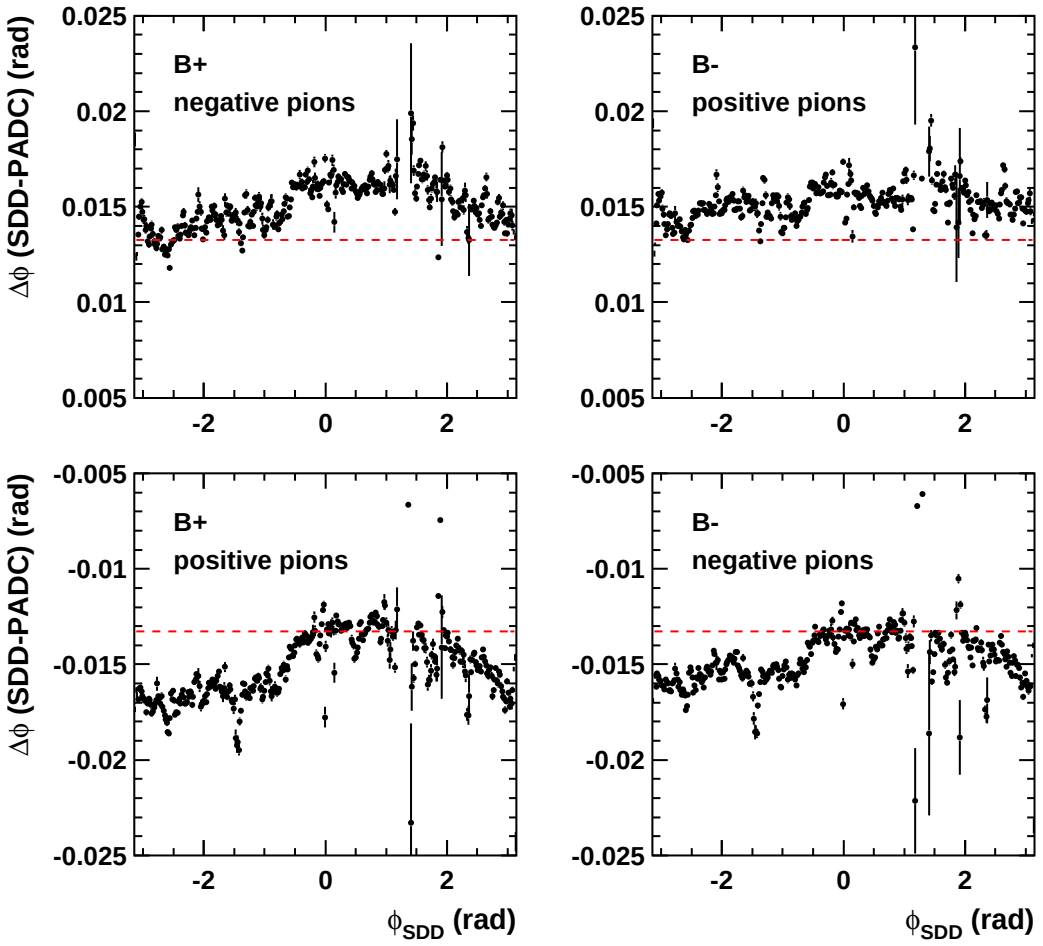

Figure 5.10: Azimuthal variations of the deflection angle between SDD and PADC for positive and negative charged pions with momenta between (7.0-7.5) GeV/c and both magnetic field polarities. The horizontal line represents the expected deflection angle.

5.3 Momentum Measurement

The CERES spectrometer allows to determine momentum by two different methods - the azimuthal deflection in the magnetic field and the ring radius in the RICH detectors. Both methods are described and compared below.

5.3.1 Azimuthal Deflection in the Magnetic Field

As described in Chapter 3.4, a charged particle experiences a *'kick'* in the azimuthal direction due to the magnetic field configuration, which is inversely proportional to its momentum. RICH2 measures 100% of the deflection angle, while the deflection at PADC is only 65% of this value as shown schematically in Fig. 5.11.

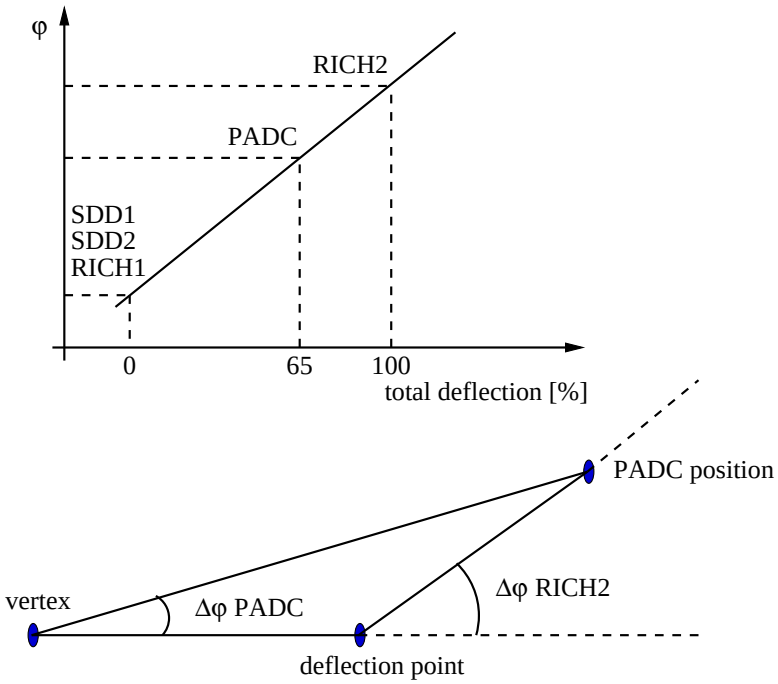

Figure 5.11: Schematic geometry of the deflection in the magnetic field (bottom). RICH2 and PADC measure different fraction of the deflection angle $\Delta\phi$ (top).

Rewriting Eq. (3.14) in a symbolic way

$$p = \frac{\phi_0}{\Delta\phi}, \tag{5.3}$$

where ϕ_0 is 144 mrad for RICH2, and 96 mrad for PADC at the full magnetic field, we can determine the momentum resolution

$$\sigma_p = \frac{dp}{d(\Delta\phi)}\sigma_{\Delta\phi} = \frac{\phi_0}{(\Delta\phi)^2}\sigma_{\Delta\phi} = \frac{p^2}{\phi_0}\sigma_{\Delta\phi} \tag{5.4}$$

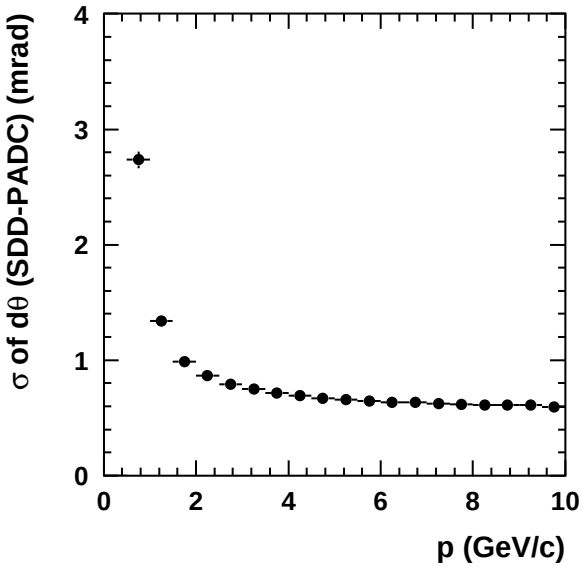

Figure 5.12: Momentum dependence of the Gaussian width of the θ-matching distribution between SDD and PADC for charged particles. The momentum was determined from the deflection in the magnetic field.

and the relative momentum resolution

$$\frac{\sigma_p}{p} = \frac{p}{\phi_0}\sigma_{\Delta\phi}. \tag{5.5}$$

There are two factors which determine the $\sigma_{\Delta\phi}$ resolution, the intrinsic resolution of the detectors, and multiple scattering which is inversely proportional to momentum. We can therefore write

$$\sigma_{\Delta\phi} = \sqrt{\left(\sigma_{\mathrm{p}>2\ \mathrm{GeV}/c}\right)^2 + \left(\frac{\sigma_{\mathrm{mult.scatt.}}}{p}\right)^2}. \tag{5.6}$$

Looking at the momentum dependence of the Gaussian width of the θ-matching distribution between the silicon detectors and the pad chamber demonstrated in Fig. 5.12,

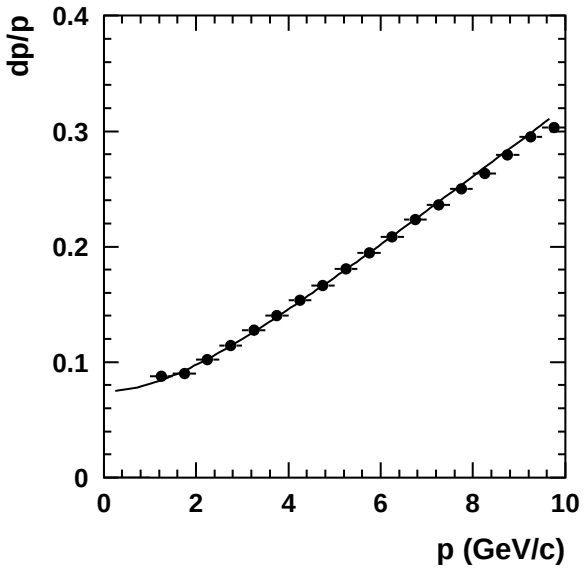

Figure 5.13: Momentum resolution for charged particles determined from the deflection in the magnetic field between SDD and PADC.

we observe a clear widening of the distribution towards small momenta due to the increasing importance of multiple scattering. Taking into account the relation between the polar and the azimuthal angles $d\theta = \sin(\theta)d\phi$ we obtain the momentum resolution of the deflection method shown in Fig. 5.13. The curve represents a fit according to Eqs. (5.5) and (5.6). The fit parameters are $\sigma_{\text{p>2 GeV}/c} = (2.985 \pm 0.005)$ mrad, and $\sigma_{\text{mult.scatt.}} = (7.15 \pm 0.02)$ mrad/(GeV/c).

5.3.2 RICH Ring Radius Measurement

The momentum of charged particles which are sufficiently fast to produce Cherenkov light in the RICH detectors can be determined from the ring radius R according to

$$p = \frac{m\gamma_{\text{th}}}{\sqrt{1-(R/R_\infty)^2}}, \tag{5.7}$$

where m is the particle mass. Since pions reach R_∞ only for momenta around 30 GeV/c we can use this method for their identification and momentum measurement. For pion momenta below 15 GeV/c, the background generated by other particles is negligible. Kaons start to produce Cherenkov light only if their momentum reaches 16 GeV/c.

Using Eq. (5.7) we derive the momentum resolution

$$\sigma_p = \frac{dp}{dR}\sigma_R = \frac{R}{R_\infty^2 - R^2} p\sigma_R. \tag{5.8}$$

The corresponding relative momentum resolution is given by

$$\frac{\sigma_p}{p} = \frac{R}{R_\infty^2 - R^2}\sigma_R \simeq \frac{\sigma_R}{R_\infty(m_\pi\gamma_{\text{th}})^2}p^2, \tag{5.9}$$

where σ_R is the ring radius resolution. In the absence of background, σ_R depends on the number of hits N, and on the single hit resolution σ_{sh}[1] as

$$\sigma_R = \frac{\pi}{2}\frac{\sigma_{\text{sh}}}{\sqrt{N-3}}. \tag{5.10}$$

Coefficient 3 in the denominator represents the number of degrees of freedom. These are x, y position of the ring center, and the ring radius. In practice, the background hits dilute the $1/\sqrt{N}$ dependence (for details see Chapter 6.1).

From Eq. (5.9) follows that for very high momenta the momentum resolution diverges when ring radius approaches its asymptotic value. For momenta in the vicinity of the Cherenkov threshold, where the number of created photons approaches zero, the resolution is governed by $1/\sqrt{N-3}$ term. Since in the praxis we have to have always at least 4 hits in order to find a ring, the term $1/\sqrt{N-3}$ influences strongly the reconstruction efficiency, but it is not visible on the momentum resolution.

5.3.3 Comparison of Both Methods

The sample of high-p_T pions provides for a direct comparison of both methods above $p =$ 5 GeV/c. Fig. 5.14 shows the correlation between the ring radius in RICH2 and the

[1] The single hit resolution has value of σ_{sh}(RICH1)=1.2 mrad for RICH1, and σ_{sh}(RICH2)=0.76 mrad for RICH2, respectively [9].

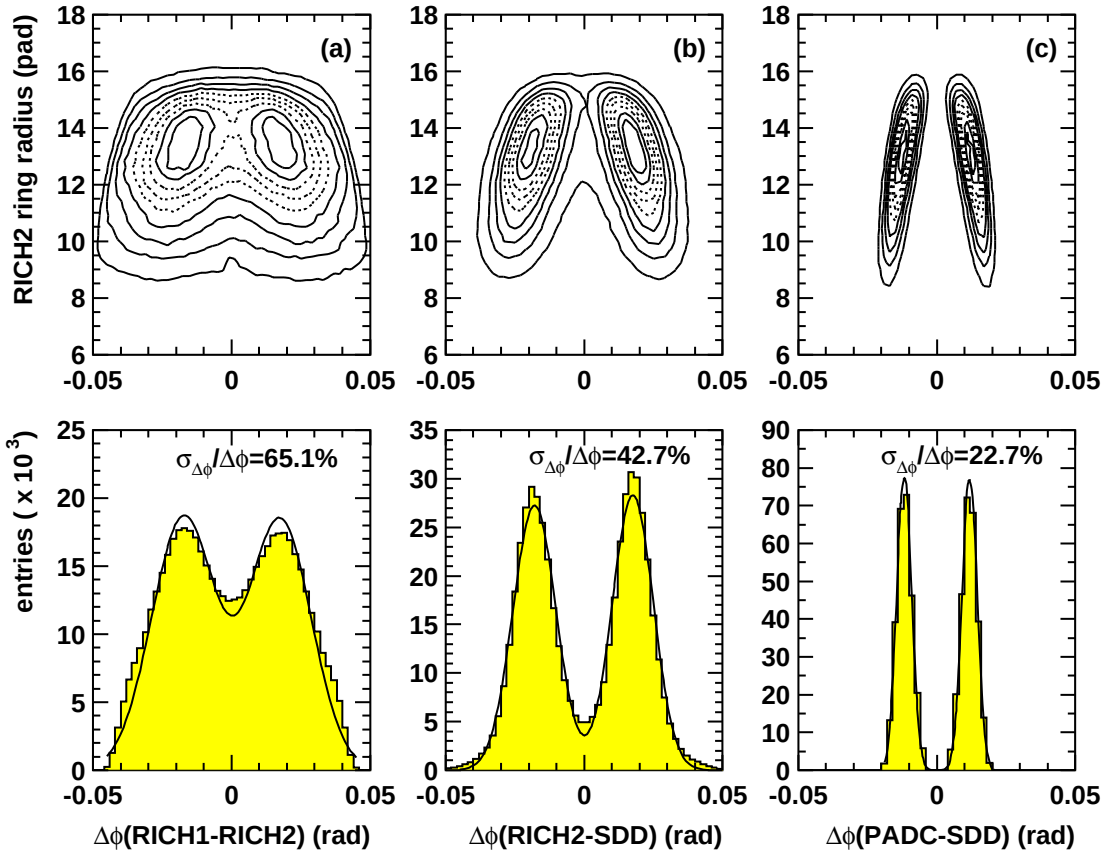

Figure 5.14: Correlation between the RICH2 ring radius and the azimuthal deflection angle for different detector combinations (top) and the corresponding momentum resolutions obtained for high-p_T pions with the ring radius in the interval of (13,14) pads ($p \approx 8$ GeV/c) (bottom).

azimuthal deflection obtained using different detector combinations. If only the RICH detectors are used to calculate $\Delta\phi$ (Fig. 5.14(a)), the two bands representing pions with positive and negative charge strongly overlap. Replacing RICH1 by silicon drift detectors with much better angular resolution, the two charges become clearly separated (Fig. 5.14(b)). The charge separation becomes even more pronounced using the SDD-PADC combination (Fig. 5.14(c)), even though the smaller azimuthal deflection measured by PADC partially compensates its better angular resolution with respect to RICH2.

The momentum resolution can be determined experimentally in the following way. By choosing a small ring radius interval ΔR corresponding to a certain momentum interval Δp the Gaussian width $\sigma_{\Delta\phi}$ of the resulting $\Delta\phi$ distribution is a measure for the azimuthal resolution for the chosen momentum interval Δp (see Eq. 5.5). One such example is depicted in the bottom part of Fig. 5.14(c).

In Fig. 5.15 the momentum resolutions corresponding to the different methods are shown. The best momentum measurement is given by the RICH2 ring radius measurement. RICH1 momentum resolution shows the same quadratic dependence as RICH2, however, with a steeper rise caused by higher background contamination in comparison to

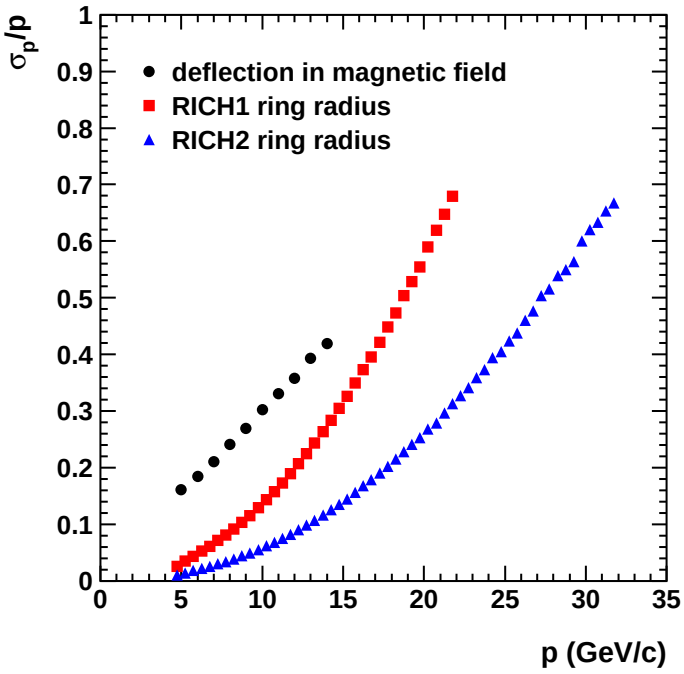

Figure 5.15: Momentum resolution of the CERES spectrometer determined from the deflection in magnetic field and from the ring radius measurement in the RICH detectors.

RICH2. The method of azimuthal deflection has the worst resolution. Consequently, the RICH2 ring radius measurement is chosen for the momentum determination of identified high-p_T pions. For charged particles with momentum below of the Cherenkov threshold we have to use for the momentum measurement the deflection in the magnetic field.

6

Monte-Carlo Simulation

Besides rather well defined properties of the spectrometer, like the geometrical and kinematical acceptance, or momentum resolution, there is a large variety of complex effects mostly tied to the analysis software that potentially affect the physics results. Their impact has to be carefully studied and well understood before the data can be interpreted. Since the full simulation of a heavy-ion collision based on various models and the subtleties in response of the apparatus are not realistic enough, we use an *overlay Monte-Carlo technique*: one or more particles of interest are embedded into real events serving as a background. The full Monte-Carlo simulation is employed only to derive corrections of the measured charged particle multiplicity in the silicon detectors used for centrality measurement. This correction together with its limitations is discussed in Chapter 7.

The CERES Monte-Carlo simulation proceeds in several steps. The first part is based on the software package GEANT [142], which allows to define geometry and material composition of the detectors as well as the magnetic field [143]. It calculates the path of a particle and all subsequently generated particles passing through the spectrometer modified by multiple scattering and deflection in magnetic field. In the output of the GEANT simulation all information necessary for the simulation of the detector responses is stored. In the second part, the output from GEANT is used to generate detector signals in a format identical to that of the measured data so that both can be analyzed with the same analysis software. [1] This allows later to extract the reconstruction efficiency dependent on momentum, centrality of collision, etc.

6.1 Detector Response

A comparison of the simulated and the measured response of the various detectors is the first important step to be taken. Several quantities, like hit characteristics in the silicon detectors, or ring properties in the RICH detectors, have to be checked and tuned in order to obtain good agreement between the simulated and the measured data.

[1] The output is stored in column-wise ntuples as for the real data and in addition contains one block with Monte-Carlo information about the embedded particles.

Silicon drift detectors

GEANT simulates the ionization processes of a charged particle passing through the silicon wafer following the Bethe-Bloch formula and calculates the energy deposited in the detector. For each particle we can calculate the amount of the deposited charge, using 3.6 eV [123] for creation of one electron-hole pair. However, this signal is influenced by the readout electronics. The preamplifier chip transfers and amplifies the deposited charge into the voltage signal. This amplification factor has to be tuned such that the simulated hit amplitude distribution agrees with that observed in the data. The hit amplitude is not homogenous over the wafer, because it changes in the radial direction due to the ballistic deficit and in the azimuthal direction it shows variations due to the anode dependent gain. These effects have to be taken into account in order to obtain a realistic description. Fig. 6.1 compares the hit amplitude distribution in the data and with that in

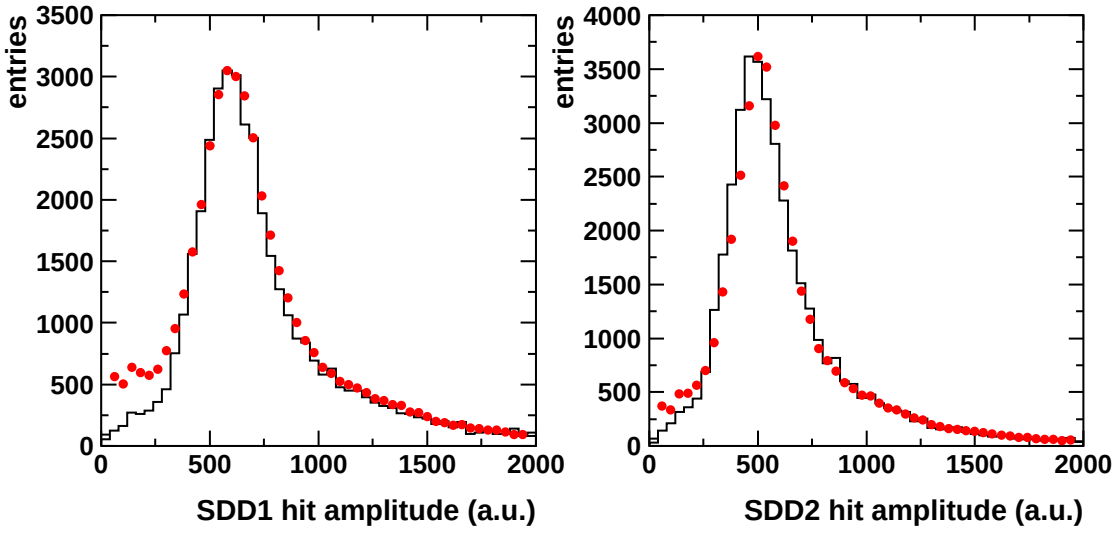

Figure 6.1: Comparison between the hit amplitude distribution in data (points) and in the Monte-Carlo simulation (histogram) for SDD1 (left) and SDD2 (right).

the simulation. The agreement is very good for SDD2, but there is a difference at small hit amplitudes between the data and the simulation in SDD1. It is due to the artificial hit splitting caused by sensitivity of the hit reconstruction software on the anode dependent pulse shape which is not implemented with sufficient accuracy in the simulation.

Hit dimensions are controlled in the simulation by several parameters. While in the azimuthal direction the width of a hit is given solely by diffusion and geometry, in the radial direction an additional broadening due to the shaping time of the preamplifier chip comes into play. In the simulation, the generated signal is spread over 13 time bins and 5 anodes, in total 65 cells, using the realistic interlaced anode structure. On top of each cell is added a Gaussian distributed electronic noise. In the last step the behavior of the 6-bit non-linear FADC and the scanner is simulated. The comparison of the azimuthal hit width in the data and in the simulation is shown in Fig. 6.2.

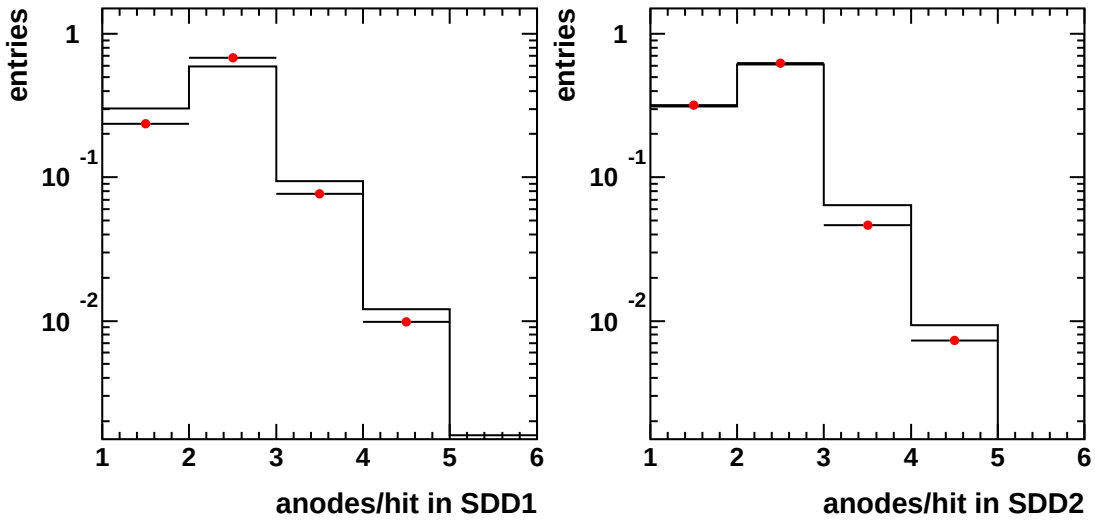

Figure 6.2: Probability distribution of the number of anodes per hit in data (points) and in the Monte-Carlo simulation (histogram) for SDD1 (left) and SDD2 (right).

RICH detectors

For the RICH detectors, GEANT calculates positions of Cherenkov photon hits in the UV-detectors produced by charged particles[2]. The hit position is influenced by several effects. GEANT takes into account the slight bend of the particle trajectory in the second radiator due to deviations of the magnetic field lines from straight lines pointing to the vertex, chromatic aberration, and multiple scattering. Other effects, such as transverse diffusion of photoelectrons in the conversion zone and the first amplifier stage, mirror

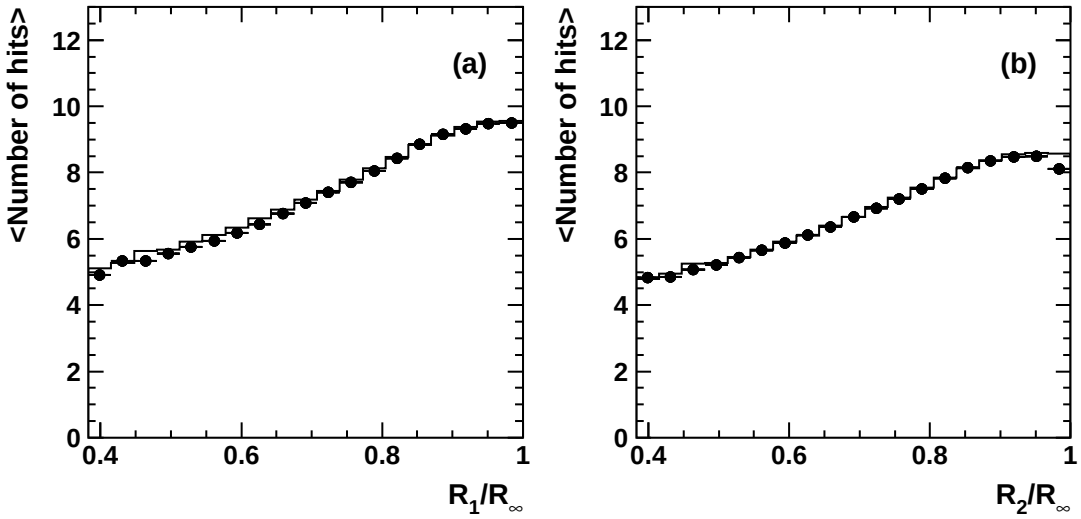

Figure 6.3: Dependence of the number of Cherenkov photon hits on ring radius (given as a fraction of R_∞) in data (symbols) and in the simulation (histogram) for RICH1 (a) and RICH2 (b).

[2]Since PADC is an almost identical copy of the RICH2 UV-detector, its simulation proceeds in an analogic way and is not described here. Details can be found e.g. in [9].

quality, and wire digitization, are simulated by an additional Gaussian smearing of the hit position in the COOL library. The signal created by a photon in the UV-detector is several times amplified and distributed over 5 x 5 readout pads [144]. In addition, a Gaussian distributed electronics noise and gain variations of the readout modules are included. Details can be found in [9].

The simulation of the RICH detectors plays a key role in pion reconstruction. Since we determine the pion momentum from the ring radius, we have to carefully check the number of photon hits and the ring radius in the simulation. Fig. 6.3 shows the mean number of the reconstructed photon hits as a function of the ring radius, which is given in a fraction of the asymptotic radius. We can see that data and simulation are in very good agreement for both RICH detectors. According to Eqs. (3.11) and (3.12), we would expect a parabolic increase of the number of hits with ring radius as shown in Fig. 6.4(a). However, the data show only a linear increase. For small ring radii, where the number

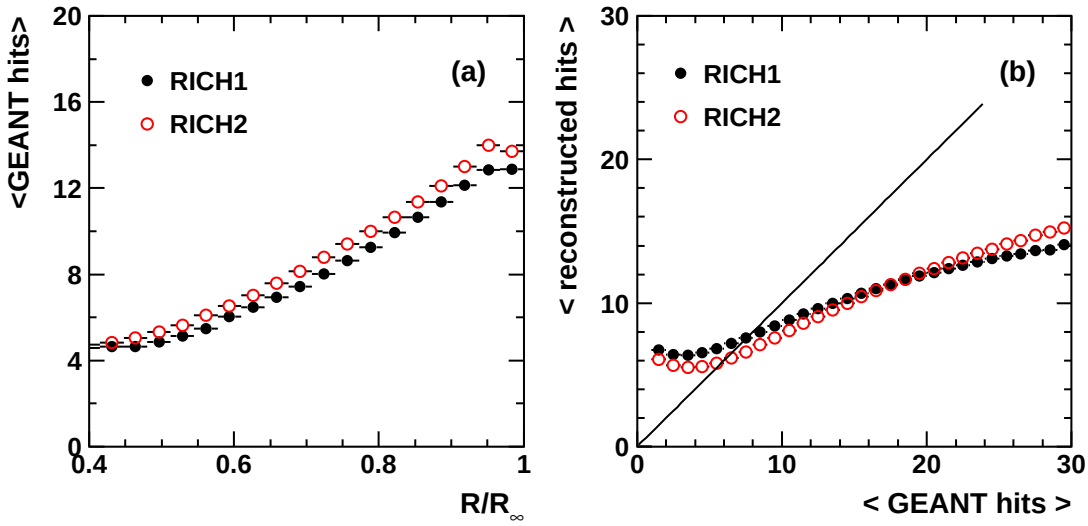

Figure 6.4: Dependence of the number of GEANT Cherenkov photon hits on the ring radius (a). Correlation between the number of the reconstructed and the GEANT Cherenkov photon hits (b).

of produced Cherenkov photons is small, background in the detector artificially increases the number of hits on rings. For larger number of Cherenkov photons, the finite single hit resolution and the limitations of the hit splitting algorithm, which is not able to resolve overlapping hits, cause a deficit of the observed hits (Fig. 6.4(b)).

6.2 Matching Description and Magnetic Field

The reconstructed hits (or rings) from all detectors are eventually combined to particle tracks. The next step in the simulation is to check the matching distributions between various detectors. In particular, we are interested in a proper description of the matching between the two silicon drift detectors, and between silicon detectors and the pad chamber, since we employ in the data analysis selection cuts on those distributions (cf. Chapter 8.2.1). Fig. 6.5 shows the θ matching and ϕ matching distributions between

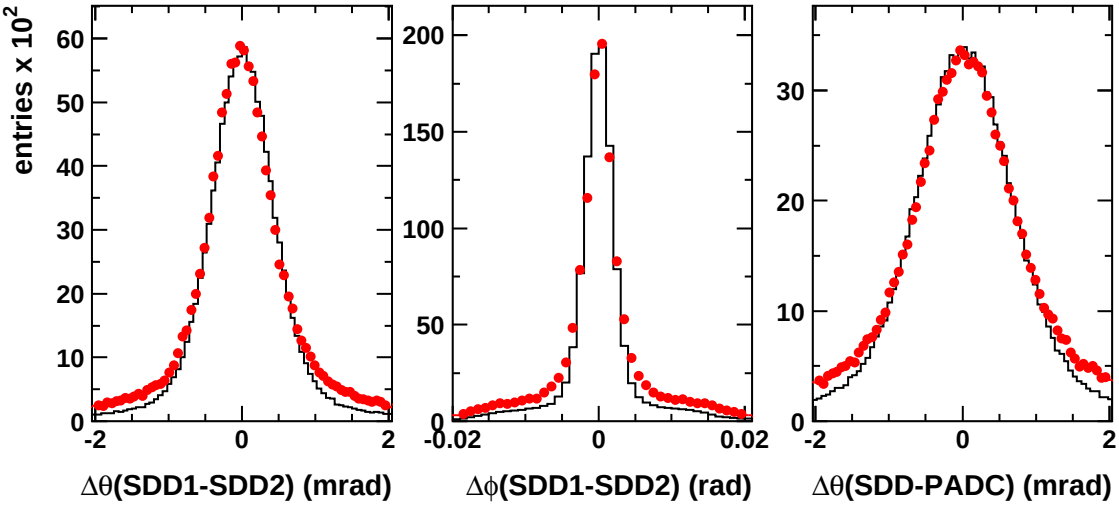

Figure 6.5: Comparison of the θ-matching distributions in the data (points) and Monte-Carlo (histogram) for the various detector combinations.

SDD1 and SDD2, and the θ matching distribution between SDD and PADC. The shape of the simulated distributions agrees well with those obtained for the measured data.

The good understanding of the magnetic field configuration in the simulation is important for momentum determination of charged particles. It can be checked by selecting pions within a small ring radius interval as employed for determination of the momentum resolution (cf. Chapter 5.3). Fig. 6.6 shows the comparison of the azimuthal deflection angle measured by RICH2 and PADC detectors with respect to the silicon detectors for pion tracks with the ring radius $R_2 =$ (13,14) pads. The agreement is very good.

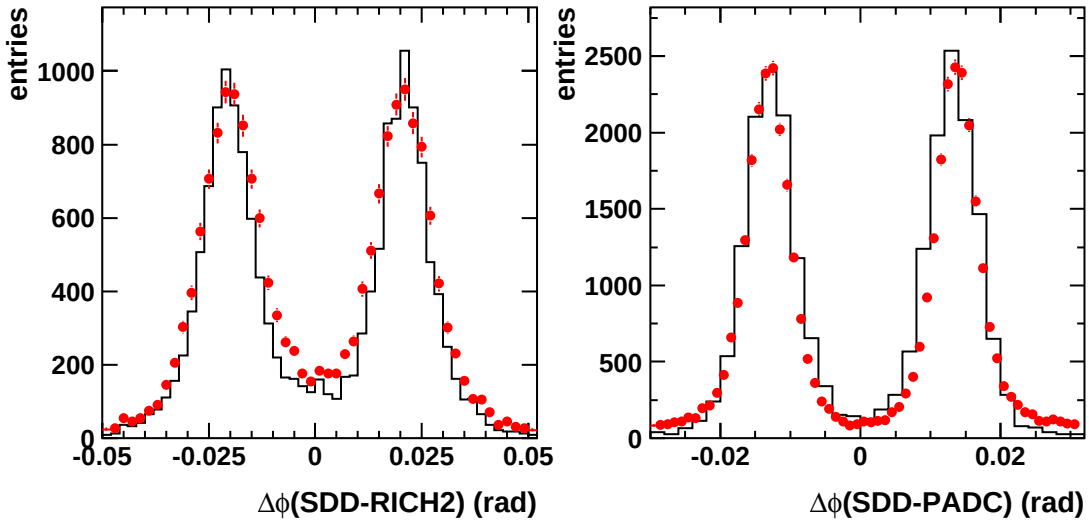

Figure 6.6: Comparison of the azimuthal deflection angle in data (points) and in the Monte-Carlo simulation (histogram) measured between SDD and RICH2 (left), and SDD and PADC (right), respectively. Identified pions with the ring radius of 13-14 pads were used.

6.3 Momentum Resolution

The limited momentum resolution of the spectrometer results in a smearing of the measured particle momentum and has to be corrected for in the data. Using the overlay Monte-Carlo simulation, we have embedded into real events pions with a uniform momentum distribution in the interval of $p = (0,20)$ GeV/c.

Fig. 6.7 demonstrates by several examples the effect of the finite momentum resolution. Clearly, we observe a significantly better resolution for the ring radius method by comparing to the momentum determined from the deflection in the magnetic field as demonstrated in Fig. 6.7. For both methods, the reconstructed momentum distributions have tails towards higher momenta. This results in a systematic shift of the measured momentum to higher values.

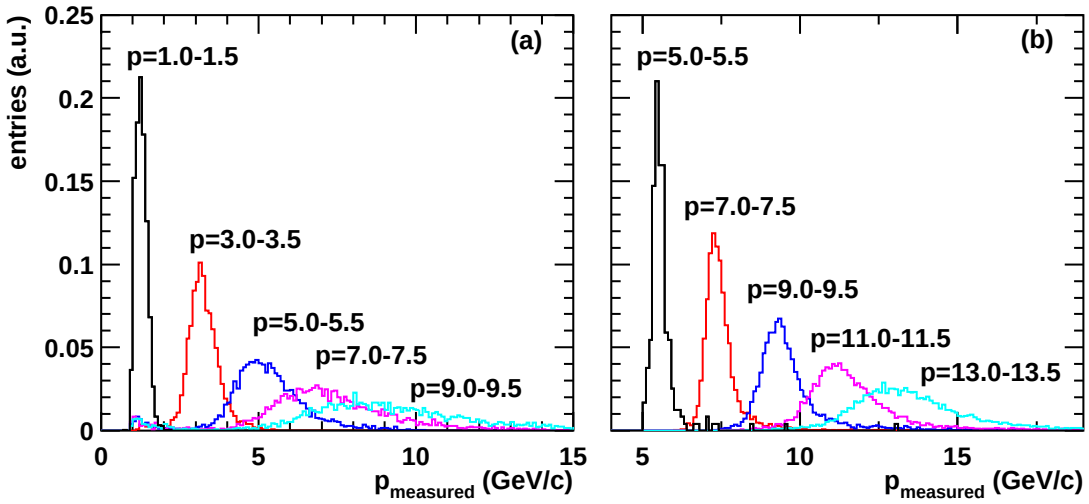

Figure 6.7: Momentum reconstructed from the deflection in magnetic field (a) and from RICH2 ring radius (b) for simulated pion tracks with different input momentum.

6.4 Reconstruction Efficiency

The reconstruction efficiency correction takes into account to our best knowledge various detector defects (dead regions, gain variations) and inefficiencies in the track reconstruction algorithm. Below we discuss separately the reconstruction efficiency ϵ of charged particles and of identified high-p_{T} pions which is determined using the overlay Monte-Carlo technique. The value of the reconstruction efficiency is obtained by dividing number of the reconstructed embedded tracks by the number of the embedded tracks. The reconstruction efficiency correction is applied as the inverse value of ϵ.

6.4.1 Reconstruction Efficiency of Charged Particles

In order to determine the charged particle's reconstruction efficiency we tracked through the spectrometer a large sample of charged pions with a uniform distribution in transverse

momentum p_T from 0 to 5 GeV/c and in rapidity y = (2.1,2.6).

The track reconstruction efficiency reaches on average 55% and shows only a weak decrease with increasing centrality of the collision (Fig. 6.8a) which reflects the very good resolution of the silicon drift detectors and the pad chamber. The transverse momentum dependence of the charged pion reconstruction efficiency is presented in Fig. 6.8(b). It is constant above $p_{\mathrm{T}} > 0.5$ GeV/c and decreases only for particles with $p_{\mathrm{T}} < 0.5$ GeV/c due to the fixed cutoff of 100 mrad applied on the azimuthal deflection corresponding to the momentum cut of $p = 1$ GeV/c (cf. Chapter 5.1.1).

The detection efficiency of the various charged particle species, e.g. pions, protons, or kaons, is from the SDD and PADC point of view identical, while the CERES geometrical acceptance is not. This issue will be in detail discussed in Chapter 8.

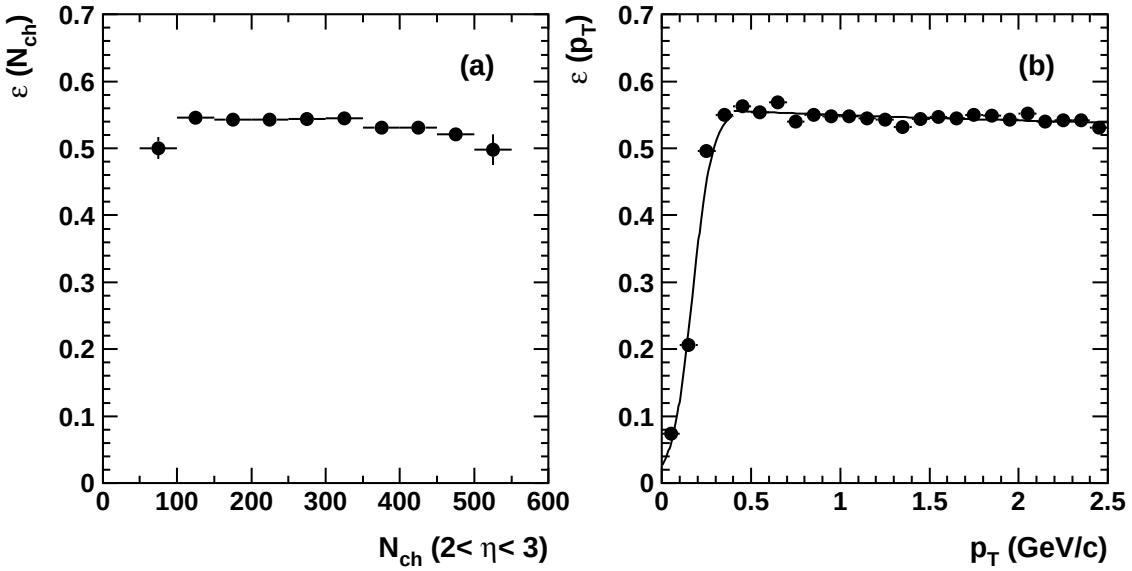

Figure 6.8: Transverse momentum (a) and centrality (b) dependence of the reconstruction efficiency for π^-.

6.4.2 Reconstruction Efficiency of Identified Pions

The description of the reconstruction efficiency of high-p_{T} pions is more complicated in comparison to that of the charged particles, because both RICH detectors come into play. Dependence of the number of generated Cherenkov photons on pion momentum (cf. Fig. 6.3) is directly reflected in the strong momentum dependence of the reconstruction efficiency. This behavior is demonstrated in Fig. 6.9 by a steep rise of the efficiency curve in the vicinity of the Cherenkov threshold ($p \approx 5$ GeV/c) followed by a plateau for pions with p = (10-15) GeV/c. For pion momenta above 20 GeV/c, the ring radius starts to approach its asymptotic value and the finite resolution leads to a decrease of the reconstruction efficiency.

Centrality of a collision also strongly influences pion recognition in the RICH detectors. The same effect is observed in polar angle θ due to higher charged particle density

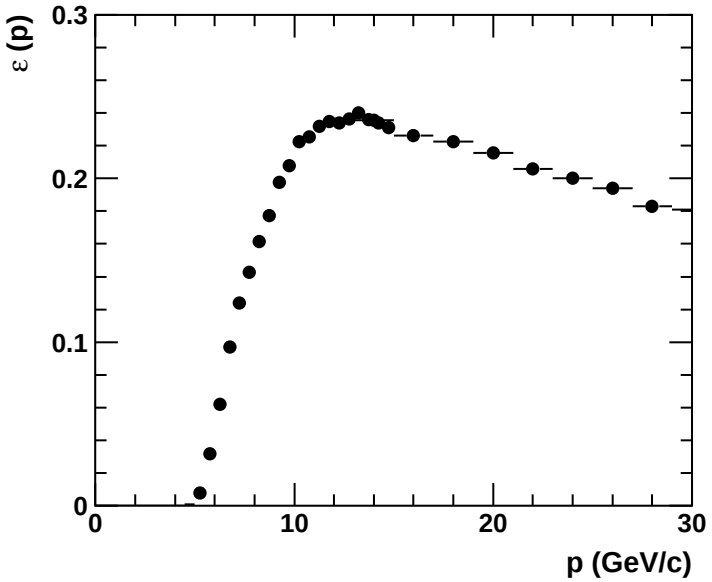

Figure 6.9: Transverse momentum dependence of the pion reconstruction efficiency.

at smaller polar angles. Taking into account all these facts, we are dealing with a three-dimensional problem. The following paragraph describes the main features of the efficiency correction procedure $\epsilon(N_{\rm ch}, \theta, p)$. that has been developed. Dividing the measured charged particle multiplicity $N_{\rm ch}$ and the spectrometer θ-acceptance into several bins, we construct a two dimensional matrix ($N_{\rm ch} \times \theta$) schematically shown in Fig. 6.10. We have chosen the matrix with size (7 x 7), corresponding to a bin size of 50 charged particles in $N_{\rm ch}$ and 15 mrad in θ-space. In each of the grid points the momentum dependent part of the pion reconstruction efficiency $\epsilon(p)$ derived from the overlay Monte-Carlo is parametrized by a polynomial function of the 4-th order.

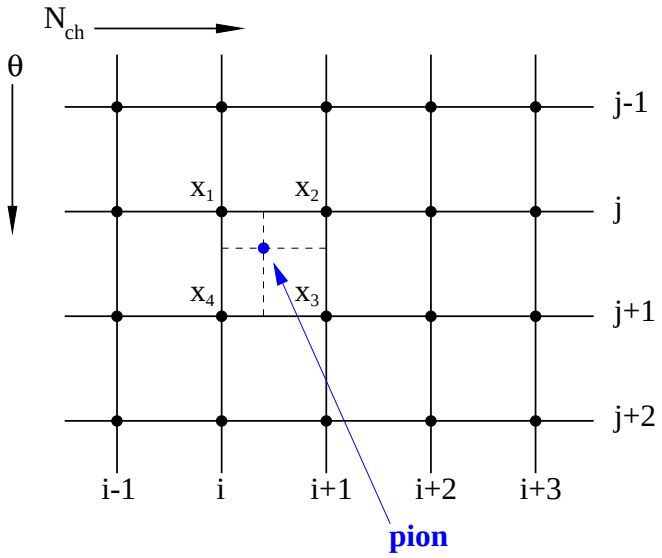

Figure 6.10: Schematic view of the $N_{\rm ch}$ x θ matrix for the high-p_T pion Monte-Carlo efficiency correction.

Fig. 6.11 shows the $\epsilon(p)$ values obtained for several grid points. The reconstruction efficiency varies over the CERES θ-acceptance by a factor of two for peripheral and by a factor of four for central collisions. As it can be seen, the shape of $\epsilon(p)$ is not constant in momentum and depends also on $N_{\rm ch}$ and θ.

The value of the reconstruction efficiency for a given pion in the experiment is obtained in the following way. Knowing the measured polar angle of the pion track and the event multiplicity, we first find the cell in the two dimensional ($N_{\rm ch} \times \theta$) matrix where the pion track belongs (see Fig. 6.10). This cell is defined by the grid points (x_1, x_2, x_3, x_4). For the pion momentum (corrected for the finite momentum resolution), we calculate the values of $\epsilon(p)$ in the grid points and use a bilinear interpolation [145] between them to extract the value of the pion reconstruction efficiency.

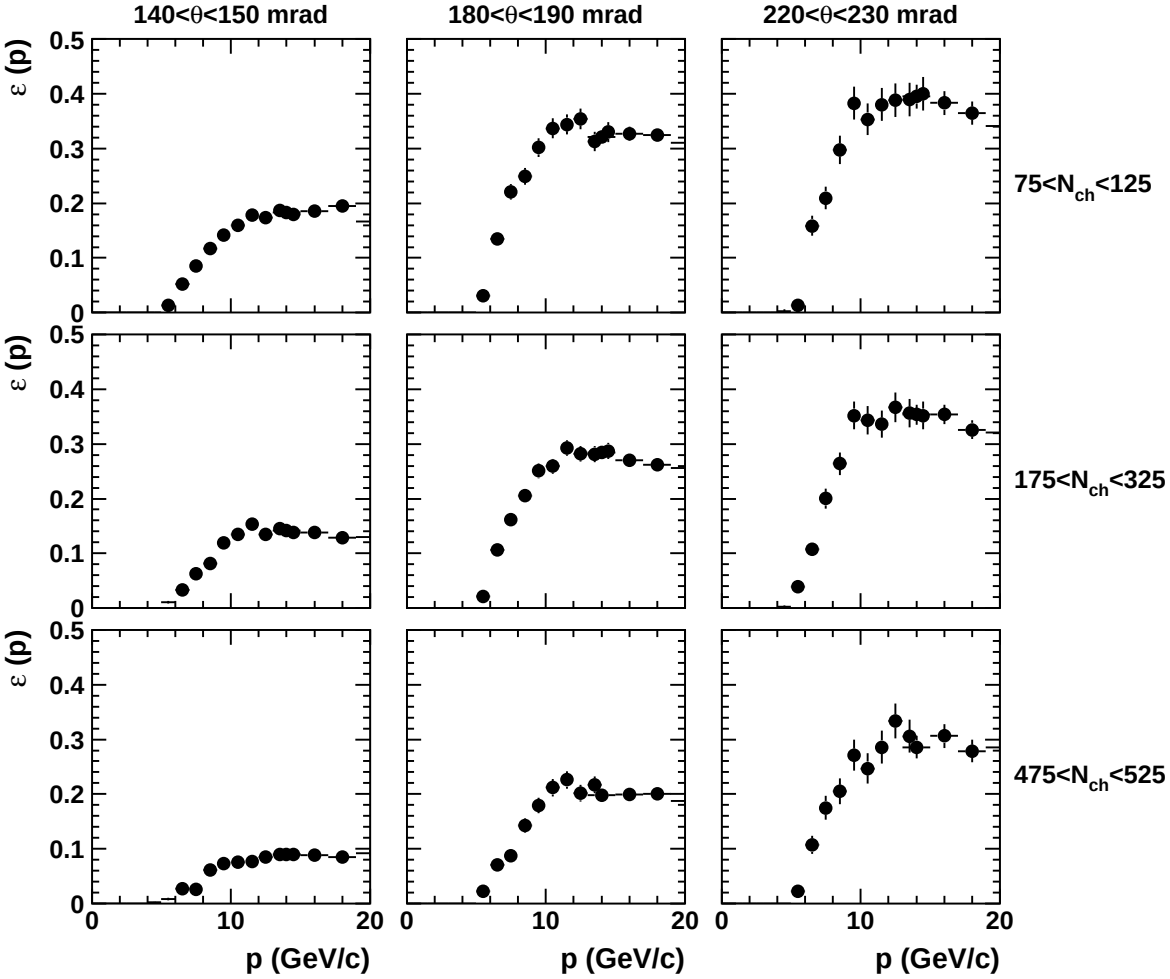

Figure 6.11: Examples of the pion reconstruction efficiency for three different centralities (shown from top to bottom) and three θ ranges (shown from left to right) as a function of pion momentum.

7

Centrality Determination

The centrality of a heavy-ion collision, defined by the impact parameter of the two colliding nuclei, strongly influences the evolution of the hot and dense system created. Consequently, various quantities of interest, like inclusive spectra, or the magnitude of elliptic flow, have to be studied in separate centrality classes. Since the direct measurement of the impact parameter is not possible, it is commonly estimated from the number of charged particles (N_{ch}) emitted, from the total transverse energy (E_{T}) produced, or by a complementary observable, the longitudinal energy (E_z) representing the energy of the *spectators*. In the CERES experiment, the centrality of a collision is determined from the charged particle multiplicity measured by the silicon drift detectors in the pseudo-rapidity

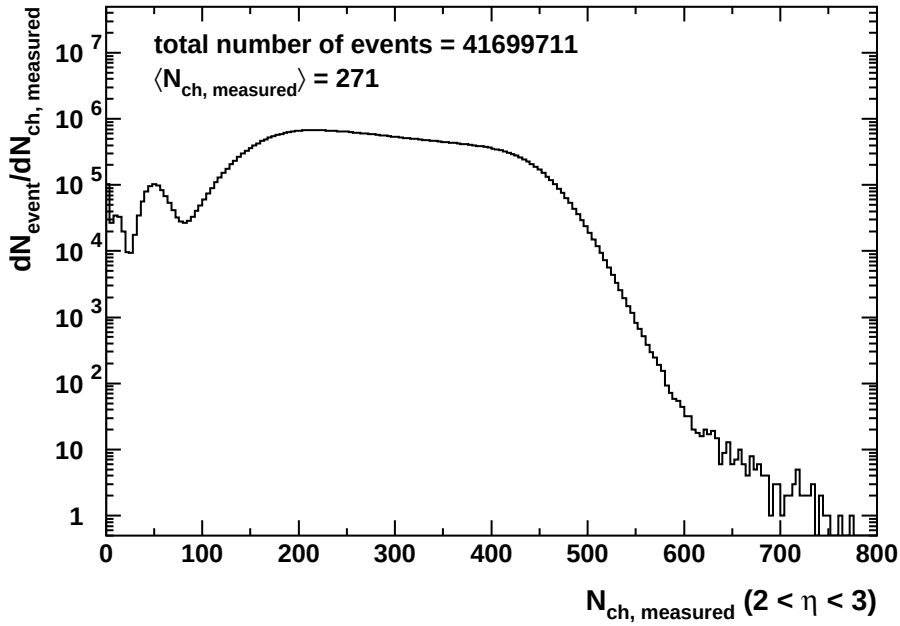

Figure 7.1: Raw charged particle multiplicity distribution measured by the silicon drift detectors in the pseudo-rapidity interval $2 < \eta < 3$.

interval $2 < \eta < 3$. In this chapter, we discuss the corrections which need to be applied to the measured $N_{\rm ch}$ distribution and connect the inferred knowledge about the impact parameter with the nuclear overlap model [146, 147] expectations.

7.1 Corrections of the Multiplicity Distribution

The charged particle multiplicity measured by SDDs in the pseudo-rapidity interval of $2 < \eta < 3$ is presented in Fig. 7.1. The peak around $N_{\rm ch}$ = 50 belongs to non-target interactions and it is removed in the offline analysis by requiring the interaction vertex. The cutoff towards small multiplicities corresponds to the multiplicity trigger threshold of 100 hits in the multiplicity detector (cf. Chapter 3.5). Before we can connect $N_{\rm ch}$ measured with information on impact parameter b, the data have to undergo several corrections.

SDD charged particle reconstruction efficiency

The determination of the SDD charged particle reconstruction efficiency is a rather complex problem. To the percent accuracy required, the efficiency is influenced not only by the hardware imperfections (i.e. dead anodes, electronic noise, pulse shape distortion), but also by capabilities of hit and track reconstruction software. In particular, 'pile-up' effects due to finite double-hit resolution and artificial hit splitting are the most important effects to be corrected for. We have accessed this task using the full Monte-Carlo sim-

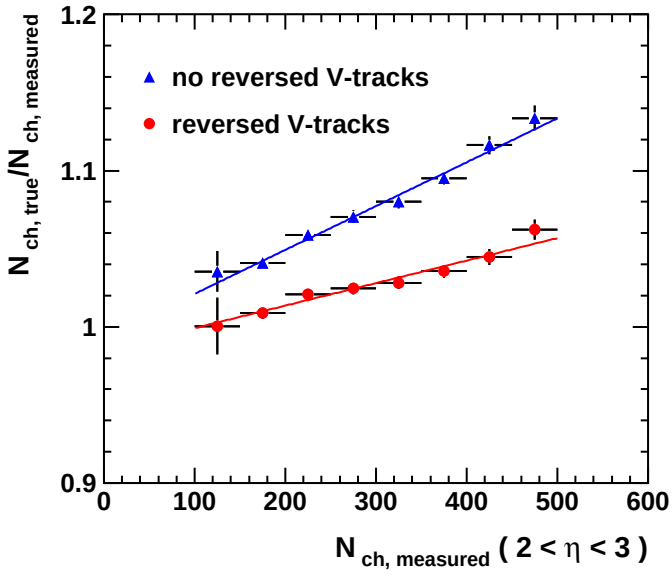

Figure 7.2: Monte-Carlo multiplicity correction with (circles) and without (triangles) including the reversed V-tracks.

ulation based on the UrQMD model [148]. By comparing the number of reconstructed charged particle tracks in simulated events with the input number (Fig. 7.2), we obtain the correction function

$$\frac{N_{\rm ch,true}}{N_{\rm ch,measured}} = 0.985 + 0.14 \cdot 10^{-3} N_{\rm ch,measured}. \qquad (7.1)$$

The first, constant term, includes not only the losses due to dead anodes, but also gains from artificial hit splitting. Both effects nearly cancel. The second term presumably describes the losses due to pile-up.

It is not too difficult to figure out the pile-up losses for cylindrical detectors exposed to particle flux of constant rapidity density $dN/dy = A$. For the total number of hits that are lost due to pile-up L we obtain the relation (see Appendix B)

$$L = \frac{A^2 \delta r \delta \phi}{4\pi z} \left(\frac{1}{\tan\theta} + \theta \right)_{\theta_2}^{\theta_1}. \tag{7.2}$$

Here, z is the distance to the vertex, and θ_1, θ_2 describe the acceptance in polar angle. As it should, the pile-up losses depend quadratically on particle density. The influence of the two-particle resolution in radial and azimuthal directions is entering via δr, and $\delta\phi$, respectively. For a reasonable choice of $\delta r = 560$ μm and $\delta\phi = 44$ mrad derived from Fig. 4.14, the pile-up losses for $A = 270$ particles per unit of rapidity and geometry $\theta_1 = 5.7°$, $\theta_2 = 15.4°$ yields the average pile-up probability of 3.0%. This corresponds to the pile-up term of P/A =1.1·10^{-4} which is in a good agreement with that of in Eq. 7.1. Strictly speaking, this concerns the pile-up of hits, not of tracks between SDD1 and SDD2 we are dealing with. However, hits on tracks in both detectors are highly correlated, and moreover, we refer here to the Monte-Carlo simulation allowing for reversed V-tracks.

The correction function in Eq. (7.1) gives the average multiplicity of $N_{\rm ch}$ = 275, which is by 11% higher than the corresponding number of $N_{\rm ch}$ = 250 obtained after the previous Monte-Carlo correction of the 1996 data [9]. The source of this discrepancy is believed to reside in the newly introduced feature of the SDD tracking software, the *reversed V-tracks*: two tracks are allowed to share the same hit in SDD2, but each of them has a different hit in SDD1. We went back to the raw data to study the influence of the reversed V-tracks on charged particle multiplicity. Fig. 7.3 demonstrates the dependence of the mean charged particle multiplicity $\langle N_{\rm ch} \rangle$ on the size of the matching window between SDD1 and SDD2 with and without including the reversed V-tracks. The size of the matching window governs whether a combination of the SDD1 and the SDD2 hit pointing to the vertex is accepted as a charged particle track or not. From about 2 mrad matching window we observe an increase of the amount of the reversed V-tracks in comparison to the old

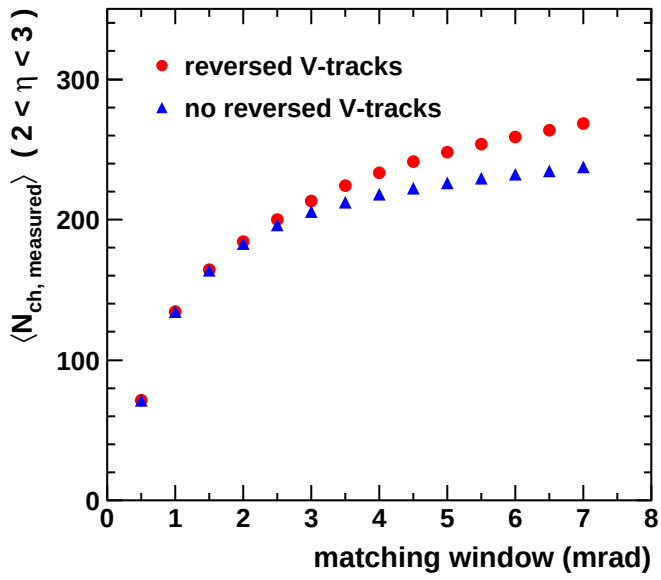

Figure 7.3: Charged particle multiplicity *vs* size of the matching window between SDD1 and SDD2 with or without inclusion of reversed V-tracks.

tracking strategy. The artificial hit splitting problem, which still exists, albeit reduced in comparison to the old hit finding algorithm as shown in [11], makes this increase even worse. For the matching window of 7 mrad used in the data production, there is an increase of 13% in $\langle N_{\text{ch}} \rangle$ observed. Without the reversed V-tracks we have obtained the correction function (cf. Fig. 7.2)

$$\frac{N_{\text{ch,true}}}{N_{\text{ch,measured}}} = 0.993 + 0.28 \cdot 10^{-3} N_{\text{ch,measured}} \tag{7.3}$$

resulting in $\langle N_{\text{ch}} \rangle$ = 252. This value is different from that obtained from the correction function in Eq. (7.1). However, if the simulation is realistic enough, there should be no difference in the value of corrected multiplicity, which is apparently not the case.

The problematics of the artificial tracks can be also accessed directly from the data [12, 149] by plotting the angular distance distribution between a fixed track and any other one in the window $w = \sqrt{d\theta^2 + d\phi^2 \cdot \sin^2\theta}$. The results both for the simulated and the real data are presented in Fig. 7.4. The artificial tracks are concentrated in the peak at distances below 5 mrad. The peak is in both types of the tracking more pronounced in the data then in the simulation. The probability for a track being associated with an artificial one can

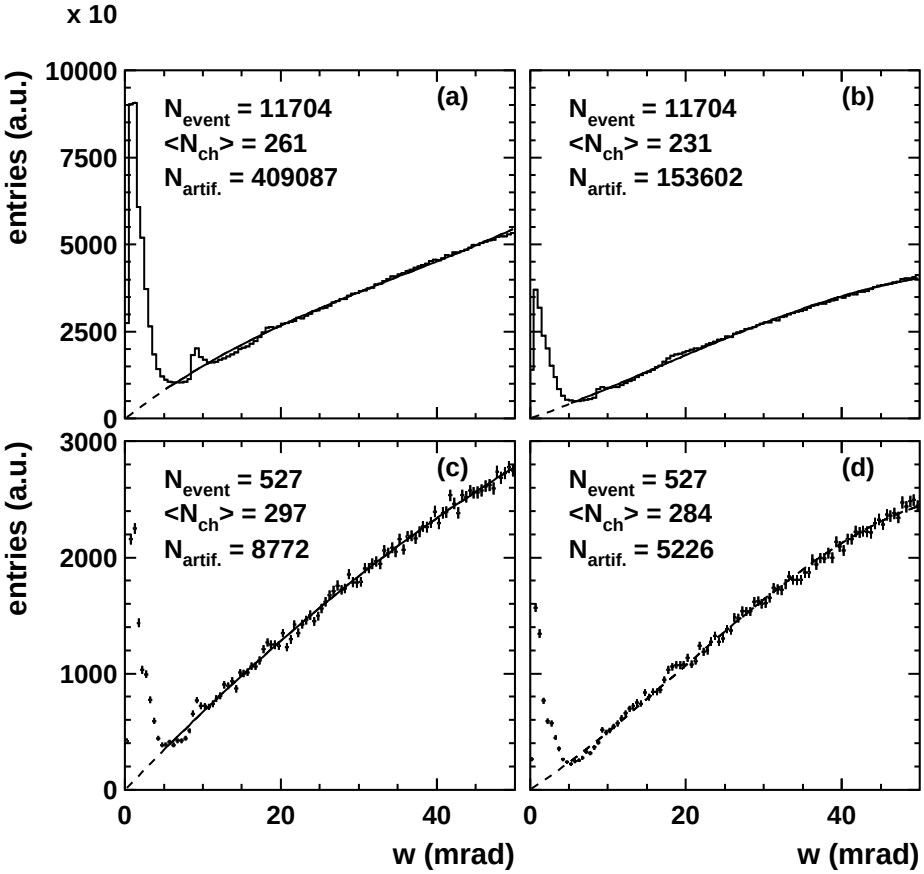

Figure 7.4: Distribution of the angular distance w between neighboring tracks in SDDs in the data with (a) and without (b) reversed V-tracks, and in the Monte-Carlo: with (c) and without (d) reversed V-tracks respectively (see text).

be calculated from

$$p = \frac{\int_0^5 (dN/dw)dw}{N_{events} \cdot \langle N_{ch} \rangle}, \tag{7.4}$$

where we have subtracted from the peak the expected contribution obtained from an extrapolation of the angular distribution for $w > 5$ mrad to zero depicted by the dashed line in Fig. 7.4. The extracted values averaged over the covered centralities are summarized in Table 7.1. For the tracking without the reversed V-tracks the discrepancy between the data and the simulation is much smaller than for the new tracking. Consequently, an additional downward correction of 8% inferred from the difference between the fraction of the artificial tracks in the data and in the simulation for the new tracking has to be applied.

SDD tracking	**Fraction of artificial tracks**	
	Data	Monte-Carlo
reversed V-tracks	13.4%	5.7%
no reversed V-tracks	5.6%	3.5%

Table 7.1: The fraction of the artificial SDD tracks in the data and in the Monte-Carlo simulation for the tracking software with/without reversed V-tracks.

Time variations in the multiplicity measurement

The positions of the left and of the right edges of the multiplicity distribution have to be checked for variation in time. Fig. 7.5 shows the positions of both edges as a function of the run number. We observe large fluctuations in the position of the left edge, which

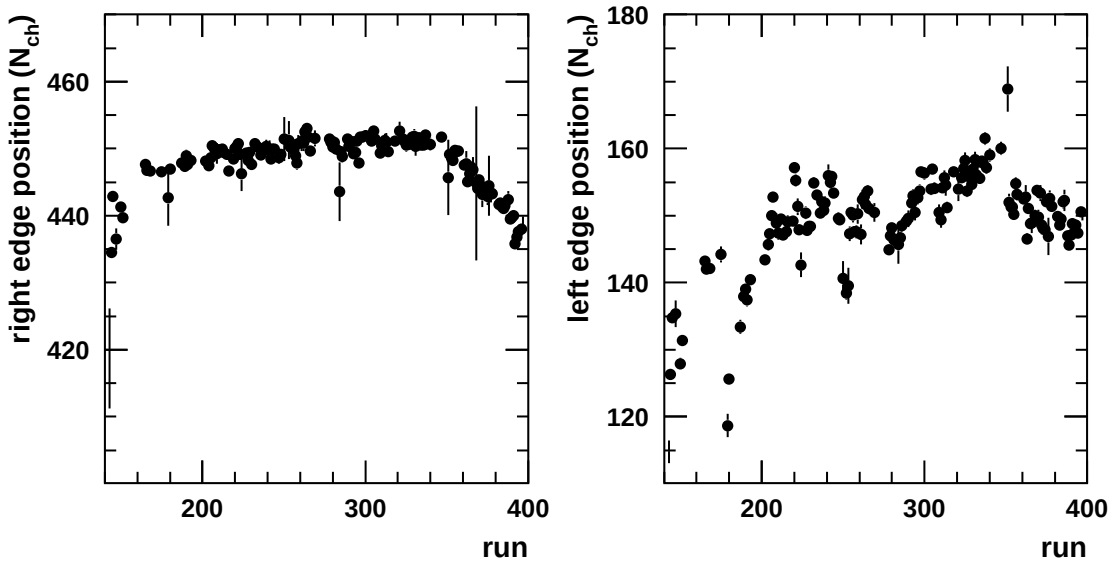

Figure 7.5: Run-to-run variations of the position of the left and of the right edges of the charged particle multiplicity distribution.

was traced to an unstable voltage supply of the multiplicity detector MD. This resulted in the variations of the centrality selection. The position of both edges clearly decreases in a correlated manner towards the end of the data taking. The reason for this behavior is a gradual decrease of the efficiency of 15 neighboring anodes in SDD2 [1]. This loss in charged particle multiplicity was corrected for.

Influence of the δ-electrons

The δ-electrons are created by beam particles traversing the target discs. In case, a nuclear interaction takes place in one of the discs, the δ-electrons production stops. There are around 25 δ-electrons falling into the SDD acceptance [141]. However, the hits created in both silicon detectors mostly do not align into a track, because in general they do not originate from the interaction vertex. Even if they do, their position suffers from multiple scattering due to their low momentum. The amount of reconstructed δ-electrons among all charged particle tracks could be in principle found by comparing the $\langle N_{\rm ch} \rangle$ values for individual target discs. However, the expected signal and the differences in the acceptance of the discs are within the errors of the multiplicity measurement.

The fully corrected multiplicity distribution is presented in Fig. 7.6. The averaged charged particle multiplicity in the covered centrality range is $\langle N_{\rm ch} \rangle = 262$. We have estimated a systematic error of 5% due to the above described correction procedures.

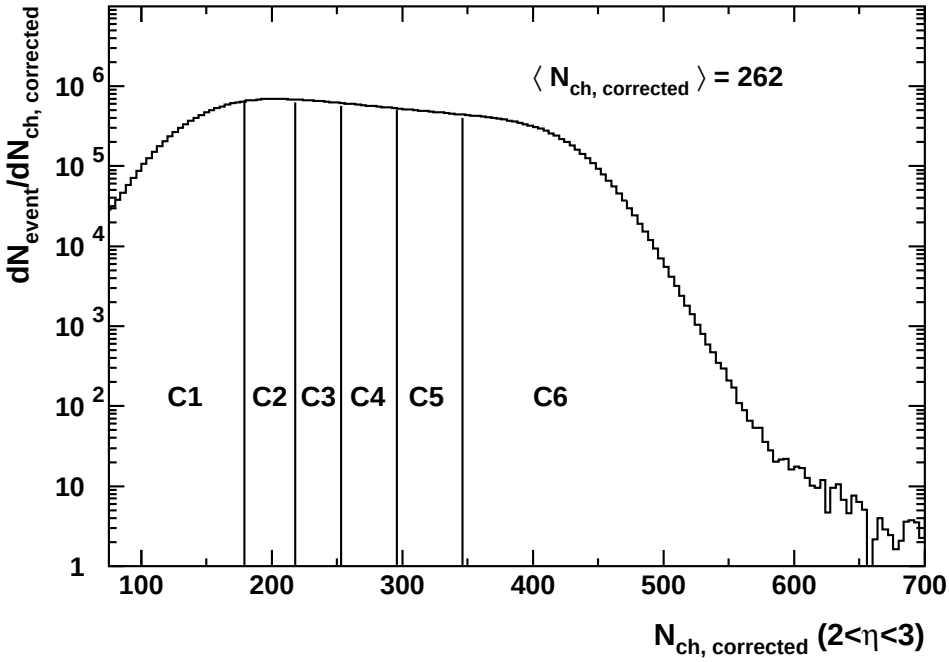

Figure 7.6: Corrected charged particle multiplicity distribution measured by the silicon drift detectors in the pseudo-rapidity window $2 < \eta < 3$. The vertical lines mark the six centrality classes (labeled C1 to C6) used in the data analysis.

[1] anode numbers 160-175

7.2 Cross Section and Impact Parameter

The centrality of a collision characterized via the charged particle multiplicity has to be calibrated by reference to the fraction of the total geometric cross section σ_{geo} defined by the size of the colliding nuclei as

$$\sigma_{\text{geo}} = \pi \cdot (R_a + R_b)^2, \qquad R_{\text{a,b}} = r_0 \cdot A^{1/3}, \tag{7.5}$$

where R_a, and R_b is the radius of the projectile, and target nucleus with A nucleons, respectively. The value of r_0 is typically around 1.2 fm.

The relation between the cut on the charged particle multiplicity and the fraction X of the covered geometric cross section defined as

$$X = \frac{1}{\sigma_{\text{geo}}} \int_{N_{\text{ch}}\text{-cut}}^{\infty} (d\sigma/dN_{\text{ch}}) dN_{\text{ch}} \tag{7.6}$$

is plotted in Fig. 7.7.

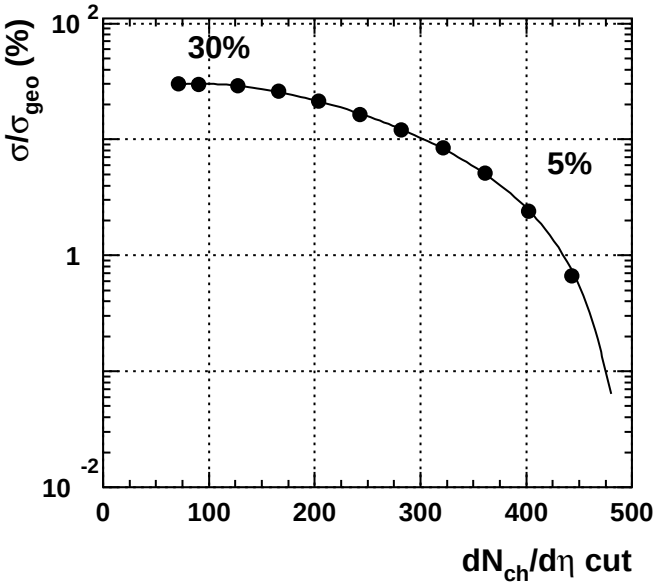

Figure 7.7: Fraction of the geometric cross section as a function of the cut on the number of charged particles measured in one unit of rapidity ($2 < \eta < 3$) by the silicon drift detectors. See text.

For comparison of data with various models, it is convenient to relate the centrality of the collision to the impact parameter b using the relation

$$\sigma = 2\pi \cdot \int_{b_{\text{min}}}^{b_{\text{max}}} b \; db. \tag{7.7}$$

The obtained values of the impact parameter for our six centrality classes are given in Table 7.2 at the end of this chapter.

7.3 Glauber Model of Nucleus-Nucleus Collision

The Glauber or *'nuclear-overlap'* model [146, 147] provides a quantitative description of the geometric configuration of two colliding nuclei. It is based on the concept of a mean free path with the assumption of an elementary baryon-baryon cross section, which is considered to be constant throughout the passage of the baryon through the other nucleus.

In this model, we describe the density distribution of the nucleus with mass number A and radius R_A by a Wood-Saxon parametrization

$$\rho_A(r) = \frac{\rho_0}{1 + e^{(r-R_A)/\xi}} \tag{7.8}$$

with the surface diffuseness parameter ξ = 0.54 fm, the nuclear density under normal conditions $\rho_0 = 0.17$ fm^{-3}, and the nuclear radius at half central density given by relation

$$R_A = (1.12A^{1/3} - 0.86A^{-1/3}) \text{ fm}. \tag{7.9}$$

The density distribution is normalized to

$$\int d^3r \rho_A(r) = A. \tag{7.10}$$

For the following considerations it is convenient to introduce the *nuclear thickness function*. It is defined as the density distribution integrated along the beam axis (z):

$$T_A(x, y) = \int_{-\infty}^{\infty} dz \rho_A(x, y, z). \tag{7.11}$$

Number of participants (wounded nucleons)

Participants, also called *'wounded nucleons'*, are nucleons which have encountered at least one binary collision and we denote their number as N_{part}. They are thought to be responsible for the soft particle production and energy deposition in a heavy-ion collision. At SPS energies an almost linear scaling of the multiplicity of charged particles with N_{part} is observed [54, 150, 151].

With the help of the introduced thickness function, the mean number of participants in an $A + B$ collision at impact parameter b can be expressed as

$$\begin{aligned} N_{part}(b) = \int dxdy \; \Bigg\{ & T_A(x + b/2, y) \left[1 - \left(1 - \tfrac{\sigma_{NN} T_B(x-b/2,y)}{B} \right)^B \right] \\ & + T_B(x - b/2, y) \left[1 - \left(1 - \tfrac{\sigma_{NN} T_A(x+b/2,y)}{A} \right)^A \right] \Bigg\}. \end{aligned} \tag{7.12}$$

The inner parentheses represent the probability for a nucleon to pass through the nucleus without any collision:

$$P \text{ (no collision)} = \left(1 - \frac{\sigma_{\text{NN}} T_A(x, y)}{A} \right)^A. \tag{7.13}$$

However, collisions at a certain impact parameter do not produce a sharp number of wounded nucleons due to fluctuations resulting from the microscopical structure. In this sense, the evaluated number of participants is an average number of wounded nucleons at fixed impact parameter.

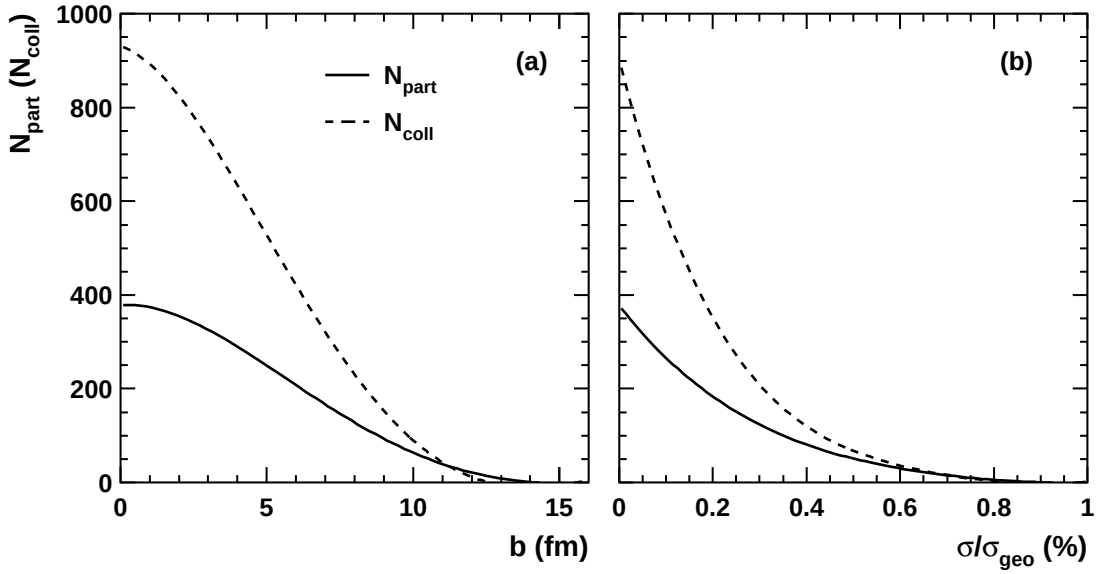

Figure 7.8: The number of participants (N_{part}) and of binary collisions (N_{coll}) as a function of impact parameter (a) and of fraction of the geometric cross section (b).

Number of binary collisions

The number of binary collisions becomes of interest in the high energy limit. A parton travelling through the medium after its first collision can still suffer further hard collisions with other partons. The occurrence of these binary collisions is easily expressed using the introduced definition of the thickness function

$$N_{coll}(b) = \sigma_{NN} \int dxdy \;\; T_A(x + b/2, y)\; T_B(x - b/2, y), \tag{7.14}$$

with σ_{NN} being the inelastic nucleon-nucleon cross section ($\sigma_{NN} = 30$ mb at $\sqrt{s} = 17$ GeV). The centrality dependence of the number of participants and of the number of binary collisions is shown in Fig. 7.8, both as a function of the impact parameter as well as the fraction of the geometric cross section.

7.4 Results on the Centrality Measurement

We have divided the data sample into six centrality classes, which are indicated by vertical lines in Fig. 7.6. Important characteristics of these classes including the corresponding fraction of the geometric cross section, impact parameter, number of participants and binary collisions are summarized in Table 7.2. The total geometric cross section calculated

from the nuclear overlap model with the Woods-Saxon density profile and σ_{NN}= 30 mb is 6.94 barn.

Class	Events (10^6)	$\langle N_{\text{ch}} \rangle$	$\sigma/\sigma_{\text{geo}}(\%)$	b(fm)	$\langle N_{\text{part}} \rangle$	$\langle N_{\text{coll}} \rangle$
C1	7.768	147	24.2 - 30.0	7.3 - 8.1	139	255
C2	6.575	198	19.3 - 24.2	6.5 - 7.3	171	332
C3	5.664	234	15.1 - 19.3	5.7 - 6.5	203	410
C4	6.058	273	10.6 - 15.1	4.8 - 5.7	239	501
C5	6.050	321	6.1 - 10.6	3.6 - 4.8	282	612
C6	8.156	395	< 6.1	< 3.6	360	840

Table 7.2: Definition of centrality classes.

8

Transverse Mass Spectra of Negative Charged Particles and High-p_T Pions

In this chapter we present the transverse momentum, or transverse mass, spectra of negative charged particles (h^-), and high-p_T pions corrected for background contributions, momentum resolution and reconstruction efficiency. The obtained spectra are studied as a function of centrality and compared to those from other p-p, p-A and A-A experiments. At the end of this chapter a hydrodynamical analysis of the spectra is presented.

8.1 The Abundance of Different Hadrons Species at the SPS and the CERES Acceptance

Since our simple charged particle tracking (cf. Chapter 5.1.1) does not allow for particle identification, the measured spectra of charged particles are composed of several kinds of particles. Table 8.1 gives an overview of the yields of the most abundant hadron species from central Pb-Pb colllisions at the SPS. Disregarding the small $\bar{p}$ contribution, the spectra of negative particles consist predominantly from π^- with an 8% admixture of K^-. The spectra of positive particles are more complicated. They are composed of π^+ with a large fraction of protons and K^+. Without particle identification it is thus impossible to make a meaningful analysis of the h^+ spectra. However, it is possible to extract 'net-proton' yields ($p - \bar{p}$) from the positive charge excess $(h^+ - h^-) = (\pi^+ - \pi^-) + (p - \bar{p}) + (K^+ - K^-)$. Since Pb-Au collisions are not isospin symmetric, π^- are more abundant than π^+ in the low-p_T region ($p_T < 0.5$ GeV/c). With growing

Particle species	Rel. abundance	Reference
K^-/π^-	0.08	NA49 [152]
K^+/π^+	0.17	NA49 [152]
$\bar{p}/\pi^-$	0.02	NA44 [153]
p/π^+	0.23	NA44 [153]

Table 8.1: Hadron yields for central Pb-Pb collisions at 158A GeV/c at the SPS.

p_T, the yields of charged pions become almost equal. The unbalanced yield of $(K^+ - K^-)$ remains, however, an important contribution to the net proton spectra. A detailed analysis of the $(h^+ - h^-)$ spectra was performed in [28, 141] and is not discussed in this work.

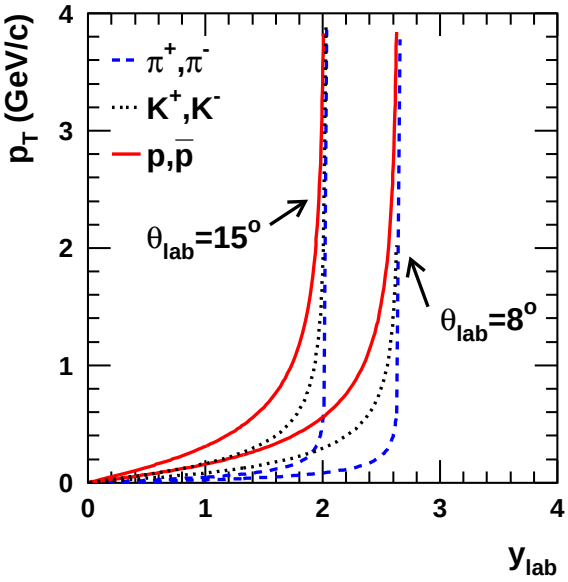

Figure 8.1: CERES rapidity acceptance in the laboratory system ($y_{\rm lab}$) as a function of p_T for pions, kaons, protons, and their antiparticles.

The limited pseudo-rapidity coverage of the CERES spectrometer ($\eta = 2.1$–2.65) results in a different rapidity acceptance for various particles as illustrated in Fig. 8.1 for pions, kaons and protons. The spectrometer covers uniformly a region of $y_{\rm lab} = 2.05$–2.65 for pions with $p_T > 0.2$ GeV/c. However, for kaons and protons is the situation different due to their larger mass. The spectrometer covers a wider range in the rapidity, but the corresponding p_T acceptance is not uniform.

8.2 Analysis Method

In this section we discuss the selection criteria applied on the charged particle and high-p_T pion candidate tracks and study the influence of background, finite momentum resolution and reconstruction efficiency on the shape of the spectra.

8.2.1 Selection Criteria for h^- and High-p_T Pion Track Candidates

The selection criteria applied on negative charged particle and high-p_T pion track candidates are summarized in Table 8.2. Although most matching distributions are not strictly Gaussian, we use the sigma of a Gaussian fit of the matching distributions (neglecting possible tails) for track definition. For both types of tracks we apply first a 2σ cut on the SDD1-SDD2 θ and ϕ matching, and for pions also a 2σ cut on the θ matching between the SDD and PADC detectors. For charged particles the latter cut had to be tightened in order to increase the signal to background ratio, S/B. The latter is shown as a function of the θ matching window size for three different centrality bins in Fig. 8.2. We have fixed the cut to 1.3 σ, where the S/B reaches approximately its maximum. Since the θ matching distribution between the silicon detectors and the pad chamber depends on particle momentum, as already shown in Fig. 5.12, this cut is momentum dependent. The variations

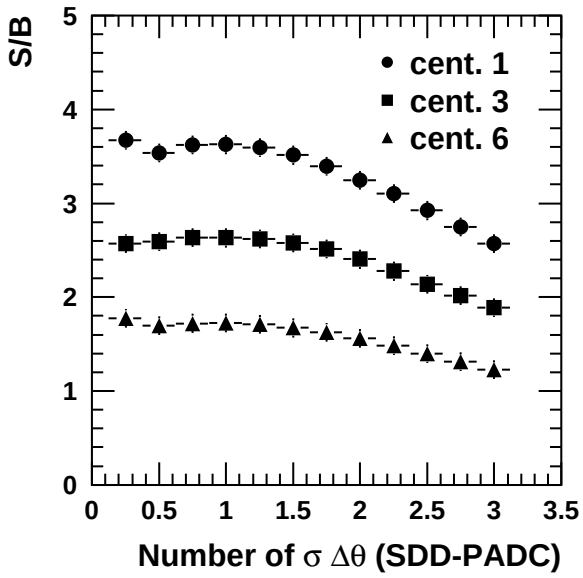

Figure 8.2: Signal to background ratio as a function of the size of the θ-matching window between SDD and PADC for different centralities.

in the width of the θ matching distributions with the target disc position as well as time variations discussed in Chapter 5 (cf. Fig. 5.7 and Fig. 5.10) were taken into account.

For pions identified in the RICH detectors, another set of cuts is applied. We require a correlation between the measured ring radius in both RICH detectors, and the deflection in magnetic field measured by PADC (cf. Fig. 5.3). The two ring radii have to match within 10% and the momentum determined from the deflection and from ring radius has to be within 2σ of the resolution.

Type of cut	Charged particles	High-p_T pions
θ, ϕ matching SDD1–SDD2	2 σ	2 σ
θ matching SDD–PADC	1.3 σ, p dependent	2 σ
ring radius in RICH1 and RICH2	–	10% rel. variation
momentum from deflection and ring radius	–	2 σ

Table 8.2: Selection criteria applied on the charged particle and high-p_T pion candidate tracks.

8.2.2 Background Contribution

Applying the above mentioned quality criteria on track candidates reduces already significantly the amount of background tracks. The remaining background, however, has to be carefully studied. In general, two different types of background contributions can be distinguished: *physics* and *random*. They are discussed below separately for charged particles and identified pions.

Negative charged particles

For the simple tracking strategy applied for charged particles, the majority of the background arises from the random combination of SDD track segments with all available PADC hits falling into the matching window. Applying the mentioned quality criteria to

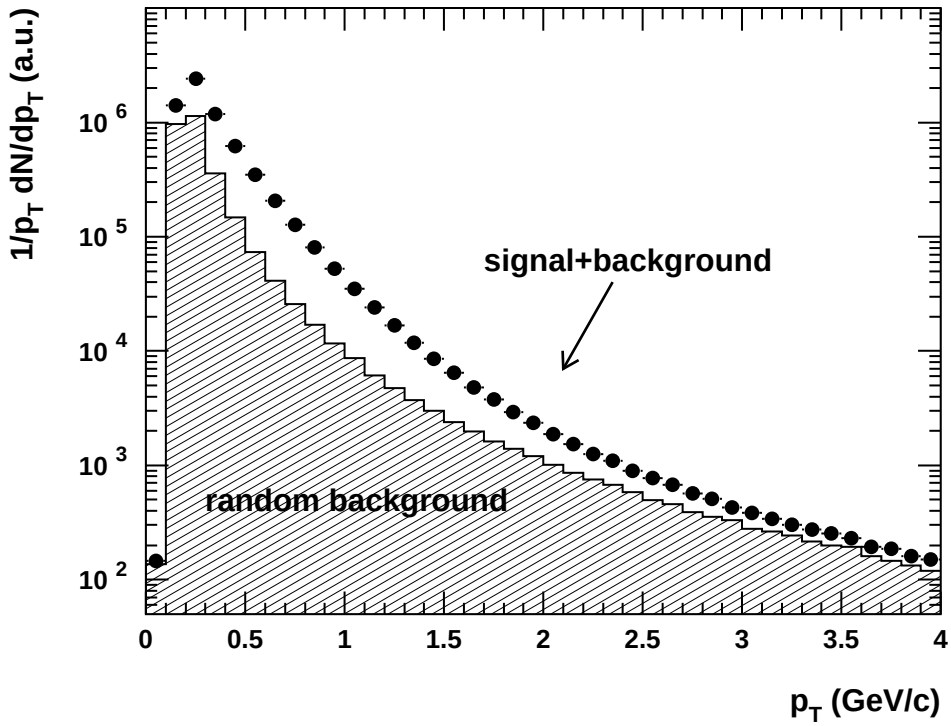

Figure 8.3: Raw p_T spectrum of h^- integrated over all centralities. The hatched area represents the random background contribution.

the data as well as to the events, where we have rotated PADC hits with respect to the SDD detectors at random event-by-event, and integrating over all centralities we obtain a raw transverse momentum spectrum of negative charged hadrons and the corresponding random background distribution displayed in Fig. 8.3. As we can infer from this figure, the S/B ratio strongly depends on the transverse momentum of charged particle. More detailed investigation of this behavior is demonstrated for three different centrality centrality classes in Fig. 8.4. For all measured centralities the S/B ratio is well above one in

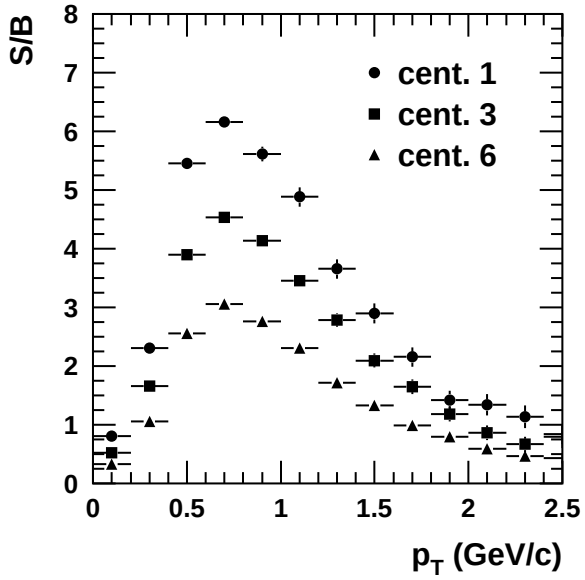

Figure 8.4: Signal to background ratio for h^- and three different centralities as a function of p_T.

the interval p_T = (0.5,1.5) GeV/c. At larger values of p_T the small particle yield results in a deterioration of the S/B ratio. In the analysis of h^- spectra the background subtraction is performed in a p_T-dependent way for each centrality bin separately. The contamination of the h^- sample by electrons is negligible for $m_T - m_0 > 0.1$ GeV/c^2 as was shown in [141].

High-p_T pions

The random background contribution can be again estimated using the method of detector rotations. We rotate the detectors behind the magnetic field (RICH2, PADC) by a random angle with respect to the detectors before the magnetic field (SDD1, SDD2 and RICH1). In this way we can estimate not only the contribution of the fake tracks arising from a random combination of the SDD track segments with PADC hit and rings in the RICH detectors, but also partially reconstructed tracks, where behind the magnetic field was a track associated with a wrong RICH2 ring and a PADC hit. Fig. 8.5 shows the raw transverse momentum distribution of charged pions together with the estimated random

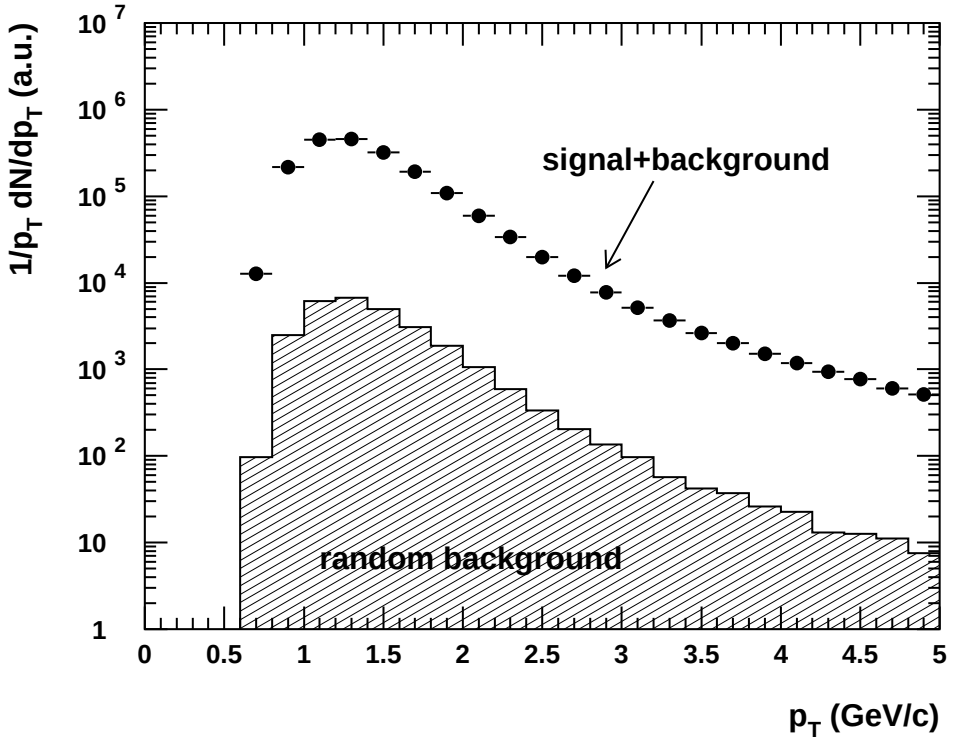

Figure 8.5: Raw p_T distribution of $\pi^{\pm}$ (circles) together with the contribution of random background (triangles).

background. Over the entire range of the spectrum, the background contribution reaches only a few percent. Thus, in comparison to the spectrum of h^-, the spectrum of identified pions is essentially free of the background.

Physics background at large p_T can originate from electron tracks which are misidentified in the RICH detectors. Since electrons with small momenta are deflected stronger in the magnetic field than pions with momentum above the Cherenkov threshold, the correlation between the measured ring radius and the deflection angle (cf. Section 8.2.1) is used to filter them out. The remaining electron tracks with high momenta, however, produce

the same signatures as pions in all detectors. A detailed study of this type of background was performed in [141] where a sample of π^0 Dalitz decays and γ conversions generated using GENESIS [6, 154] was embedded into real data. The physics background contribution was found to be negligible.

8.2.3 Momentum and Reconstruction Efficiency Corrections

After the background subtraction, the inclusive p_T distributions have to undergo momentum and reconstruction efficiency corrections, which were discussed in Chapter 6.

Negative charged particles

The influence of these corrections on the shape of the h^- spectrum is demonstrated in Fig. 8.6. The shape of the spectrum is mainly distorted due to the finite momentum resolution and the background contamination. After the correction for these imperfections, the spectrum resembles an exponential shape. The efficiency correction is in the p_T region of interest independent on the momentum and causes only a constant correction factor.

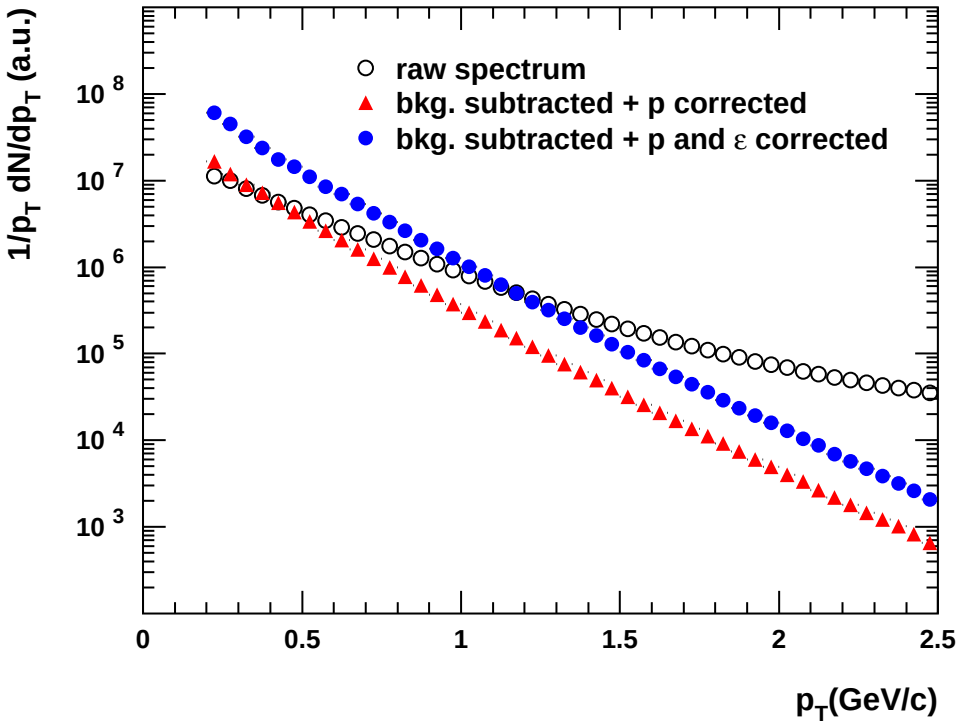

Figure 8.6: An example of the individual correction steps for the inclusive p_T spectrum of h^-. The data are integrated over centrality.

High-p_T pions

For identified pions is the situation different. The background contribution is very small and also the momentum resolution of the ring radius method is much better than the deflection in the magnetic field used for h^-. Thus this correction step causes almost no change of the spectrum below $p_T \approx 2$ GeV/c and becomes important only for larger momenta as demonstrated in Fig. 8.7. However, the reconstruction efficiency shown in Fig 6.11 is strongly dependent on pion momentum and polar angle. Below $p_T \approx 2$ GeV/c the correction factor increases steeply with decreasing transverse momentum.

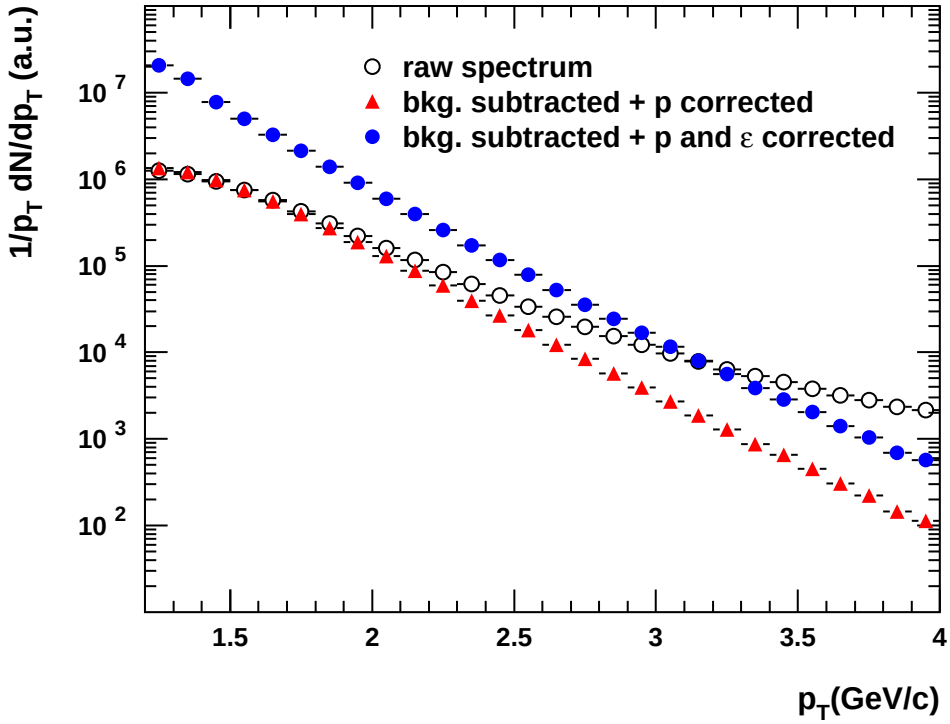

Figure 8.7: An example of the individual correction steps for the inclusive p_T spectrum of identified pions. The data are integrated over centrality.

In the off-line analysis we have found that the average number of pion tracks per event ($p_T > 1.2$ GeV/c) varies with time as depicted in Fig. 8.8. We can observe several dropouts caused probably by improper voltage settings in the RICH detectors which increased background and thus decreased the efficiency to recognize pion rings. The projection of this distribution weighted with the number of events in each run gives the average number of 0.24±0.02 pions per event.

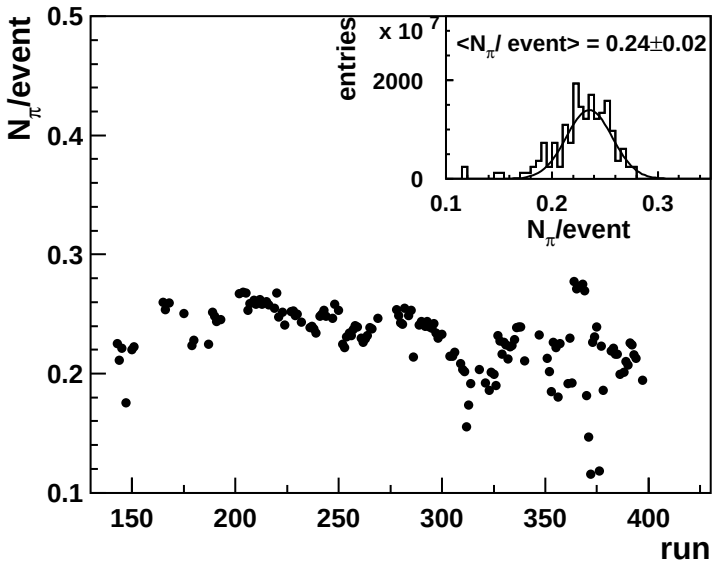

Figure 8.8: Number of good quality pions ($p_T > 1.2$ GeV/c) per minimum bias events for different runs. The small panel shows a projection weighted with number of events in a given run.

8.3 Results

The corrected transverse mass spectra of negative charged particles and high-p_T pions are studied in the following sections for centrality dependence, local inverse slope and compared to other SPS experiments. At the end of this section we extract information on freeze-out temperature T and transverse velocity β_t by employing hydrodynamical fits to the spectra.

8.3.1 Transverse Mass Spectra of Negative Charged Particles

The transverse mass spectra of negative charged particles are presented in Fig. 8.9 for six centrality classes defined in Table 7.2. For a better orientation, we have successively multiplied the spectra by a factor of 10. The statistical errors are within the symbol size.

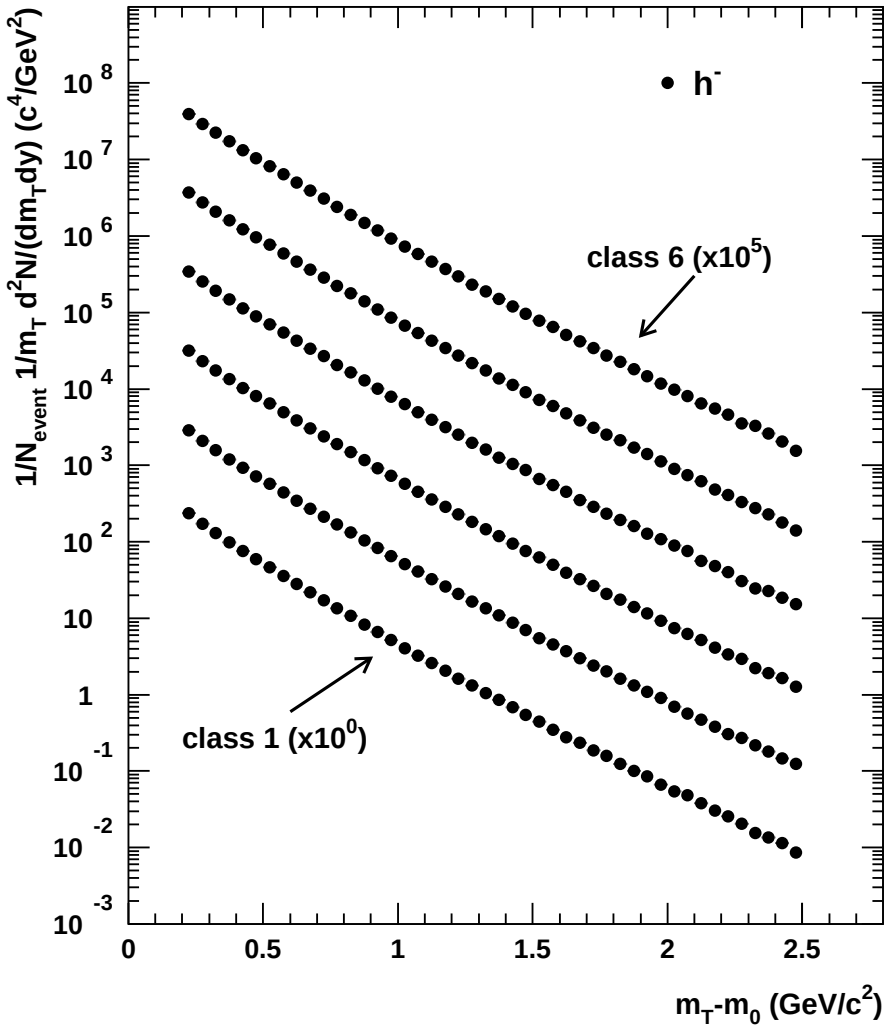

Figure 8.9: Fully corrected inclusive transverse mass spectrum of negative particles for six centrality bins. The spectra corresponding to the different centralities are successively multiplied by a factor of 10.

We estimate a systematic error of 15% due to the Monte-Carlo corrections.

The transverse mass distributions of negative particles were also investigated by other experiments. In Fig. 8.10 we compare our results for central collisions with the NA49 [155] and WA97 [156] experiments, which studied the h^- distribution in Pb-Pb 158A GeV/c collisions within the rapidity intervals indicated. The spectra were normalized at $m_T - m_0$ = 0.5 GeV/c^2. The agreement between all three experiments is very good in the transverse mass region below 1 GeV/c^2, but at higher m_T values our data show a steeper decrease than the other two experiments. We remark that the last bin of the WA97 experiment has width of 0.5 GeV/c^2 and its mean value is actually shifted to left from the bin center due to a steeply falling spectrum. This partially compensates the observed discrepancy.

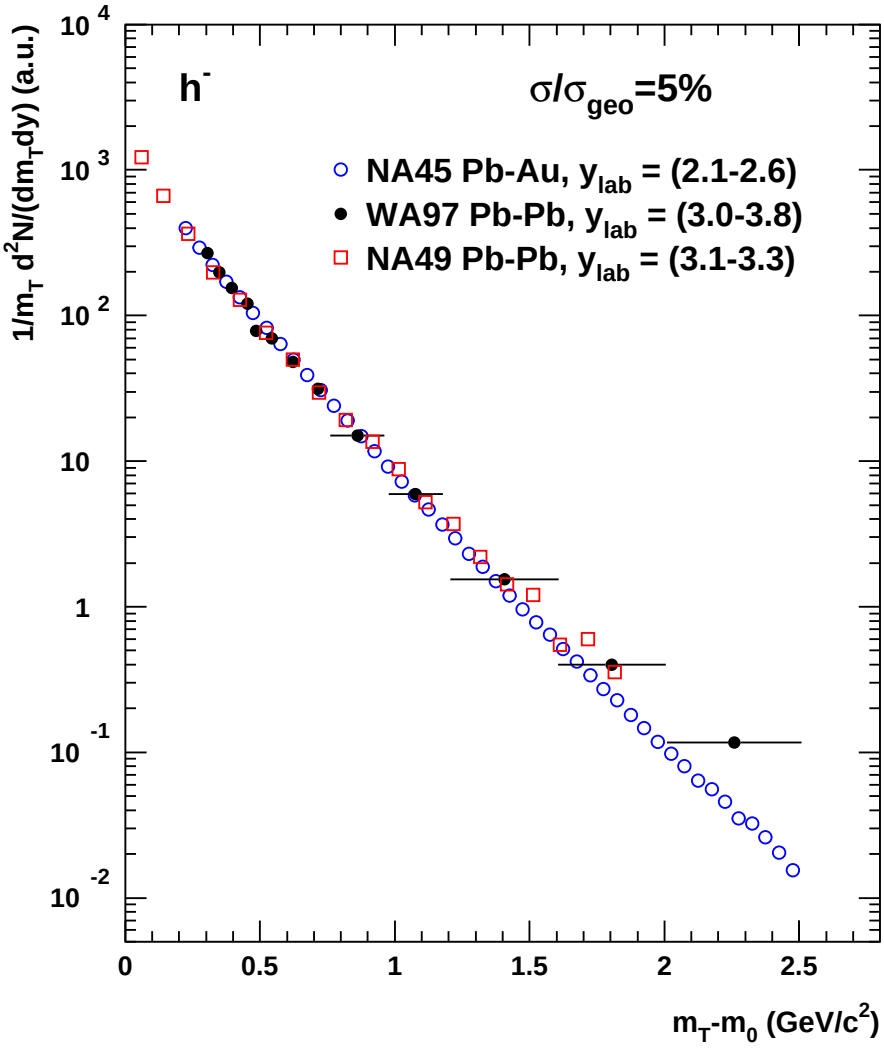

Figure 8.10: Comparison of the CERES h^- transverse mass spectrum for central collisions ($\sigma/\sigma_{geo} < 6\%$) with NA49 [155] and WA97 [156] results for centrality selection of $\sigma/\sigma_{geo} < 5\%$. The data were measured in the rapidity regions indicated.

8.3.2 Transverse Mass Spectra of Identified Pions

As for negative charged particles, we present in Fig. 8.11 the corrected m_T spectra of charged high-p_T pions in six centrality classes successively multiplied by a factor of 10. The spectra are constructed from both π^- and π^+ particles. The statistical errors are within the symbol size. The systematic errors due to the Monte-Carlo corrections were estimated to be 15%. They increase in the vicinity of the Cherenkov threshold to 30% due to a high sensitivity of the pion ring reconstruction in the RICH detectors. The run-to-run variations of the number of good pion tracks per event shown in Fig. 8.8 and discussed in the related text, cause an additional systematic error. Taking 2σ of the measured spread of $N_\pi/$event, we obtain systematic error of 20%.

There are no other data on charged high-p_T pions from other SPS experiments. The only data in the high-p_T region are m_T spectra of neutral pions measured by the WA80 [157]

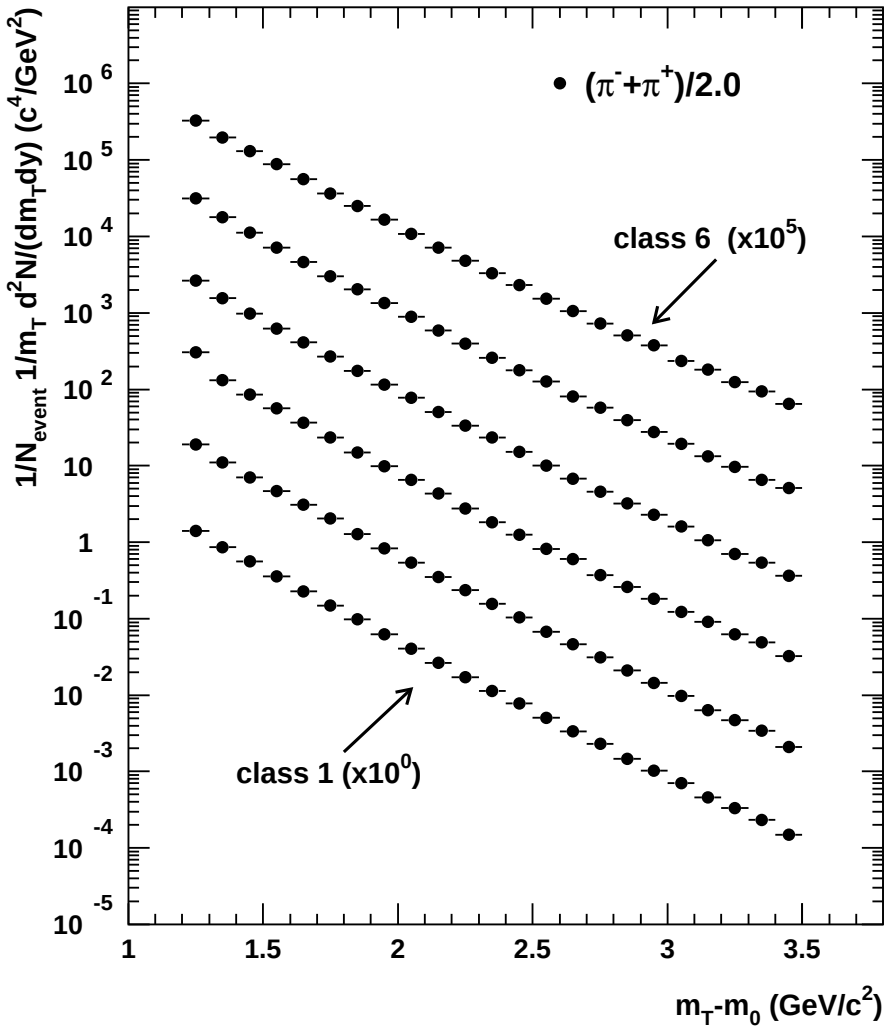

Figure 8.11: Invariant transverse mass distribution of charged pions. The spectra corresponding to six different centralities are successively multiplied by a factor of 10.

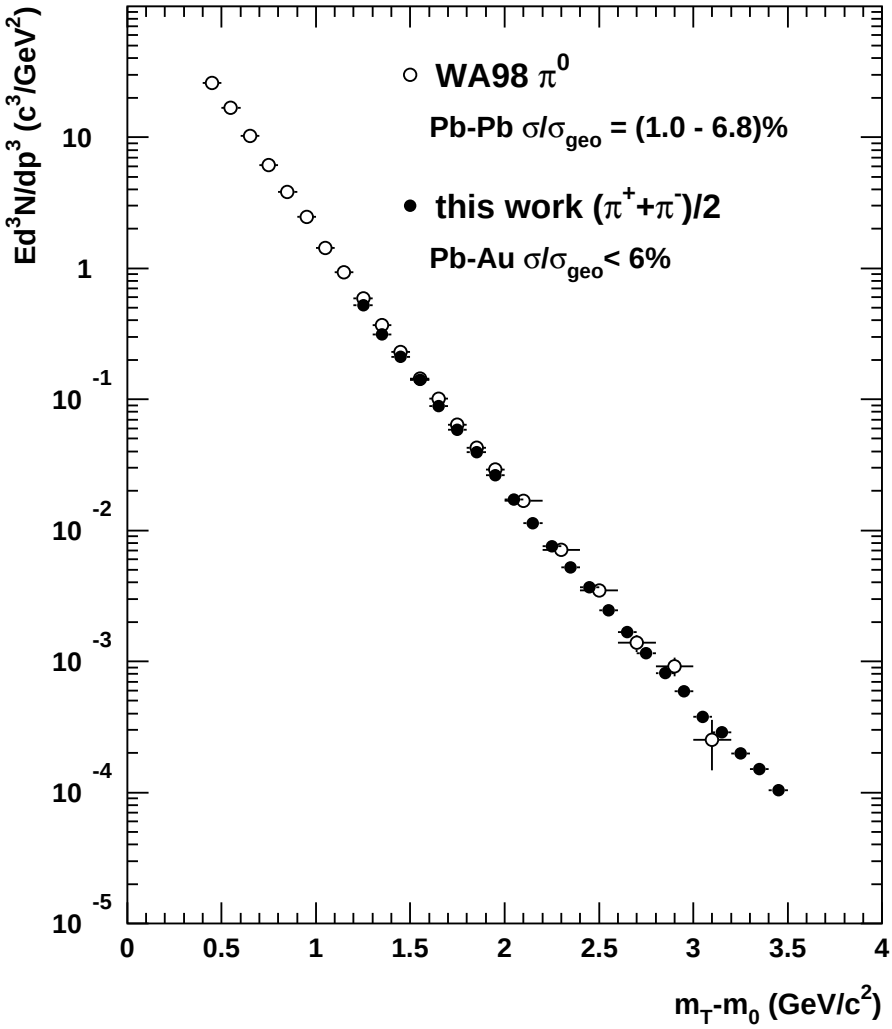

Figure 8.12: Comparison of the transverse mass spectrum of charged pions (this work) and neutral pions measured by the WA98 experiment.

experiment in Pb-Pb collisions at 200A GeV/c, and its successor, the WA98 [157–161] experiment in Pb-Pb collisions at 158A GeV/c. We will compare here our results with the WA98 measurement, since it was performed at the same beam energy. Neutral pions are reconstructed on a statistical basis from the $\pi^0 \rightarrow \gamma + \gamma$ decay in the pseudo-rapidity interval $2.3 < \eta < 3.0$. For a comparison, the results are presented in Fig. 8.12 for the best matching centrality class available[1]. The agreement of the two experiments is very good. Our data are 15% below the WA98 data in absolute terms which is perfectly within the systematic errors of both experiments. In addition, we remark that the spectra are measured in two close, but not identical rapidity regions and centrality selections. We postpone the further discussion on the shape of the two spectra to Section 8.3.5.

[1]The WA98 data shown in Fig. 8.12 correspond to the centrality class denoted 'class 7' in [160].

8.3.3 Combined Spectra of Charged Particles and High-p_T Pions

Since the spectra of negative charged particles closely resemble those of charged pions, except for a small contribution of K^-, we have combined the two data samples into one picture as shown in Fig 8.13. The very good agreement in absolute terms between the spectra obtained by two completely different methods in the overlapping region and for all centrality classes analyzed is remarkable. The combined spectra span a wide range of almost 3.5 GeV/c^2 in the transverse mass and about five orders of magnitude. In the next section we compare the data to pion spectra measured in p-p and p-A collisions.

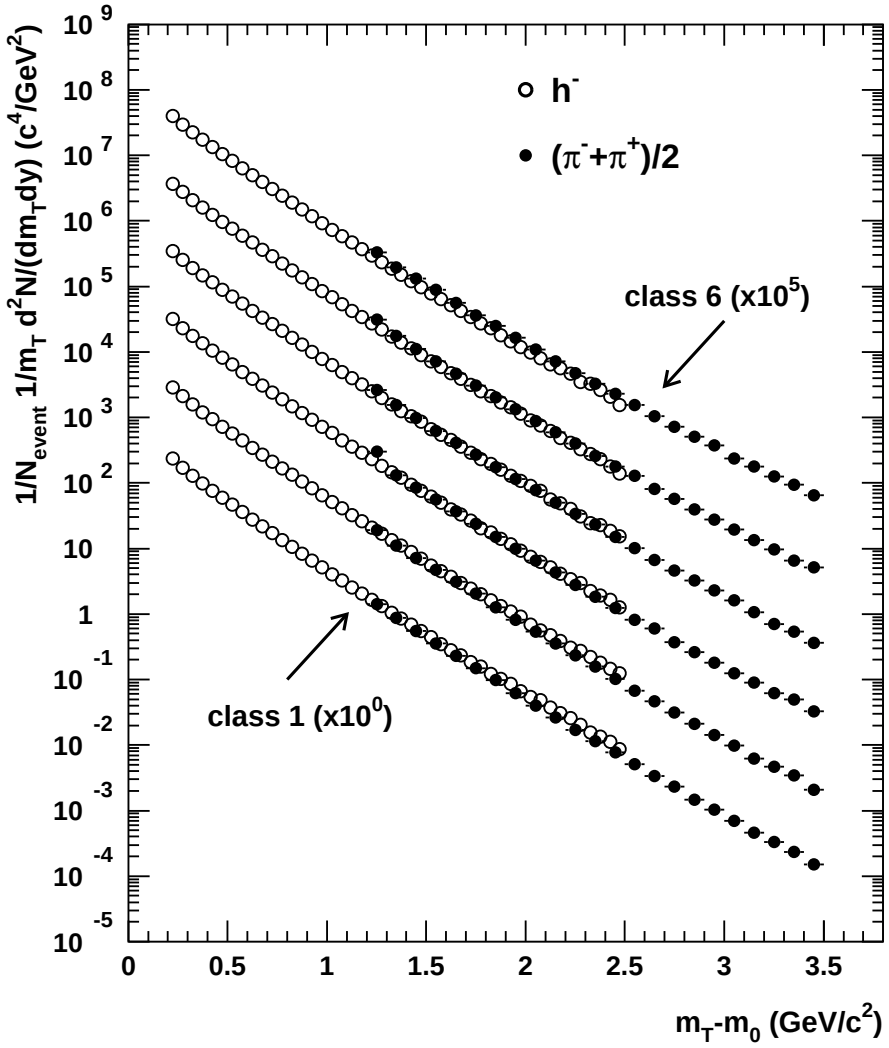

Figure 8.13: Transverse mass spectra of negative charged particles (open symbols) and identified pions (full symbols). The spectra for six different centralities are successively multiplied by a factor of 10.

8.3.4 Comparison with p-p and p-A Collisions

Systematic studies of particle production in p-p collisions became available already in 1960's. While at $\sqrt{s} < 3$ GeV the total cross section is strongly influenced by the resonances, at $\sqrt{s} > 3$ GeV it remains approximately constant at the value of about 40 mb with a large inelastic cross section part of 30 mb [162]. The energy available in the collision is used for production of new particles, mainly pions due to their small mass. The multiplicity of the produced particles depends on the energy of the collision and is conveniently parametrized by the relation

$$\langle N_{ch} \rangle = 0.88 + 0.44 \ln s + 0.188 (\ln s)^2. \tag{8.1}$$

We have made a compilation of the existing charged pion distributions in p-p collisions measured by the experiments at the CERN ISR [2] accelerator in 1970's. The inclusive cross sections of π^+ and π^- have been precisely measured as a function of rapidity for different center of mass energies $\sqrt{s}$ = 23 to 63 GeV [163–165]. For our purposes we restricted the selection to the data at $\sqrt{s}$ = 23, 31, 45 GeV measured at $y_{CM} = 0$[3].

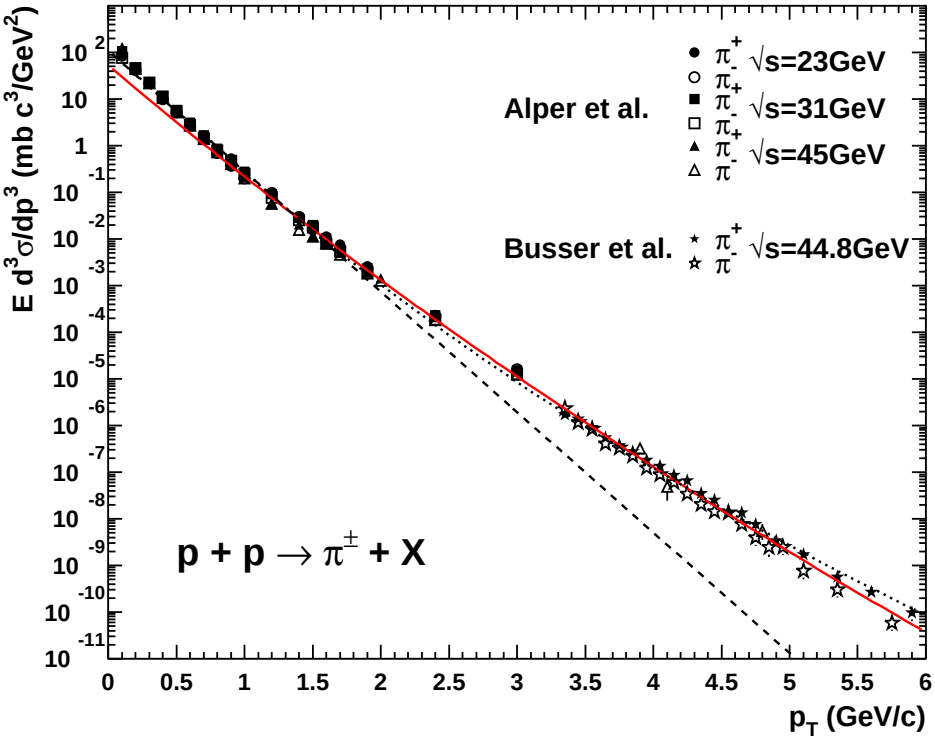

Figure 8.14: Invariant cross section of inclusive $\pi^{\pm}$ production in p-p collisions at different $\sqrt{s}$ energies scaled to $\sqrt{s}$ =17.2 GeV. The dashed line is an exponential fit for $p_T < 2$ GeV/c, the full line represents a powerlaw fit to the data, and the dotted line is the combined fit. See text.

[2] ISR = Intersecting Storage Ring

[3] The published data points were obtained from the online database in Durham, United Kingdom: http://cpt19.dur.ac.uk/cgi-hepdata/hepreac/88684.

For comparison with our measurements, these spectra have been scaled to $\sqrt{s}$ = 17.2 GeV employing a model of relativistic hard-scattering processes [166]. The inclusive cross section for the reaction $a + b \rightarrow c + d$ at $y_{CM} = 0$ is in this model given by

$$E\frac{d^3\sigma}{dp^3}\bigg|_{a+b\rightarrow c+d} \propto \frac{(1-2p_T/\sqrt{s})^F}{(p_T^2)^N}. \tag{8.2}$$

The parameters N and F in the exponent can be calculated in the framework of the *'Constituent Interchange Model'* which is based on q + meson $\rightarrow q$ + meson processes. Their values are $2N$ = 8, and F = 9 respectively [167].

The scaled transverse momentum spectra of charged pions are presented in Fig.8.14. They exhibit a nearly exponential shape up to p_T = 2 GeV/c depicted by the dashed line which may be surprising by two reasons. First, we cannot expect a thermodynamical equilibrium to be reached in p-p collisions, and second, most of the pions are not produced directly but emerge from decays of heavier resonances. Using the *bootstrap hypothesis* [168], Hagedorn succeeded to describe the exponential shape of the spectra. Beyond p_T = 2 GeV/c the shape of the spectra starts to strongly deviate from the exponential shape, which was interpreted as the onset of hard parton scatterings [169, 170]. A power-law parametrization, originally inspired by QCD [168, 171],

$$f(p_T) = C\left(\frac{p_0}{p_T + p_0}\right)^n \tag{8.3}$$

is commonly chosen to fit the spectra with C, p_0, and n taken as free fit parameters. A link to the exponential slope parameter T is obtained from the derivative of Eq. (8.3) [157],

$$T_{power-law} = -\frac{f(p_T)}{\partial f(p_T)/\partial p_T} = \frac{p_0}{n} + \frac{p_T}{n}. \tag{8.4}$$

The slope of the transverse momentum spectrum is characterized by p_0/n in the limit of $p_T \rightarrow 0$, and $1/n$ characterizes its gradient (concave curvature) along p_T.

For the scaled charged pion spectrum from p-p collisions we have obtained the following values of the fit parameters

$$\begin{aligned} C &= (53.6 \pm 3.1)\ c^3/\text{GeV}^2 \\ p_0 &= (12.44 \pm 0.15)\ \text{GeV}/c \\ n &= 71.14 \pm 0.47. \end{aligned} \tag{8.5}$$

The fit was performed in the region of ($1.0 \leq p_T \leq 6.0$) GeV/c and it describes very well the shape of the spectrum. Below p_T < 1.0 GeV/c, however, the data lie above the values extrapolated from the fit parameters presumably due to contributions of resonance decays. Thus we have decided to combine the power law parametrization with an exponential function at momenta below p_T < 1.0 GeV/c [168, 172],

$$f(p_T) = \begin{cases} C\left(\frac{nT-p_{T1}}{nT}\right)^n \exp\left(\frac{p_{T1}-p_T}{T}\right) & p_T \leq p_{T1} \\ C\left(\frac{nT-p_{T1}}{nT-p_{T1}+p_T}\right)^n & p_T > p_{T1}. \end{cases} \tag{8.6}$$

As can be easily seen, the relation to the above defined parameter is $p_0 = nT - p_{T1}$. The parameters obtained from this fit are

$$\begin{aligned} C &= (200.4 \pm 4.6)\ c^3/\text{GeV}^2 \\ T &= (166.27 \pm 0.48)\ \text{GeV}/c \\ n &= 36.22 \pm 0.48. \end{aligned} \tag{8.7}$$

We scale now the charged pion spectra from p-p to Pb-Au collisions simply by multiplying with number of nucleons in Pb and Au nuclei. Taking into account that we have measured at 30% of the total geometric cross section, we can compare the charged hadron and pion spectra in absolute terms. As shown in Fig. 8.17, the invariant cross sections from Pb-Au collisions are clearly below the scaled p-p reference at small transverse momenta; at $p_T \approx 1$ GeV/c they cross this reference, and for high p_T they lie considerably above it.

A similar observation was made in p-A already collisions [101, 173–176]. The target mass dependence of particle production is usually parametrized as $A^{\alpha(p_T)}$ connecting thus the p-p and p-A cross sections. From a compilation of the $\alpha(p_T)$ parameters determined in various experiments shown in Fig. 8.16, it is seen that $\alpha > 1$ for p_T >2 GeV/c. This effect is called *Cronin effect* and was later interpreted as the result of multiple scattering of the incident partons [177,178] but it is still not fully understood. Successive measurements of

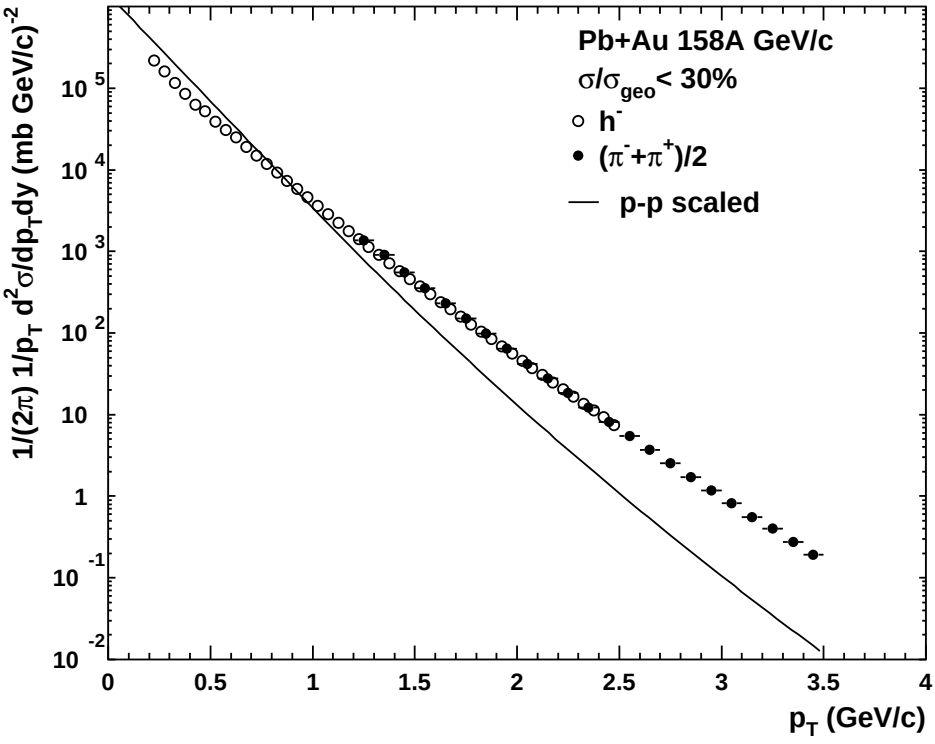

Figure 8.15: Comparison of the transverse momentum spectra of h^- and identified pions from semi-central Pb-Au collisions with p-p collisions described by the combined fit and extrapolated to Pb-Au collisions.

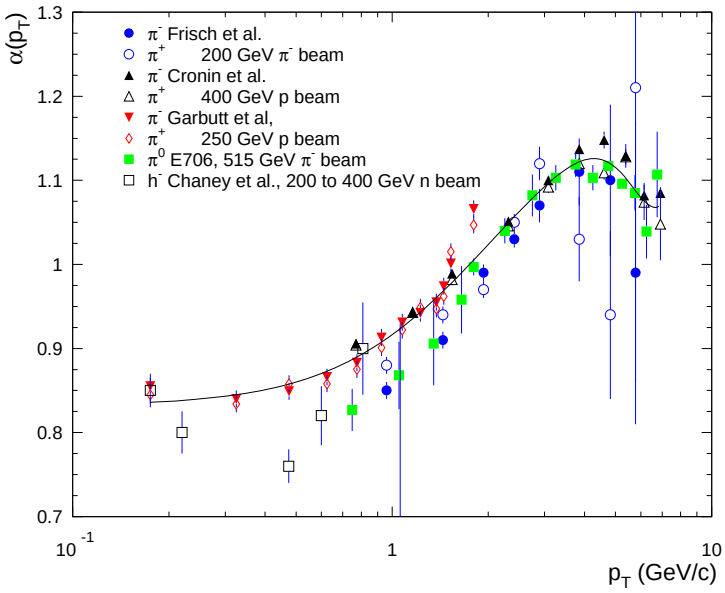

Figure 8.16: Compilation of the α exponent as a function of p_T from various experiments. Full line shows a polynomial fit (7th order) performed in [141].

p-W, O-W and S-W collisions [179, 180] showed similar behavior also for the projectile B. Consequently, it has been proposed to parametrize the nuclear dependence of the spectra as [181]

$$E\frac{d^3\sigma}{dp^3}(AB) = (AB)^{\alpha(p_T)} E\frac{d^3\sigma}{dp^3}(pp). \tag{8.8}$$

We have studied the dependence of the α parameter on transverse momentum for our data integrated over centrality as shown in Fig. 8.17. The α parameter follows the same trend as that from p-A collisions, i.e. its value increases monotonically from values considerably below one for p_T < 1 GeV/c to values above one for high p_T. It reaches the value of 1.25 at $p_T = 3$ GeV/c.

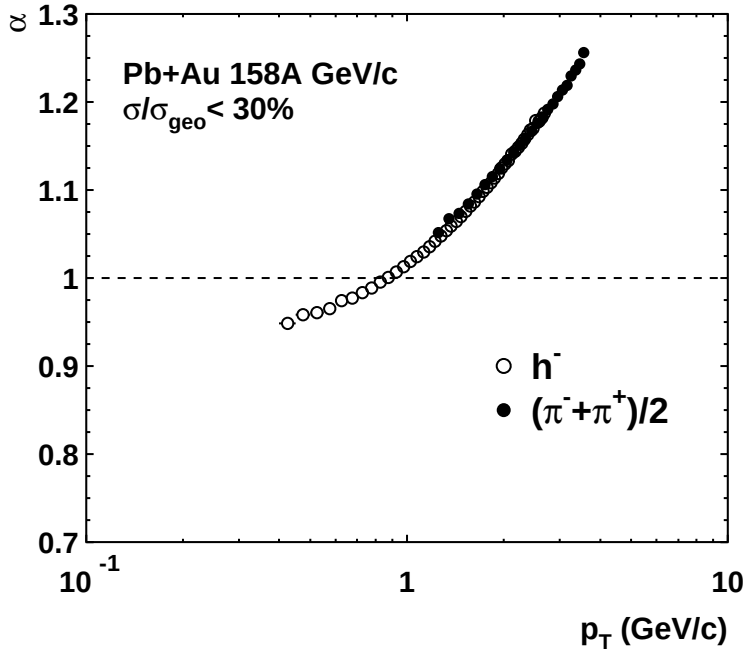

Figure 8.17: Transverse momentum dependence of $\alpha(p_T)$ for our h^- and $\pi^\pm$ data in most central 30% Pb-Au collisions at 158 AGeV/c.

8.3.5 Study of the Inverse Slope Behavior

Assuming the rapidity distribution is flat in our acceptance, we have fitted the transverse mass spectra with the expression

$$\frac{1}{m_T}\frac{dN}{dm_T} = A \exp\left(-\frac{m_T}{T}\right) \tag{8.9}$$

commonly used to extract information on the inverse slope parameter T. We have performed the fit using the minimum χ^2 method. The fit regions are $m_T - m_0 =$ (0.2-2.5) GeV/c^2 for the h^- spectra, and $m_T - m_0 =$ (1.2-3.5) GeV/c^2 for the identified pion spectra. The values of the inverse slope parameter T obtained for our six centrality classes are displayed in Fig. 8.18.

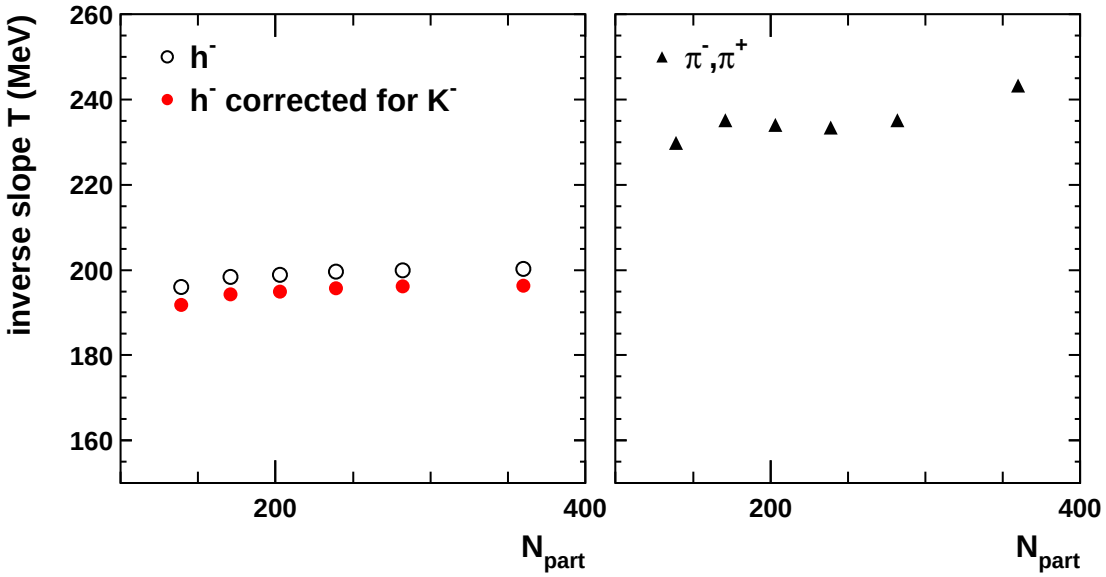

Figure 8.18: Centrality dependence of the inverse slope parameter T for h^- (left) and high-p_T pions (right). The statistical errors are within the symbol size.

Since the m_T spectrum of negative charged hadrons contains a small admixture of K^- particles, we have performed also a 'two-exponential' fit of the h^- spectra, i.e.

$$\frac{1}{m_T}\frac{dN}{dm_T}(h^-) = A\left(\exp\left(-\frac{\sqrt{p_T^2+m_\pi^2}}{T_\pi}\right) + 0.08\exp\left(-\frac{\sqrt{p_T^2+m_K^2}}{T_K}\right)\right). \tag{8.10}$$

The fit takes into account the relative abundance of 8% of K^-/π^- and the measured inverse slope of the K^- spectra, $T_{K^-} = 226$ MeV [152] which were kept fixed. This correction causes a relative decrease of the inverse slope by 3% as demonstrated in the left panel of Fig. 8.18. The errors of the inverse slope values T obtained from the fit are within the symbol size. We estimate a systematic error of 5 MeV due to the uncertainties of the input parameters of the fit to Eq. (8.10).

The comparison of the inverse slope values in central collisions with the other SPS measurements is given in Table 8.3. Since the inverse slope is very sensitive to the fitted

particle, m_T range (GeV/c^2)	$T\pm\Delta T$ **(MeV), experiment**	$T\pm\Delta T$ **(MeV), CERES**
π^-, (0.28-1.2)	$201\pm3\pm^2_1$, NA44 [153]	202 ± 1 (199 ± 1)
π^-, (0.2-0.7)	$180\pm3\pm10$, NA49 [152]	193 ± 1 (189 ± 1)
h^-, (0.2-1.0)	197 ± 2, WA97 [156]	197 ± 1

Table 8.3: Comparison of the inverse slopes with those from other SPS experiments in central Pb-Pb (Pb-Au) collisions. The CERES inverse slope values in brackets are for K^- corrected spectra.

range, we have adjusted it to that of an experiment we compare to. The agreement of our results with that of the other SPS experiments is remarkably good.

The spectra clearly have a concave curvature. This can be demonstrated by calculating the local slope at each m_T given by

$$T^{-1}_{local} = -\left(E\frac{d^3\sigma}{dp^3}\right)^{-1}\frac{d}{dm_T}\left(E\frac{d^3\sigma}{dp^3}\right). \tag{8.11}$$

The local inverse slopes were extracted from the adjacent data points within a small interval of $m_T = 0.5$ GeV/c^2. The results are plotted in Fig. 8.19. Similar studies were done for the π^0 transverse mass spectra measured by the WA98 experiment [159]. Their measurement shows a change in the local inverse slope from $T = 180$ MeV at $m_T - m_0 = 0.5$ GeV/c^2 to $T = 270$ MeV at $m_T - m_0 = 2.9$ GeV/c^2, in perfect agreement with our observations.

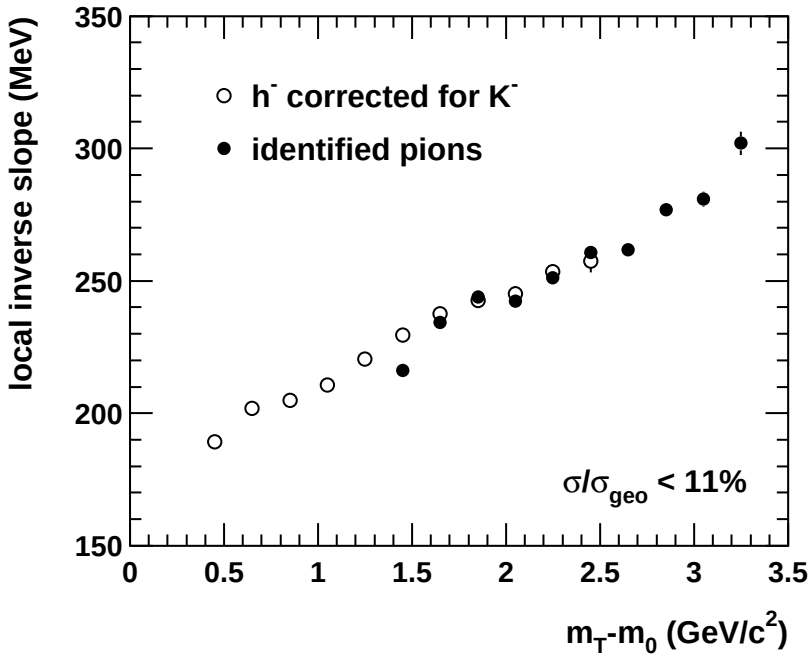

Figure 8.19: The m_T dependence of the local inverse slope parameter for h^- (open symbols) and identified pions (closed symbols) in central collisions ($\sigma/\sigma_{geo} < 11\%$).

8.3.6 Hydrodynamical Description of the m_T-Spectra

The description of transverse mass spectra in heavy-ion collisions by hydrodynamical models is well established although, it is not clear how well the requirement of local thermalization is actually fulfilled. Furthermore, at high transverse momenta hard processes are expected to significantly contribute to particle production.

In the following paragraphs we assume the validity of the hydrodynamical approach and extract the freeze-out parameters, the temperature T and the transverse velocity β_t, for two hydrodynamical models. The emission function of the source is generally defined as

$$S(x,P) = \frac{2J+1}{(2\pi)^3} M_T \cosh(Y-\eta) \exp\left(-\frac{P\cdot u(x)-\mu}{T}\right) H(x), \tag{8.12}$$

where J is the spin, y the rapidity, P 4-momentum of the emitted particle, and μ the corresponding chemical potential. The factor $M_T \cosh(Y-\eta)$ describes the geometry of the freeze-out hypersurface. The Lorentz invariant Boltzmann distribution reflects the assumption of local thermal equilibrium at freeze-out. The source is described by its space-time rapidity $\eta = \frac{1}{2}\log\left[(t+z)/(t-z)\right]$ and the 4-velocity $u(x)$,

$$u(x) = (\cosh\eta_t \cosh\eta, \cos\phi \sinh\eta_t, \sin\phi \sinh\eta_t, \cosh\eta_t \sinh\eta), \tag{8.13}$$

which expresses the motion of the different fluid elements of the source. The space-time distribution of the volume elements is expressed by $H(x)$ [182–184][4],

$$H(x) = G(r) \exp\left(-\frac{(\eta-\eta_0)^2}{2(\Delta\eta)^2}\right) \frac{\tau}{\sqrt{2\pi(\Delta\tau)^2}} \exp\left(-\frac{(\tau-\tau_0)^2}{2(\Delta\tau)^2}\right), \tag{8.14}$$

where $G(r)$ describes the transverse geometry. Two types of $G(r)$ profiles are commonly used: a Gaussian one

$$G(r) = \exp\left(-\frac{r^2}{2R_G^2}\right), \tag{8.15}$$

and a box-shaped one

$$G(r) = \theta(R_B - r). \tag{8.16}$$

The transverse flow rapidity η_t is assumed to increase linearly with the distance from the collision axis,

$$\eta_t(x) = \eta_f \frac{r}{r_{rms}}. \tag{8.17}$$

The scaling factor η_f specifies the value of $\eta_t(x)$ at the transverse rms radius given by

$$r_{rms} = \sqrt{2} R_G \tag{8.18}$$

for the Gaussian transverse profile and by

$$r_{rms} = \frac{R_B}{\sqrt{2}} \tag{8.19}$$

[4] We remark that there exist differences in the normalization between various authors, but the general form is identical.

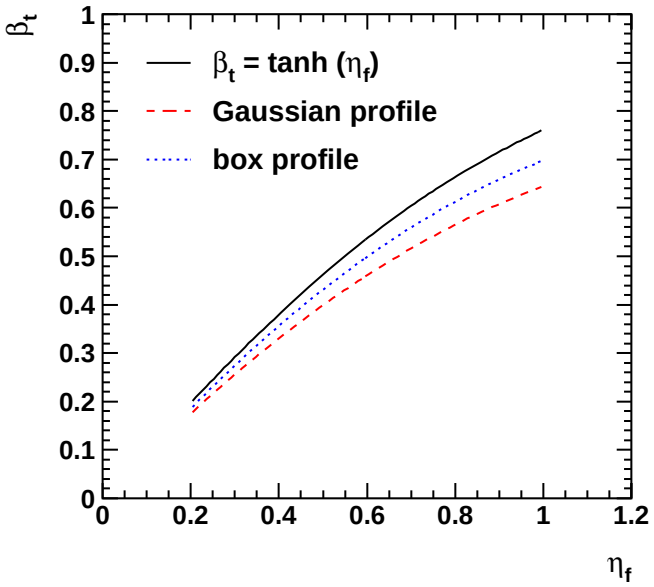

Figure 8.20: Dependence of the average transverse expansion velocity β_t on η_f for Gaussian (dashed line) and box (dotted line) transverse density profiles. The full line shows for a comparison the approximate relation $\beta_t \approx \tanh \eta_f$.

for the box-shaped one. In the literature the transverse flow is often quoted in terms of the average transverse expansion velocity β_t,

$$\beta_t = \frac{\int_0^\infty r dr \tanh \eta_t(r) G(r)}{\int_0^\infty r dr G(r)}. \tag{8.20}$$

Its value is approximately given by the radial velocity at the transverse rms radius, $\beta_t(r_{rms}) \approx \tanh \eta_f$. The exact solution shown in Fig. 8.20 results, however, in slightly smaller values of β_t.

The single-particle transverse mass spectrum is obtained from integration of Eq. (8.12)

$$\frac{dN}{dm_T^2} = \pi \int dy \int d^4x S(x,P). \tag{8.21}$$

Below we describe briefly two different hydrodynamical models used later for the extracting of the freeze-out parameters from the measured transverse mass spectra.

Model 1 (Chapman et al.)

The model of Chapman *et al.* [182] employs the Gaussian parametrization of $G(r)$, a longitudinal expansion of the Bjorken type [68], and linear transverse expansion profile. Since the integration of Eq. (8.12) is analytically not possible, the authors have used several approximations to derive an analytical non-relativistic expression for pions ($J = 1$, $\mu = 0$) which is given by

$$\begin{aligned} \frac{1}{m_T}\frac{dN}{dm_T} &\propto m_T R_*^2 \Delta\eta_* \left[1 + \frac{R_*^2}{2R_G^2}(\Delta\eta)_*^2 - \frac{m_T}{8T}(\Delta\eta)_*^4\right] \\ &\times \exp\left[-\frac{m_T}{T} + \frac{\beta_t^2(m_T^2 - m^2)}{2T(T + m_T\beta_t^2)} - \frac{0.5y^2}{(\Delta\eta)^2 + T/m_T}\right], \end{aligned} \tag{8.22}$$

where the parameters R_* and η_* are defined as

$$\frac{1}{R_*^2} = \frac{1}{R_G^2}\left(1+\beta_t^2\frac{m_T}{T}\right) \tag{8.23}$$

$$\frac{1}{(\Delta\eta)_*^2} = \frac{1}{(\Delta\eta)^2}+\frac{m_T}{T}. \tag{8.24}$$

The transverse geometrical radius of the source R_G was measured by the CERES experiment and its value for the central Pb-Au collisions is $R_G = 6.86^{+0.30}_{-0.27}$ fm [185]. The width of the source in the space-time rapidity $\Delta\eta$ is related to the width of the rapidity distribution Δy by

$$(\Delta y)^2 = (\Delta\eta)^2+\frac{T}{m_T}. \tag{8.25}$$

As was shown in [186], the value of the space-time rapidity is $\Delta\eta = 1.3\pm0.1$. Keeping fixed the R_G and $\Delta\eta$ parameters, there are only two unknown parameters left, the temperature T and the velocity β_t.

Model 2 (Wiedemann et al.)

The model of Wiedemann *et al.* [183] includes contributions from the most important two- and three-body resonance decays with pion(s) in the final state: ρ, Δ, K^*, Σ^*, K_S^0, Σ, Λ, η, ω, and η', since their contribution is crucial for a correct description of the yield and shape of the measured spectra. The transverse mass spectra of the directly emitted resonances (with the rest mass M) are given by the expression

$$\frac{dN^{\rm dir}_{\rm resonance}}{dM_T^2} \propto (2J_r+1)\,M_T\int d\xi e^{-\xi^2/2}\,K_1\left(\frac{M_T}{T}\cosh\eta_t(\xi)\right)\,I_0\left(\frac{P_T}{T}\sinh\eta_t(\xi)\right), \tag{8.26}$$

where we have introduced $\xi = r/R_G$. All integrals are in Model 2 evaluated numerically.[5] The geometrical parameters, like R_G, $\Delta\eta$, τ_0, $\Delta\tau$ affect only the absolute normalization of the single-particle spectrum, but not its shape as was shown in [60, 187]. The transverse momentum dependence of the single-particle spectrum is thus fully determined by the temperature T (or $T(\xi)$ if T depends on r), the transverse flow profile $\eta_t(\xi)$, and the rest masses and chemical potentials of the included resonances. Influence of various resonance decays on pion transverse mass spectrum is demonstrated in Fig. 8.21. This spectrum was calculated with Model 2 for the freeze-out temperature of $T = 160$ MeV and the transverse flow of $\eta_f = 0.3$. We can see that the main contribution to the spectrum, besides directly emitted pions, comes from decays of ρ resonances. Other resonance species considered in this model influence the spectrum only at low transverse masses, i.e. below $m_T - m_0 = 0.2$ GeV/c^2.

Below we apply the above described models to the measured transverse mass spectrum of h^- in central collisions. The fit to the spectrum was performed with the CERN package MINUIT [188], in which we have implemented the analytical form of the transverse mass spectrum from Model 1 given by Eq. (8.22), and the Fortran code of Model 2, respectively.

[5] The Fortran code calculating transverse mass spectra supplemented to [183] was obtained from http://www.aip.org/epaps/epaps.html (document number: E-PRVCAN-56-3265).

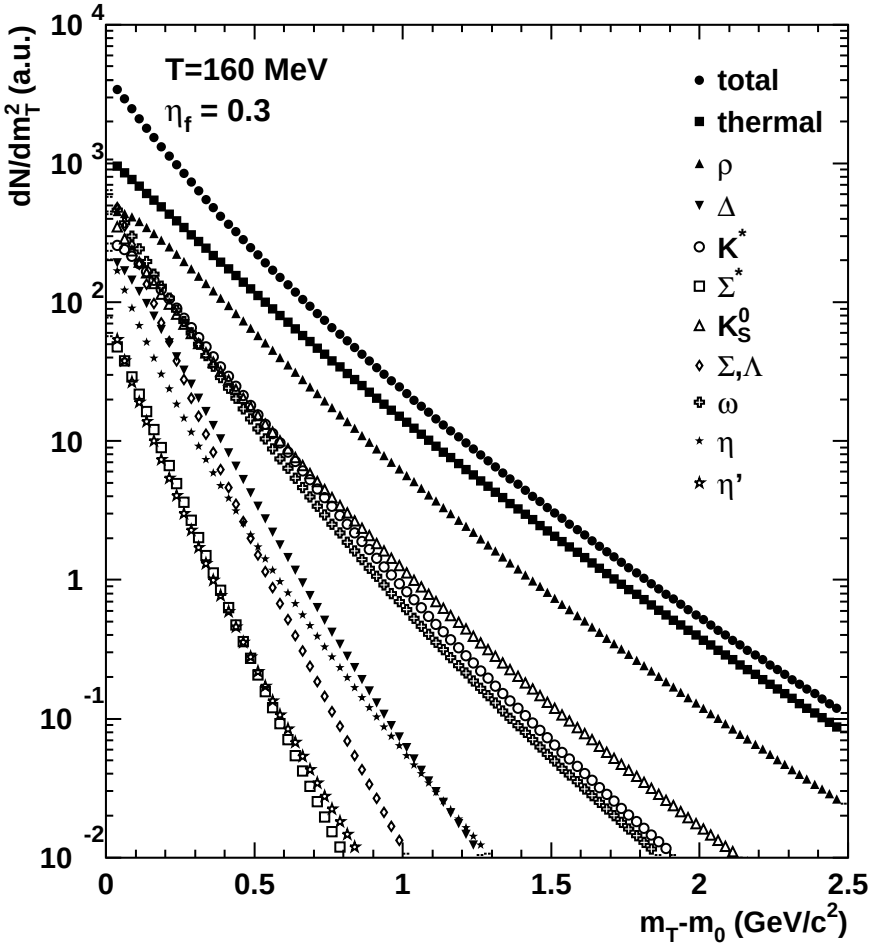

Figure 8.21: The pion transverse mass spectrum for freeze-out temperature of $T = 160$ MeV and transverse flow of $\eta_f = 0.3$ obtained from Model 2 including resonance contributions. The normalization of this spectrum is arbitrary. The relative normalizations of various resonance contributions are fixed by the assumption of thermal and chemical equilibrium.

Hydrodynamical Fit without Resonance Contributions

The hydrodynamical fits of the h^- spectrum from central collisions which include only direct pion contribution are for both models presented in Fig. 8.22. The fit was performed in the transverse mass range of $m_T - m_0 =$ (0.5-2.5) GeV/c^2. Both models describe the overall spectrum, albeit Model 1 shows larger deviations for transverse mass of $m_T > 1.5$ GeV/c^2, which is not the case for Model 2. The best fit values of the freeze-out parameters obtained from Model 1 are $T =$ (145.4$\pm$0.1) MeV and $\beta_t = 0.278\pm0.001$, and from Model 2 $T =$ (152.9$\pm$0.1) MeV and $\eta_f = 0.232\pm0.002$, respectively.

Besides the best fits, other combinations of T and β_t also allow description of the m_T spectrum. Keeping the transverse velocity β_t fixed at certain value, we have fitted the spectrum leaving the temperature and the normalization constant as free fit parameters. The obtained result is shown in Fig. 8.23. We observe a very different result for the two discussed models. While in the case of Model 2 the dependence of the freeze-out temperature on β_t shows a steep decrease with increasing β_t, for Model 1 and the velocities

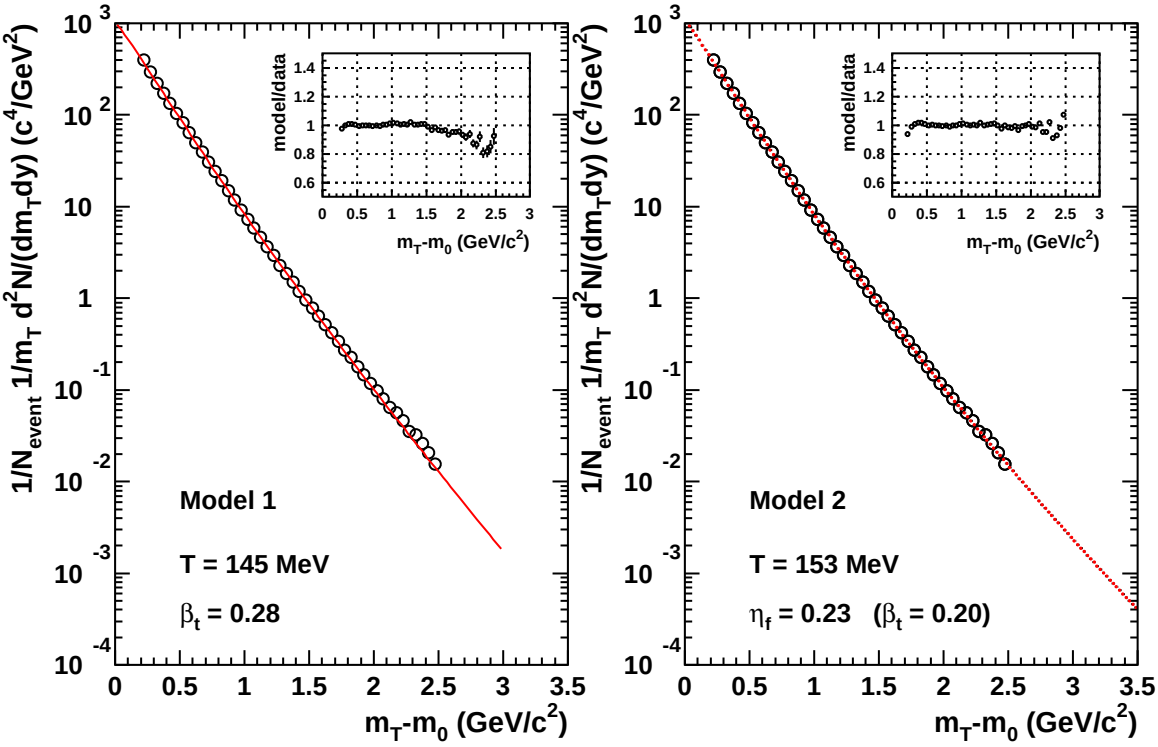

Figure 8.22: The hydrodynamical fits to the transverse mass spectrum of h^- measured in central Pb-Au collisions ($\sigma/\sigma_{geo} < 6\%$). The data were fitted with Model 1 (left) and Model 2 (right), respectively. The fit range is chosen as $m_T - m_0 = (0.5\text{-}2.5)$ GeV/c^2. Only direct pion contribution is considered. The given freeze-out parameters are the values of the best fit.

$\beta_t > 0.4$ the temperature is about constant and approaches the value of $T = 115$ MeV. This behavior of Model 1 can be ascribed to the non-relativistic approximation used.

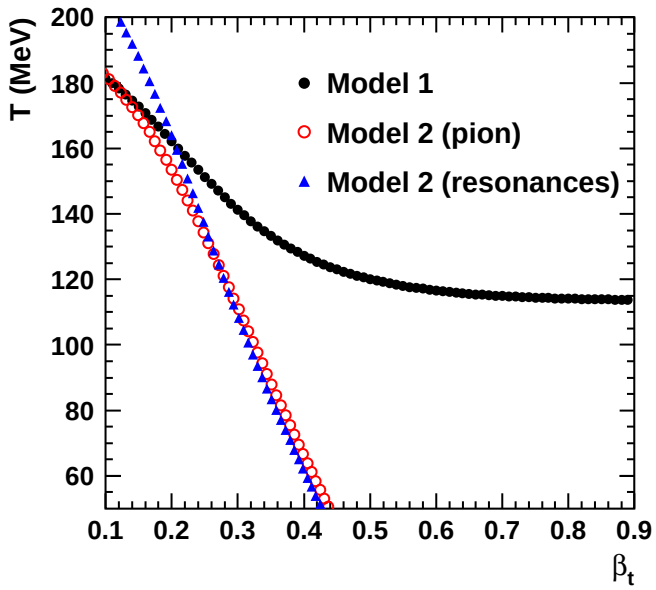

Figure 8.23: Dependence of the freeze-out temperature T on the transverse velocity β_t from the fit to the h^- spectra obtained from Model 1 and Model 2. The latter model was used with/without resonance contributions. The fit was performed in the $m_T - m_0 = (0.5\text{-}2.5)$ GeV/c^2 range.

Hydrodynamical Fit with Resonance Contributions

We investigate now the effect of resonance decays implemented in Model 2 on the values of the freeze-out parameters. Since we require all particle tracks to point back to the interaction vertex, Model 2 was used including all resonances except Λ and K^0_S. From the shape of the direct pion spectrum and that of pions emitted from various resonance decays (cf. Fig. 8.21), we expect to obtain a higher freeze-out temperature if resonance contributions are included. The results of the best fit are shown in Fig. 8.24. Indeed, the obtained freeze-out parameters are T = (191.5±0.2) MeV and η_f = 0.161±0.002. The fit was again performed in the range of $m_T - m_0$ = (0.5-2.5) GeV/c^2. Its extrapolation to lower m_T values shows an increasing discrepancy between the data and the model. The relative difference between the data and the model reaches 18% for $m_T - m_0$ = 0.2 GeV/c^2.

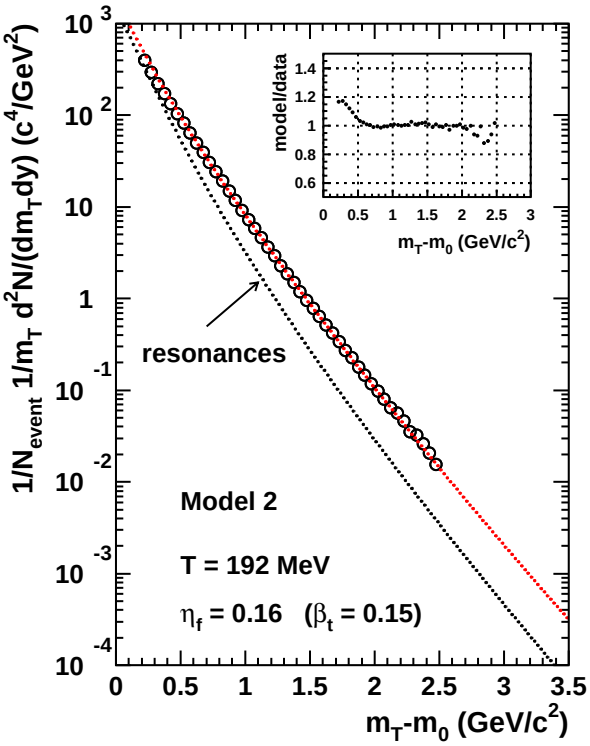

Figure 8.24: The hydrodynamical fit to the transverse mass spectrum of h^- measured in central Pb-Au collisions ($\sigma/\sigma_{geo} < 6\%$) with Model 2 including the resonance contributions (see text). The fit range is chosen as $m_T - m_0$ = (0.5-2.5) GeV/c^2. The given freeze-out parameters are the values of the best fit.

We remark at this place that applicability of Model 2 on our h^- spectra is limited, since the spectra contain also contributions from K^- and antiprotons. More sophisticated hydrodynamical calculations are thus necessary including e.g. that of [184, 189, 190]. Such investigations are, however, beyond the framework of this thesis.

9

Collective Elliptic Flow

In this chapter we present an analysis of elliptic flow obtained from the azimuthal correlations of particles with respect to the reaction plane using the Fourier expansion method. We describe first the procedure to determine the event plane together with the corrections applied. Since the knowledge of the event plane is essential for the flow analysis, we employ the Monte-Carlo simulations in order to test the reliability of the methods. Next, we discuss centrality and transverse momentum dependence of elliptic flow for charged hadrons and high-p_T pions. The chapter is closed with the comparison of our results to other experiments and models. Some of the results are published in [191, 192].

9.1 Fourier Expansion of Azimuthal Distributions

It is very convenient to describe the azimuthal distributions of particles with respect to the reaction plane by means of a Fourier expansion [70, 72]

$$E\frac{d^3N}{d^3p} = \frac{1}{2\pi}\frac{d^2N}{p_T dp_T dy}\left\{1 + \sum_{n=1}^{\infty} 2v_n \cos[n(\phi - \Psi_R)]\right\}, \tag{9.1}$$

where Ψ_R denotes the true reaction plane angle and ϕ the azimuthal angle of an emitted particle. The sine terms vanished due to the reflection symmetry with respect to the reaction plane.

The essence of the Fourier expansion method is to first estimate the reaction plane, which we denote *event plane* in order to distinguish it from the true reaction plane. The method uses the anisotropic flow itself to determine the event plane (cf. Section 9.2).

Next, the Fourier coefficients in the expansion of azimuthal distribution of particles with respect to this event plane are evaluated. The physics meaning of the first two Fourier coefficients is schematically depicted in Fig. 9.1. The coefficient v_1 quantifies *directed flow*. A positive (negative) value of the v_1 coefficient indicates a shift of the particle distribution parallel (antiparallel) to the x-axis. The coefficient v_2 represents the elliptic deformation of the particle distribution from which the name *elliptic flow* is derived. If the major axis of the ellipse-like distribution lies in the reaction plane the value of v_2 is

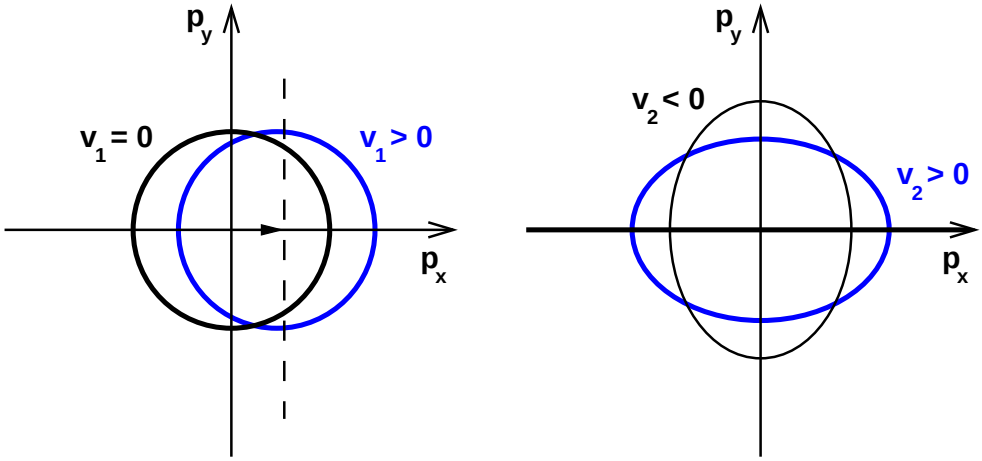

Figure 9.1: Schematic picture of azimuthal distributions demonstrating meaning of the v_1 and v_2 Fourier coefficients.

positive (*in-plane elliptic flow*). If it is oriented perpendicular to the reaction plane, v_2 is negative and it is referred to it as *out-of-plane elliptic flow*.

Since the finite number of detected particles results in a limited resolution of the event plane angle, the measured Fourier coefficients have to be corrected up to what they would be if determined relative to the true reaction plane. This is done by dividing the observed v_n coefficients by the event plane resolution estimated from the correlation of the event planes of independent subevents (cf. Section 9.3).

9.2 Event Plane Determination

The standard method for the event plane determination requires knowledge of three-momentum vectors of the identified particles in the final state [193]. We use the silicon drift detectors for the event plane determination taking advantage of their full azimuthal acceptance. However, they do not provide momentum information and thus we have reconstructed the event plane angle without momentum weighting factors as

$$\Psi_n = \frac{1}{n}\arctan\left(\frac{Q_{n,y}}{Q_{n,x}}\right) = \frac{1}{n}\arctan\left(\frac{\sum_{i=1}^{N}\sin(n\phi_i)}{\sum_{i=1}^{N}\cos(n\phi_i)}\right), \tag{9.2}$$

where ϕ_i is the azimuthal angle of the i-th detected particle and n is the order of the Fourier harmonics.

The two silicon drift detectors can be either used as two independent devices and the event plane is determined from positions of the detected hits, or as one combined device using then silicon track segments for the event plane determination. Both approaches have their pro and con. Since the resolution of the event plane, which will be discussed later in this chapter (see Section 9.3), improves with the number of particles used for its reconstruction, the higher number of hits than tracks would favor the first case. Moreover, the influence of the dead regions in the detectors is cumulated if they are used in

a combined way, which also gives a priority to hits. However, the reconstruction of the event plane from tracks is favored from point of view of smaller background contamination originating e.g. from electronics noise or artificially split hits. We have decided to use both approaches.

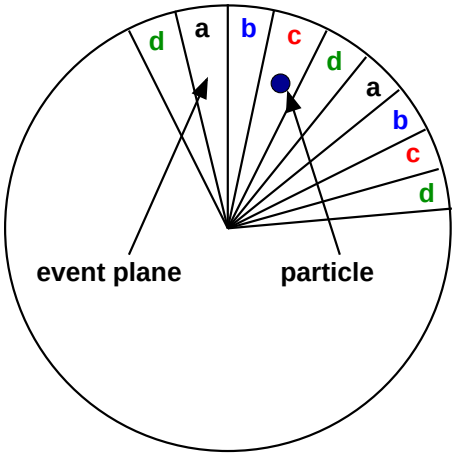

Figure 9.2: Definition of the sample division for the event plane determination.

To avoid autocorrelation effects, we have divided the silicon detectors into 100 slices in ϕ direction as shown in Fig. 9.2. Every fourth slice is combined into a sample resulting in four samples, which we have denoted a, b, c, and d. In each event we thus obtain four event plane angles: Ψ_n^a, Ψ_n^b, Ψ_n^c, and Ψ_n^d for a given order n. For the extraction of the flow signal we use then non-adjacent slices only, i.e. if the particle is located in the sample a, the event plane is taken from the sample c.

For an ideal detector with full azimuthal coverage, the distribution of the event plane angle is isotropic due to random orientation of the collision geometry. However, in reality different effects like dead regions in the detector, gain inequalities, geometrical offset between the beam position and the center of the detector in the $x-y$ plane introduce non-flatness into the event plane angle distribution. An example of the measured event plane angle distribution is demonstrated in Fig. 9.3 and Fig. 9.4 for the event plane determined from the SDD hits (for the SDD tracks is the situation similar). Clearly, the shape of the measured distribution is not uniform. Below we show that the origin of the observed non-uniformities is very well understood in the Monte-Carlo simulation.

9.2.1 Event Plane Distribution in the Monte-Carlo Simulation

For a detailed understanding of the event plane distribution observed in the data the Monte-Carlo simulation was performed. It is based on the event generator *MEVSIM* [194] developed for the RHIC experiments. The main advantage of this event generator, besides its CPU-speed, is that the user has more control over the simulated particle distributions compared to standard event generators such as UrQMD [148]. The event plane angle distribution in the simulation was chosen to be uniform in the interval of $\langle -\pi, \pi \rangle$ and the multiplicities of charged particles were tuned to those observed in the data. The underlying parametrization of the anisotropic flow in *MEVSIM* comes from [72]. In the

simulation we have used value of $v_2 = 4\%$, which is approximately the magnitude of elliptic flow observed at the SPS in semi-peripheral collisions. Strictly speaking, on the top of the *MEVSIM* simulation a GEANT simulation followed by the CERES analysis chain as presented in Chapter 6 should be performed. However, since a high statistics GEANT simulation of about $\approx 10^5$ Pb-Au collisions needed for careful studies is too much CPU-time consuming, we have decided to write a simplified standalone simulation. It includes to our best knowledge all necessary information about:

- the interaction vertex distribution along the beam axis together with the proper distribution of the reconstructed interaction vertices in the $x - y$ plane reflecting the beam position on the target discs.
- the geometrical alignment of the silicon detectors described by x, y and ϕ offsets. Moreover, since the aluminum ring on which both SDDs are mounted was inserted into the carbon target tube with a tilt it is taken into account as well. The tilt is described by two parameters, an amplitude of the tilt and a tilt angle
- the dead and noisy anodes in both SDDs. For a good agreement between the data

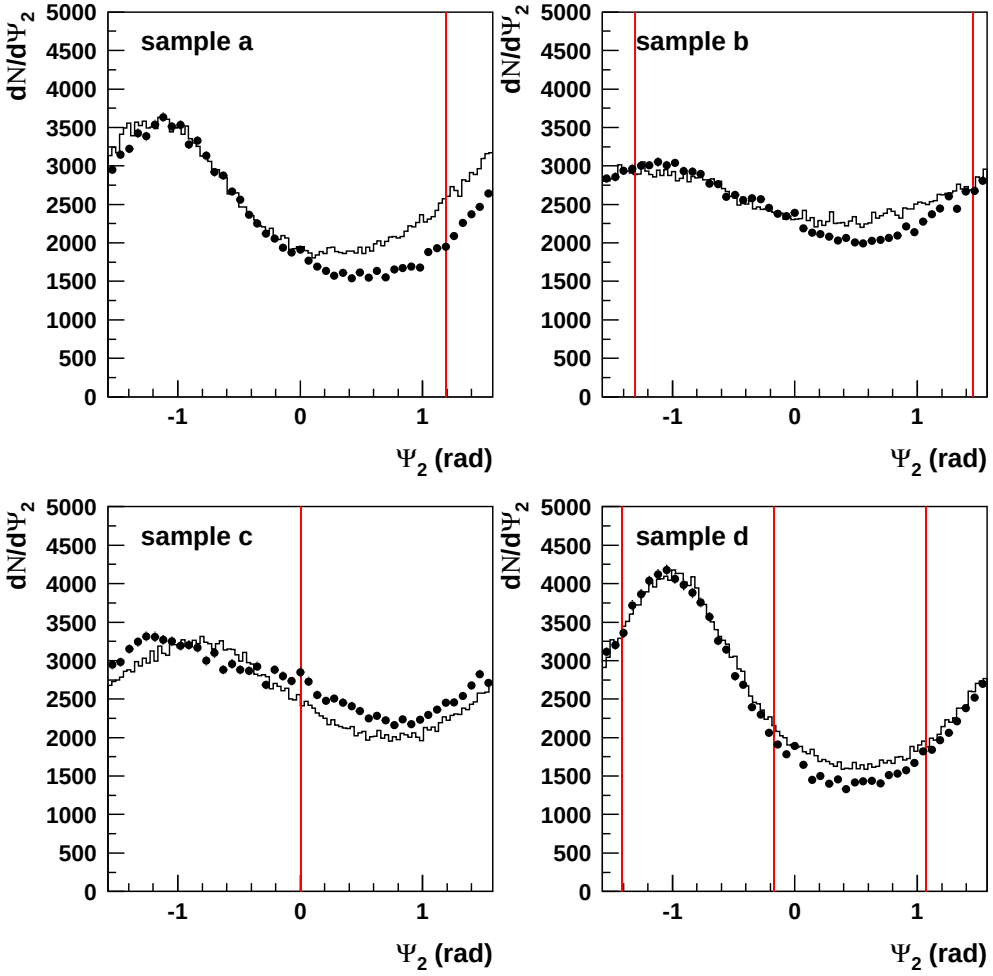

Figure 9.3: Comparison of the event plane angle distribution between the data (histogram) and the simulation (circles) for SDD1. The vertical lines show the dead regions in SDD1.

and simulation also the surrounding of the dead anodes needs to be described properly, since a neighboring anode of a dead anode looks like a 'noisy' anode.

The comparison between the measured and simulated event plane angle distributions for the four samples is shown in Fig. 9.3 and Fig. 9.4 for the event plane determined from the hits in SDD1 and SDD2. For the event plane determined from the SDD tracks is the situation similar (not shown here). Our simulation is able to reproduce very well the distributions observed in the data. There is a clear difference visible in the event plane distribution in the two detectors. Since SDD1 had only seven dead anodes (represented by the vertical lines in Fig. 9.3), the distribution of the measured event plane angles is not so much distorted and the influence of the geometrical offset, which results in a sine structure, is visible. SDD2 had on contrary 31 dead anodes concentrated in two big regions each consisting of 6, and 16 dead anodes, respectively. The effect of the dead anodes dominates the influence of the geometrical offset.

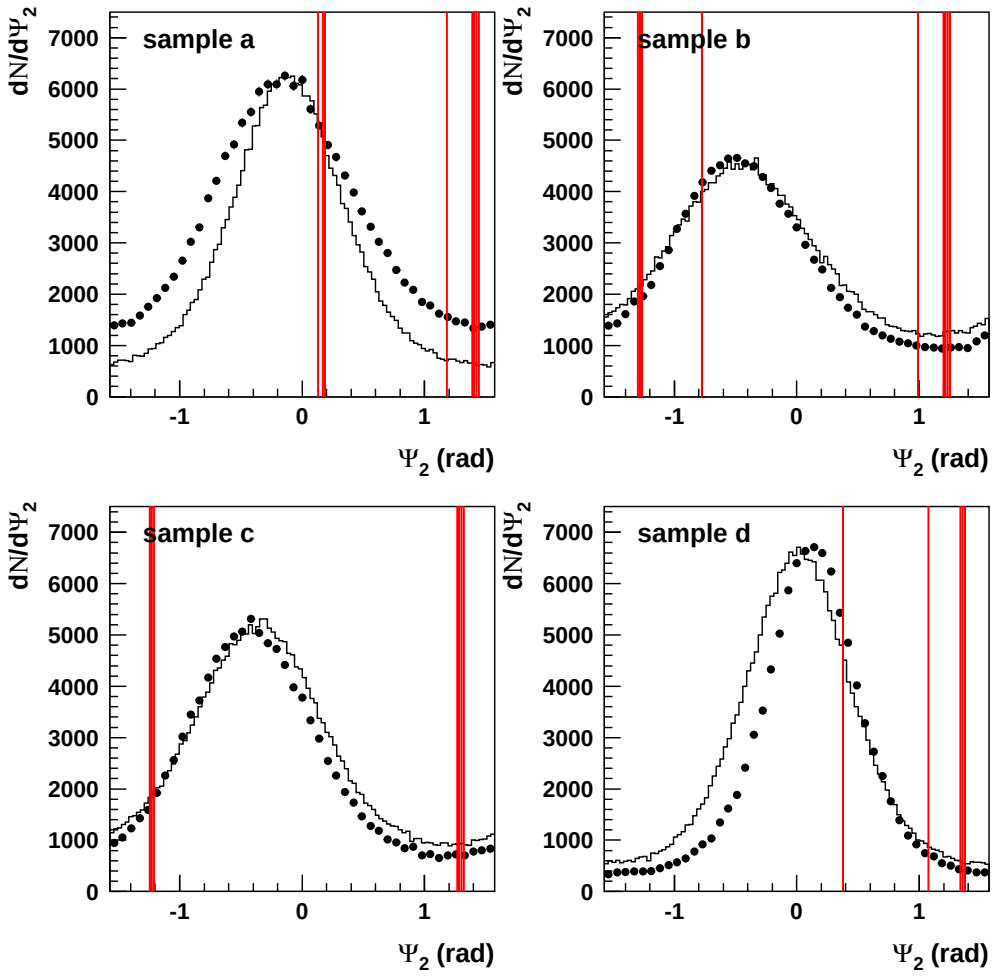

Figure 9.4: Comparison of the event plane angle distribution between the data (histogram) and the simulation (circles) for SDD2. The vertical lines show the dead regions in SDD2.

9.2.2 Flattening of the Event Plane Distribution

As already shown in the previous section, the distribution of the reconstructed event plane angles is not uniform (cf. Fig. 9.5(a)) and this non-flatness propagates further and affects the measurement of the flow signal. To account for this effect the so called *'flattening procedure'* has to be applied. Several techniques such as re-centering, weighting, mixed event method, Fourier expansion method, etc. have been developed [72, 88, 195]. The flattening procedure used in this work is based on the combination of the recentering and Fourier expansion method. It is a global correction in a sense that the reconstructed event plane angle distribution is averaged over a run containing typically around 2 - 4$\cdot 10^5$ events, supposing that all the distortions are stable within the run. It proceeds in the following steps:

1. From the data, which are divided into six multiplicity classes, we calculate the mean values of $Q_{n,x}$ and $Q_{n,y}$:

$$\langle Q_{n,x} \rangle = \langle \sum_{i=1}^{N} \cos(n\phi_i) \rangle$$
$$\langle Q_{n,y} \rangle = \langle \sum_{i=1}^{N} \sin(n\phi_i) \rangle, \tag{9.3}$$

   where $\langle ... \rangle$ indicates the event averaging. Then we shift the raw $Q_{n,x}$ and $Q_{n,y}$ distribution to zero, recalculate the event plane and obtain a new one which we denote $\Psi_n^{(1)}$ (Fig. 9.5(b)):

$$\Psi_n^{(1)} = \frac{1}{n} \arctan \left(\frac{Q_{n,y} - \langle Q_{n,y} \rangle}{Q_{n,x} - \langle Q_{n,x} \rangle} \right) \tag{9.4}$$

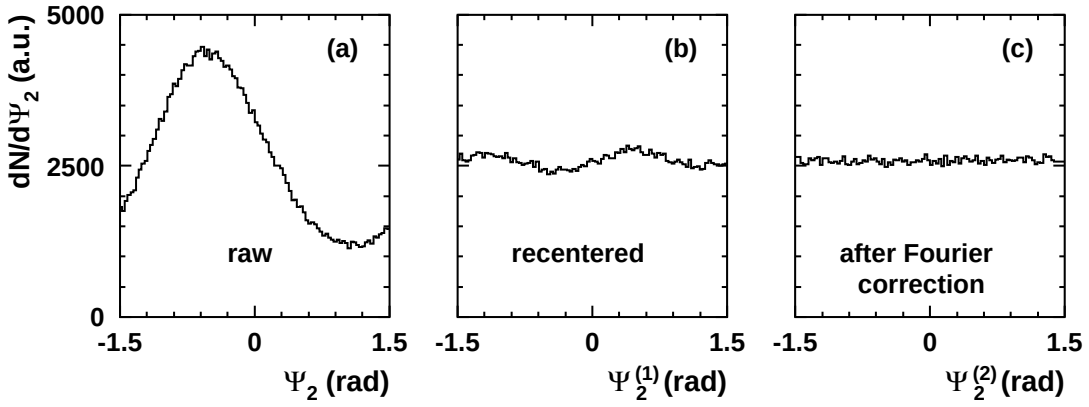

Figure 9.5: Individual steps of the flattening procedure. The measured event plane distribution for $n = 2$ calculated from the SDD tracks in the sample a (a), after recentering (b), and after Fourier correction (c).

2. The final event plane $\Psi_n^{(2)}$, which has already a uniform azimuthal distribution (Fig. 9.5(c)), is obtained from $\Psi_n^{(1)}$ as

$$\Psi_n^{(2)} = \Psi_n^{(1)} + \Delta\Psi_n^{(1)}, \tag{9.5}$$

where

$$\Delta\Psi_n^{(1)} = \sum_m \left(A_m \cos(mn\Psi_n^{(1)}) + B_m \sin(mn\Psi_n^{(1)})\right) \tag{9.6}$$

By requiring the m-th Fourier components of the new distribution vanish we can evaluate the coefficients A_m and B_m. Using the Taylor expansion we can write

$$\begin{aligned} \langle \sin(mn\Psi_n^{(2)})\rangle &= \langle \sin(mn\Psi_n^{(1)} + mn\Delta\Psi_n^{(1)})\rangle \\ &\simeq \langle \sin(mn\Psi_n^{(1)})\rangle + \langle \cos(mn\Psi_n^{(1)}) mn\Delta\Psi_n^{(1)}\rangle \\ &= \langle \sin(mn\Psi_n^{(1)})\rangle + mnA_m/2 = 0 \end{aligned} \tag{9.7}$$

$$\begin{aligned} \langle \cos(mn\Psi_n^{(2)})\rangle &= \langle \cos(mn\Psi_n^{(1)} + mn\Delta\Psi_n^{(1)})\rangle \\ &\simeq \langle \cos(mn\Psi_n^{(1)})\rangle - \langle \sin(mn\Psi_n^{(1)}) mn\Delta\Psi_n^{(1)}\rangle \\ &= \langle \cos(mn\Psi_n^{(1)})\rangle - mnB_m/2 = 0. \end{aligned} \tag{9.8}$$

The coefficients A_m and B_m have to satisfy the following conditions:

$$\begin{aligned} A_m &= -\frac{2}{mn}\langle \sin(mn\Psi_n^{(1)})\rangle \\ B_m &= \frac{2}{mn}\langle \cos(mn\Psi_n^{(1)})\rangle \end{aligned} \tag{9.9}$$

We have calculated A_m and B_m coefficients upto $m = 4$, which turned to be enough precise. The final result of the flattening procedure of the event plane distribution reconstructed from the hits and tracks for the second Fourier harmonics can be seen in Fig. 9.6.

9.3 Event Plane Resolution

The measured Fourier coefficients are smaller due to the finite resolution of the measured event plane Ψ_n^i (where $i = a$, b, c, or d) as compared to the true event plane Ψ_R and they have to be corrected up. For simplicity, we omit below the index n in Ψ_n^i. The true azimuthal distribution is given by Eq. (2.11), however, in the experiment we measure:

$$\frac{dN}{d(\phi - \Psi^i)} = A\{1 + \sum_{n=1}^{\infty} 2v_n' \cos[n(\phi - \Psi^i)]\}, \tag{9.10}$$

where v_n' are the measured Fourier coefficients. Introducing the deviation $\Delta\Psi$ between the true and the reconstructed event plane angles

$$\Delta\Psi = \Psi^i - \Psi_R, \tag{9.11}$$

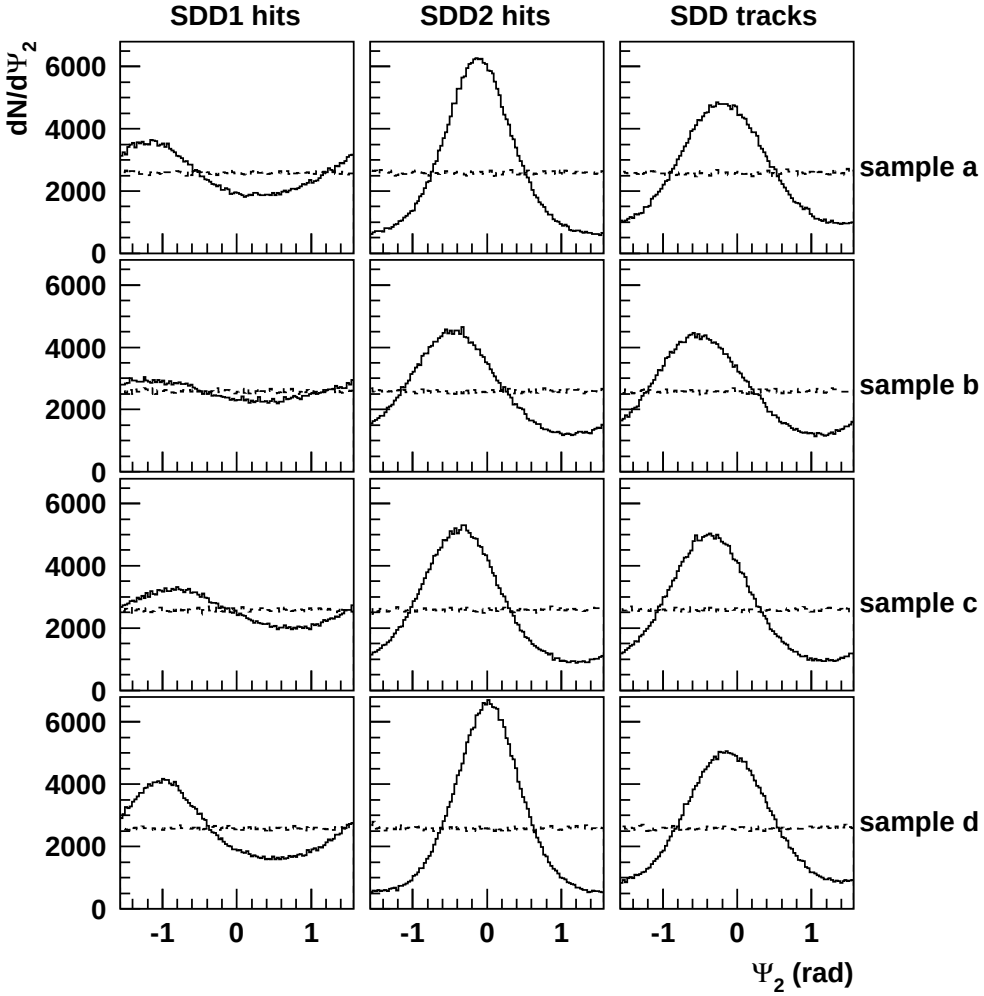

Figure 9.6: The second Fourier harmonics event plane angle distribution measured (full line) and after the flattening procedure (dashed line) determined from the SDD1 hits (left), SDD2 hits (middle) and SDD tracks (right). From top to bottom are shown the 4 ϕ-samples a, b, c, and d.

we can derive the relation between v_n and v_n' coefficients, i.e.

$$\begin{aligned} v_n' &= \frac{\langle A\cos(n(\phi-\Psi^i))\rangle}{\langle A\rangle} = \frac{\langle A\cos(n(\phi-\Psi_R-\Delta\Psi))\rangle}{\langle A\rangle} \\ &= \frac{\langle A\cos(n(\phi-\Psi_R))\rangle\langle\cos(n\Delta\Psi)\rangle}{\langle A\rangle} + \frac{\langle A\sin(n(\phi-\Psi_R))\rangle\langle\sin(n\Delta\Psi)\rangle}{\langle A\rangle} \\ &= \frac{\langle A\cos(n(\phi-\Psi_R))\rangle\langle\cos(n\Delta\Psi)\rangle}{\langle A\rangle} = v_n\langle\cos(n\Delta\Psi)\rangle, \end{aligned} \tag{9.12}$$

where the sine terms cancelled out because of the symmetry. The true magnitude of the v_n coefficients is then given by relation

$$v_n = \frac{v_n'}{\langle\cos(n\Delta\Psi)\rangle} = \frac{v_n'}{\langle\cos(n(\Psi^i-\Psi_R))\rangle}. \tag{9.13}$$

The denominator contains the unknown angle Ψ_R of the true reaction plane which can be expressed by the measured differences between the event plane angles in the individual samples Ψ^i and Ψ^j, i.e.

$$\begin{aligned}\cos(n(\Psi^i-\Psi^j)) &= \cos(n((\Psi^i-\Psi_R)-(\Psi^j-\Psi_R)))\\ &= \cos(n(\Psi^i-\Psi_R))\cos(n(\Psi^j-\Psi_R))\\ &\quad +\sin(n(\Psi^i-\Psi_R))\sin(n(\Psi^j-\Psi_R))\end{aligned} \tag{9.14}$$

and the event averaging gives

$$\begin{aligned}\langle\cos(n(\Psi^i-\Psi^j))\rangle &= \langle\cos(n(\Psi^i-\Psi_R))\cos(n(\Psi^j-\Psi_R))\rangle\\ &\quad +\langle\sin(n(\Psi^i-\Psi_R))\sin(n(\Psi^j-\Psi_R))\rangle\\ &= \langle\cos(n(\Psi^i-\Psi_R))\rangle\langle\cos(n(\Psi^j-\Psi_R))\rangle\\ &\quad +\langle\sin(n(\Psi^i-\Psi_R))\rangle\langle\sin(n(\Psi^j-\Psi_R))\rangle\\ &= \langle\cos(n(\Psi^i-\Psi_R))\rangle\langle\cos(n(\Psi^j-\Psi_R))\rangle. \qquad (9.15)\end{aligned}$$

Analogically, by exchanging j by k, or i by j, we can write

$$\langle\cos(n(\Psi^i-\Psi^k))\rangle = \langle\cos(n(\Psi^i-\Psi_R))\rangle\langle\cos(n(\Psi^k-\Psi_R))\rangle, \tag{9.16}$$

$$\langle\cos(n(\Psi^j-\Psi^k))\rangle = \langle\cos(n(\Psi^j-\Psi_R))\rangle\langle\cos(n(\Psi^k-\Psi_R))\rangle. \tag{9.17}$$

Combining Eq. (9.15) and Eq. (9.16) we can express the denominator of Eq. (9.13) as

$$\langle\cos(n(\Psi^i-\Psi_R))\rangle = \sqrt{\frac{\langle\cos(n(\Psi^i-\Psi^j))\rangle}{\langle\cos(n(\Psi^j-\Psi_R))\rangle}\frac{\langle\cos(n(\Psi^i-\Psi^k))\rangle}{\langle\cos(n(\Psi^k-\Psi_R))\rangle}}. \tag{9.18}$$

Substituting for $\langle\cos(\mathrm{n}(\Psi^{\mathrm{j}}-\Psi_{\mathrm{R}}))\rangle$ using Eq. (9.17), we obtain eventually the desired relation

$$\langle\cos(n(\Psi^i-\Psi_R))\rangle = \sqrt{\frac{\langle\cos(n(\Psi^i-\Psi^j))\rangle\langle\cos(n(\Psi^i-\Psi^k))\rangle}{\langle\cos(n(\Psi^j-\Psi^k))\rangle}}. \tag{9.19}$$

In the case of the random sample selection (which is not our case) where are all slices equally influenced by dead anodes etc., Eq. (9.19) simplifies to

$$\langle\cos(n(\Psi^i-\Psi_R))\rangle = \langle\cos(n(\Psi^j-\Psi_R))\rangle = \sqrt{\langle\cos(n(\Psi^i-\Psi^j))\rangle}. \tag{9.20}$$

Eq. (9.19) provides a way to estimate the event plane resolution in the data using correlation between the samples. An example of such correlation between samples a and b is shown in Fig. 9.7. Since we have divided each event into four samples, we have for each of the samples three possibilities to determine the event plane resolution. Fig. 9.8 shows the centrality dependence of these three correction factors for the second Fourier harmonics event plane. We observe that always two correction factors for a given sample are very close to each other but the third one exhibits a certain offset. This behavior is most pronounced for the event plane determined from the SDD1 hits. The described observation is an evidence of an additional correlation between the samples which is not due to flow. This issue is discussed in detail in the next section.

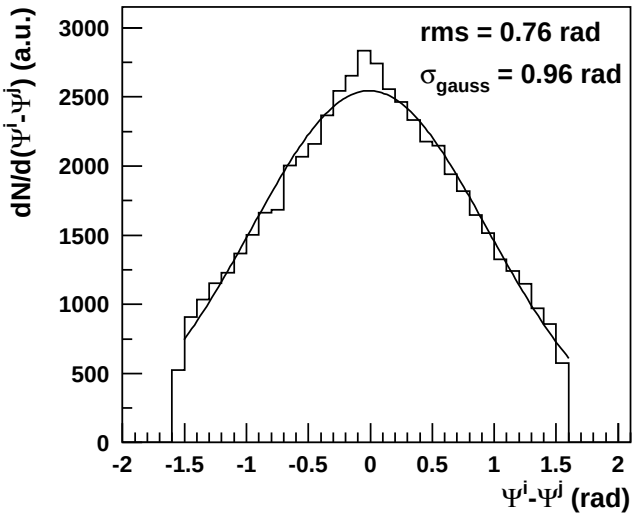

Figure 9.7: Correlation between the measured event plane angles in sample a and b in semi-central collisions (σ/σ_{geo} = (24-30) %).

9.3.1 Correction for 'Non-Flow' Correlations Between Samples

In reality, the subevents (samples) are not completely independent from each other. The reason for that is existence of 'non-flow' correlations which have either physics origin (momentum conservation, particle decays, two- and many-particle correlations, jet production etc.), or are due to various correlations in detectors used for the event plane estimation. The first type of the additional source of correlation will be discussed later in Section 9.5.2. Here we concentrate only on the second mentioned type.

As for example the E877 experiment at the AGS in BNL reported [196], the showering effect in the calorimeters used for the event plane estimation can induce additional correlations between the samples. In our case a natural candidate of such correlations is the artificial hit splitting in the silicon detectors. It increases the strength of the correlation between the neighboring samples since a hit belonging to a certain particle is shared between two samples. A supporting argument for this explanation is that the observed difference between the three possibilities of the correction factors is higher in SDD1 than in SDD2 coinciding with the observation that the artificial hit splitting is higher in the first of the two detectors [11]. Moreover, there is almost no difference between the three possible correction factors in the case when the SDD tracks are used for the event plane estimation.

Let us simplify the notation used in the previous section and define

$$C_{ij} \equiv \langle \cos(n(\Psi^i - \Psi^j)) \rangle, \tag{9.21}$$

where i and j is one of the 4 samples (a, b, c, or d), $i \neq j$. If only correlations due to flow exist, we can write

$$C_{ij} = \langle \cos(n(\Psi^i - \Psi_R)) \rangle \langle \cos(n(\Psi^j - \Psi_R)) \rangle \tag{9.22}$$

and for our four samples the following constraints have to be satisfied

$$C_{ab}C_{cd} = C_{ac}C_{bd} = C_{ad}C_{bc}. \tag{9.23}$$

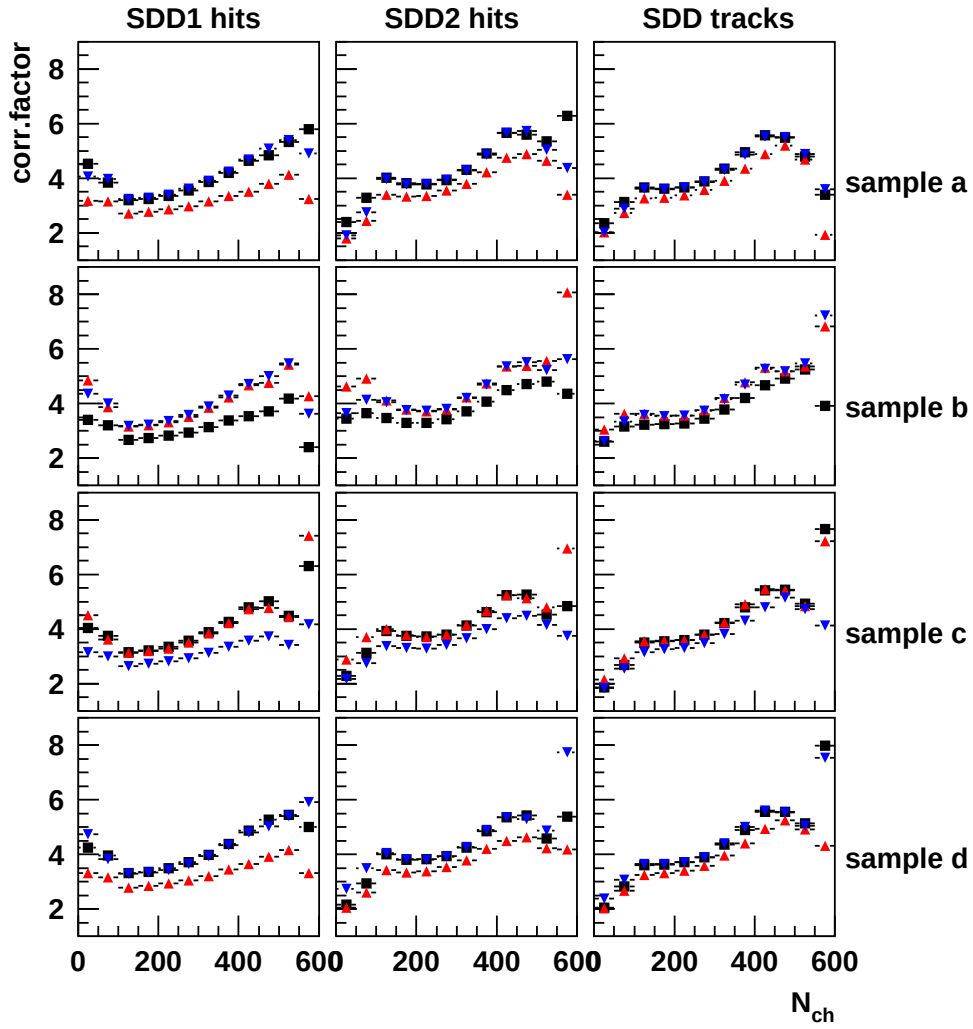

Figure 9.8: Centrality dependence of the 3 possibilities of the event plane resolution correction factor of the second Fourier harmonics event plane for the event plane determined from SDD1 hits (left), SDD2 hits (middle) and SDD tracks (right) and different samples (from top to bottom).

However, if in addition non-flow correlations are present Eq. (9.21) is modified to

$$\widetilde{C_{ij}} = \langle \cos(n(\Psi^i - \Psi_R)) \rangle \langle \cos(n(\Psi^j - \Psi_R)) \rangle + f_{ij} = C_{ij} + f_{ij}, \tag{9.24}$$

where the parameters f_{ij} describe the non-flow contributions. Using the new notation, we can rewrite Eq. (9.19) as

$$\langle \cos(n(\Psi^i - \Psi_R)) \rangle \quad = \quad \sqrt{\frac{(C_{ij} + f_{ij})(C_{ik} + f_{ik})}{(C_{jk} + f_{jk})}}. \tag{9.25}$$

Let us now try to explain the observed behavior of the correction factors (cf. Fig. 9.8). If the hit splitting is the dominant non-flow contribution, we would expect that $f_{ij} > 0$ between direct neighbors (f_{ab}, f_{ad}, f_{bc}, f_{cd}) and $f_{ij} = 0$ in the case of f_{ac} and f_{bd}. Hence,

according to Eq. (9.25), the three possibilities of correction factor for sample a are given by

$$\begin{aligned}
\langle\cos(n(\Psi^{a,1}-\Psi_R))\rangle &= \sqrt{\frac{(C_{ab}+f_{ab})(C_{ac}+f_{ac})}{(C_{bc}+f_{bc})}} = \sqrt{\frac{C_{ac}(C_{ab}+f_{ab})}{(C_{bc}+f_{bc})}},\\
\langle\cos(n(\Psi^{a,2}-\Psi_R))\rangle &= \sqrt{\frac{(C_{ab}+f_{ab})(C_{ad}+f_{ad})}{(C_{bd}+f_{bd})}} = \sqrt{\frac{(C_{ab}+f_{ab})(C_{ad}+f_{ad})}{C_{bd}}},\\
\langle\cos(n(\Psi^{a,3}-\Psi_R))\rangle &= \sqrt{\frac{(C_{ac}+f_{ac})(C_{ab}+f_{ab})}{(C_{ad}+f_{ad})}} = \sqrt{\frac{C_{ac}(C_{ad}+f_{ad})}{(C_{cd}+f_{cd})}}.
\end{aligned} \tag{9.26}$$

If all of C_{ij} and f_{ij} factors have approximately the same magnitudes which we denote C and f, we can easily see that the first and the third correction factors (which are the inverse of Eq. (9.26)) behave like $1/\sqrt{C}$ and the second one behaves like $1/\sqrt{C+2f}$. Here, we have neglected the terms of the order of f^2. This situation corresponds exactly to our observation.

Further check, which supports our explanation, is based on six instead of four samples used for the event plane determination. Since in the output of the produced data the event plane is already calculated using only four samples, we have reproduced a small part of the data for SDD1 and made a new estimation of the event plane using six samples. There are now 10 possibilities how to construct the correction factor of each sample. They can be schematically grouped into five types which we denote by A, B, C, D, and E:

$$\begin{aligned}
&\text{TYPE A:} && \sqrt{\frac{C+f}{C(C+f)}} = \frac{1}{\sqrt{C}},\\
&\text{TYPE B:} && \sqrt{\frac{C}{C(C+f)}} = \frac{1}{\sqrt{C+f}},\\
&\text{TYPE C:} && \sqrt{\frac{C}{(C+f)(C+f)}} = \frac{1}{\sqrt{C+2f}},\\
&\text{TYPE D:} && \sqrt{\frac{C+f}{C\cdot C}} > \frac{1}{\sqrt{C}},\\
&\text{TYPE E:} && \sqrt{\frac{C}{C\cdot C}} = \frac{1}{\sqrt{C}}.
\end{aligned} \tag{9.27}$$

From these relations we can expect the following ordering of the corrections factors (from high to low): type D, followed by types A and E, which should have similar values, type B and finally type C. We remark here that the two types of correction factors in the case of four samples correspond to the type A and type C. The obtained centrality dependence of the correction factors is shown in Fig. 9.9 and agrees very well with our expectation.

Since there is no handle how to separate these additional correlations, we use a semi-empirical approach suggested in [196] to correct for them. A deviation from Eq. (9.23) can be measured by calculating

$$\Delta \equiv (\widetilde{C_{ab}}\widetilde{C_{cd}} - \widetilde{C_{ac}}\widetilde{C_{bd}})^2 + (\widetilde{C_{ab}}\widetilde{C_{cd}} - \widetilde{C_{ad}}\widetilde{C_{bc}})^2 + (\widetilde{C_{ac}}\widetilde{C_{bd}} - \widetilde{C_{ad}}\widetilde{C_{bc}})^2. \tag{9.28}$$

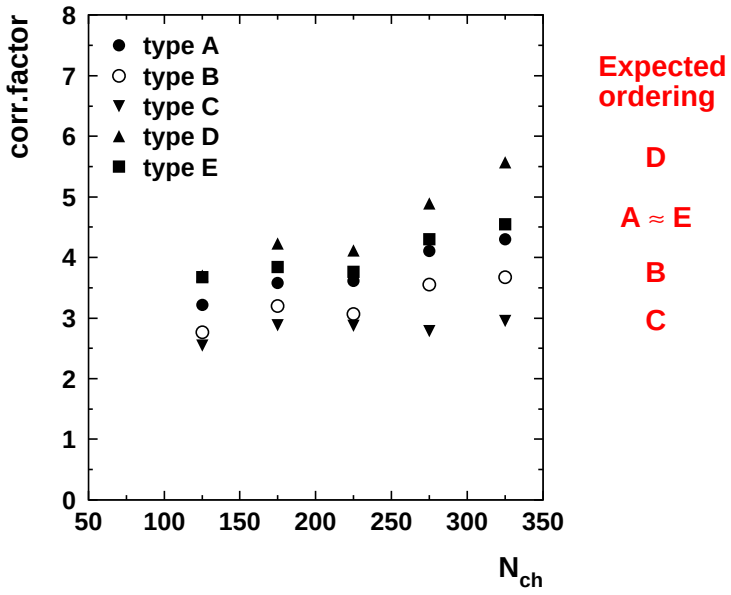

Figure 9.9: Centrality dependence of five different possibilities of the resolution correction factor of the second Fourier harmonics event plane determined from SDD1 hits together with expectation (for details see text).

Supposing now that the f_{ij} parameters are in the first order independent on centrality, we can establish their values using a minimization fitting procedure of the function

$$\Delta_{\text{tot}} = \sum_{N_{ch}-bin} \Delta(N_{ch}), \tag{9.29}$$

where $\Delta(N_{ch})$ is the Δ defined by Eq. (9.28) in a given centrality bin. Table 9.1 shows the values of the six f_{ij} parameters derived from the numerical minimization of Eq. (9.29) for the second Fourier harmonics event plane.

	SDD1 hits	SDD2 hits	SDD tracks
f_{ab}	0.0177	0.0160	0.0101
f_{ac}	0.0000	0.0000	0.0000
f_{ad}	0.0138	0.0089	0.0042
f_{bc}	0.0162	0.0100	0.0119
f_{bd}	0.0000	0.0000	0.0000
f_{cd}	0.0163	0.0000	0.0051

Table 9.1: The values of the f_{ij} parameters obtained from the minimization procedure.

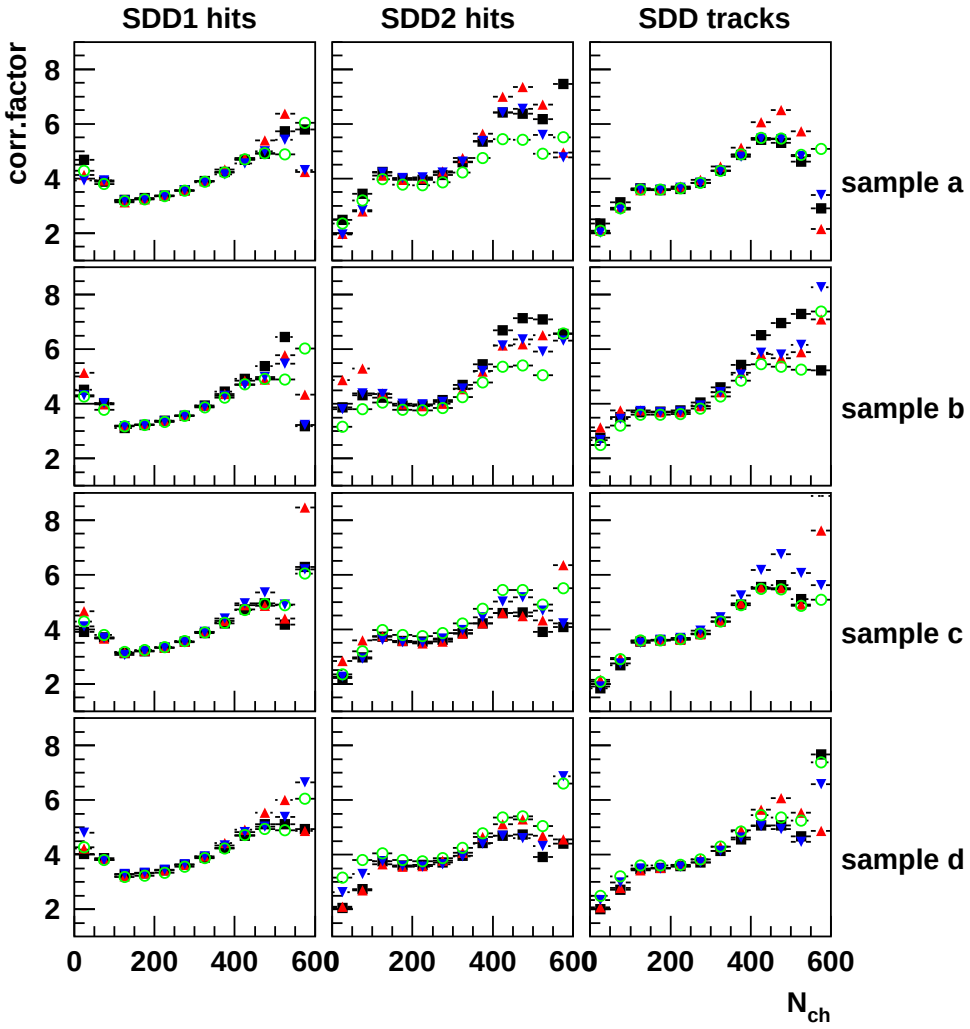

Figure 9.10: Centrality dependence of the 3 possibilities of the event plane resolution correction factor of the second Fourier harmonics event plane determined from SDD1 hits (left), SDD2 hits (middle) and SDD tracks (right) and different samples (from top to bottom) after correction for 'non-flow' effects between samples. For completness are also shown correction factors calculated according to Eq. (9.20) (open circles).

9.4 Extraction of the Flow Signal

Let us here explain how is the flow signal extracted. As already mentioned, in order to avoid autocorrelation effects we have to be careful which of four possible event planes in a given event to use. Since we have four samples, there exists always a pair of samples which is separated by another sample and is free of the autocorrelation effects. This means, if a particle of interest belongs to the sample a, we correlate it with the event plane determined in the sample c and analogically for other combinations. The measured flow values are in each sample corrected with the corresponding correction factor for the event plane resolution. The final flow value is obtained by averaging over the samples. For the determination of directed flow we use the event plane of the first Fourier harmonics,

and for the elliptic flow the second Fourier harmonics event plane, respectively.

9.4.1 Flow Signal in the Monte-Carlo Simulation

Before coming to the evaluation of the flow signal in the data, let us prove that in the Monte-Carlo simulation, which includes all known detector deffects and geometrical offsets, we obtain the flow value which was used as an input, namely $v_2 = 4.0$ %. The elliptic flow values obtained from the simulation after applying the flattening procedure (cf. Section 9.2.2) and corrections for the event plane resolution (cf. Section 9.3) for all three possibilities of the event plane determination, are listed in Table 9.2. They are all within the errors consistent with the input value. Thus, we can be sure that all correction procedures applied lead to correct flow results, even in the case of the large distortions of the measured event plane distribution.

event plane determination	v_2 [%]
ideal	4.0
SDD1 hits	4.090±0.041
SDD2 hits	4.012±0.045
SDD tracks	4.050±0.047

Table 9.2: Values of the elliptic flow obtained in the simulation for the three different event plane determinations.

9.4.2 Flow Signal in the Data

An example of the measured azimuthal distribution is shown in Fig. 9.11 for charged particles with respect to the first and second Fourier harmonics event plane determined from the sample a in semi-central collisions (centrality class 1). Both distributions are integrated over the transverse momentum and pseudo-rapidity. The data show a cosine shape typical for anisotropic flow. The distribution of particles with respect to the first Fourier harmonics event plane has maximum at $\phi - \Psi_1^a = 0$, which means that the directed flow is oriented in the event plane. This is in line with our expectations because we measure left from the mid-rapidity. Elliptic flow is also oriented in the event plane as confirmed from the observed maxima of the azimuthal distribution with respect to the second Fourier harmonics event plane at $\phi - \Psi_2^a = 0$ and $\phi - \Psi_2^a = \pi$.

The results on directed flow measured by the CERES experiment can be found in [76, 90]. Below we concentrate only on the analysis of elliptic flow, which is analyzed with respect to the event plane determined from the SDD tracks. The values of elliptic flow agree very well with each other for the event plane determined from the SDD1 and the SDD2 hits. The elliptic flow obtained from the correlations with respect to the event plane reconstructed from the SDD tracks is about 15–20% higher than from the hit event planes. Our explanation of this effect is that our effort to account for the additional 'non-flow' correlations between samples due to the hit splitting as described in Chapter 9.3.1 is not realistic enough. But still, the confirmation of the results obtained from correlations with respect to event plane determined in two different ways is satisfactory.

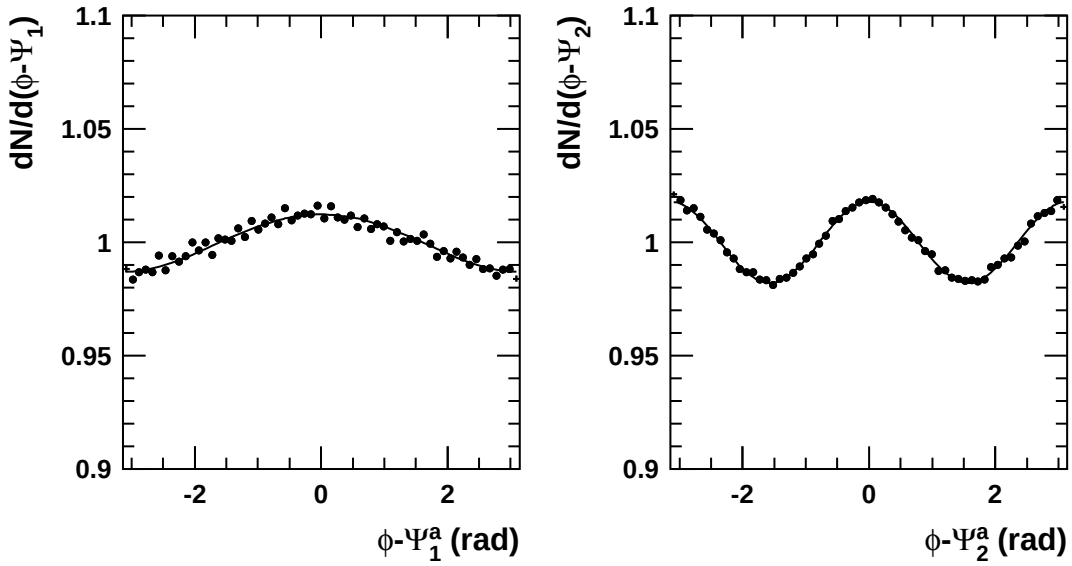

Figure 9.11: Example of experimental azimuthal distributions of $h^{\pm}$ integrated over transverse momentum and pseudo-rapidity in semi-central collisions with respect to the first (left) and the second (right) Fourier harmonics event plane determined from the SDD1 hits in the sample a.

9.5 Results

9.5.1 Differential Elliptic Flow of $h^{\pm}$ and High-p_T Pions

Since the elliptic flow is constant within the small CERES pseudo-rapidity coverage of $2.1 < \eta < 2.65$, we study in detail only its centrality and transverse momentum dependence. The centrality dependence of the v_2 parameter is shown separately for charged hadrons and identified pions in Fig. 9.12. For $h^{\pm}$ were the data integrated over the p_T

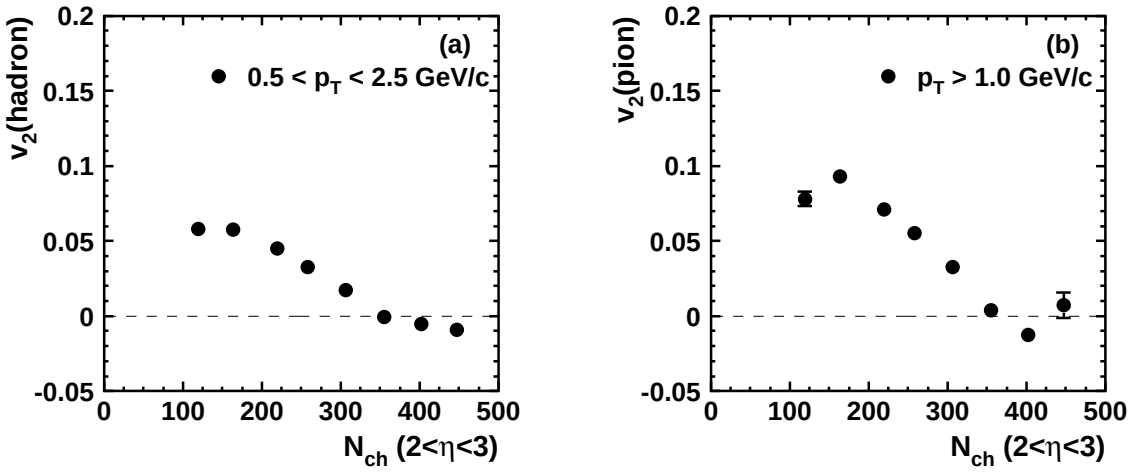

Figure 9.12: Centrality dependence of v_2 for charged hadrons (a) and high-p_T pions (b).

range of (0.5-2.5) GeV/c. For pions the transverse momentum cut of $p_{\mathrm{T}} > 1.0$ GeV/c was used. In both cases, we observe a linear decrease of the elliptic flow magnitude with centrality. In the most central collisions values of v_2 have to approach zero since there is no more asymmetry in the transverse plane present. However, in the most central bins are the v_2 values slightly negative. This is caused by the poor event plane resolution in very central collisions. The systematic uncertainties in v_2 are mainly caused by the finite event plane resolution which is quantified by the spread in the correction factors. We have estimated the absolute systematic errors in v_2 to vary between 0.005 for the most peripheral events, to 0.015 for the most central events.

Comparing the v_2 magnitudes for charged particles, where low p_T selection is applied, with those for high-p_T pions in the same centrality bins, we can infer that the magnitude of elliptic flow is increasing with transverse momentum. The dependence of v_2 on transverse momentum is shown for three different centrality classes in Fig. 9.13 for charged particles

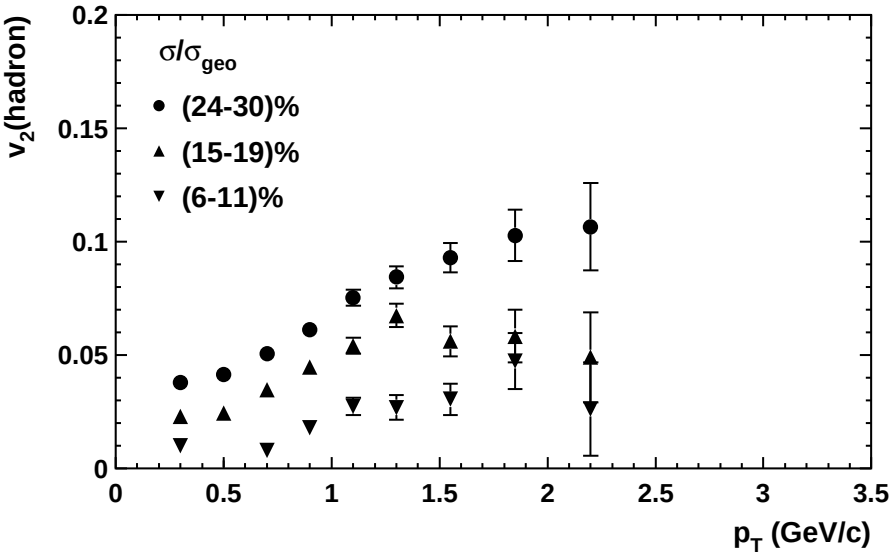

Figure 9.13: Transverse momentum dependence of v_2 for charged hadrons in three centrality selections.

and in Fig. 9.14 for high-p_T pions, respectively. Indeed, in all presented centralities the strength of v_2 is increasing linearly with p_T with a trend to level off at $p_T \approx 1.5$ GeV/c.

This trend is more pronounced if we combine the data on charged hadrons, which are from 85% compound from pions (cf. Table 8.1), and high-p_T pions together. In order to decrease the statistical errors we have integrated the data over the first three centrality classes. This corresponds to the fraction of the geometric cross section of $\sigma/\sigma_{\mathrm{geo}} =$ (15-30)%. The combined results are shown in Fig. 9.15. The transverse momentum dependence of v_2 is measured for the first time at the SPS with good statistics from low transverse momenta up to $p_T = 3$ GeV/c. Charged particles with $p_T < 0.3$ GeV/c were discarded from the elliptic flow analysis due to high background contamination, which cannot be corrected for on contrary to the analysis of the transverse momentum distributions.

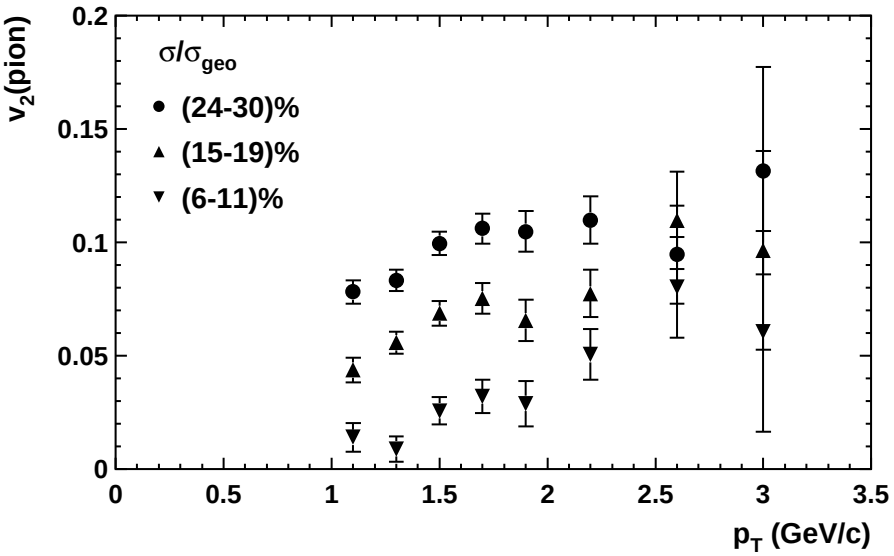

Figure 9.14: Transverse momentum dependence of v_2 for identified pions in three centrality selections.

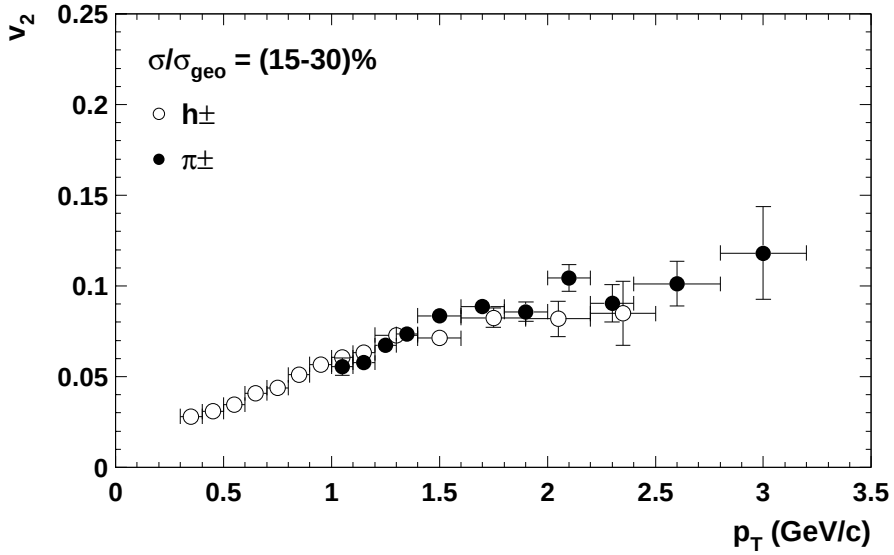

Figure 9.15: Transverse momentum dependence of v_2 in semi-central collisions combined for charged hadrons (open circles) and identified pions (full circles).

9.5.2 Effects of HBT Correlations on Flow Measurement

Various non-flow effects influence the flow measurement and have to be accounted for. Transverse momentum conservation influences only directed flow [197], which is not discussed in this work. The effect of resonance decays is not very clear at present, and here is no procedure available. We will discuss in this section the effects resulting from quantum HBT correlations following [198].

Since about 85% of particles produced in a Pb-Au collision at 158A GeV/c are pions, we can expect that subsamples become partially correlated due to the HBT effect among identical pions if one pion of the HBT pair belongs to one sample and the second one into the neighboring one. The HBT effect produces a space-momentum correlation between two pions (of the same charge), if the product of their momentum difference and the source radius R is below the uncertainty limit, i.e. $|\mathbf{p_2} - \mathbf{p_1}| \lesssim \hbar/R$. In semi-central collisions, R is typically 4–5 fm (cf. Table 9.3), and consequently $1/R \sim 50$ MeV/c is much smaller than $\langle p_T \rangle \sim 400$ MeV/c. The HBT effect thus correlates only pion pairs with low relative momenta. Moreover, the azimuthal correlation due to the HBT effect is short-ranged and is significant only if $|\phi_2 - \phi_1| \lesssim 1/(Rp_T) \sim 0.1$. For pions as bosons the correlation is positive as flow itself, and therefore applying the flow analysis to the HBT correlations would result in a spurious flow.

Let us first introduce the notation used. Following [198] any two-particle distribution can be generally written as

$$\frac{dN}{d^3\mathbf{p_1}d^3\mathbf{p_2}} = \frac{dN}{d^3\mathbf{p_1}}\frac{dN}{d^3\mathbf{p_2}}\left(1 + C(\mathbf{p}_1, \mathbf{p}_2)\right), \tag{9.30}$$

where $C(\mathbf{p}_1, \mathbf{p}_2)$ is the two-particle correlation function, which vanishes for independent particles. The Fourier coefficients of order n of the relative azimuthal distribution are given by

$$c_n(p_{T1}, y_1, p_{T2}, y_2) \equiv \langle \cos n(\phi_1 - \phi_2) \rangle = \frac{\iint \cos n(\phi_1 - \phi_2) \frac{dN}{d^3\mathbf{p}_1 d^3\mathbf{p}_2} d\phi_1 d\phi_2}{\iint \frac{dN}{d^3\mathbf{p}_1 d^3\mathbf{p}_2} d\phi_1 d\phi_2}. \tag{9.31}$$

We can write c_n as the sum of two terms,

$$c_n(p_{T1}, y_1, p_{T2}, y_2) = c_n^{\text{flow}}(p_{T1}, y_1, p_{T2}, y_2) + c_n^{\text{non-flow}}(p_{T1}, y_1, p_{T2}, y_2), \tag{9.32}$$

where the first term is due to collective flow

$$c_n^{\text{flow}}(p_{T1}, y_1, p_{T2}, y_2) = v_n(p_{T1}, y_1) v_n(p_{T2}, y_2), \tag{9.33}$$

and the remaining results from any direct two-particle correlation,

$$c_n^{\text{non-flow}}(p_{T1}, y_1, p_{T2}, y_2) = \frac{\iint \cos n(\phi_1 - \phi_2) C(\mathbf{p}_1, \mathbf{p}_2) \frac{dN}{d^3\mathbf{p}_1} \frac{dN}{d^3\mathbf{p}_2} d\phi_1 d\phi_2}{\iint \frac{dN}{d^3\mathbf{p}_1 d^3\mathbf{p}_2} d\phi_1 d\phi_2}. \tag{9.34}$$

Let us denote the average value of c_n over (p_{T2}, y_2) in the domain $\mathcal{D}$ by $c_n(p_{T1}, y_1, \mathcal{D})$, and the average over both (p_{T1}, y_1) and (p_{T2}, y_2) by $c_n(\mathcal{D}, \mathcal{D})$. Averaging now Eq.(9.33) over (p_{T1}, y_1) and (p_{T2}, y_2) in the domain $\mathcal{D}$, we obtain:

$$v_n(\mathcal{D}) = \pm\sqrt{c_n(\mathcal{D}, \mathcal{D})}. \tag{9.35}$$

Finally, integrating Eq. (9.33) over (p_{T2}, y_2), and using Eq. (9.35), we get the expression for differential $v_n(p_T, y_1)$ as a function of the Fourier coefficient c_n

$$v_n(p_{T1}, y_1) = \pm\frac{c_n(p_{T1}, y_1, \mathcal{D})}{\sqrt{c_n(\mathcal{D}, \mathcal{D})}}. \tag{9.36}$$

Let us come back to the non-flow contribution from the HBT effect. For the parametrization of the HBT correlation function we use the standard Bertsch-Pratt Gaussian parametrization [199, 200]

$$C(\mathbf{p}_1, \mathbf{p}_2) \propto \lambda e^{-q_{side}^2 R_{side}^2 - q_{out}^2 R_{out}^2 - q_{long}^2 R_{long}^2} \tag{9.37}$$

and we choose the so called 'longitudinal co-moving system' (LCMS), which is the frame boosted along the beam axis such that $p_{1z} + p_{2z} = 0$. In this frame, q_{long}, q_{out}, and q_{side} denote the projections of $\mathbf{p}_2 - \mathbf{p}_1$ along the beam axis, the direction of $\mathbf{p}_1 + \mathbf{p}_2$ and the third direction, respectively. The corresponding parameters R_{side}, R_{out}, and R_{long} describe the source dimensions. The remaining parameter λ is the so called chaoticity parameter and it was introduced to describe the coherence of the particle source. Experimentally, the λ parameter is influenced by decays of long-lived resonances, momentum resolution, and by contamination from particle pairs in which at least one of the two particles is not a primary pion. For the chosen HBT parametrization, the correlation function yields [198]

$$c_n^{\mathrm{HBT}}(p_{T1}, y_1, \mathcal{D}) = \frac{\lambda\pi^{3/2}}{R_{side}R_{out}R_{long}} \exp\left(-\frac{n^2}{4p_{T1}^2 R_{side}^2}\right) \frac{\frac{1}{m_{T1}}\frac{dN}{d^2\mathbf{p_{T}}_1 dy_1}}{\int_{\mathcal{D}} \frac{dN}{d^2\mathbf{p_{T}}_2 dy_2} d^2\mathbf{p_{T}}_2 dy_2}. \tag{9.38}$$

At $p_T \sim 1/R$ the exponential term has to be substituted by

$$\exp\left(-\frac{n^2}{4\chi^2}\right) \to \frac{\sqrt{\pi}}{2}\chi e^{-\chi^2/2}\left(I_{\frac{n-1}{2}}\left(\frac{\chi^2}{2}\right) + I_{\frac{n+1}{2}}\left(\frac{\chi^2}{2}\right)\right), \tag{9.39}$$

where $\chi = R_{side}p_T$ and I_k is the modified Bessel function of order k. Numerical estimates were upto now performed only for the data measured by the NA49 experiment [198] and we will use the same approach. Assuming for simplicity that the p_T and y dependence of the particle distribution factorize, we can parametrize the rapidity distribution of charged pions as

$$\frac{dN}{dy} = \frac{1}{\sigma\sqrt{2\pi}} \exp\left(-\frac{(y - y_{mid})^2}{2\sigma^2}\right) \tag{9.40}$$

with $\sigma = 1.4$ and mid-rapidity $y_{mid} = 2.9$. The normalized p_T distribution is parametrized by

$$\frac{dN}{d^2\mathbf{p_T}} = \frac{e^{m/T}}{2\pi T(m + T)} \exp\left(-\frac{m_T}{T}\right). \tag{9.41}$$

σ/σ_{geo} (%)	$\lambda \pm \Delta\lambda$	$R_{long} \pm \Delta R_{long}$ (fm)	$R_{side} \pm \Delta R_{side}$ (fm)	$R_{out} \pm \Delta R_{out}$ (fm)
15–20	0.199±0.003	4.89±0.07	4.00±0.05	4.38±0.06
10–15	0.190±0.003	5.05±0.06	4.09±0.04	4.56±0.05
5–10	0.187±0.002	5.26±0.05	4.42±0.04	4.94±0.05
<5	0.189±0.002	5.63±0.05	4.70±0.03	5.31±0.04

Table 9.3: Centrality dependence of the HBT parameters in Pb-Au collisions at 158A GeV/c integrated over pion pair transverse momentum k_T.

with $T \simeq 180$ MeV from [152]. This parametrization underestimates the number of low-p_T pions. The values of λ, R_{out}, R_{side} and R_{long} used in our computations were obtained from the CERES HBT data [119,185] after integrating over the transverse pair momentum k_T [201]. Their values for four centrality selections are summarized in Table 9.3.

Substituting the correlation calculated from Eq. (9.38) into Eq. (9.36), we obtain the spurious flow due to the HBT effect which we denote v_n^{HBT}. The domain $\mathcal{D}$ is in our case the acceptance of the silicon drift detectors $1.9 < y < 3.1$. We assume that the charged particles in $\mathcal{D}$ are from 85% charged pions, half π^+, half π^-. To obtain the apparent HBT flow of an identified pion, e.g. π^-, the right hand side of Eq. (9.36) has to be multiplied by a factor expressing probability that a particle in $\mathcal{D}$ is also π^-. As can be easily viewed, this multiplicative factor is 0.85 × 0.5.

Fig. 9.16 demonstrates its dependence on the transverse momentum for the first two Fourier harmonics. As expected, v_n^{HBT} depends on the order of the Fourier harmonics n only at low p_T, where it vanishes due to the exponential factor in Eq. (9.38). HBT correlations, which follow the momentum distribution, also vanish if p_T is much larger than the average transverse momentum. It is due to this behavior that the HBT effect influence the elliptic flow values only for p_T < 0.4 GeV/c while its influence is negligible for higher transverse momenta. However, keeping in mind that the event plane is determined from all charged particles without momentum cut, there remains influence on the event plane determination. The HBT effect improves the event plane resolution so that values of the correction factors for finite event plane resolution are underestimated.

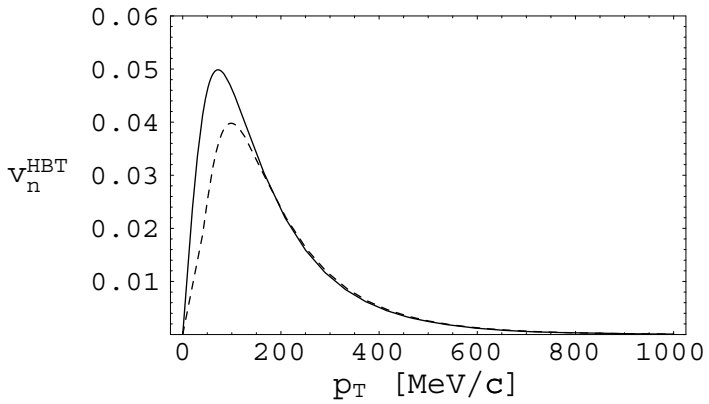

Figure 9.16: Apparent directed (full line) and elliptic (dashed line) flow from HBT correlations as a function of transverse momentum.

The elliptic flow values corrected for the HBT effect are then obtained using relation

$$v_2(p_T)^{corrected} = \frac{v_2(\mathcal{D})v_2(p_T) - v_2^{HBT}(\mathcal{D})v_2^{HBT}(p_T)}{\sqrt{(v_2(\mathcal{D}))^2 - (v_2^{HBT}(\mathcal{D}))^2}}. \tag{9.42}$$

The integrated spurious flow $v_2^{HBT}(\mathcal{D})$ reaches values of 0.9% for the most central collisions and 1.3% for our most peripheral centrality class. As follows from Eq. (9.42), for values $|v_2(\mathcal{D})| \leq |v_2^{HBT}(\mathcal{D})|$ is the denominator negative. Consequently, in such case is the applicability of the HBT correction questionable.

Qualitatively we expect from Eq. (9.42) that the correction factors will change the sign and become negative at small p_T. At $p_T > 0.5$ GeV/c, where the direct contribution from v_2^{HBT} is negligible, there is only a common relative HBT correction factor. Dependence of these relative correction factors on $v_2(\mathcal{D})$ for the centrality classes listed in Table 9.3 is shown in Fig. 9.17 by the full lines. Since the HBT parameters were measured by TPC, not by the silicon drift detectors used for the event plane determination, one can expect that the value of λ parameter does not need to be exactly the same, since it depends on the detector resolution. Varying λ by $\pm$50%, and taking into account also measured uncertainties in the R_{long}, R_{side}, and R_{out} parameters we have obtained the relative correction factors indicated by the dashed lines in Fig. 9.17. For the transverse momenta $p_T < 0.5$ GeV/c, where the direct HBT contributions cannot be neglected, the HBT correction factors have to be evaluated at each p_T point separately.

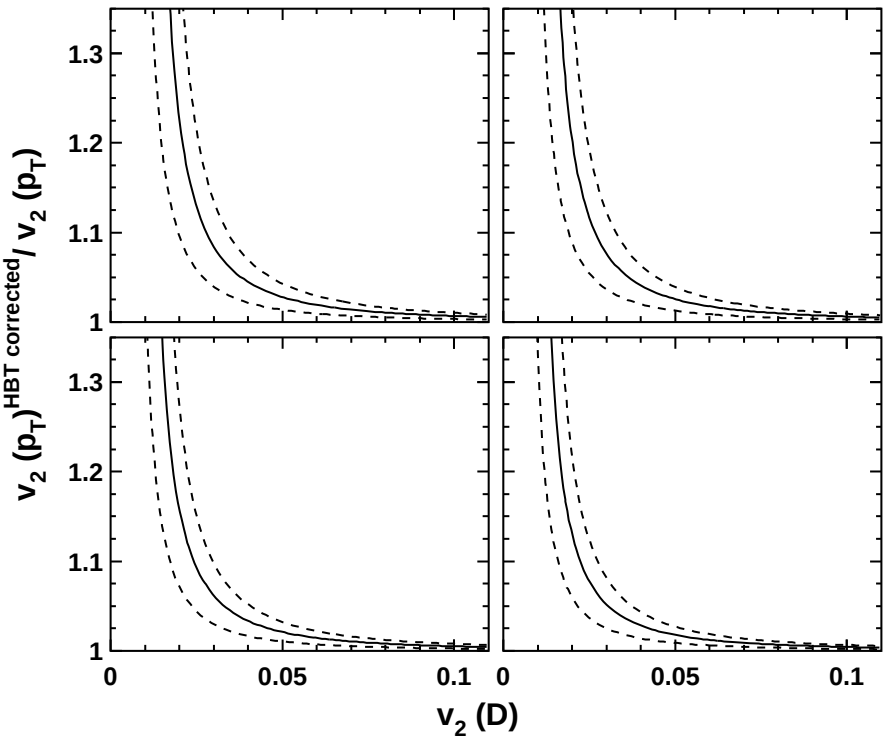

Figure 9.17: Dependence of the relative HBT correction factors on $v_2(\mathcal{D})$ for pions with $p_T > 0.5$ GeV/c in the centrality classes given by Table 9.3 (full lines). The dashed lines indicate the upper and lower boundaries estimated from the uncertainties in the HBT parameters.

The relative corrections in semi-central collisions were found to vary between -15% of v_2 at $p_T = 0.25$ GeV/c and +10% of v_2 at $p_T > 1.0$ GeV/c. The HBT corrected transverse momentum dependence of v_2 is shown in Fig. 9.18 below.

9.5.3 Comparison with Other Experiments

The elliptic flow was studied also by other experiments at the SPS. Here, we compare to the recently available data from Pb-Pb collisions measured by the NA49 experiment [91] in the rapidity range of $1.1 < y < 3.1$. Their transverse momentum dependence of v_2 in semi-central collisions is presented in Fig. 9.18 together with our results. The errors shown are only statistical. The authors give a systematic error of $\Delta v_2 = 0.005$. We observe a very good agreement between both experiments for $p_T < 0.5$ GeV/c. At higher transverse momenta our v_2 data show a different slope than those of NA49. This results in an average discrepancy of about 25% for $1.0 < p_T < 2.0$ GeV/c. At this stage of analysis, the reason for this discrepancy between our results and that of NA49 is not understood. It requires to evaluate the NA49 data in a smaller rapidity interval corresponding to the CERES acceptance as well as revisiting of the centrality measurement between the two experiments. Since the elliptic flow magnitude falls steeply with increasing centrality, a difference in the centrality estimation could lead to the observed discrepancy. The centrality dependence of elliptic flow measured by the NA49 experiment decreases about linearly with centrality as our data. However, due to different p_T cuts applied a direct quantitative comparison is not possible.

We compare our v_2 results also to the measurements done at RHIC. The transverse momentum dependence of v_2 measured by the STAR experiment [202] in Au-Au collisions at $\sqrt{s} = 200$ GeV is shown in Fig. 9.19 for three centrality selections. We observe that our transverse momentum dependence of v_2 has certain similarities with the RHIC

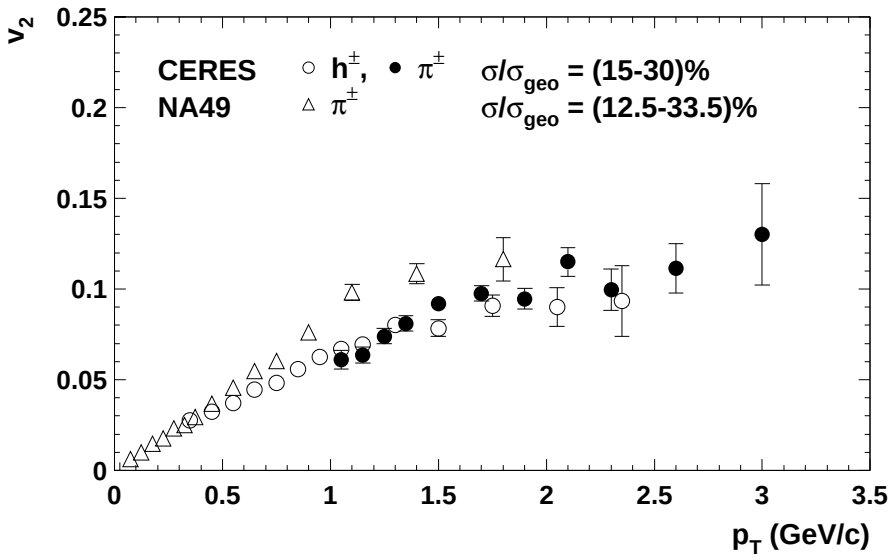

Figure 9.18: Transverse momentum dependence of elliptic flow in semi-central Pb-Au (Pb-Pb) collisions measured by the CERES (NA49) experiment.

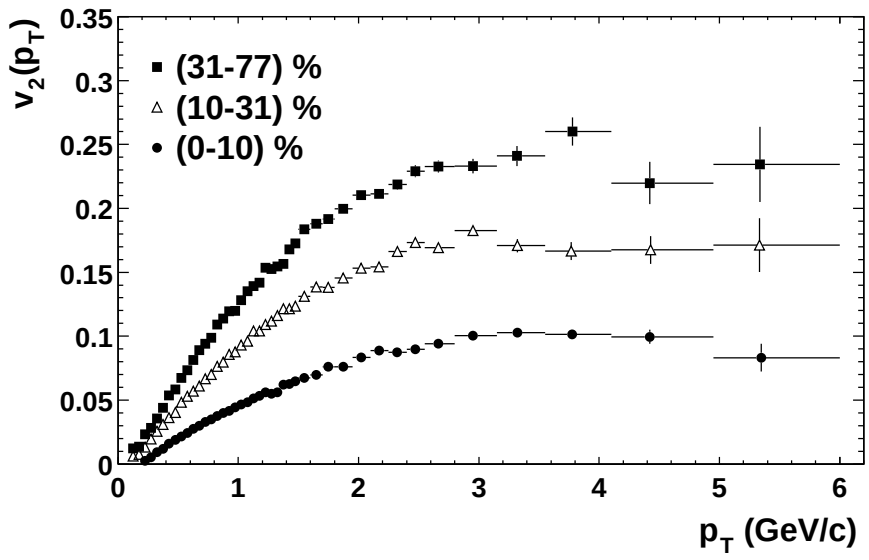

Figure 9.19: Transverse momentum dependence of elliptic flow of charged particles for three centrality selections measured by the STAR experiment at RHIC ($\sqrt{s} = 200$ GeV).

data, albeit the magnitude of elliptic flow at the SPS is smaller. Up to $p_T \approx 1.5$ GeV/c, the elliptic flow at RHIC energy increases its magnitude about linearly and then it starts to level off and eventually saturates at $p_T > 3$ GeV/c.

9.5.4 Comparison with Hydrodynamical Models

Elliptic flow reflects the rescattering among particles produced in a heavy-ion collision which transfers the initial spatial anisotropy of the nuclear overlap region in the transverse plane to the observed distribution of particle yields. For a given initial spatial deformation, the largest elliptic flow is obtained in the hydrodynamical limit where rescattering is so intense that the matter in the reaction zone reaches a state of local thermal equilibrium. Since the spatial anisotropy is largest at the beginning of the evolution and decreases thereafter due to flow itself, the magnitude of elliptic flow is especially sensitive to the early stages of the evolution [26]. A measurement of v_2 thus provides access to the fundamental thermalization time scale in the early stages of a relativistic heavy-ion collision.

We compare our results on elliptic flow to ideal hydrodynamical calculations of P. Huovinen [203] based on [204] and adjusted to our centrality and p_T selections. Since the full hydrodynamic treatment of a non-central collision is a tedious 3+1 dimensional problem, the authors reduced its complexity to 2+1 dimensions by assuming boost-invariant longitudinal flow. The evolution of the system is determined by conditions and the equation of state. The initial conditions were fixed by requiring a good fit to the p_T-spectra of negative charged particles and protons in central Pb-Pb collisions at the SPS [205]. The calculations were performed for the equation of state with the first order phase transition to QGP at the temperature $T = 165$ MeV and freeze-out at $T_f = 120$ MeV. The differences in the calculations for a pure hadron gas and freeze-out at $T_f = 140$ MeV are only marginally

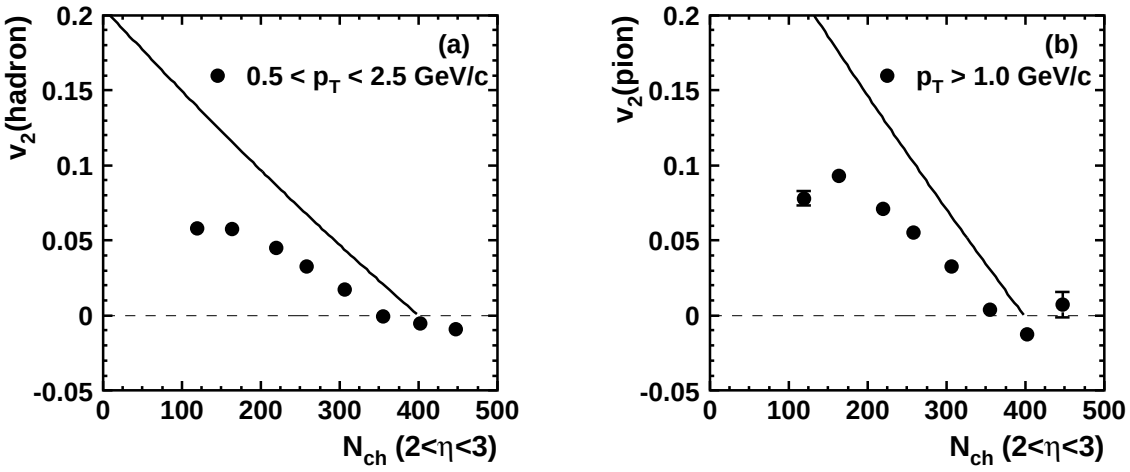

Figure 9.20: Centrality dependence of v_2 for charged hadrons (a) and pions (b).

different.

The centrality dependence of v_2 in the data and in these calculations is compared in Fig. 9.20. We can observe, that the magnitude of v_2 remains well below the expected hydrodynamical values, both for charged hadrons and high-p_T pions. The discrepancy is in both cases increasing with decreasing centrality.

We turn now to the transverse momentum dependence of v_2. Since the difference in v_2 magnitude between hadrons and pions is very small and it is within the errors of our measurement, we compare the data in semi-central collisions to hydrodynamical calculation performed for pions. As can be seen from Fig. 9.21, the data are again significantly

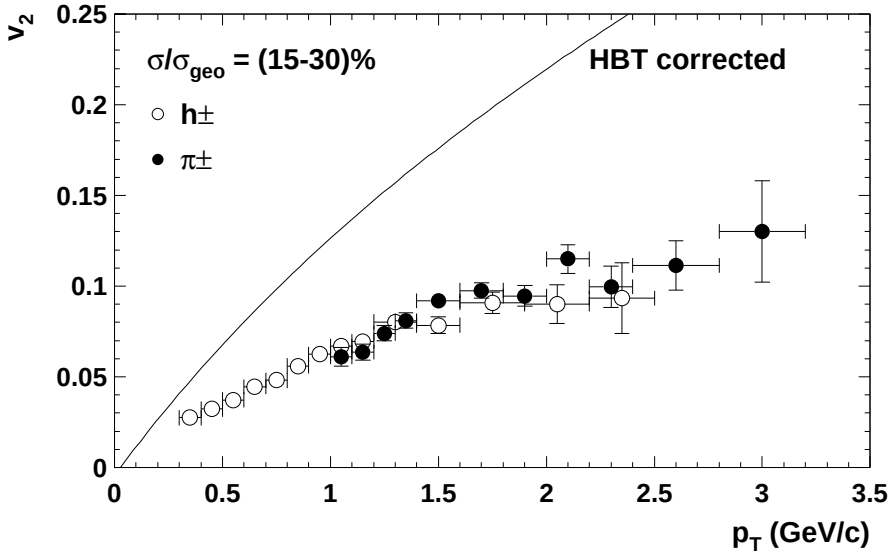

Figure 9.21: Comparison of the transverse momentum dependence of v_2 in semi-central collisions with the hydrodynamical predictions (full line). The data points correspond to charged hadrons (open circles) and pions (full circles), respectively. Correction for the HBT effects is applied.

below the hydrodynamical expectations and the observed discrepancy is increasing with p_T. At $p_T = 1$ GeV/c the model predicts $v_2 = 12\%$ while the data are close to v_2 = 7%.

A better agreement with the data can be naturally reached for a higher freeze-out temperature of $T_f = 160$ MeV [206], which may as well be consistent with the freeze-out parameters extracted from the inclusive transverse mass distributions (cf. Chapter 8.3.6) and freeze-out densities of hadrons [37, 207, 208]. Such calculations predict v_2 = 10% at $p_T = 1$ GeV/c. The authors of [206] has also shown that similar results can be obtained by coupling the above discussed hydrodynamical model with $T_f = 120$ MeV to a transport model. In both cases, the data would still remain below the calculations. Another possibility to reduce the magnitude of elliptic flow in calculations is a recently introduced hydrodynamical model including viscosity [209, 210]. This model has been up to now only applied for RHIC energies, and calculations for SPS energies are not yet available. Given these facts, the hydrodynamical models tend to overestimate elliptic flow at the highest SPS energy which suggests that thermalization is achieved only partially.

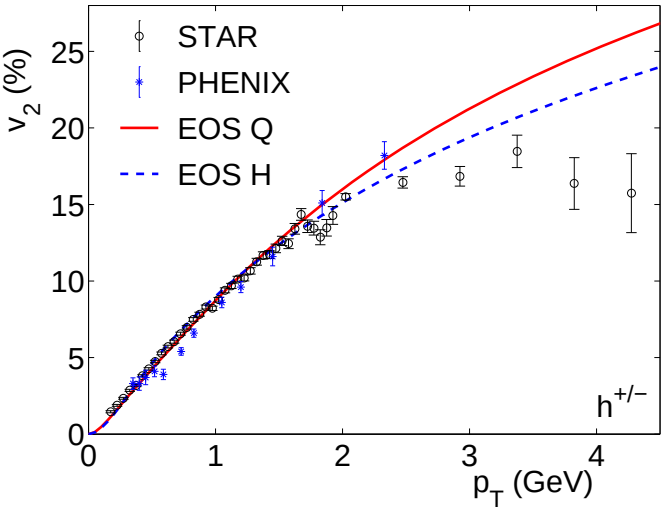

Figure 9.22: Comparison of the transverse momentum dependence of v_2 for charged particles at mid-rapidity in minimum bias collisions at $\sqrt{s} = 130$ AGeV with hydrodynamical calculations. The figure is taken from [211].

This discussion would be incomplete without referring to a comparison to transverse momentum dependence of elliptic flow measured at RHIC energies with hydrodynamical calculations. The data measured by the STAR [92, 93, 212] and PHENIX [213] collaborations at $\sqrt{s} = 130$ AGeV are compared in Fig. 9.22 to the hydrodynamical calculations with a first order phase transition (EOS Q) and without it (EOS H). The kinetic freeze-out temperature was fixed to $T_f = 130$ MeV [211]. In marked contrast to the situation at the SPS, the RHIC the data exhaust the hydrodynamical calculations below $p_T = 2$ GeV/c and fall below only for high transverse momenta.

9.5.5 Scaled Elliptic Flow

Elliptic flow reflects both the spatial asymmetry of the overlap zone and the response of the system to pressure gradients created in the course of a heavy-ion collision. As pointed out in [214] one may try to disentangle the purely geometric effects from the dynamics by studying the properties of the elliptic flow divided by the initial spatial asymmetry ε.

This asymmetry is defined in the framework of the Glauber model (cf. Chapter 7.3) as

$$\varepsilon = \frac{\langle y^2 \rangle - \langle x^2 \rangle}{\langle y^2 \rangle + \langle x^2 \rangle}, \tag{9.43}$$

where $\langle x^2 \rangle$ and $\langle y^2 \rangle$ describe the initial geometrical extension of the system in x and y directions. The brackets indicate averaging over the relevant density function under investigation. Dependence of ε on the impact parameter for participating nucleons and binary collision distributions is demonstrated in Fig. 9.23(a).

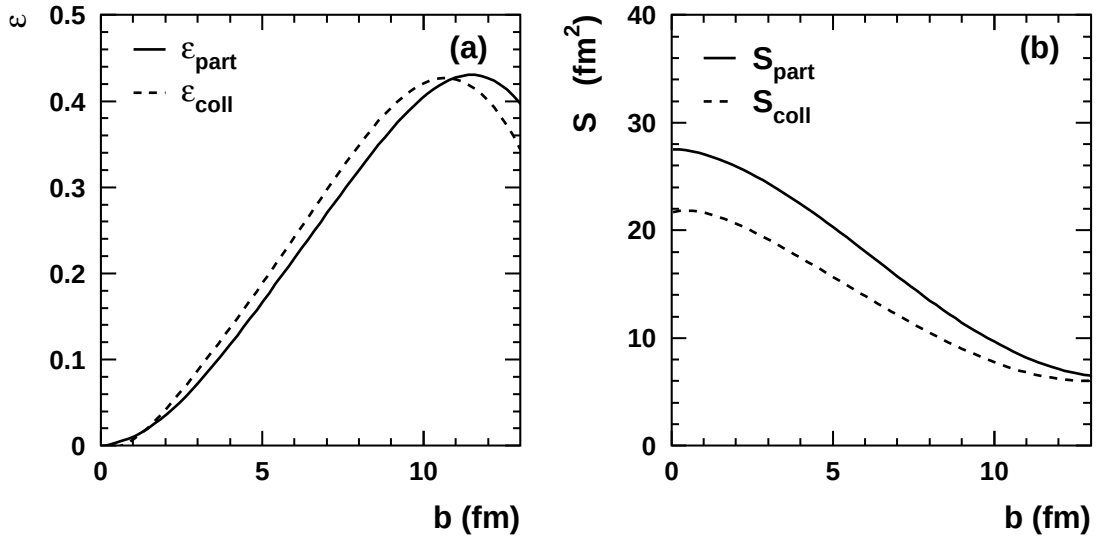

Figure 9.23: Initial spatial anisotropy (a) and the area (b) of the initial overlap zone in the participant and binary collision distributions for Pb-Au collisions at $\sqrt{s} = 17$ AGeV.

In the hydrodynamical limit, the mean free path is much smaller than the system size, and the centrality dependence of elliptic flow is governed by the eccentricity ε. In the other limiting case, the so called *low density limit (LDL)* applicable for dilute systems, the mean free path is comparable or larger than the system size. Rescattering during the evolution changes the particle momenta on average therefore only very little. Consequently, the corresponding change in the distribution functions can be treated as a first order perturbation to the collisionless limit [215]. Under this assumption, elliptic flow is proportional to the initial particle space density dN/dy, which is related to the probability of particles to rescatter, and to the initial spatial anisotropy of overlap region ε,

$$v_2 \propto \varepsilon \frac{1}{S} \frac{dN}{dy}. \tag{9.44}$$

The parameter S is the area of the overlapping zone in the transverse plane $S = \pi R_x R_y$ with $R_x^2 = \langle x^2 \rangle$ and $R_y^2 = \langle y^2 \rangle$. Dependence of this area on the impact parameter for both above discussed density distributions is shown in Fig. 9.23(b).

We have studied the centrality behavior of the scaled elliptic flow for different p_T selections, which may provide greater sensitivity to pressure gradients and energy densities associated with the expanding system. The results are presented in Fig. 9.24 for

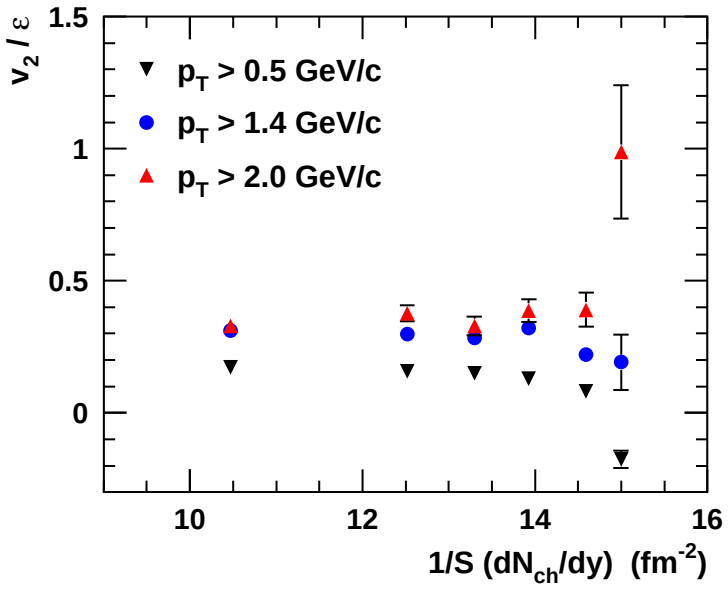

Figure 9.24: Centrality dependence of the elliptic flow divided by the initial spatial anisotropy of the overlap region (ε) for three different p_T thresholds.

$p_T > 0.5$ GeV/c, $p_T > 1.4$ GeV/c, and $p_T > 2.0$ GeV/c. The observed centrality dependence is for all three p_T selections compatible with ε scaling. Only in the last two centrality classes there seems to be an indication of different behavior for low-p_T than for high-p_T particles. The corresponding errors are however rather large. We remark that the correction factors for HBT effects (not applied, for reasons see Section 9.5.2) grow continuously with centrality and they would lead to a relative increase of the scaled elliptic flow magnitude by about 20% between our most peripheral and the most central class.

10

Two-Particle Azimuthal Correlations

In this chapter a study of azimuthal correlations of two high-p_T pions is presented with an aim to disentagle possible contributions of semi-hard processes from collective dynamics. After the description of the method and corrections which need to be taken into account, we compare the obtained results on v_2 with those from the event-plane measurement (cf. Chapter 9). The observed discrepancy between the two methods is attributed to a 'non-flow' component of presumably semi-hard origin and we discuss its centrality and transverse momentum dependence. The study is concluded with the measurement of the degree of alignment of the semi-hard particles with respect to the reaction plane. Some of the results are published in [191, 192].

10.1 Description of the Method

In analogy to correlations of particles with respect to the reaction plane, we can write the Fourier decomposition of the pair-wise distribution in the azimuthal angle difference ($\Delta\phi = \phi_i - \phi_j$) between pairs of emitted particles as [72]

$$\frac{dN_{pairs}}{d\Delta\phi} = B[1 + \sum_{n=1}^{\infty} 2p_n \cos(n\Delta\phi)], \tag{10.1}$$

where the coefficient B corresponds to the uncorrelated pair background. To obtain the relation of the Fourier coefficients p_n to the coefficients v_n describing anisotropy of particles with respect to the reaction plane, we write the latter as

$$v_n = \mathbf{Re}\langle \mathrm{e}^{in(\phi - \Psi_R)} \rangle. \tag{10.2}$$

Then it can be easily shown that in the case of pure collective flow, the relation is $p_n = v_n^2$, i.e.

$$p_n = \mathbf{Re}\langle \mathrm{e}^{in(\phi_i - \phi_j)} \rangle = \mathbf{Re}\langle \mathrm{e}^{in(\phi_i - \Psi_R)} \mathrm{e}^{in(\Psi_R - \phi_j)} \rangle = \mathbf{Re}\langle \mathrm{e}^{in(\phi_i - \Psi_R)} \rangle \mathbf{Re}\langle \mathrm{e}^{in(\Psi_R - \phi_j)} \rangle = v_n^2. \tag{10.3}$$

Generally, however, this is not the case and we have to write (in a symbolic way)

$$p_n = v_n^2 + c_n, \tag{10.4}$$

where the coefficients c_n describe genuine particle-particle correlations.

10.2 Two-Particle Correlations Observed in the Data

The two-particle azimuthal distribution is constructed by incrementing into a spectrum event-by-event the azimuthal angle difference $\Delta\phi = \phi_i - \phi_j$ for all possible pair combinations as schematically displayed in Fig. 10.1. An example of the measured distribution

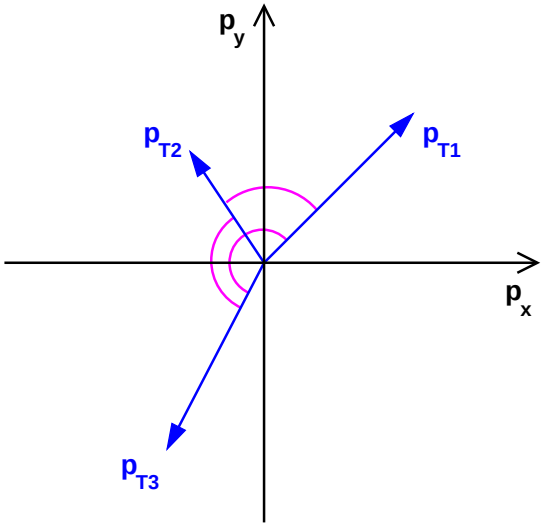

Figure 10.1: Schematic view of the construction of the two-particle azimuthal correlation function in the transverse plane.

for pion pairs with $p_T > 1.2$ GeV/c is shown in Fig. 10.2. In semi-central collisions, the measured distribution has a $\cos(2\Delta\phi)$ shape with a peak at $\Delta\phi = \pi$, which seems to disappear in central collisions. Unfortunately, the region at $\Delta\phi \approx 0$ is strongly affected by the finite two-track resolution of the spectrometer which is manifested by a dip in the

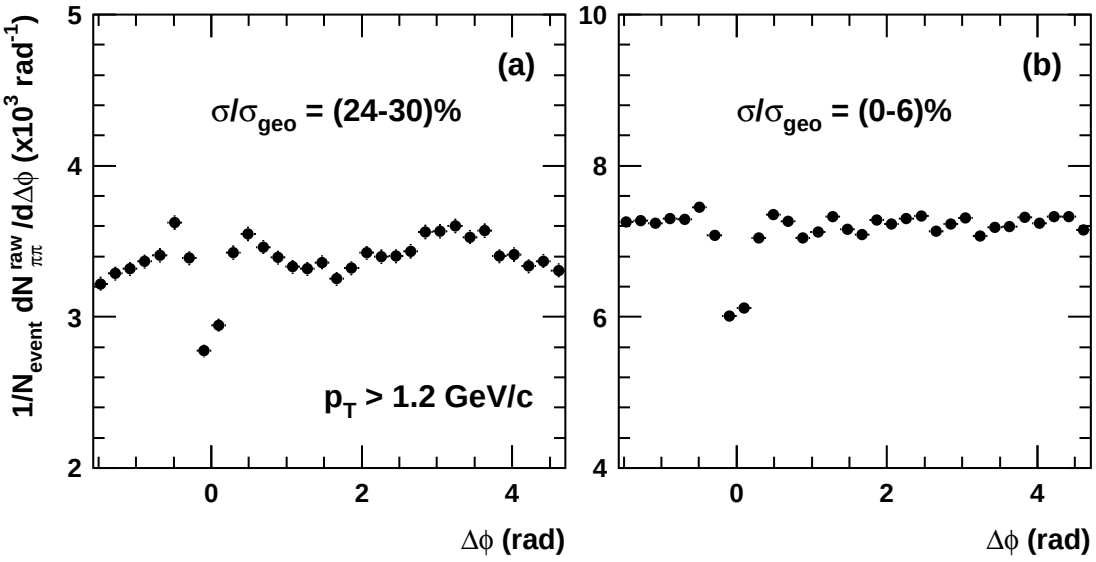

Figure 10.2: The measured azimuthal correlation for pions ($p_T > 1.2$ GeV/c) in semi-central ($\sigma/\sigma_{geo} = (24\text{-}30)\%$) (a) and central collisions ($\sigma/\sigma_{geo} < 6\%$) (b).

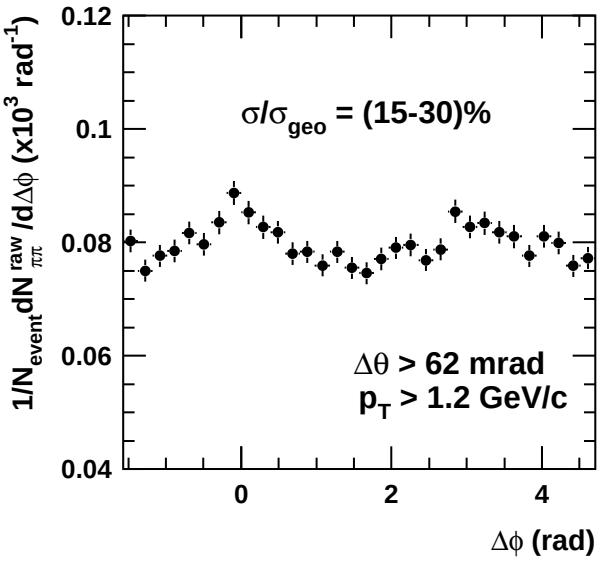

Figure 10.3: The measured azimuthal correlation for pions ($p_T > 1.2$ GeV/c) in semi-central collisions ($\sigma/\sigma_{geo} = (15\text{-}30)\%$) after applying a separation cut $\Delta\theta = 62$ mrad.

correlation function. The two-track resolution is dominated by the two-ring resolution of the RICH detectors, the magnitude of which is set by the asymptotic ring radius of about 30 mrad. It can be accounted for by using the Monte-Carlo simulations described in detail below.

An alternative way, which avoids the Monte-Carlo correction of the efficiency loss at $\Delta\phi \approx 0$ altogether, is to enforce the two rings in the RICH detectors to separate by applying a cut on polar angle difference between the pion tracks. In Fig. 10.3 the correlation function after applying $\Delta\theta = 62$ mrad cut is displayed. This cut assures full separation of the pion rings in the RICH detectors.With this provision, clearly a peak is observed also at $\Delta\phi = 0$. This method, however, suffers from poor statistics. As can be inferred from Fig. 10.4, which illustrates the relative decrease in the number of pairs as a function of the size of the $\Delta\theta$ cut, only about 10% of the data is left for the cut of $\Delta\theta = 62$ mrad.

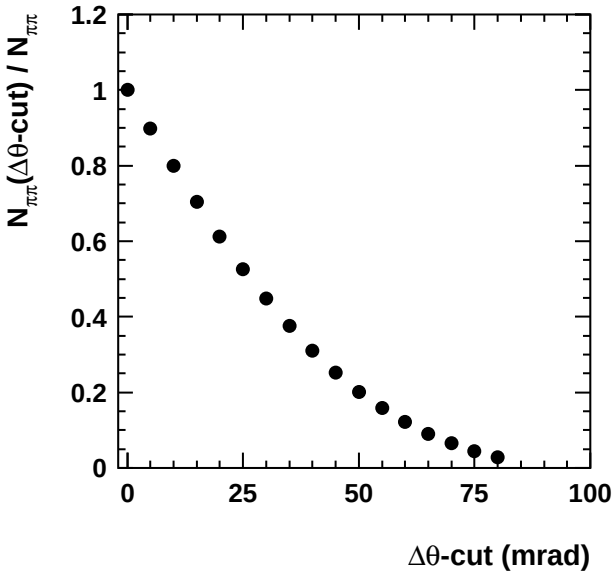

Figure 10.4: Influence of the size of $\Delta\theta$-cut between pion tracks on the number of pion pairs entering the correlation function for $p_{\mathrm{T}} > 1.2$ GeV/c.

10.3 Corrections for Momentum Resolution and Reconstruction Efficiency

The measured correlation function still have to undergo several corrections before it can be interpreted. First of all, we have to apply the momentum and reconstruction efficiency correction procedures developed in Chapter 6.4. The reconstruction efficiency of a pion pair can be found as a product of the single pion efficiencies

$$\epsilon(\pi_1, \pi_2) = \epsilon(\pi_1) \cdot \epsilon(\pi_2), \tag{10.5}$$

where π_1 and π_2 denote two pions forming the pair. This approach is valid provided the two pion tracks are sufficiently displaced to not be influenced by the finite two-track resolution of the spectrometer.

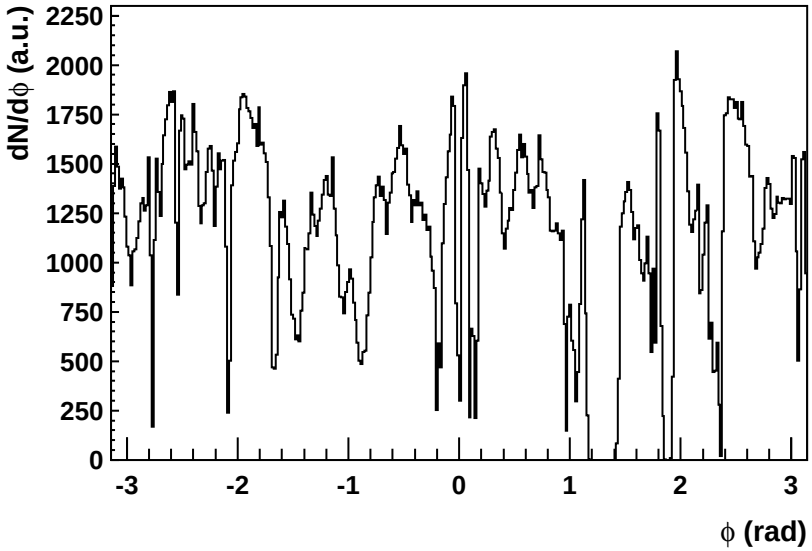

Figure 10.5: Azimuthal distribution of charged pion tracks with $p_T > 1.2$ GeV/c integrated over centrality.

Next, non-uniformities in the azimuthal acceptance could propagate to two-particle azimuthal distribution and influence thus its shape. Fig. 10.5 shows the azimuthal distribution of pion tracks with $p_T > 1.2$ GeV/c which is clearly far from being uniform. To account for this acceptance effect, we employed the mixed event method. Mixed events were obtained by randomly selecting each member of a particle pair from different events having similar charged particle multiplicity. The two-pion azimuthal distribution obtained from the mixed events and integrated over centrality is plotted in Fig. 10.6. The efficiency loss at small azimuthal angle differences ($\Delta\phi \approx 0$) is not present in this distribution. This is due to a fact that two tracks from two different events can come infinitely close to each other in space and do not suffer from the finite spectrometer resolution. Rather, the mixed event distribution has a sharp peak around $\Delta\phi = 0$ which reflects the sharp structures in the single track azimuthal acceptance.

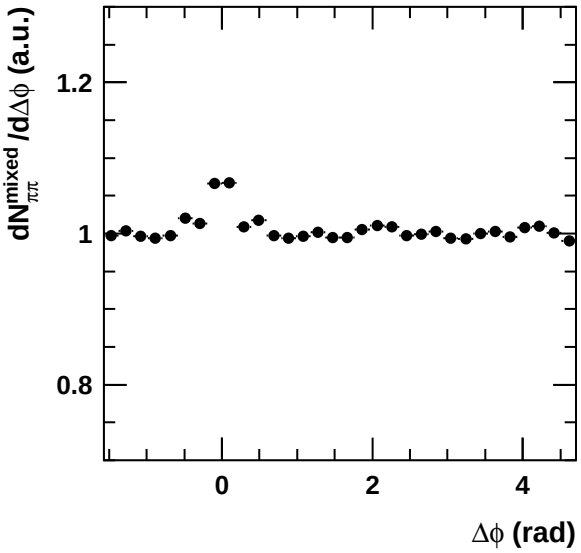

Figure 10.6: Two-particle azimuthal correlation obtained in the mixed event method for $p_T > 1.2$ GeV/c and integrated over all centralities.

In order to obtain the proper correction function, full Monte-Carlo simulations of the region $\Delta\phi \approx 0$ are required. We have tracked uncorrelated pion pairs displaced by $|\Delta\phi| \leq \pi/2$ through the GEANT simulation of the CERES spectrometer and embedded them into the measured events. This correction was determined in an iterative way in order to reproduce the measured transverse momentum, θ and ϕ distributions. After this correction, all observables show the proper distributions as in the experiment. The remaining part of the $\Delta\phi$ region, which is not affected by the finite two-ring resolution, is corrected by the mixed event method, which has also advantage of high statistics and

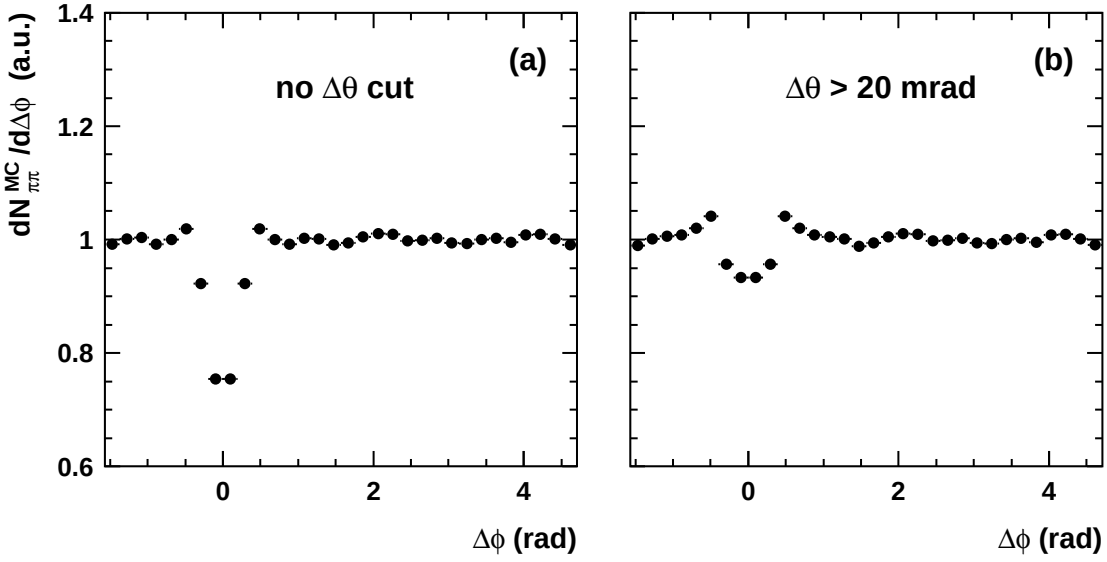

Figure 10.7: Combined two-particle azimuthal correlation obtained from the Monte-Carlo simulations in $|\Delta\phi| < \pi/2$ and in the mixed event method without (a) and with (b) the cut on polar track separation $\Delta\theta > 20$ mrad.

does not introduce additional statistical errors. The two correction functions, the simulated one and that from the mixed event method, are then smoothly connected to each other at $|\Delta\phi| \approx 1$ rad. The combined correction function is shown in Fig. 10.7. The correction for the pair efficiency according to Eq. (10.5) is done independently.

The azimuthal distribution in semi-central collisions shown in Fig. 10.2(a) including all correction steps is represented by full symbols Fig. 10.8(a). For completeness, the open symbols which correspond to the azimuthal distribution after applying only the pair efficiency correction are shown as well. As we can see, we have recovered the peak at $\Delta\phi = 0$ which is in line with the results shown in Fig. 10.3, where we forced the rings to separate by employing the cut on the polar angle track separation $\Delta\theta = 62$ mrad.

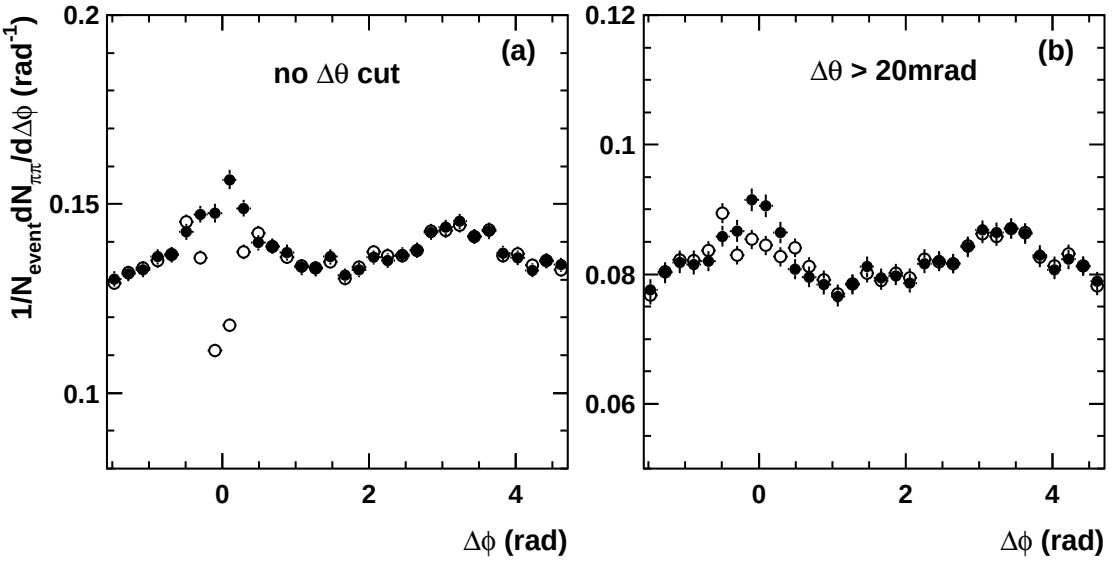

Figure 10.8: The azimuthal correlations of high-p_T pions ($p_{\rm T}$ >1.2 GeV/c) in semi-central collisions after Monte-Carlo corrections without (a) and with (b) $\Delta\theta = 20$ mrad cut applied. Open symbols show the raw correlation corrected for two-pion reconstruction efficiency, closed symbols are after additional accounting for the two-track resolution.

However, in order to render results less dependent on details of the Monte-Carlo correction of the dip, we make a compromise and apply a moderate cut of $\Delta\theta > 20$ mrad on the polar two track separation. On one hand, we still keep about 60% of the data statistics as can be seen from Fig. 10.4. On the other hand, this cut diminishes at the same time the instrumental anomaly by a factor of four as can be viewed by comparing the open symbols in top and bottom of Fig. 10.8(b).

10.4 Results

10.4.1 Centrality and Transverse Momentum Dependence of Two-Particle Azimuthal Correlations

The fully corrected two-particle azimuthal distributions of pions with $p_T > 1.2$ GeV/c are displayed in Fig. 10.9 for six centrality classes defined in Table 7.2. Assuming that only contributions due to collective flow are present, the distributions were fitted according to Eq. (10.1). The anisotropy is quantified by $\sqrt{p_2}$ parameter in analogy to the event plane method.

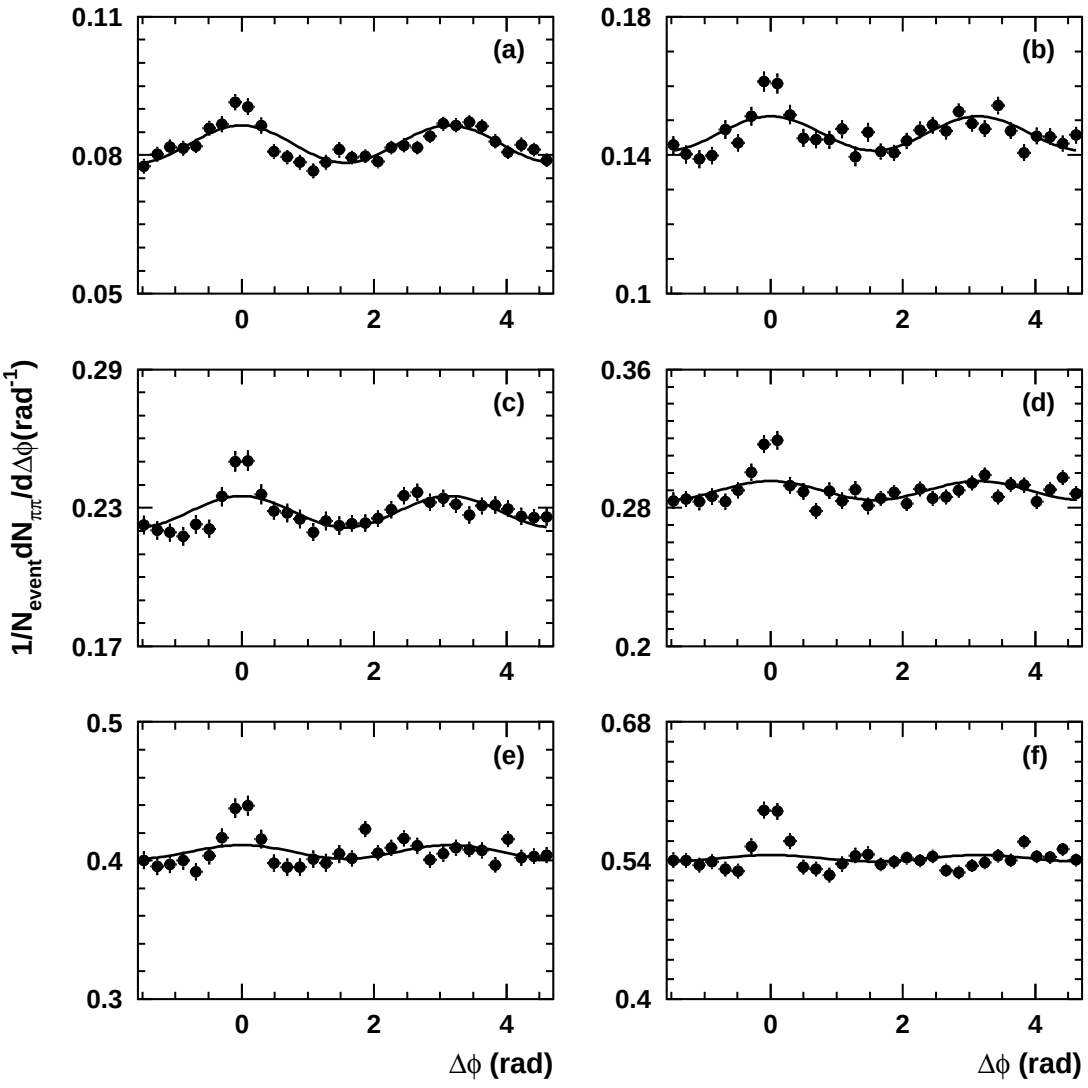

Figure 10.9: Two-particle azimuthal distribution of pions ($p_T > 1.2$ GeV/c, $\Delta\theta > 20$ mrad) for six different centralities, going from semi-central (C1) in (a) to central (C6) in (f). The full line shows $\cos(2\Delta\phi)$-fit according to Eq. (10.1). The data are fully corrected. Please note the zero suppressed y-scale.

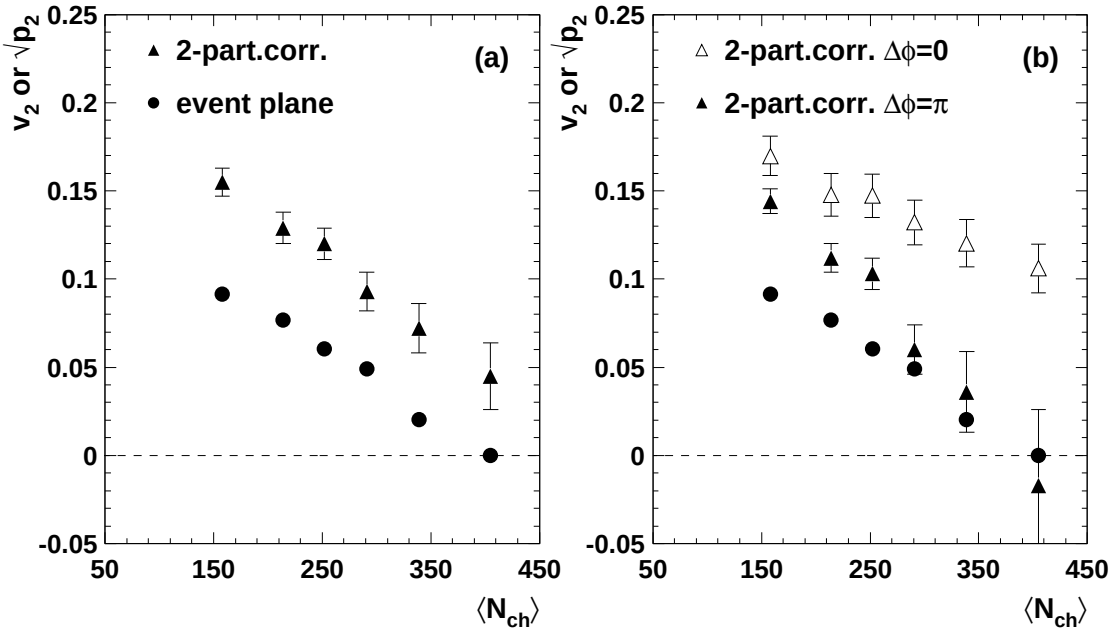

Figure 10.10: Centrality dependence of $\sqrt{p_2}$ from $\pi\pi$ (triangles) and v_2 from event plane correlations (circles) for p_T >1.2 GeV/c. The triangles in (a) are obtained from the full $\Delta\phi$ range, while in (b) the back-to-back (closed triangles) and near-side (open triangles) correlation peaks are investigated separately.

Extracting $\sqrt{p_2}$ parameter from the full $\Delta\phi$ range, we obtain the centrality dependence displayed in Fig. 10.10(a). The results are compared to the v_2 values obtained from the event plane method. The anisotropies from $\pi\pi$ correlation are systematically higher than the elliptic flow values. In semi-central collisions they exceed the flow values by about 50% demonstrating a presence of a strong non-flow component. Accounting for the quantum HBT effects discussed in Section 9.5.2, this excess is reduced to 40%. It is unlikely that elliptic flow values obtained from the event plane method are significantly lowered due to a bias on the event plane reconstruction by the high-p_T particles due to their very small abundance of about $\approx 10^{-3}$ of all charged particles used for the event plane determination.

Let us now investigate separately the centrality behavior of the $\sqrt{p_2}$ anisotropy for the back-to-back, and near-side correlation peak, respectively. The corresponding values of $\sqrt{p_2}$ are shown in Fig. 10.10(b) and compared again to the v_2 values from the event plane method. With increasing centrality, the $\sqrt{p_2}$ anisotropy at back-to-back angles decreases more strongly and approaches the elliptic flow values to reach zero for central collisions. The near-side correlation, however, remains finite also in central collisions.

We turn now to the transverse momentum dependence of two-particle correlations. The results for semi-central collisions, where the observed discrepancy between $\sqrt{p_2}$ and v_2 is largest, are plotted in Fig. 10.11. We distinguish here two types of presentation. In Fig. 10.11(a), the p_T bins are differential, i.e. both pions have p_T within a given p_T bin. Since this approach costs a tremendous amount of the data statistics, we have decided to

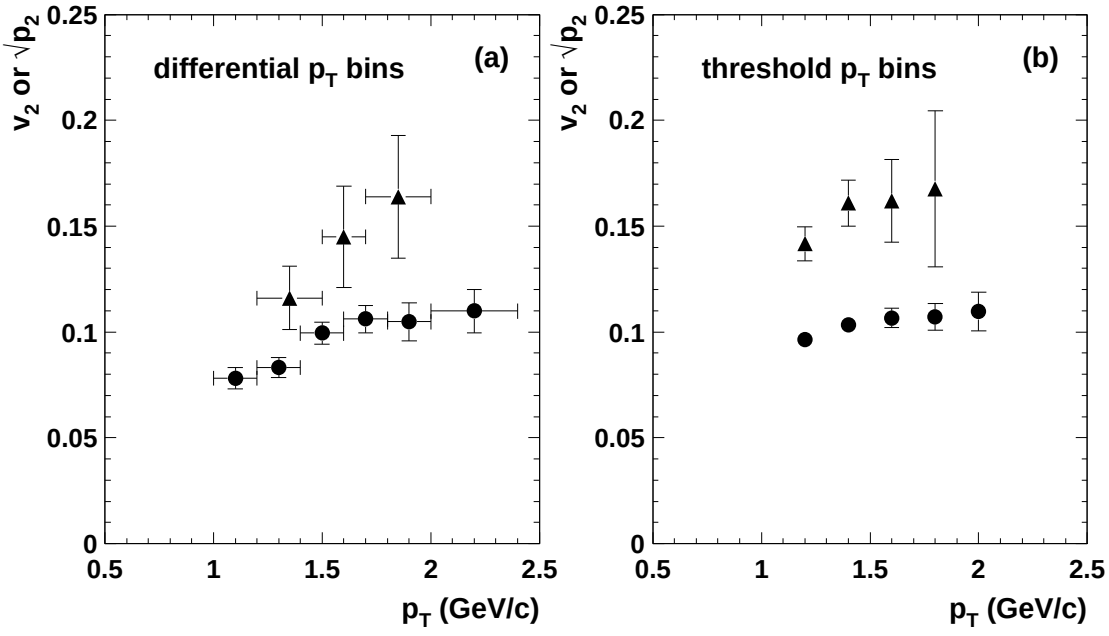

Figure 10.11: Transverse momentum dependence of $\sqrt{p_2}$ from $\pi\pi$ (triangles) and v_2 from event plane correlations (circles) in semi-central collisions ($\sigma/\sigma_{geo} =$ (24-30)%) for differential (a), and threshold (b) p_T bins (for definition see text).

use a threshold p_T bin representation as well. In this representation, we demand that p_T of both pions is above a certain p_T threshold value indicated by a point in Fig. 10.11(b). The discrepancy between the results obtained from the two-particle correlation and the event plane method has a tendency to increase with transverse momentum.

10.4.2 Extraction and Properties of Semi-Hard Components

Clearly, the observed excess in the v_2 magnitude reported in the previous section is due to direct pion-pion correlations. An interpretation of this non-flow component in terms of resonance decays is unlikely in view of a high invariant mass required. For a resonance decaying into two pions with $p_T = 1.2$ GeV/c which fall into the CERES pseudo-rapidity acceptance and have the azimuthal angle difference of $\Delta\phi = \pi$, the invariant mass would reach a value of about 2.5 GeV/c^2.

The shape of the two-particle azimuthal distribution suggests a description by two Gaussians centered at $\Delta\phi = 0$ and $\Delta\phi = \pi$, respectively, situated on top of elliptic flow modulated background. We have fitted the data with the function

$$C(\Delta\phi) = B\left(1 + 2v_2^2\cos(2\Delta\phi)\right) + A_0\exp\left(-\frac{\Delta\phi^2}{2\sigma_0^2}\right) + A_\pi\exp\left(-\frac{(\Delta\phi-\pi)^2}{2\sigma_\pi^2}\right) \quad (10.6)$$

Fit parameters are the Gaussian amplitudes A_0 and A_π, the widths σ_0 and σ_π of the Gaussian peaks, and the background B. The v_2 values are fixed independently from the event

plane method. The results of the fit for the studied six centrality classes are shown in Fig. 10.12 by the full line. The dashed line in the same figure indicates the contribution due to the collective flow as given by the first term in Eq. (10.6).

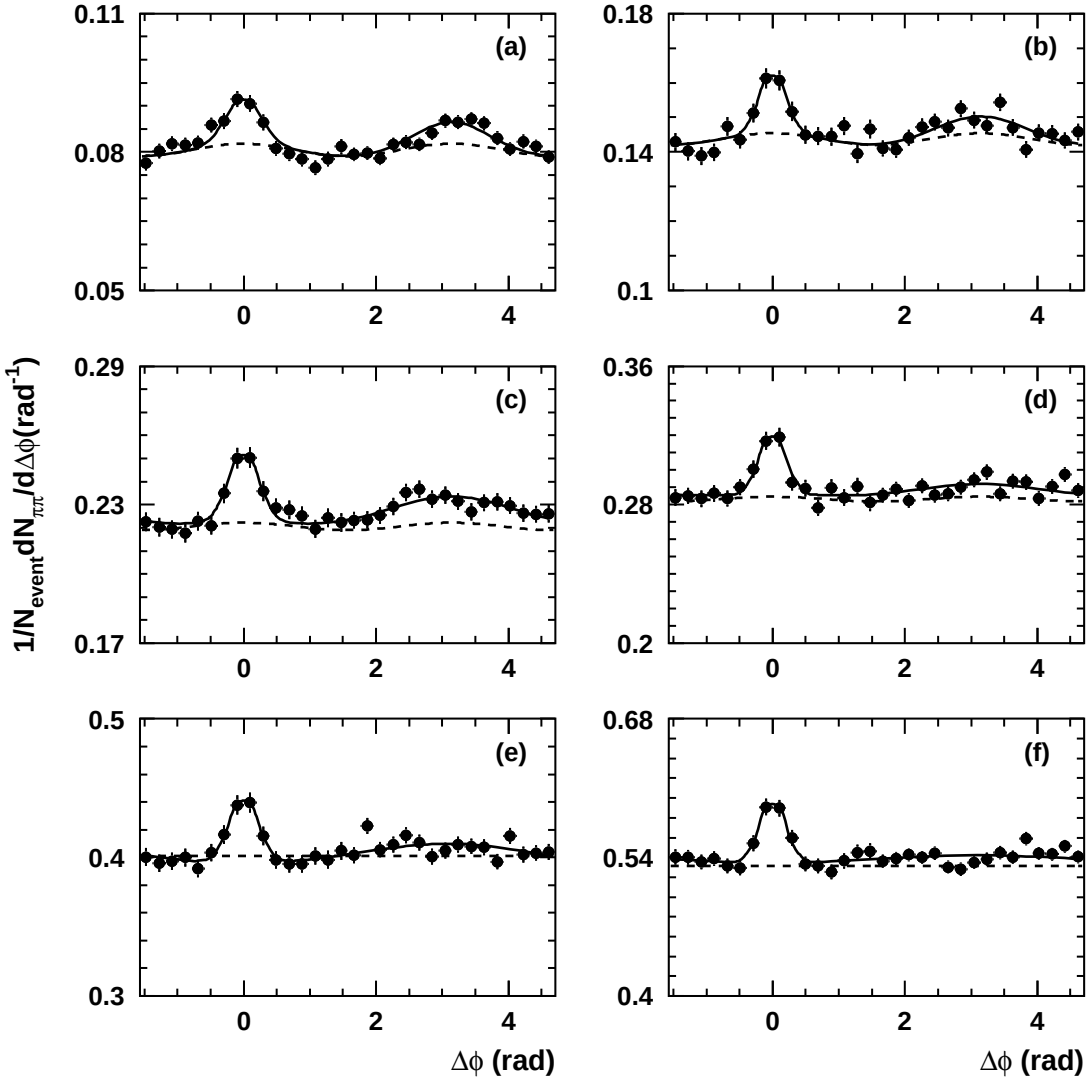

Figure 10.12: Two-particle azimuthal correlation of pions with $p_T > 1.2$ GeV/c for six centrality classes. The full line shows Gaussian fits to semi-hard components on top of elliptic flow modulated background (dashed line). Please note the zero suppressed y-scale.

The centrality dependence of the Gaussian widths obtained from the fit is for both peaks summarized in Fig. 10.13. The two peaks show very different behavior. The near-side peak stays narrow at $\sigma_0 = (0.23 \pm 0.03)$ rad, which is consistent with the fragmentation [216]. On the other hand, the back-to-back peak broadens with increasing centrality up to $\sigma_\pi = (1.26 \pm 0.28)$ rad. This centrality corresponds to the number of binary collisions of $N_{coll} \approx 550$. In more central collisions, the semi-hard back-to-back component cannot be discerned from background anymore.

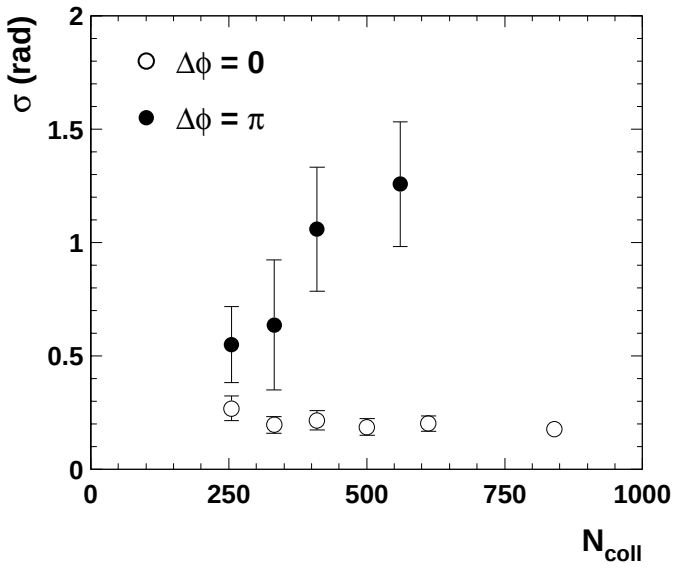

Figure 10.13: Centrality dependence of the Gaussian widths of the correlation peaks at $\Delta\phi = 0$ (open symbols), and $\Delta\phi = \pi$ (closed symbols).

The yields of the semi-hard pion pairs are calculated as Gaussian areas. Their centrality dependence is displayed in Fig. 10.14, alternatively by the number of participants N_{part} and number of binary collisions N_{coll}, respectively. Within the statistical errors the yield of the near-side component as contained in the Gaussian peaks grows linearly with centrality. However, for scaling with the number of binary collisions the better fit quality is obtained. This supports the interpretation of the semi-hard origin of the non-flow component. The back-to-back component escapes detection in central collisions due to broadening described above, but does not appear to be suppressed in yield.

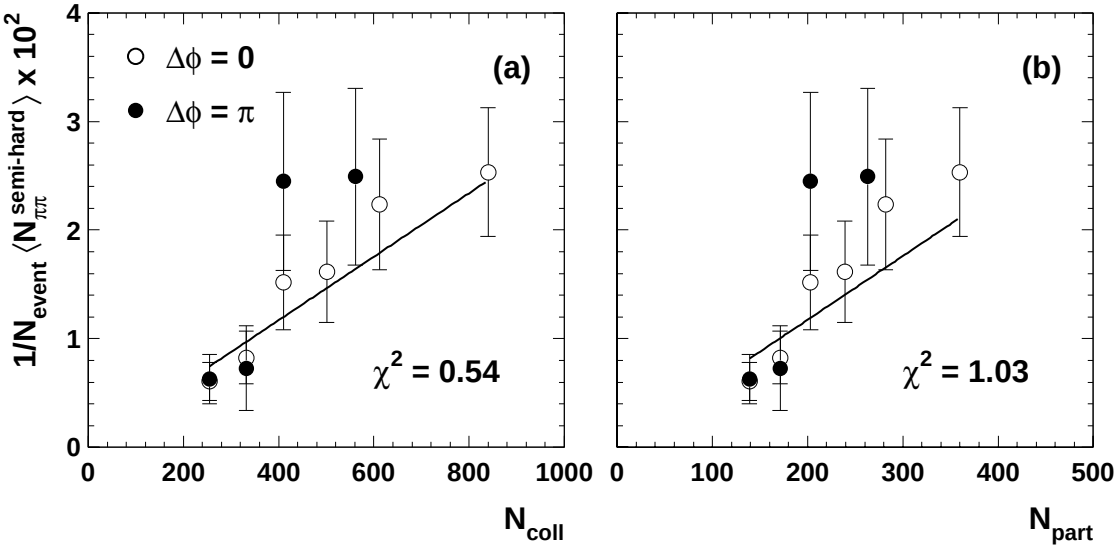

Figure 10.14: Centrality dependence of the semi-hard yield of pion pairs for the near-side (open symbols) and back-to-back (closed symbols) peaks. The centrality is expressed in terms of number of binary collisions N_{coll} (a), and number of participants N_{part} respectively (b). The full line shows a linear fit to the yield of pion pairs in the near-side peak.

10.4.3 p_T Broadening

Partonic rescatterings in medium cause a transverse momentum imbalance perpendicular to the initial hard scattering plane [102, 103, 217]. In a statistical analysis, summing over many events leads to a broadening of the relative azimuthal angle of two hadrons that originate from back-to-back parton scattering. This is reflected in the width of the back-to-back peak [218]. In contrast, the near-side peak is not affected because the pions originate from fragmentation of the same parton and propagate as color singlets. A related quantity, more appropriate to describe the underlying physics processes, is the transverse momentum broadening $\langle \Delta p_T^2 \rangle^{1/2}$. We approximate the p_T broadening by

$$\langle \Delta p_T^2 \rangle^{1/2} \approx \langle p_T \rangle (\sigma_\pi^2 - \sigma_0^2)^{1/2}, \tag{10.7}$$

where $\langle p_T \rangle = 1.45$ GeV/c for the p_T cut of 1.2 GeV/c. Using this approximation we obtain for $\langle N_{coll} \rangle = 550$ value of $\langle \Delta p_T^2 \rangle^{1/2} = (1.8 \pm 0.4)$ GeV/c. However, this intuitive

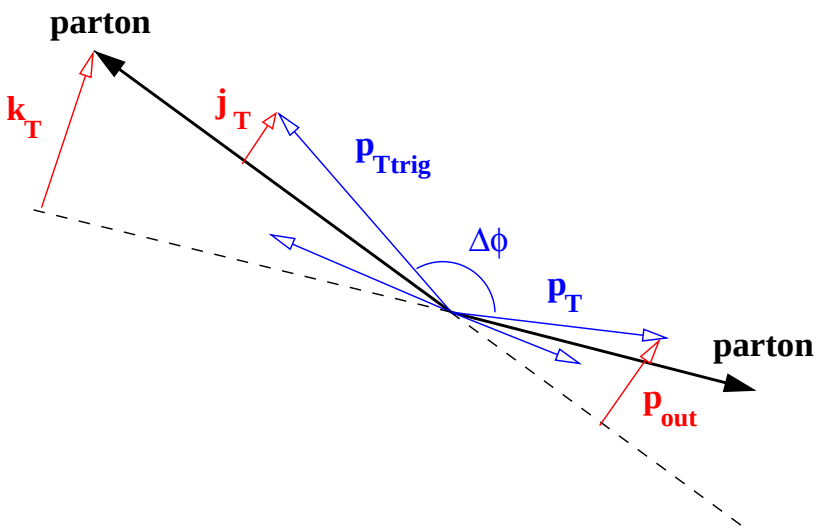

Figure 10.15: Schematic view of hard scattering in transverse plane. Two back-to-back produced partons fragment and produce high-p_T particles.

approximation is only valid in the limiting case of small angles. A more appropriate result can be obtained in the spirit of the parton model. Let us denote by p_{out} the out-of-plane component of the momentum formed by the beam and the trigger particle. In the following, we sketch an analysis of p_T broadening effects in p-p collisions formulated in the framework of the parton model [96,219,220]. In this analysis, two effects are believed to produce finite values of p_{out}: the intrinsic transverse momentum k_T of the partons that enter the hard scattering, and the transverse momentum relative to the jet axis j_T, which a produced particle obtains during the fragmentation of its parent parton after scattering,

$$\langle |j_T| \rangle = \langle p_T \rangle \sin \langle |\phi_i - \phi_{jet}| \rangle. \tag{10.8}$$

In our analysis of nucleus-nucleus collisions, a new source of broadening is due to collisions of partons after the primary hard scattering inside the medium which does not exist in p-p collisions. However, these two contributions to k_T cannot be distinguished.

Since we can only measure the mean relative azimuthal angle difference between two 'jet fragments'

$$\sigma_0 = \sqrt{\langle(\phi_i - \phi_j)^2\rangle}, \tag{10.9}$$

and assuming a Gaussian distribution[1] in σ_0, we can rewrite Eq. (10.8) into

$$\langle|j_T|\rangle = \langle p_T\rangle \sin\frac{\sqrt{\langle(\phi_i - \phi_j)^2\rangle}}{\sqrt{2}} = \langle p_T\rangle \sin\frac{\sigma_0}{\sqrt{\pi}}. \tag{10.10}$$

In this picture, the relationship between these quantities can be approximated by [96, 219, 220]

$$\langle|p_{out}|\rangle^2 = 2\langle|k_T|\rangle^2 x_E^2 + \langle|j_T|\rangle^2(1 + x_E^2), \tag{10.11}$$

where $\langle|k_T|\rangle$ and $\langle|j_T|\rangle$ are the average values of the components of k_T and j_T out of the scattering plane, and

$$x_E = -\frac{\vec{p}_T \cdot \vec{p}_{Ttrig}}{|\vec{p}_{Ttrig}|^2} = -\cos(\langle|\Delta\phi|\rangle) = -\cos(\sqrt{\frac{2}{\pi}}\sigma_\pi), \tag{10.12}$$

where in the last step we have expressed $\langle|\Delta\phi|\rangle$ with the help of the measured σ_π assuming again it is Gaussian distributed. As can be inferred from Fig. 10.15

$$\langle|p_{out}|\rangle = \langle p_T\rangle \sin(\langle|\Delta\phi|\rangle) = \langle p_T\rangle \sin(\sqrt{\frac{2}{\pi}}\sigma_\pi) \tag{10.13}$$

and with the help of Eq. (10.10), Eq. (10.12) and simple trigonometric relations, we obtain from Eq. (10.11) for $\langle|k_T|\rangle$ the expression [124]

$$\langle|k_T|\rangle = \langle p_T\rangle \cos\frac{\sigma_0}{\sqrt{\pi}} \sqrt{\frac{1}{2}\tan^2\left(\sqrt{\frac{2}{\pi}}\sigma_\pi\right) - \tan^2\left(\sqrt{\frac{1}{\pi}}\sigma_0\right)}, \tag{10.14}$$

which contains only the measured quantities. Inserting the Gaussian widths of the near-side and back-to-back angle peaks for $N_{coll} \approx 550$, we get $\langle|k_T|\rangle = (2.8\pm0.6)$ GeV/c.

The effects of a nucleus on partons which have undergone hard scattering, were investigated in a systematic way in p-A collisions at 400 GeV/c [218], where clear dijet events were observed for nuclei ranging from H to Pb. While those data shown that the angular size of individual jets is only slightly different from that in p-p collisions, a dramatic change in the coplanarity of the two jets in dijet events was found. For hydrogen data, an rms value of $k_T = (0.9\pm0.2)$ GeV/c was measured, which increases to (2.0 ± 0.2) GeV/c for p-Pb collisions. Our values from Pb-Au collisions are higher than those from 'cold nuclear matter' created in p-Pb collisions, however within the errors quoted the two measurements agree. We remark here that we cannot exclude a larger broadening from our data in the most central collisions where the pion detection efficiency in the RICH detectors is very small due to a high background contamination.

[1] We remind reader that the average value of x which is Gaussian distributed is given by $\frac{\int x \exp^{-x^2/(2\sigma^2)}\,dx}{\int \exp^{-x^2/(2\sigma^2)}\,dx} = \sqrt{\frac{2}{\pi}}$.

10.4.4 Correlation of Pion Pairs with the Event Plane

It is very interesting to find out whether the observed semi-hard components bear any relation to the event plane. Due to the asymmetric shape of the overlap zone in non-central collisions, the yield of the semi-hard components could be suppressed if those propagate perpendicular to the reaction plane rather than along it. Up to now no similar studies have been described in literature, only [221] reports on some preliminary results obtained from HIJING and RQMD event generators.

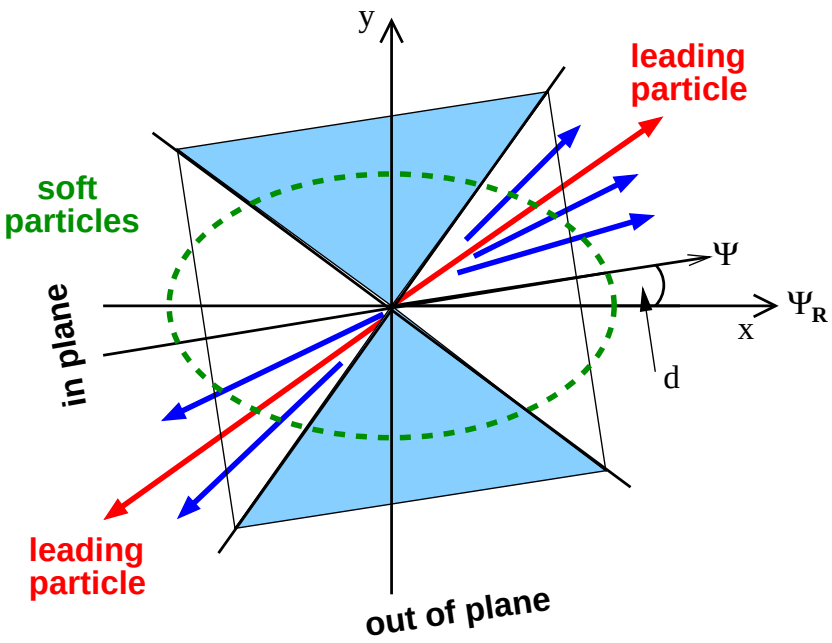

Figure 10.16: Definition of the in-plane and of the out-of-plane regions of size $\pm\pi/4$ around the reconstructed event plane Ψ. The true event plane is denoted by Ψ_R and the difference between Ψ_R and Ψ is defined by d.

We construct two-particle correlation functions by keeping one particle fixed in a certain region with respect to the event plane. In particular, we study the shape of the correlation under conditions confining one particle in the *in-plane* or *out-of-plane* regions which are schematically displayed in Fig. 10.16. The in-plane region is defined by a *'conus'* (in two dimensions) of $\pm\pi/4$ around the reconstructed event plane Ψ, and the out-of-plane region is a conus of the same size centered perpendicularly to Ψ. The difference between the reconstructed event plane angle Ψ and the true reaction plane angle Ψ_R in a given event is denoted by the parameter d.

Properties of the in-plane/out-of-plane correlations for collective elliptic flow

Let us first discuss the general properties of the in and out-of-plane distributions in the case of pure collective flow. We restrict ourselves to elliptic flow and define the correlation of particles with respect to the reaction plane Ψ_R as

$$f(\phi_i - \Psi_R) = A\{1 + 2v_2 \cos[2(\phi_i - \Psi_R]\}. \tag{10.15}$$

The two-particle correlation we write in the form

$$c(\phi_i - \phi_j) = B\{1 + 2p\cos[2(\phi_i - \phi_j)]\}. \tag{10.16}$$

For the in and out-of-plane correlations, we obtain

$$c_{in}(\phi_i - \phi_j) = B_{in}\{1 + 2p_{in}\cos[2(\phi_i - \phi_j)]\} \tag{10.17}$$

and

$$c_{out}(\phi_i - \phi_j) = B_{out}\{1 + 2p_{out}\cos[2(\phi_i - \phi_j)]\}, \tag{10.18}$$

respectively.[2]

Our aim is to express parameters B_{in}, B_{out}, p_{in} and p_{out} in terms of the parameters B and p from the standard two-particle correlation function of Eq. (10.16). Confining one particle in the pair to a restricted region of $\langle a, b\rangle$ results in

$$p_{a,b} = v_2 \cdot \frac{\int_a^b f(x)\cos(2x)dx}{\int_a^b f(x)dx}, \tag{10.19}$$

where $x = \phi - \Psi_R$. In analogy, the constant term $B_{a,b}$ can be expressed as

$$B_{a,b} = \frac{\sqrt{B}}{2} \cdot \frac{\int_a^b f(x)dx}{\int_a^b dx}, \tag{10.20}$$

Assuming perfect resolution of the reaction plane, we obtain with the help of the integrals evaluated in Appendix C (for $d = 0$) the following relations,

$$p_{in} = v_2\frac{\pi v_2 + 2}{\pi + 4v_2} \quad , \quad p_{out} = v_2\frac{\pi v_2 - 2}{\pi - 4v_2}, \tag{10.21}$$

and

$$B_{in} = \frac{B}{2}\left(1 + \frac{4v_2}{\pi}\right) \quad , \quad B_{out} = \frac{B}{2}\left(1 - \frac{4v_2}{\pi}\right). \tag{10.22}$$

An example is shown in Fig. 10.17. We can see that the two functions are shifted in phase by $\pi/2$. It is easy to visualize the observed behavior: by fixing one particle directly in the reaction plane, the flow pattern stays in phase, i.e. correlation function will have maxima at $\Delta\phi = 0$ and $\Delta\phi = \pi$ and will show larger anisotropy. On the other hand, if we confine one particle perpendicular to the reaction plane orientation, the pattern shifts by $\pi/2$ since the largest particle yield will be at $\Delta\phi = \pi/2$ and $\Delta\phi = 3\pi/2$, respectively, and the anisotropy will be reduced.

In the experiment, however, the orientation of the reaction plane is a priori unknown and we have to take into account the finite dispersion of the measured event plane. As it is shown in Appendix C, for our conus selection we obtain

$$p_{in} = v_2\frac{\pi v_2 + 2\cos(2d)}{\pi + 4v_2\cos(2d)}, \tag{10.23}$$

$$p_{out} = v_2\frac{\pi v_2 - 2\cos(2d)}{\pi - 4v_2\cos(2d)}, \tag{10.24}$$

[2]For simplicity, we have dropped out the subscript '2' indicating the second Fourier harmonics in the parameter p.

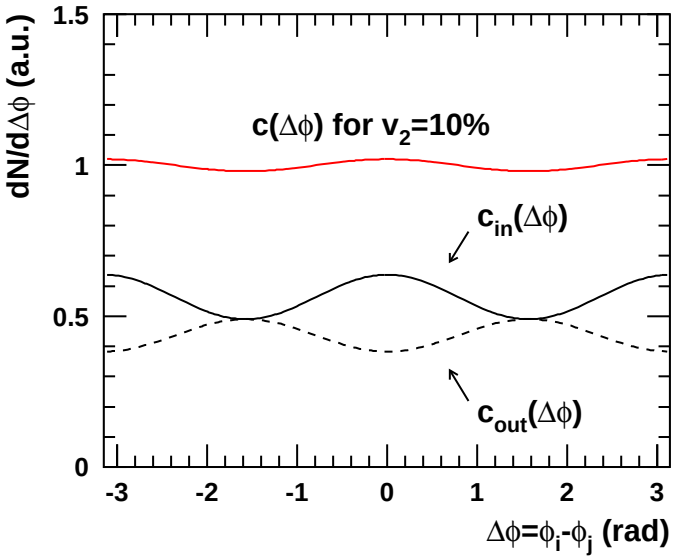

Figure 10.17: Illustration of the two-particle correlation function c, together with the in-plane c_{in} and the out-of-plane c_{out} correlation functions for $v_2 = 10\%$.

and

$$B_{in} = \frac{B}{2}\left[1 + \frac{4v_2}{\pi}\cos(2d)\right], \tag{10.25}$$

$$B_{out} = \frac{B}{2}\left[1 - \frac{4v_2}{\pi}\cos(2d)\right]. \tag{10.26}$$

We can notice that the $\cos(2d)$ term corresponds to the correction factor for the finite dispersion of the measured event plane which was used for elliptic flow (cf. Eq. (9.19)). Fig. 10.18 shows a comparison of the c_{in} and c_{out} correlation functions for $v_2 = 10\%$ for the true reaction plane and for the event plane with finite dispersion. We can observe that the absolute values of p_{in} and p_{out} parameters are smaller than those obtained for the true

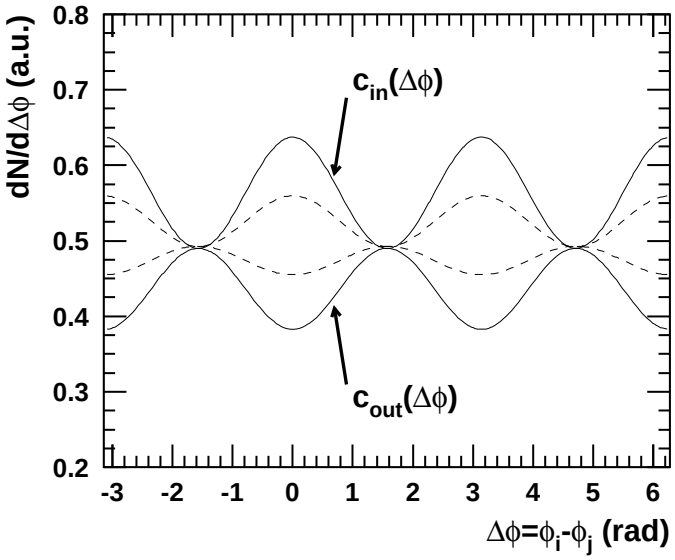

Figure 10.18: Illustration of c_{in} and c_{out} functions for $v_2 = 10\%$ in the case of the true reaction plane (full lines) and after accounting for the finite resolution of the measured event plane (dashed lines).

reaction plane. This is easy to understand, since the finite event plane resolution causes that the in-plane region receives also contributions from the out-of-plane region and vice versa.

The dependence of the studied parameters on v_2 is displayed in Fig. 10.19. While the lines are calculated for the true reaction plane (cf. Eq. (10.21) and Eq. (10.22)), the points

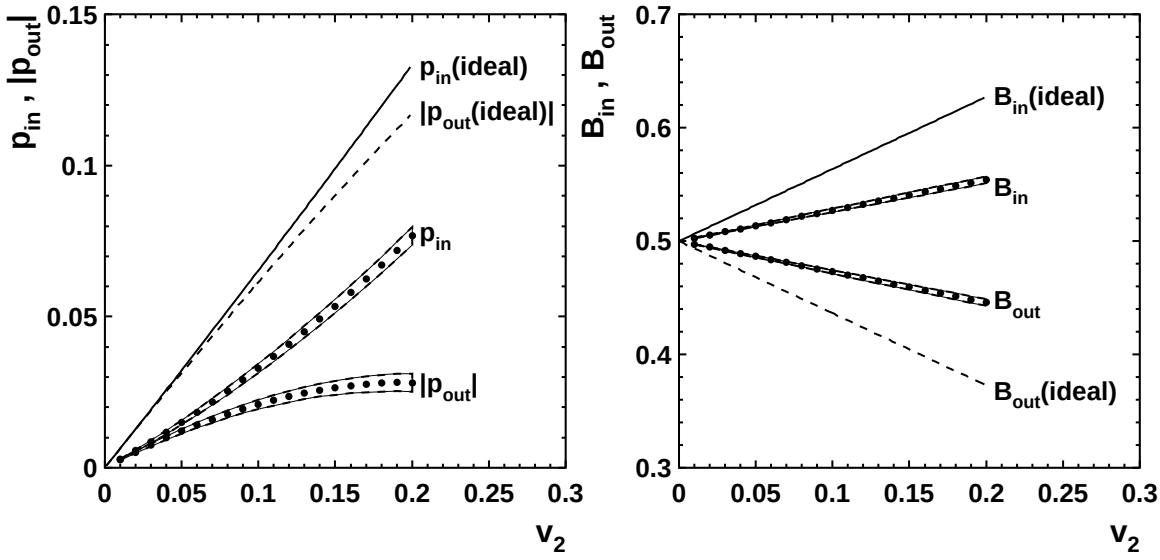

Figure 10.19: Dependence of the p_{in}, p_{out} parameters (left) and B_{in} and B_{out} parameters on v_2 for the true reaction plane (lines) and for the measured event plane (circles). The band around the circles indicates upper and lower limit as expected for different centrality selections.

are obtained for the measured event plane. Since the event plane resolution strongly depends on centrality of the collision, we have studied the parameters for different centrality classes. The results are indicated by a band around the points in Fig. 10.19, which corresponds to the lower and upper limits on the values of the studied parameters for the covered centrality range of 30% of geometric cross section (cf. Chapter 7).

In-plane/out-of-plane two-particle correlations in the data

We turn now to the measured in-plane and out-of-plane two-particle azimuthal distributions. The data for semi-central collisions are displayed in Fig. 10.20 together with the expected contribution due to collective elliptic flow, which was calculated with $v_2 = 8.5\%$ and is depicted by the dashed line. We can observe that in both cases, the data lie above the elliptic flow reference.

After subtracting the contributions due to flow, we can again extract the yields of the semi-hard components from the Gaussian fit parameters as it was done for the conventional two-particle correlation (cf. Fig. 10.14). For the near-side component we have obtained the ratios of the in-plane to out-of-plane yields (1.32 ± 0.37). For the back-to-back component has this ratio value of (1.39 ± 0.44). In addition to the statistical errors, we estimate a systematic uncertainty due to subtraction of the expected collective flow contribution to 15%. We can conclude that within the errors quoted both semi-hard components exhibit only a weak preference to the reaction plane.

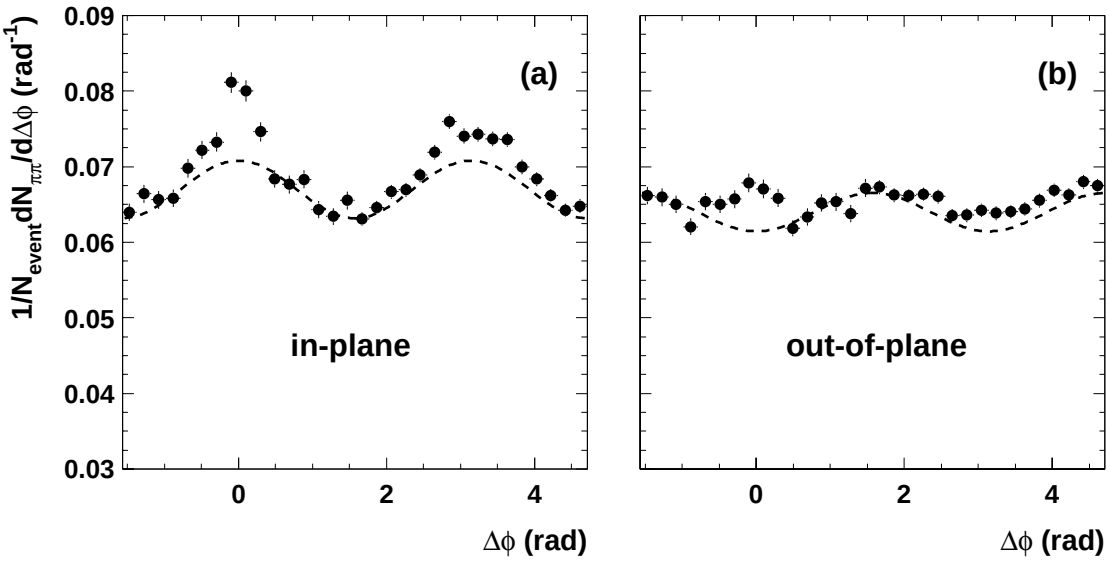

Figure 10.20: Measure in-plane (a) and out-of-plane (b) two-pion azimuthal distributions. Dashed lines are calculated for pure elliptic flow as measured by the event plane method and corrected for HBT correlations. Data are for centrality σ/σ_{geo} = (15-30)%, $p_T \geq 1.2$ GeV/c, $\Delta\theta \geq 20$ mrad cut, and are efficiency corrected.

10.4.5 Comparison with Other Experiments

At the SPS, there are no experimental results on two-particle azimuthal correlations of high-p_T charged pions available. Azimuthal $\gamma - \gamma$ correlations at high-p_T were studied by the WA98 experiment [116, 117] in search for jet-like structures. These photons mainly originate from decays of neutral hadrons, π^0, and η. A clear indication of back-to-back correlations was found in p-A collisions and in peripheral Pb-Pb collisions. In the latter, the shape of the correlation is not well described by pure elliptic flow. The authors of [117] have investigated the $\gamma - \gamma$ correlations using cuts in pseudo-mass M which is defined as $M = p_{T1} + p_{T2}$. For Pb-Pb collisions at $N_{part} = 60$ and the pseudo-mass cut of $1.2 < M < 1.8$ GeV/c, elliptic flow reaches a value of $v_2 = 0.085 \pm 0.005$. [3] Fitting the data with a Gaussian peak at $\Delta\phi = \pi$ on the elliptic flow modulated background reduces the v_2 value to $v_2 = 0.065 \pm 0.007$. For the higher pseudo-mass cut of $1.8 < M < 2.4$ GeV/c, the data suffer already from quite large statistical errors, however, there is about 15-30% relative discrepancy in v_2 observed in the centrality range of $50 < N_{part} < 250$. We remind here that our results correspond to even higher pseudo-mass cut of $M > 2.4$ GeV/c, since we require both pions to have transverse momentum of $p_T > 1.2$ GeV/c.

Azimuthal two-particle correlations of large transverse momentum charged hadrons have been recently reported by the STAR Collaboration at RHIC [202, 222–224]. The measurement was done both for p-p and Au-Au collisions at $\sqrt{s_{NN}} = 200$ GeV. Their results on two-hadron azimuthal correlations around $\Delta\phi = 0$ in Au-Au collisions at

[3] Remark: This v_2 coefficient corresponds to our $\sqrt{p_2}$ coefficient.

$p_T > 4$ GeV/c show a quantitative agreement with the p-p data implying that nearly all hadrons in the mentioned transverse momentum range originate from jet fragmentation. The near-side correlations are present in all centralities up to the most central ones (Fig. 10.21) indicating that the fragmentation is not substantially modified in the hot and dense medium created in the Au-Au collision. However, strong back-to-back correlations exist only in peripheral Au-Au collisions and they are considerably reduced in the most

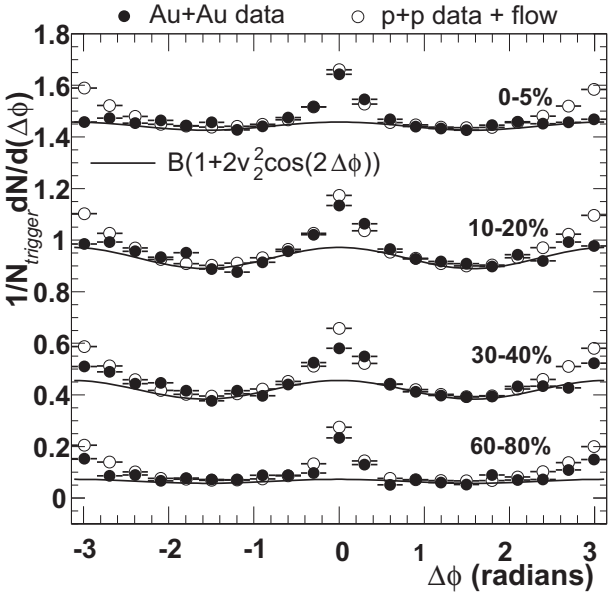

Figure 10.21: Azimuthal distributions ($0 < |\Delta\eta| < 1.4$, $4 < p_T^{trig} < 6$ GeV/c) for Au-Au collisions at $\sqrt{s_{NN}} = 200$ GeV measured by STAR (solid circles) and their comparison to the expected distributions from p-p data (open circles). Also shown is the elliptic flow contribution for each centrality (solid line). The figure is taken from [222].

central Au-Au collisions. This points to a significant interaction of the hard-scattered partons and their fragmentation products while traversing the medium and it is also in line with observed strong suppression (jet quenching) of inclusive yields at RHIC energies [110, 112].

Our results on two-particle correlations show similar features as the findings of the STAR experiment, but the back-to-back correlation disappears in our case in central collisions without sign of its suppression or quenching. Moreover, at RHIC energies there is hardly any difference between the v_2 values obtained from correlation of particles with the reaction plane and from two-particle correlations below $p_T = 3$ GeV/c [225] .

11

Conclusions and Outlook

The observation of dijet-like two-particle azimuthal correlations at large transverse momenta of charged pions embedded in collective flow is novel for SPS energies. The broadening of the back-to-back correlation with increasing centrality suggests that we observe in-medium partonic scattering which affects both parts of a dijet independently. Although the back-to-back correlation disappears in central collisions, there is no sign of its suppression. The absence of broadening of the near-side correlation supports the view that the pions originate from fragmentation of the same parton.

Novel in this work is also the method and the study of appearance of the semi-hard components with respect to the reaction plane, probing the thermalization of the high-p_T pions passing through the anisotropic overlap region of the colliding nuclei. A rather weak alignment of the semi-hard pions with the reaction plane points to a 'weak rescattering' and is corroborated by the large excess of the two-particle azimuthal anisotropies above the elliptic flow. Semi-hard particles, if well aligned with the reaction plane, would raise v_2 up to similar magnitudes. This, combined with the small rapidity acceptance of the CERES spectrometer, might explain the exceptionally large excess of two-particle correlations above the elliptic flow.

The elliptic flow depends on centrality and small transverse momenta as expected from hydrodynamical calculations with the kinetic freeze-out temperature of $T_f = 120$ MeV but remains below in magnitude. This indicates that only a partial equilibration is reached even at the highest SPS energy ($\sqrt{s} = 17$ AGeV). A better agreement can be reached for higher freeze-out temperatures of about 160 MeV which would not be in contrast with the freeze-out parameters extracted from the hydrodynamical analysis of the inclusive transverse mass distributions of h^-.

The transverse momentum dependence of elliptic flow was measured with high statistics up to $p_T = 3$ GeV/c and enlarges significantly our knowledge on $v_2(p_T)$ behavior at the SPS. The observed onset of flattening around $p_T = 1.5$ GeV/c is very similar to the findings at RHIC energies.

Our results thus exhibit similar features, but also important differences, to the recent findings at RHIC. At RHIC, there is hardly any difference between the elliptic flow magnitude determined from the event plane method and two-particle correlations below

$p_T = 3$ GeV/c and the data exhaust for $p_T < 2$ GeV/c also the hydrodynamical calculations. At this place we thus allow ourselves to conjecture that high-p_T particles at RHIC are well aligned with the reaction plane because of jet-quenching.

In 2000, a high statistics Pb-Au data sample consisting of 33 millions of events was taken with the CERES spectrometer upgraded by the large time-projection chamber (TPC). We expect that the analysis of this data set will bring more information on the physics topics discussed in this work. The analysis of not identified charged particles measured by TPC alone is expected to increase the covered p_T range up to 4 GeV/c. This in combination with the excellent position resolution of TPC will avoid the large efficiency losses at small two-track separation from which suffered the analysis of the 1996 data presented here.

Appendix A

Frequently Used Kinematic Variables

This appendix summarizes the variables commonly used throughout this work. The reader is also referred e.g. to Chapter 2 of [31].

A.1 Transverse Momentum and Mass

In fixed target experiments, the transversal plane is usually the plane perpendicular to the beam axis (z direction). We can define the *transverse momentum* as

$$p_T = p \cdot \sin\theta, \tag{A.1}$$

where θ is the polar angle of a particle track. Since CERES covers only θ angles between 8 and 15 degrees, it allows us to make an approximation $p_T \approx p/5$.

Having defined the transverse momentum, we can define another useful quantity, the *transverse mass*,

$$m_T = \sqrt{p_T^2 + m_0^2}, \tag{A.2}$$

where m_0 is the rest mass of particle.

A.2 Rapidity and Pseudo-Rapidity

The *rapidity* y is a very useful variable for description of the longitudinal motion of particles with non zero rest mass. If the particle has an energy E and momentum component along the beam axis p_z, we can define its rapidity as

$$y = \frac{1}{2}\ln\frac{E + p_z}{E - p_z}. \tag{A.3}$$

The definition looks at the first glance complicated, but its advantage shows up in the Lorentz transformation between different reference systems. Suppose, we have two reference systems S_1 and S_2. If the system S_2 is moving with respect to the S_1 with the velocity β_z along the z-axis, its rapidity y_{S_2} differs from y_{S_1} just by an additive constant

$$y_{S_2} = y_{S_1} - y_\beta, \tag{A.4}$$

where

$$y_\beta = \frac{1}{2}\ln\frac{1+\beta_z}{1-\beta_z} \tag{A.5}$$

is the rapidity of the moving frame. In our case, the beam has momentum $p = 158$ AGeV/c, the target has rapidity $y_{\text{target}} = 0$, and the beam $y_{\text{beam}} = 5.84$.

For symmetric systems, the center of mass moves with the rapidity of

$$y_{\text{cms}}=0.5y_{\text{beam}},$$

called therefore *mid-rapidity*.

However, to calculate the rapidity, the mass and particle's momentum has to be known. Much easier is to determine the so called *pseudo-rapidity* η given by

$$\eta = -\ln(\tan\frac{\theta}{2}), \tag{A.6}$$

where it is enough to measure the polar angle θ of the particle track. The CERES spectrometer covers the pseudorapidity range of η=(2.1,2.65). In the case of small masses and large rapidities $\eta \approx y$.

Appendix B

Pile-Up Effect in Cylindrical Detectors

In this appendix, we give an estimation of pile-up losses in cylindrical detectors on the hit level [226]. These losses are directly connected with the finite position resolution of a given detector, and in addition with the double-hit resolution of a hit reconstruction algorithm employed.

We divide a detector into n cells, where the cell size is the largest size for which multiple hits cannot be resolved. Let us assume that we have N particles distributed randomly among n cells and we measure the particle number by counting the number of hits, or number of cells which are occupied,

$$n_{\text{occupied}} = n(1 - e^{-\mu}). \tag{B.1}$$

Here $\mu = N/n$ is the mean occupancy. The *pile-up loss* L is then defined as the difference between the count of the cells occupied and the number of particles N falling onto the detector, i.e.

$$L = N - n_{\text{occupied}} = N - n(1 - e^{-\mu}). \tag{B.2}$$

Correspondingly, the *pile-up probability* P is given by

$$P = \frac{L}{N} = 1 - \frac{1}{\mu}(1 - e^{-\mu}) \approx \frac{\mu}{2}, \tag{B.3}$$

where the approximation holds for $\mu \ll 1$.

To figure out how many particles fall onto a ring of width $d\theta$, we assume a constant particle rapidity density

$$dN/dy = A = \text{const.}, \tag{B.4}$$

which is certainly good for CERES small acceptance[1], and also that pseudo-rapidity is a fair replacement for rapidity,

$$\frac{dN}{d\theta} = \frac{dN}{dy}\frac{dy}{d\theta} = \frac{A}{\sin\theta}. \tag{B.5}$$

[1]The correct $\cosh$-dependence can be easily installed in numerical calculations.

The occupation of particles per ring is

$$\mu = \frac{dN}{dn} = \frac{dN}{d\theta}\frac{dn}{d\theta}. \tag{B.6}$$

Here the first term is given by Eq. (B.5), and the second one can be easily calculated. We divide the detector area into concentric rings of width dr and work out how many cells of size δr, $\delta\phi$ there are per ring:

$$dn = \frac{2\pi r dr}{r\delta\phi\delta r} = \frac{2\pi dr}{\delta\phi\delta r}. \tag{B.7}$$

Expressing geometry entirely by angles and the distance z from the interaction vertex to the detector via $dr/d\theta = z/\cos^2\theta$, we obtain

$$\frac{dn}{d\theta} = \frac{2\pi z}{\delta\phi\delta r\cos^2\theta}. \tag{B.8}$$

The number of cells per ring would be actually constant would not the projection produce a weak θ dependence. Inserting Eq. (B.5) and Eq. (B.8) to Eq. (B.6) we obtain

$$\mu = \frac{A\delta\phi\delta r}{2\pi z}\frac{\cos^2\theta}{\sin\theta}. \tag{B.9}$$

To calculate the pile-up loss, we multiply the pile-up probability P with the number of particles per ring and obtain

$$dL = PdN \approx \frac{\mu}{2}dN = \frac{A^2\delta\phi\delta r}{4\pi z}\frac{d\theta}{\tan^2\theta} \tag{B.10}$$

from which we may calculate the total pile-up loss

$$L = \frac{A^2\delta\phi\delta r}{4\pi z}\left[\frac{1}{\tan\theta} + \theta\right]_{\theta_2}^{\theta_1}. \tag{B.11}$$

(B.12)

Appendix C

In-plane and Out-of-Plane Correlation Functions for Elliptic Flow

In this appendix the parameters describing the strength of the in-plane and out-of-plane two-particle azimuthal correlations are evaluated in the case that only correlations due to collective elliptic flow are present. For completeness let us here once more repeat the definitions already introduced in Chapter 10.4.4.

We describe the correlations of particles with the event plane Ψ due to collective elliptic flow by function

$$f(x) = A[1 + 2v_2 \cos(2x)] \tag{C.1}$$

with $x = \phi - \Psi$, where ϕ is an azimuthal angle of the emitted particle. The two-particle correlation we write in the form

$$c(x) = B[1 + 2p \cos(2x)] \tag{C.2}$$

with $x = \phi_i - \phi_j$ and ϕ_i and ϕ_j being the azimuthal angles of the emitted particles i, j. Confining one particle in the pair in a region restricted by $\phi = (a, b)$, then the Fourier coefficient $p_{a,b}$ is calculated according to relation

$$p_{a,b} = v_2 \cdot \frac{\int_a^b f(x) \cos(2x) dx}{\int_a^b f(x) dx}. \tag{C.3}$$

Analogically, the constant term $B_{a,b}$ can be expressed as

$$B_{a,b} = \frac{\sqrt{B}}{2} \cdot \frac{\int_a^b f(x) dx}{\int_a^b dx}. \tag{C.4}$$

As can be easily seen for a choice of $a = -\pi/2$ and $b = \pi/2$, we again obtain the well known relation $p = v_2^2$.

In order to evaluate Eq. (C.3) and Eq. (C.4) the three following types of integrals are needed:

$$\begin{aligned} I &= \int_{a+d}^{b+d} f(x)\cos(2x)dx = A[v_2(b-a) \\ &+ \frac{1}{2}[(\sin(2b)-\sin(2a))\cos(2d)+(\cos(2b)-\cos(2a))\sin(2d)] \\ &+ \frac{v_2}{4}[(\sin(4b)-\sin(4a))\cos(4d)+(\cos(4b)-\cos(4a))\sin(4d)]] \qquad \text{(C.5)} \\ J &= \int_{a+d}^{b+d} f(x)dx = A[b-a+v_2(\sin(2b)-\sin(2a))\cos(2d) \\ &+ v_2(\cos(2b)-\cos(2a))\sin(2d)] \qquad \text{(C.6)} \\ K &= \int_{a+d}^{b+d} dx = b-a \qquad \text{(C.7)} \end{aligned}$$

For our choice of the conus size we obtain using results on I and J following relations for the p_{in} and p_{out} coefficients:

$$p_{in} = v_2\frac{\pi v_2 + 2\cos(2d)}{\pi + 4v_2\cos(2d)} \qquad \text{(C.8)}$$

and

$$p_{out} = v_2\frac{\pi v_2 - 2\cos(2d)}{\pi - 4v_2\cos(2d)}. \qquad \text{(C.9)}$$

Analogically, using J and K and our border definitions we get

$$B_{in} = \frac{B}{2}\left[1+\frac{4v_2}{\pi}\cos(2d)\right] \qquad \text{(C.10)}$$

and

$$B_{out} = \frac{B}{2}\left[1-\frac{4v_2}{\pi}\cos(2d)\right]. \qquad \text{(C.11)}$$

Bibliography

[1] K. A. Olive, *The Quark-Hadron Transition in Cosmology and Astrophysics*, Science **251**, 1194 (1991).

[2] E. Kolb and M. Turner, *The Early Universe* (Addison-Wesley, Redwood City, 1990).

[3] J. R. Ellis, J. I. Kapusta, and K. A. Olive, *Phase transition in dense nuclear matter with quark and gluon condensates*, Phys. Lett. **B273**, 123 (1991).

[4] J. R. Ellis, J. I. Kapusta, and K. A. Olive, *Strangeness, glue and quark matter content of neutron stars*, Nucl. Phys. **B348**, 345 (1991).

[5] N. K. Glendenning, *Fast Pulsar in SN1987A: Candidate for Strange Quark Matter*, Phys. Rev. Lett. **63**, 2629 (1989).

[6] T. Ullrich, *Produktion von e^+e^--Paaren in ultrarelativistischen S-Au-Kollisionen bei 200 GeV/n*, PhD thesis, University of Heidelberg, Germany, 1994.

[7] C. P. d. l. Heros, *Low-mass e^+e^- production in S-Au collisions at 200 GeV/c*, PhD thesis, Weizmann Institute of Science Rehovot, Izrael, 1996.

[8] C. Voigt, *Produktion von e^+e^--Paaren in ultrarelativistischen Pb-Au-Kollisionen bei 160 AGeV*, PhD thesis, University of Heidelberg, Germany, 1998.

[9] B. Lenkeit, *Elektron-Positron-Paar Emission in Pb-Au-Kollisionen bei 158 A GeV*, PhD thesis, University of Heidelberg, Germany, 1998.

[10] E. Socol, *Dilepton production in Pb-Au collisions at 158 GeV per nucleon using the CERES detector*, PhD thesis, Weizmann Institute of Science Rehovot, Izrael, 1999.

[11] G. Hering, *Dielectron production in heavy-ion collisions at 158 GeV/c per nucleon*, PhD thesis, Technical University Darmstadt, Germany, 2002.

[12] S. Damjanovic, *Electron-pair production in Pb-Au collisions at 40 AGeV*, PhD thesis, University of Heidelberg, Germany, 2002.

[13] G. Agakishiev *et al.*, *Neutral meson production in p-Be and p-Au collisions at 450 GeV beam energy*, Eur. Phys. J. **C4**, 249 (1998).

[14] G. Agakishiev *et al.* (CERES Collaboration), *Enhanced production of low mass electron pairs in 200 GeV/u S-Au collisions at the CERN SPS,* Phys. Rev. Lett. **75**, 1272 (1995).

[15] D. Adamova *et al.* (CERES Collaboration), *Enhanced production of low-mass electron pairs in 40 AGeV Pb-Au collisions at the CERN SPS*, (2002), nucl-ex/0209024.

[16] G. Agakishiev *et al.* (CERES Collaboration), *Low-mass e^+e^- pair production in 158 A GeV Pb-Au collisions at the CERN SPS, its dependence on multiplicity and transverse momentum,* Phys. Lett. **B422**, 405 (1998), nucl-ex/9712008.

[17] B. Lenkeit *et al.* (CERES Collaboration), *Recent results from Pb-Au collisions at 158 GeV/c per nucleon obtained with the CERES spectrometer,* Nucl. Phys. **A661**, 23 (1999), nucl-ex/9910015.

[18] G.-Q. Li, C. M. Ko, and G. E. Brown, *Enhancement of low mass dileptons in heavy ion collisions,* Phys. Rev. Lett. **75**, 4007 (1995), nucl-th/9504025.

[19] G. E. Brown and M. Rho, *Scaling effective Lagrangians in a dense medium,* Phys. Rev. Lett. **66**, 2720 (1991).

[20] T. Hatsuda and S. H. Lee, *QCD sum rules for vector mesons in nuclear medium,* Phys. Rev. **C46**, 34 (1992).

[21] G. E. Brown and M. Rho, *On the manifestation of chiral symmetry in nuclei and dense nuclear matter,* Phys. Rept. **363**, 85 (2002), hep-ph/0103102.

[22] R. Rapp, G. Chanfray, and J. Wambach, *Rho meson propagation and dilepton enhancement in hot hadronic matter*, Nucl. Phys. **A617**, 472 (1997), hep-ph/9702210.

[23] W. Cassing, E. L. Bratkovskaya, R. Rapp, and J. Wambach, *Probing the ρ spectral function in hot and dense nuclear matter by dileptons,* Phys. Rev. **C57**, 916 (1998), nucl-th/9708020.

[24] R. Rapp and J. Wambach, *Low-mass dileptons at the CERN-SpS: Evidence for chiral restoration?,* Eur. Phys. J. **A6**, 415 (1999), hep-ph/9907502.

[25] J.-Y. Ollitrault, *Anisotropy as a signature of transverse collective flow,* Phys. Rev. **D46**, 229 (1992).

[26] H. Sorge, *Elliptical flow: A signature for early pressure in ultrarelativistic nucleus nucleus collisions,* Phys. Rev. Lett. **78**, 2309 (1997), nucl-th/9610026.

[27] M. Messer, *Photons in Pb-Au collisions at 158 AGeV/c,* PhD thesis, University of Heidelberg, Germany, 1998.

[28] A. Cherlin, *Charged hadron production in Pb-Au collisions at 158 A GeV using the CERES spectrometer,* Diploma thesis, Weizmann Institute of Science Rehovot, Izrael, 1998.

[29] A. Chodos, R. L. Jaffe, K. Johnson, C. B. Thorn, and V. F. Weisskopf, *A New Extended Model of Hadrons,* Phys. Rev. **D9**, 3471 (1974).

[30] K. Johnson, *The M.I.T. Bag Model,* Acta Phys. Polon. **B6**, 865 (1975).

[31] C. Wong, *Introduction to High-Energy Heavy-Ion Collisions* (World Scientific, Singapore, 1994).

[32] F. Karsch, *Lattice results on QCD thermodynamics,* Nucl. Phys. **A698**, 199 (2002), hep-ph/0103314.

[33] W. Busza and A. S. Goldhaber, *Nuclear stopping power,* Phys. Lett. **B139**, 235 (1984).

[34] S. Beolé, *Looking for Quark Gluon Plasma in Pb-Pb collisions at 158 GeV/c,* PhD thesis, Universit Degli Studi Di Torino, 1998.

[35] J. Stachel, *Towards the quark-gluon plasma,* Nucl. Phys. **A654**, 119c (1999), nucl-ex/9903007.

[36] J. W. Harris and B. Muller, *The search for the quark-gluon plasma,* Ann. Rev. Nucl. Part. Sci. **46**, 71 (1996), hep-ph/9602235.

[37] P. Braun-Munzinger, J. Stachel, J. P. Wessels, and N. Xu, *Thermal equilibration and expansion in nucleus-nucleus collisions at the AGS,* Phys. Lett. **B344**, 43 (1995), nucl-th/9410026.

[38] P. Braun-Munzinger, J. Stachel, J. P. Wessels, and N. Xu, *Thermal and hadrochemical equilibration in nucleus-nucleus collisions at the SPS,* Phys. Lett. **B365**, 1 (1996), nucl-th/9508020.

[39] P. Braun-Munzinger, I. Heppe, and J. Stachel, *Chemical equilibration in Pb+Pb collisions at the SPS,* Phys. Lett. **B465**, 15 (1999), nucl-th/9903010.

[40] P. Braun-Munzinger, D. Magestro, K. Redlich, and J. Stachel, *Hadron production in Au-Au collisions at RHIC,* Phys. Lett. **B518**, 41 (2001), hep-ph/0105229.

[41] S. Z. Belenkij and L. D. Landau, *Hydrodynamic theory of multiple production of particles,* Nuovo Cim. Suppl. **3S10**, 15 (1956).

[42] W. Scheid, H. Mueller, and W. Greiner, *Nuclear Shock Waves in Heavy-Ion Collisions,* Phys. Rev. Lett. **32**, 741 (1974).

[43] G. F. Chapline, M. H. Johnson, E. Teller, and M. S. Weiss, *Highly excited nuclear matter,* Phys. Rev. **D8**, 4302 (1973).

[44] A. A. Amsden, G. F. Bertsch, F. H. Harlow, and J. R. Nix, *Relativistic hydrodynamic theory of heavy ion collisions,* Phys. Rev. Lett. **35**, 905 (1975).

[45] M. I. Sobel, H. A. Bethe, P. J. Siemens, and J. P. Bondorf, *Shock wawes in colliding nuclei,* Nucl. Phys. **A251**, 502 (1975).

[46] H. A. Gustafsson *et al.*, *Collective flow observed in relativistic nuclear collisions,* Phys. Rev. Lett. **52**, 1590 (1984).

[47] R. E. Renfordt *et al.*, *Stopping power and collective flow of nuclear matter in the reaction Ar+Pb Aat 0.8-GeV/U,* Phys. Rev. Lett. **53**, 763 (1984).

[48] W. Reisdorf and H. G. Ritter, *Collective flow in heavy-ion collisions,* Ann. Rev. Nucl. Part. Sci. **47**, 663 (1997).

[49] N. Herrmann, J. P. Wessels, and T. Wienold, *Collective flow in heavy-ion collisions,* Ann. Rev. Nucl. Part. Sci. **49**, 581 (1999).

[50] G. D. Westfall *et al.*, *Nuclear fireball model for proton inclusive spectra from relativistic heavy ion collisions,* Phys. Rev. Lett. **37**, 1202 (1976).

[51] I. G. Bearden *et al.* (NA44 Collaboration), *Collective expansion in high energy heavy ion collisions,* Phys. Rev. Lett. **78**, 2080 (1997).

[52] I. G. Bearden *et al.* (NA44 Collaboration), *Kaon and proton ratios from central Pb+Pb collisions at the CERN SPS,* Nucl. Phys. **A638**, 419 (1998).

[53] I. G. Bearden *et al.* (NA44 Collaboration), *One-, two- and three-particle hadron spectra: Recent results from CERN/SPS experiment NA44,* Nucl. Phys. **A638**, 103 (1998).

[54] H. Appelshauser *et al.* (NA49 Collaboration), *Recent results on central Pb+Pb collisions from experiment NA49,* Nucl. Phys. **A638**, 91 (1998).

[55] H. Appelshauser *et al.* (NA49 Collaboration), *Phi emission in central Pb+Pb collisions at 158 GeV/u,* Nucl. Phys. **A638**, 431 (1998).

[56] H. Appelshauser *et al.* (NA49 Collaboration), Ξ *and* $\bar{\Xi}$ *production in 158 GeV/nucleon Pb+Pb collisions,* Phys. Lett. **B444**, 523 (1998), nucl-ex/9810005.

[57] E. Andersen *et al.*, *Enhancement of central* Λ, Ξ *and* Ω *yields in Pb-Pb collisions at 158 A GeV/c,* Phys. Lett. **B433**, 209 (1998).

[58] E. Andersen *et al.* (WA97 Collaboration), *Strangeness enhancement at mid-rapidity in Pb-Pb collisions at 158 A GeV/c,* J. Phys. **G25**, 181 (1999).

[59] M. M. Aggarwal *et al.* (WA98 Collaboration), *Recent results on Pb+Pb collisions at 158 A GeV from the WA98 experiment at CERN,* Nucl. Phys. **A638**, 147 (1998).

[60] E. Schnedermann, J. Sollfrank, and U. W. Heinz, *Thermal phenomenology of hadrons from 200 A/GeV S+S collisions,* Phys. Rev. **C48**, 2462 (1993), nucl-th/9307020.

[61] Y. Akiba *et al.* (E802 Collaboration), *Particle production in Au+Au collisions from BNL E866,* Nucl. Phys. **A610**, 139c (1996).

[62] L. Ahle *et al.* (E802 Collaboration), *Particle production at high baryon density in central Au+Au reactions at 11.6 A GeV/c,* Phys. Rev. **C57**, 466 (1998).

[63] R. Lacasse *et al.* (E877 Collaboration), *Hadron yields and spectra in Au+Au collisions at the AGS,* Nucl. Phys. **A610**, 153c (1996), nucl-ex/9609001.

[64] R. Lacasse, *Hadron production in 10.8 AGeV/c Au+Au collisions*, PhD thesis, McGill University, Montréal, Canada, 1998.

[65] S. Ahmad *et al.*, *Lambda production by 11.6 AGeV/c Au beam on Au target,* Phys. Lett. **B382**, 35 (1996).

[66] K. S. Lee and U. W. Heinz, *Collective flow model for the pion transverse momentum spectra from relativistic nuclear collisions at CERN*, Z. Phys. **C43**, 425 (1989).

[67] K. S. Lee, U. W. Heinz, and E. Schnedermann, *Search for collective transverse flow using particle transverse momentum spectra in relativistic heavy ion collisions,* Z. Phys. **C48**, 525 (1990).

[68] J. D. Bjorken, *Highly relativistic nucleus-nucleus collisions: the central rapidity region,* Phys. Rev. **D27**, 140 (1983).

[69] H. von Gersdorff, *Is there evidence for flow in heavy ion collisions?,* Nucl. Phys. **A525**, 697c (1991).

[70] S. Voloshin and Y. Zhang, *Flow study in relativistic nuclear collisions by Fourier expansion of azimuthal particle distributions*, Z. Phys. **C70**, 665 (1996), hep-ph/9407282.

[71] S. Wang *et al.*, *Measurement of collective flow in heavy ion collisions using particle pair correlations,* Phys. Rev. **C44**, 1091 (1991).

[72] A. M. Poskanzer and S. A. Voloshin, *Methods for analyzing anisotropic flow in relativistic nuclear collisions,* Phys. Rev. **C58**, 1671 (1998), nucl-ex/9805001.

[73] N. Borghini, P. M. Dinh, and J.-Y. Ollitrault, *A new method for measuring azimuthal distributions in nucleus nucleus collisions,* Phys. Rev. **C63**, 054906 (2001), nucl-th/0007063.

[74] N. Borghini, P. M. Dinh, and J.-Y. Ollitrault, *Flow analysis from multiparticle azimuthal correlations,* Phys. Rev. **C64**, 054901 (2001), nucl-th/0105040.

[75] N. Borghini, P. M. Dinh, and J.-Y. Ollitrault, *Flow analysis from cumulants: A practical guide,* (2001), nucl-ex/0110016.

[76] D. Adamova *et al.* (CERES Collaboration), *New results from CERES,* Nucl. Phys. **A698**, 253 (2002).

[77] L. Phair *et al.*, *Azimuthal Correlations as a Test for Centrality in Heavy Ion Collisions,* Nucl. Phys. **A564**, 453 (1993).

[78] N. Bastid *et al.* (FOPI Collaboration), *Out-of-plane emission of nuclear matter in Au+Au collisions between 100 MeV and 800 MeV,* Nucl. Phys. **A622**, 573 (1997).

[79] D. L'Hote, *Experimental investigation of the nuclear equation of state,* Nucl. Phys. **A488**, 457 (1988).

[80] H. H. Gutbrod *et al.*, *A new component of the collective flow in relativistic heavy ion collisions,* Phys. Lett. **B216**, 267 (1989).

[81] S. Wang *et al.*, *In-Plane Retardation of Collective Expansion in Au+Au Collisions,* Phys. Rev. Lett. **76**, 3911 (1996).

[82] D. Brill *et al.*, *Study of the out-of-plane emission of protons and light fragments in symmetric heavy-ion collisions,* Z. Phys. **A355**, 61 (1996).

[83] N. N. Ajitanand *et al.* (E895 Collaboration), *Collective flow in Au+Au collisions between 2 A GeV to 8 A GeV at AGS,* Nucl. Phys. **A638**, 451 (1998).

[84] C. Pinkenburg *et al.* (E895 Collaboration), *Elliptic flow: Transition from out-of-plane to in-plane emission in Au+Au collisions,* Phys. Rev. Lett. **83**, 1295 (1999), nucl-ex/9903010.

[85] P. Chung *et al.* (E895 Collaboration), *Differential elliptic flow in 2 A GeV - 6 A GeV Au+Au collisions: A new constraint for the nuclear equation of state,* Phys. Rev. **C66**, 021901 (2002), nucl-ex/0112002.

[86] J. Barrette *et al.* (E877 Collaboration), *Observation of anisotropic event shapes and transverse flow in Au+Au collisions at AGS energy,* Phys. Rev. Lett. **73**, 2532 (1994), hep-ex/9405003.

[87] J. Barrette *et al.* (E877 Collaboration), *Energy and charged particle flow in 10.8 A GeV/c Au+Au collisions,* Phys. Rev. **C55**, 1420 (1997), nucl-ex/9610006.

[88] J. Barrette *et al.* (E877 Collaboration), *Proton and pion production relative to the reaction plane in Au+Au collisions at 11 A GeV/c,* Phys. Rev. **C56**, 3254 (1997), nucl-ex/9707002.

[89] H. Appelshauser *et al.* (NA49 Collaboration), *Directed and elliptic flow in 158-GeV/nucleon Pb+Pb collisions,* Phys. Rev. Lett. **80**, 4136 (1998), nucl-ex/9711001.

[90] K. Filimonov *et al.* (CERES Collaboration), *New results on Pb-Au collisions at 40 A GeV from the CERES/NA45 experiment,* (2001), nucl-ex/0109017.

[91] C. Alt *et al.* (NA49 Collaboration), *Directed and elliptic flow of charged pions and protons in Pb+Pb collisions at 40 A GeV and 158 A GeV,* (2003), nucl-ex/0303001.

[92] K. H. Ackermann *et al.* (STAR Collaboration), *Elliptic flow in Au+Au collisions at* $\sqrt{s_{NN}}$ *=130 GeV,* Phys. Rev. Lett. **86**, 402 (2001), nucl-ex/0009011.

[93] C. Adler *et al.* (STAR Collaboration), *Identified particle elliptic flow in Au+Au collisions at* $\sqrt{s_{NN}}$ *=130 GeV,* Phys. Rev. Lett. **87**, 182301 (2001), nucl-ex/0107003.

[94] K. Adcox (PHENIX Collaboration), *Flow measurements via two-particle azimuthal correlations in Au+Au collisions at* $\sqrt{s_{NN}} = 130$ *GeV,* Phys. Rev. Lett. **89**, 212301 (2002), nucl-ex/0204005.

[95] B. B. Back *et al.* (PHOBOS Collaboration), *Pseudorapidity and centrality dependence of the collective flow of charged particles in Au+Au collisions at* $\sqrt{s_{NN}} = 130$ *GeV,* Phys. Rev. Lett. **89**, 222301 (2002), nucl-ex/0205021.

[96] R. P. Feynman, R. D. Field, and G. C. Fox, *Correlations among particles and jets produced with large transverse momenta,* Nucl. Phys. **B128**, 1 (1977).

[97] R. P. Feynman, R. D. Field, and G. C. Fox, *Quantum-chromodynamic approach for the large-transverse- momentum production of particles and jets,* Phys. Rev. **D18**, 3320 (1978).

[98] J. F. Owens and J. D. Kimel, *Parton-transverse-momentum effects and the quantum-chromodynamic description of high-*p_T *processes,* Phys. Rev. **D18**, 3313 (1978).

[99] J. F. Owens, *Large momentum transfer production of direct photons, jets, and particles,* Rev. Mod. Phys. **59**, 465 (1987).

[100] M. Arneodo *et al.* (European Muon Collaboration), *Measurements of the nucleon structure function in the range 0.002 GeV* $^2 < x <$ *0.17 GeV* ^{2} *and 0.2 GeV* $^2 < Q^2 <$ *8 GeV* ^{2} *in deuterium, carbon and calcium,* Nucl. Phys. **B333**, 1 (1990).

[101] D. Antreasyan *et al., Production of hadrons at large transverse momentum in 200 GeV, 300 GeV and 400 GeV p-p and p-N collisions,* Phys. Rev. **D19**, 764 (1979).

[102] D. A. Appel, *Jets as a probe of quar - gluon plasmas,* Phys. Rev. **D33**, 717 (1986).

[103] J. P. Blaizot and L. D. McLerran, *Jets in expanding quark - gluon plasmas,* Phys. Rev. **D34**, 2739 (1986).

[104] M. Rammerstorfer and U. W. Heinz, *Jet acoplanarity as a quark-gluon plasma probe,* Phys. Rev. **D41**, 306 (1990).

[105] M. Gyulassy and X.-n. Wang, *Multiple collisions and induced gluon Bremsstrahlung in QCD,* Nucl. Phys. **B420**, 583 (1994), nucl-th/9306003.

[106] X.-N. Wang, M. Gyulassy, and M. Plumer, *The LPM effect in QCD and radiative energy loss in a quark gluon plasma,* Phys. Rev. **D51**, 3436 (1995), hep-ph/9408344.

[107] R. Baier, Y. L. Dokshitzer, S. Peigne, and D. Schiff, *Induced gluon radiation in a QCD medium,* Phys. Lett. **B345**, 277 (1995), hep-ph/9411409.

[108] R. Baier, Y. L. Dokshitzer, A. H. Mueller, S. Peigne, and D. Schiff, *Radiative energy loss and p(T)-broadening of high energy partons in nuclei*, Nucl. Phys. **B484**, 265 (1997), hep-ph/9608322.

[109] B. G. Zakharov, *Fully quantum treatment of the Landau-Pomeranchuk-Migdal effect in QED and QCD,* JETP Lett. **63**, 952 (1996), hep-ph/9607440.

[110] K. Adcox *et al.* (PHENIX Collaboration), *Suppression of hadrons with large transverse momentum in central Au+Au collisions at* $\sqrt{s_{NN}}$ *=130 GeV,* Phys. Rev. Lett. **88**, 022301 (2002), nucl-ex/0109003.

[111] K. Adcox *et al.* (PHENIX Collaboration), *Centrality dependence of the high p(T) charged hadron suppression in Au + Au collisions at* $\sqrt{s_{NN}} = 130$ *GeV,* Phys. Lett. **B561**, 82 (2003), nucl-ex/0207009.

[112] J. L. Klay (STAR Collaboration), *High p(T) inclusive charged hadron spectra from Au+Au collisions at* $\sqrt{s_{NN}}$ *=200 GeV,* (2002), nucl-ex/0210026.

[113] S. S. Adler *et al.* (PHENIX Collaboration), *Suppressed* π^0 *production at large transverse momentum in central Au + Au collisions at* $\sqrt{s_{NN}} = 200$ *GeV,* (2003), nucl-ex/0304022.

[114] X.-N. Wang, *Resolving mini - jets in the minimum biased events of hadronic interactions,* Phys. Rev. **D46**, 1900 (1992).

[115] X.-N. Wang, *Where is the jet quenching in Pb+Pb collisions at 158A GeV?,* Phys. Rev. Lett. **81**, 2655 (1998), hep-ph/9804384.

[116] H. Busching (WA98 Collaboration), *Angular correlations of high momentum photons at 158 A GeV p+A and Pb+Pb collisions,* Nucl. Phys. **A698**, 635 (2002).

[117] S. Bathe (WA98 Collaboration), *High* p_T π^0 *production and angular correlations in 158 A GeV p+A and Pb+Pb collisions,* (2002), nucl-ex/0209022.

[118] W. Schmitz, *Lambda-Production in Pb-Au-Kollisionen bei 40 AGeV,* PhD thesis, University of Heidelberg, Germany, 2001.

[119] H. Tilsner, *Two-particle correlations at 40, 80, and 158 AGeV Pb-Au collisions,* PhD thesis, University of Heidelberg, Germany, 2002.

[120] E. Gatti and P. Rehak, *Semiconductor drift chamber - an application of a novel charge transport scheme,* Nucl. Instrum. Meth. **A225**, 608 (1984).

[121] P. Rehak *et al.*, *Semiconductor drift chambers for position and energy measurements,* Nucl. Instrum. Meth. **A235**, 224 (1985).

[122] P. Rehak *et al., Progress in semiconductor drift detectors*, Nucl. Instrum. Meth. **A248**, 367 (1986).

[123] W. Leo, *Techniques for nuclear and particle physics experiments* (Springer-Verlag, 1994).

[124] J. Rak (CERES Collaboration), private communication.

[125] A. Wörner, *Messungen an einer linearen Multianodensiliziumdriftkammer und Untersuchungen zur Integration einer radialen Driftkammer in das Experiment CERES*, Diploma thesis, University of Heidelberg, Germany, 1990.

[126] E. Gatti, A. Longoni, M. Sampietro, and P. Rehak, *Dynamics of electrons in drift detectors*, Nucl. Instrum. Meth. **A253**, 393 (1987).

[127] V. Petráček (CERES Collaboration), private communication.

[128] S. Sze, *Physics of semiconductor devices* (John Wiley & Sons, New York, 1981).

[129] P. Holl *et al., A 55-cm^2 cylindrical silicon drift detector*, Nucl. Instrum. Meth. **A377**, 367 (1996).

[130] U. Faschingbauer *et al., A doublet of 3-inch cylindrical silicon drift detectors in the CERES experiment*, Nucl. Instrum. Meth. **A377**, 362 (1996).

[131] W. Dabrowski *et al., OLA, a low-noise bipolar amplifier for the readout of silicon drift detectors*, Nucl. Phys. Proc. Suppl. **44**, 637 (1995).

[132] G. Gramegna, P. O'Connor, P. Rehak, and S. Hart, *Low-noise CMOS preamplifier-shaper for silicon drift detectors*, IEEE Trans. Nucl. Sci. **44**, 385 (1997).

[133] O. Nix, *Einsatz und Lasertest von 4" Siliziumdriftdetektoren*, Diploma thesis, University of Heidelberg, Germany, 1996.

[134] J. Ousterhout, *Tcl an the Tk Toolkit* (Addison-Wesley Prof. Comp. Series, 1994).

[135] G. Agakishiev *et al., Effective pulse resolution algorithms for detectors with Gaussian like signal shape*, JINR-E10-97-105.

[136] G. Agakishiev *et al., A new robust fitting algorithm for vertex reconstruction in the CERES experiment*, Nucl. Instrum. Meth. **A394**, 225 (1997).

[137] L. D. Landau, J. Exp. Phys. (USSR) **8**, 201 (1944).

[138] R. Brun *et al., HBOOK - Statistical Analysis and Histogramming*, CERN Program Library Long Writeup Y250, 1994.

[139] B. Jähne, *Digitale Bildverarbeitung* (Springer-Verlag, 1993).

[140] G. Agakishiev *et al., Čerenkov ring fitting techniques for the CERES RICH detectors*, Nucl. Instrum. Meth. **A371**, 243 (1996).

[141] F. Ceretto, *Charged hadron production in Pb-Au collisions at 158 AGeV/c*, PhD thesis, University of Heidelberg, Germany, 1998.

[142] R. Brun *et al.*, *GEANT*, CERN DD/EE/84-1, 1984.

[143] P. Glässel (CERES Collaboration), private communication.

[144] S. Tapprogge, *Pad-Auslese der RICH-Detektoren des CERES/NA45-Experimentes: Entwicklungsarbeiten und Untersuchung der Signale einzelner UV-Photonen*, Diploma thesis, University of Heidelberg, Germany, 1992.

[145] W. Press, *Numerical Recepies in C++* (Cambridge University Press, 1992).

[146] R. Glauber, *Lectures in Theoretical Physics* (Interscience, N.Y., 1959).

[147] K. J. Eskola, K. Kajantie, and J. Lindfors, *Quark and gluon production in high-energy nucleus-nucleus collisions*, Nucl. Phys. **B323**, 37 (1989).

[148] S. A. Bass *et al.*, *Microscopic models for ultrarelativistic heavy ion collisions*, Prog. Part. Nucl. Phys. **41**, 225 (1998), nucl-th/9803035.

[149] H.-J. Specht (CERES Collaboration), private communication.

[150] T. Alber *et al.* (NA35 Collaboration), *Charged particle production in proton, deuteron, oxygen and sulphur nucleus collisions at 200 GeV per nucleon*, Eur. Phys. J. **C2**, 643 (1998), hep-ex/9711001.

[151] M. M. Aggarwal *et al.* (WA98 Collaboration), *Scaling of particle and transverse energy production in ^{208}Pb+^{208}Pb collisions at 158 A GeV*, Eur. Phys. J. **C18**, 651 (2001), nucl-ex/0008004.

[152] S. V. Afanasiev *et al.* (NA49 Collaboration), *Energy dependence of pion and kaon production in central Pb + Pb collisions*, Phys. Rev. **C66**, 054902 (2002), nucl-ex/0205002.

[153] I. G. Bearden *et al.* (NA44 Collaboration), *Particle production in Pb+Pb collisions at the CERN-SPS*, (2002), nucl-ex/0202019.

[154] D. Irmscher, *Photonen in ultrarelativistischen S-Au-Kollisionen bei 200 GeV pro Nukleon*, PhD thesis, University of Heidelberg, Germany, 1993.

[155] H. Appelshauser *et al.* (NA49 Collaboration), *Baryon stopping and charged particle distributions in central Pb+Pb collisions at 158-GeV per nucleon*, Phys. Rev. Lett. **82**, 2471 (1999), nucl-ex/9810014.

[156] F. Antinori *et al.* (WA97 Collaboration), *Transverse mass spectra of strange and multi-strange particles in Pb-Pb collisions at 158 A GeV/c*, Eur. Phys. J. **C14**, 633 (2000).

[157] R. Albrecht *et al.* (WA80 Collaboration), *Transverse momentum distributions of neutral pions from nuclear collisions at 200-A-GeV,* Eur. Phys. J. **C5**, 255 (1998), nucl-ex/9805007.

[158] M. M. Aggarwal *et al.* (WA98 Collaboration), *Centrality dependence of neutral pion production in 158 A GeV ^{208}Pb+^{208}Pb collisions,* Phys. Rev. Lett. **81**, 4087 (1998), nucl-ex/9806004.

[159] M. M. Aggarwal *et al.* (WA98 Collaboration), *Freeze-out parameters in central 158 A GeV ^{208}Pb+^{208}Pb collisions,* Phys. Rev. Lett. **83**, 926 (1999), nucl-ex/9901009.

[160] M. M. Aggarwal *et al.* (WA98 Collaboration), *Transverse mass distributions of neutral pions from ^{208}Pb induced reactions at 158 A GeV,* Eur. Phys. J. **C23**, 225 (2002), nucl-ex/0108006.

[161] M. M. Aggarwal (WA98 Collaboration), *One-, two- and three-particle distributions from 158 A GeV/c central Pb+Pb collisions,* Phys. Rev. **C67**, 014906 (2003), nucl-ex/0210002.

[162] K. Hagiwara *et al.* (Particle Data Group Collaboration), *Review of particle physics,* Phys. Rev. **D66**, 010001 (2002).

[163] B. Alper *et al.* (British-Scandinavian Collaboration), *Production spectra of $\pi^{\pm}$, $K^{\pm}$, $\rho^{\pm}$ at large angles in proton-proton collisions in the CERN intersecting storage rings,* Nucl. Phys. **B100**, 237 (1975).

[164] F. W. Busser *et al., Observation of π^0 mesons with large transverse momentum in high-energy proton-proton collisions,* Phys. Lett. **B46**, 471 (1973).

[165] F. W. Busser *et al., A study of inclusive spectra and two particle correlations at large transverse momentum,* Nucl. Phys. **B106**, 1 (1976).

[166] D. W. Sivers, S. J. Brodsky, and R. Blankenbecler, *Large transverse momentum processes,* Phys. Rept. **23**, 1 (1976).

[167] R. Blankenbecler and S. J. Brodsky, *Unified description of inclusive and exclusive reactions at all momentum transfers,* Phys. Rev. **D10**, 2973 (1974).

[168] R. Hagedorn, *Multiplicities, p(T) distributions and the expected hadron $\rightarrow$ quark - gluon phase transition,* Riv. Nuovo Cim. **6N10**, 1 (1984).

[169] M. A. Faessler, *Experiments with alpha particles at the CERN Intersecting Storage Rings,* Phys. Rept. **115**, 1 (1984).

[170] W. M. Geist, D. Drijard, A. Putzer, R. Sosnowski, and D. Wegener, *Hadronic production of particles at large transverse momentum: Its relevance to hadron structure, parton fragmentation and scattering,* Phys. Rept. **197**, 263 (1990).

[171] R. Hagedorn, *Statistical thermodynamics of strong interactions at high- energies*, Nuovo Cim. Suppl. **3**, 147 (1965).

[172] T. Peitzmann, *Influence of hydrodynamics on the interpretation of the high p_T hadron suppression at RHIC*, (2003), nucl-th/0303046.

[173] J. W. Cronin *et al.*, *Production of hadrons with large transverse momentum at 200 GeV, 300 GeV, and 400 GeV*, Phys. Rev. **D11**, 3105 (1975).

[174] D. A. Garbutt *et al.*, *Nuclear size dependence of inclusive particle production*, Phys. Lett. **B67**, 355 (1977).

[175] D. Chaney *et al.*, *Inclusive charged particle production in neutron - nucleus collisions*, Phys. Rev. **D19**, 3210 (1979).

[176] H. J. Frisch *et al.*, *Inclusive production of hadrons at high P_T in 200 and 300 GeV π^-p and π^-- nucleus collisions*, Phys. Rev. **D27**, 1001 (1983).

[177] A. Krzywicki, J. Engels, B. Petersson, and U. Sukhatme, *Does a nucleus act like a gluon filter?*, Phys. Lett. **B85**, 407 (1979).

[178] M. Lev and B. Petersson, *Nuclear effects at large transverse momentum in a QCD parton model*, Z. Phys. **C21**, 155 (1983).

[179] A. Drees, *Inklusive Produktion von negativ geladenen Teilchen in p-Kern und Kern-Kern Kollisionen bei 200 GeV pro Nukleon*, PhD thesis, University of Heidelberg, Germany, 1989.

[180] T. Akesson *et al.* (Helios Collaboration), *Inclusive negative particle $p_\perp$ spectra in p-nucleus and nucleus-nucleus collisions at 200 GeV per nucleon*, Z. Phys. **C46**, 361 (1990).

[181] H. R. Schmidt and J. Schukraft, *The Physics of ultrarelativistic heavy ion collisions*, J. Phys. **G19**, 1705 (1993).

[182] S. Chapman, P. Scotto, and U. W. Heinz, *Model independent features of the two-particle correlation function*, Heavy Ion Phys. **1**, 1 (1995), hep-ph/9409349.

[183] U. A. Wiedemann and U. W. Heinz, *Resonance contributions to HBT correlation radii*, Phys. Rev. **C56**, 3265 (1997), nucl-th/9611031.

[184] B. Tomasik, U. A. Wiedemann, and U. W. Heinz, *Reconstructing the freeze-out state in Pb+Pb collisions at 158 A GeV/c*, Heavy Ion Phys. **17**, 105 (2003), nucl-th/9907096.

[185] D. Adamova *et al.* (CERES Collaboration), *Beam energy and centrality dependence of two-pion Bose-Einstein correlations at SPS energies*, Nucl. Phys. **A714**, 124 (2003), nucl-ex/0207005.

[186] H. Appelshauser *et al.* (NA49 Collaboration), *Hadronic expansion dynamics in central Pb+Pb collisions at 158 GeV per nucleon,* Eur. Phys. J. **C2**, 661 (1998), hep-ex/9711024.

[187] U. A. Wiedemann and U. W. Heinz, *Particle interferometry for relativistic heavy-ion collisions,* Phys. Rept. **319**, 145 (1999), nucl-th/9901094.

[188] F. James and M. Roos, *'MINUIT' a system for function minimization and analysis of the parameter errors and correlations,* Comput. Phys. Commun. **10**, 343 (1975).

[189] W. Broniowski and W. Florkowski, *Explanation of the RHIC p(T)-spectra in a thermal model with expansion,* Phys. Rev. Lett. **87**, 272302 (2001), nucl-th/0106050.

[190] W. Broniowski and W. Florkowski, *How much is RHIC different from SPS? Comparison of the p(T)-spectra,* Acta Phys. Polon. **B33**, 1935 (2002), nucl-th/0204025.

[191] J. Slívová (CERES/NA45 Collaboration), *Flow and non-flow event anisotropies at the SPS,* Nucl. Phys. **A715**, 615 (2003), nucl-ex/0212013.

[192] G. Agakichiev *et al.* (CERES/NA45 Collaboration), *Semi-hard scattering unraveled from collective dynamics by two-pion correlations in 158-A-GeV/c Pb + Au collisions,* (2003), nucl-ex/0303014.

[193] P. Danielewicz and G. Odyniec, *Transverse momentum analysis of collective motion in relativistic nuclear collisions,* Phys. Lett. **B157**, 146 (1985).

[194] R. L. Ray and R. S. Longacre, *MEVSIM: A Monte Carlo event generator for STAR,* (2000), nucl-ex/0008009.

[195] W. Chang, *The azimuthally anisotropic flow of transverse energy and identified protons and charged pions in 10.8 AGeV/c Au+Au collisions at AGS,* PhD thesis, SUNY Stony Brook, USA, 1997.

[196] Y. Dai, *Study of directed flow in Au+Au Collisions at 11.5 AGeV/c,* PhD thesis, McGill University Montréal, Canada, 1998.

[197] N. Borghini, P. M. Dinh, and J.-Y. Ollitrault, *Are flow measurements at SPS reliable?,* Phys. Rev. **C62**, 034902 (2000), nucl-th/0004026.

[198] P. M. Dinh, N. Borghini, and J.-Y. Ollitrault, *Effects of HBT correlations on flow measurements,* Phys. Lett. **B477**, 51 (2000), nucl-th/9912013.

[199] G. Bertsch, M. Gong, and M. Tohyama, *Pion interferometry in ultrarelativistic heavy ion collisions,* Phys. Rev. **C37**, 1896 (1988).

[200] S. Pratt, T. Csoergoe, and J. Zimanyi, *Detailed predictions for two pion correlations in ultrarelativistic heavy ion collisions,* Phys. Rev. **C42**, 2646 (1990).

[201] H. Tilsner (CERES Collaboration), private communication.

[202] C. Adler *et al.* (STAR Collaboration), *Azimuthal anisotropy and correlations in the hard scattering regime at RHIC*, (2002), nucl-ex/0206006.

[203] P. Huovinen, private communication.

[204] P. F. Kolb, P. Huovinen, U. W. Heinz, and H. Heiselberg, *Elliptic flow at SPS and RHIC: From kinetic transport to hydrodynamics*, Phys. Lett. **B500**, 232 (2001), hep-ph/0012137.

[205] P. F. Kolb, J. Sollfrank, and U. W. Heinz, *Anisotropic flow from AGS to LHC energies*, Phys. Lett. **B459**, 667 (1999), nucl-th/9906003.

[206] D. Teaney, J. Lauret, and E. V. Shuryak, *A hydrodynamic description of heavy ion collisions at the SPS and RHIC*, (2001), nucl-th/0110037.

[207] J. Sollfrank, *Chemical equilibration of strangeness*, J. Phys. **G23**, 1903 (1997), nucl-th/9707020.

[208] F. Becattini, M. Gazdzicki, and J. Sollfrank, *On chemical equilibrium in nuclear collisions*, Eur. Phys. J. **C5**, 143 (1998), hep-ph/9710529.

[209] D. Teaney, *Chemical freezeout in heavy ion collisions*, (2002), nucl-th/0204023.

[210] D. Teaney, *The effect of viscosity on spectra, elliptic flow, and HBT radii*, (2003), nucl-th/0301099.

[211] U. W. Heinz and P. F. Kolb, *Two RHIC puzzles: Early thermalization and the HBT problem*, (2002), hep-ph/0204061.

[212] R. J. M. Snellings (STAR Collaboration), *Elliptic flow in Au+Au collisions at* $\sqrt{s_{NN}}$ *=130 GeV*, Nucl. Phys. **A698**, 193 (2002), nucl-ex/0104006.

[213] R. A. Lacey (PHENIX Collaboration), *Elliptic flow measurements with the PHENIX detector*, Nucl. Phys. **A698**, 559 (2002), nucl-ex/0105003.

[214] H. Sorge, *Highly sensitive centrality dependence of elliptic flow: A novel signature of the phase transition in QCD*, Phys. Rev. Lett. **82**, 2048 (1999), nucl-th/9812057.

[215] H. Heiselberg and A.-M. Levy, *Elliptic flow and HBT in non-central nuclear collisions*, Phys. Rev. **C59**, 2716 (1999), nucl-th/9812034.

[216] G. Arnison *et al.* (UA1 Collaboration), *Jet fragmentation into charged particles at the CERN proton - anti-proton collider*, Phys. Lett. **B132**, 223 (1983).

[217] B. Z. Kopeliovich, *Initial / final state interaction in dijet production off nuclei*, Phys. Lett. **B343**, 387 (1995).

[218] M. D. Corcoran *et al.* (E609 Collaboration), *Evidence for multiple scattering of high-energy partons in nuclei*, Phys. Lett. **B259**, 209 (1991).

[219] E. M. Levin and M. G. Ryskin, *How large is the average transverse momentum of partons, is is larger than 1 GeV/c?,* Sov. Phys. JETP **42**, 783 (1975).

[220] A. L. S. Angelis *et al.* (CERN-Columbia-Oxford-Rockefeller Collaboration), *A measurement of the transverse momenta of partons, and of jet fragmentation as a function of $\sqrt{s}$ in p-p collisions,* Phys. Lett. **B97**, 163 (1980).

[221] S. A. Voloshin, *Azimuthal and rapidity correlations of high-p_t particles in Pb+Pb collisions at the CERN SPS,* 1999, NA49 note, number 179.

[222] C. Adler *et al.* (STAR Collaboration), *Disappearance of back-to-back high p(T) hadron correlations in central Au+Au collisions at $\sqrt{s_{NN}} = 200$ GeV,* Phys. Rev. Lett. **90**, 082302 (2003), nucl-ex/0210033.

[223] D. Hardtke (STAR Collaboration), *Jets and dijets in Au+Au and p+p collisions at RHIC,* (2002), nucl-ex/0212004.

[224] R. L. Ray (STAR Collaboration), *Correlations, fluctuations, and flow measurements from the STAR experiment,* (2002), nucl-ex/0211030.

[225] C. Adler *et al.* (STAR Collaboration), *Elliptic flow from two- and four-particle correlations in Au+Au collisions at $\sqrt{s_{NN}}$ =130 GeV,* Phys. Rev. **C66**, 034904 (2002), nucl-ex/0206001.

[226] J. P. Wurm (CERES Collaboration), private communication.

Acknowledgements

At this place, I would like to express my gratitude to many people who have been important for me during this work.

Foremost, I am deeply thankful to prof. Johann Peter Wurm for being an excellent supervisor and for inviting me to work during the first part of my PhD in the Max-Planck-Institut für Kernphysik in Heidelberg. His enthusiasm and experience helped me to make the research interesting and enjoyable.

I am also very thankful to prof. Johanna Stachel for her offer to stay during the second part of my PhD study in the Physikalisches Institut der Universität Heidelberg to finish my thesis and for her encouragement.

Next, I would like to thank to my consultants, Dr. Michal Šumbera and Dr. Jan Rak for their support during my research. Especially, I am thankful to Dr. Michal Šumbera for introducing me to the CERES experiment, and Dr. Jan Rak for the possibility to learn many things about the silicon drift detectors.

I express also many thanks to Ana Marin and Vojtěch Petráček for their help and careful reading of the manuscript.

For nice working atmosphere and many encouraging words, I would like to thank to my Ceresian colleagues in Heidelberg: prof. Hannes Wessels, prof. Peter Glässel, Heinz Tilsner, Jovan Milošević, Sergej Iourevitch, ShinIchi Esumi, Harry Appelshäuser, Kirill Filimonov, Hejdar Agakichiev, Wolfgang Schmitz, Hans-Kristian Soltveit, and Wilrid Ludolphs. I thank also to the members of the CERES group in GSI Darmstadt, especially to Gunar Hering, Dariusz Miśkowiec and Hiroyuki Sako.

I would like to thank to Pasi Huovinen for providing me with the hydrodynamical calculations of elliptic flow, to Phuo Mai Dinh and Jean-Yves Ollitrault for the discussions on HBT corrections to elliptic flow, to prof. Thomas Peitzmann for providing me with the WA98 π^0 data, to Christoph Blume for the discussion on hydrodynamical fits of the transverse mass spectra, and to Alberto Accardi and prof. Hans Jürgen Pirner for many interesting discussions on minijet production.

Last but not least, I want to thank to my boyfriend Jaro and my family for their love, constant support and patience.

CERES/NA45 Collaboration

P. Rehak
BNL, Upton, U.S.A.

B. Lenkeit, A. Pfeiffer, J. Schukraft
CERN, Geneva, Switzerland

G. Agakichiev, P. Braun-Munzinger, C. Garabatos, G. Hering, J. Holeczek, A. Maas, A. Marín, D. Miśkowiec, H. Sako, S. Sedykh,
GSI Darmstadt, Germany

H. Appelshäuser, S. Damjanović, T. Dietel, L. Dietrich, S. I. Esumi, K. Filimonov, P. Glässel, W. Ludolphs, J. Milošević, V. Petráček, W. Schmitz, H. J. Specht, J. Stachel, H. Tilsner, J. P. Wessels, T. Wienold, B. Windelband, S. Iourevitch
Physikalisches Institut der Universität Heidelberg, Heidelberg, Germany

J. Rak, J. Slívová, J. P. Wurm
Max-Planck-Institut für Kernphysik, Heidelberg, Germany

V. Belaga, K. Fomenko, Yu. Panebrattsev, O. Petchenova, S. Shimansky, V. Yurevich
JINR Dubna, Russia

D. Adamová, V. Kushpil, M. Šumbera
NPI ASCR, Řež, Czech Republic

A. Drees, F. Messer
SUNY at Stony Brook, U.S.A.

A. Cherlin, Z. Fraenkel, A. Gnaenski, A. Milov, I. Ravinovich, I. Tserruya, W. Xie
Weizmann Institute, Rehovot, Israel